A STUDY OF THE PARAMETERS AFFECTING THE PROPAGATION OF ULTRASONIC WAVES IN PIEZO-ELECTRIC SEMICONDUCTORS

A THESIS SUBMITTED FOR THE
DEGREE OF DOCTOR OF PHILOSOPHY
IN THE UNIVERSITY OF ASTON IN BIRMINGHAM

ROBERT MICHAEL ROLLASON, B.Sc.

Physics Department

March 1969

ABSTRACT

An investigation was carried out of the variation of acoustic attenuation coefficient of a single crystal of photoconducting cadmium sulphide, with frequency, crystal resistivity, applied voltage and input acoustic power level.

Suitable techniques were developed for fabricating acoustic amplifier structures consisting of transmitting and receiving shear wave ultrasonic transducers bonded to silica rods between which the cadmium sulphide crystal was sandwiched.

The measurement of the acoustic attenuation coefficient was carried out for applied electric fields of up to $\pm$ 2 kV cm^{-1}. These measurements were carried out for a wide range of crystal resistivities and at frequencies from 15.6 MHz to 358.8 MHz. The measurements showed the attenuation-voltage curves for a given frequency to deviate considerably from that expected from theoretical considerations.

An experimental technique to measure crystal non-uniformity was developed. The technique involved phasing the application of the d.c. applied voltage pulse with respect to the entry of the pulse of ultrasonics into the cadmium sulphide. Analysis showed the presence of high resistance regions adjacent to the electrical contact areas.

The effect of these regions on the ultrasonic propagation was considerable under certain conditions and was shown to be a significant factor in the deviation of the experimental attenuation -

voltage curves from theory.

Several previously unreported measurements were taken of the propagation of large amplitude ultrasonics in cadmium sulphide. The behaviour of the acoustic harmonics generated in the cadmium sulphide was monitored and shown to be consistent with an explanation given for certain features of the non-linear behaviour.

The non-linearity was shown to modify considerably the attenuation-voltage curves unless the input acoustic power was limited.

The acousto-electric effect was used to compare the input acoustic powers at several frequencies. The input acoustic power at 46.8 MHz was measured by an insertion-loss technique and was used for calibration of the input power at other frequencies.

INDEX

SECTION 1

INTRODUCTION

1.1 General Note

The research described in this Thesis was concerned with the study of the propagation of ultrasonic waves in cadmium sulphide (CdS). In this introduction a description is given of the field of electro-acoustic interaction in CdS and the scope of this thesis is delineated.

The discovery of piezoelectrically active acoustic waves in semiconducting materials is described and their nature is discussed.

A review is given of experimental and theoretical work, as published in the literature, of the behaviour of ultrasonic waves in CdS with particular reference to the acoustic amplification process, and of related phenomena.

The techniques used for the growth and quality assessment of single crystal CdS are briefly reviewed.

1.2 The background to the present research

1.2.1. The electro-acoustic interaction

In 1959 Hutson[1] found a large phonon-drag contribution to the Seebeck coefficient whilst looking at the thermo-electric properties of ZnO. Debye's theory of specific heats[2] predicts that the lattice vibrations in a solid are quantized and the term phonon is used to describe a quantized lattice vibration. The phonon-drag

FIG. 1. PIEZOELECTRIC POLARISATION PRODUCED BY PLANE ACOUSTIC WAVES (AFTER McFEE[8])

particle motion parallel to the 'C' axis were found to be photo-sensitive whilst those with particle motion perpendicular to the 'C' axis, and longitudinal waves, were not photo-sensitive. The particle motion referred to is the periodic displacement of atoms in the crystal lattice caused by the propagation of an acoustic wave. The work of Hutson provided an explanation for Nine's results. The observed directional properties of photosensitive ultrasonic propagation were attributed to piezo-electric electron-phonon coupling. The waves affected by the illumination were those that should couple to the conduction electrons if the coupling mechanism was piezoelectricity. Also the waves which were unaffected by illumination corresponded to the waves which are piezoelectrically inactive in CdS.

The piezoelectric coupling between acoustic waves and electrons is only significant in certain cases, namely for the piezoelectrically active waves. For plane acoustic waves propagating through a piezoelectric material the transverse components of the piezoelectric polarisation will give rise to charges only at the boundaries of the crystal fig. 1(a). Electric charges separated by only half an acoustic wavelength are produced by the longitudinal component of piezo-electric polarisation, fig. 1(b). The longitudinal electrostatic fields are much stronger than the transverse fields. Piezoelectrically active waves are those acoustic plane waves whose propagation direction and particle motion are such that a longitudinal component of piezoelectric polarisation is produced.

CdS has a di-hexagonal polar (wurtzite) structure. This consists of two interpenetrating close-packed hexagonal lattices, one

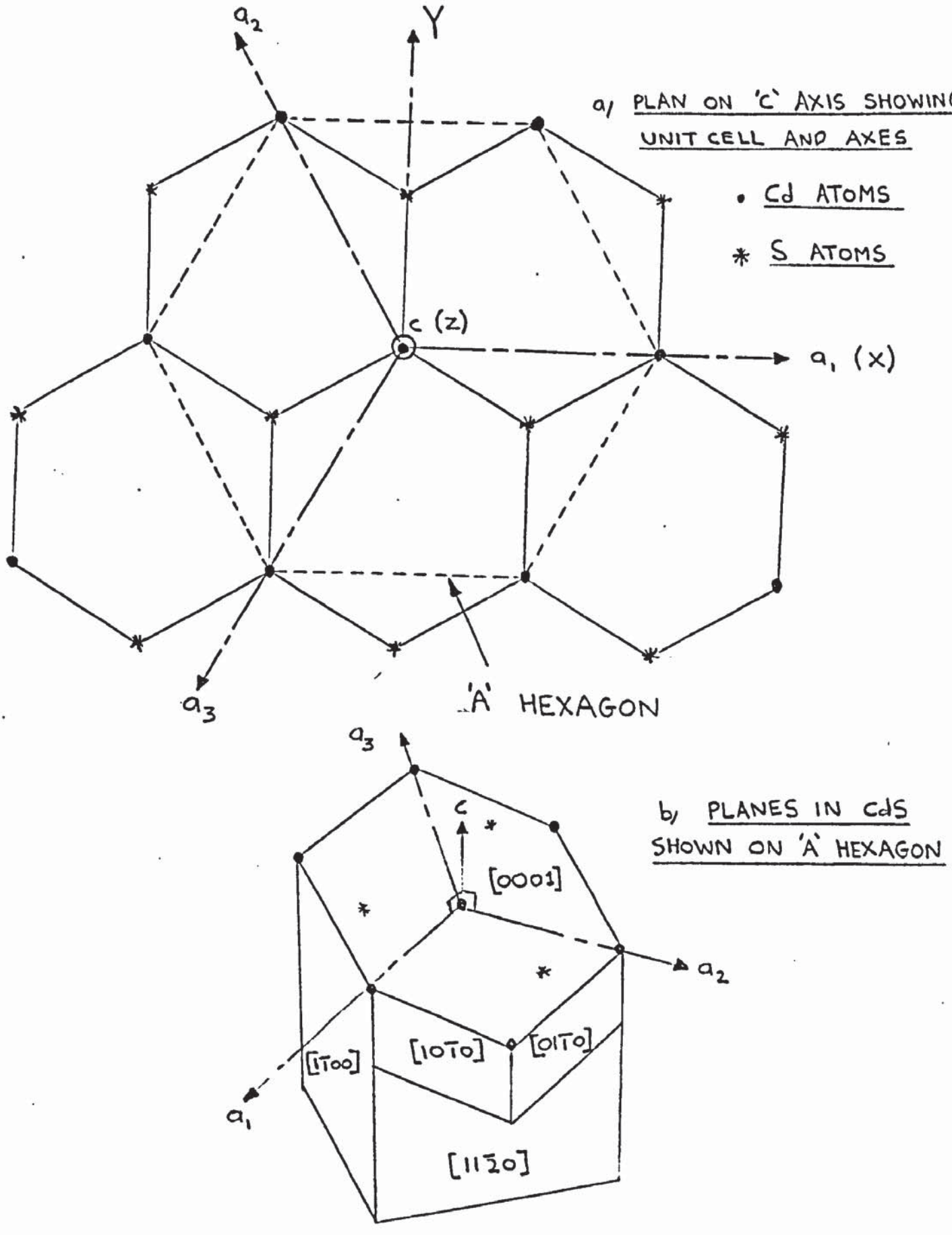

FIG. 2. CRYSTALLOGRAPHIC PLANES IN CdS

of Cd atoms and one of S atoms. Each S atom is at the centre of a tetrahedron whose corners are occupied by Cd atoms and each Cd atom is at the centre of a tetrahedron of S atoms. Fig.2 (a) shows a plan of the unit cell. The two types of tetrahedron point in opposite directions along the 'C' axis so that the opposite directions of this axis are not equivalent. A compressive strain along the 'C' axis causes the centres of the positive and negative charges in each type of tetrahedron to move apart along the 'C' axis. This produces a longitudinal piezoelectric field and hence a longitudinal wave propagating along the 'C' axis is piezoelectrically active.

In general the mechanical strain S_h produced by an electrical field E_i in a piezoelectric material is given by:

$$S_h = d_{ih} E_i \quad \ldots\ldots\ldots\ldots\ldots\ldots \quad 1.1$$

d_{ih} are the piezoelectric constants.

The strain can be resolved into six components, three of tensile strain, S_1, S_2 and S_3 along the X , Y, Z axes respectively and another three of shear strain, S_4, S_5 and S_6 about those axes.

Expanding eqn. 1.1 we get:

$$\left.\begin{aligned} S_1 &= d_{11} E_1 + d_{21} E_2 + d_{31} E_3 \\ S_2 &= d_{12} E_1 + d_{22} E_2 + d_{32} E_3 \\ S_3 &= d_{13} E_1 + d_{23} E_2 + d_{33} E_3 \\ S_4 &= d_{14} E_1 + d_{24} E_2 + d_{34} E_3 \\ S_5 &= d_{15} E_1 + d_{25} E_2 + d_{35} E_3 \\ S_6 &= d_{16} E_1 + d_{26} E_2 + d_{36} E_3 \end{aligned}\right\} \quad \ldots\ldots\ldots \quad 1.2$$

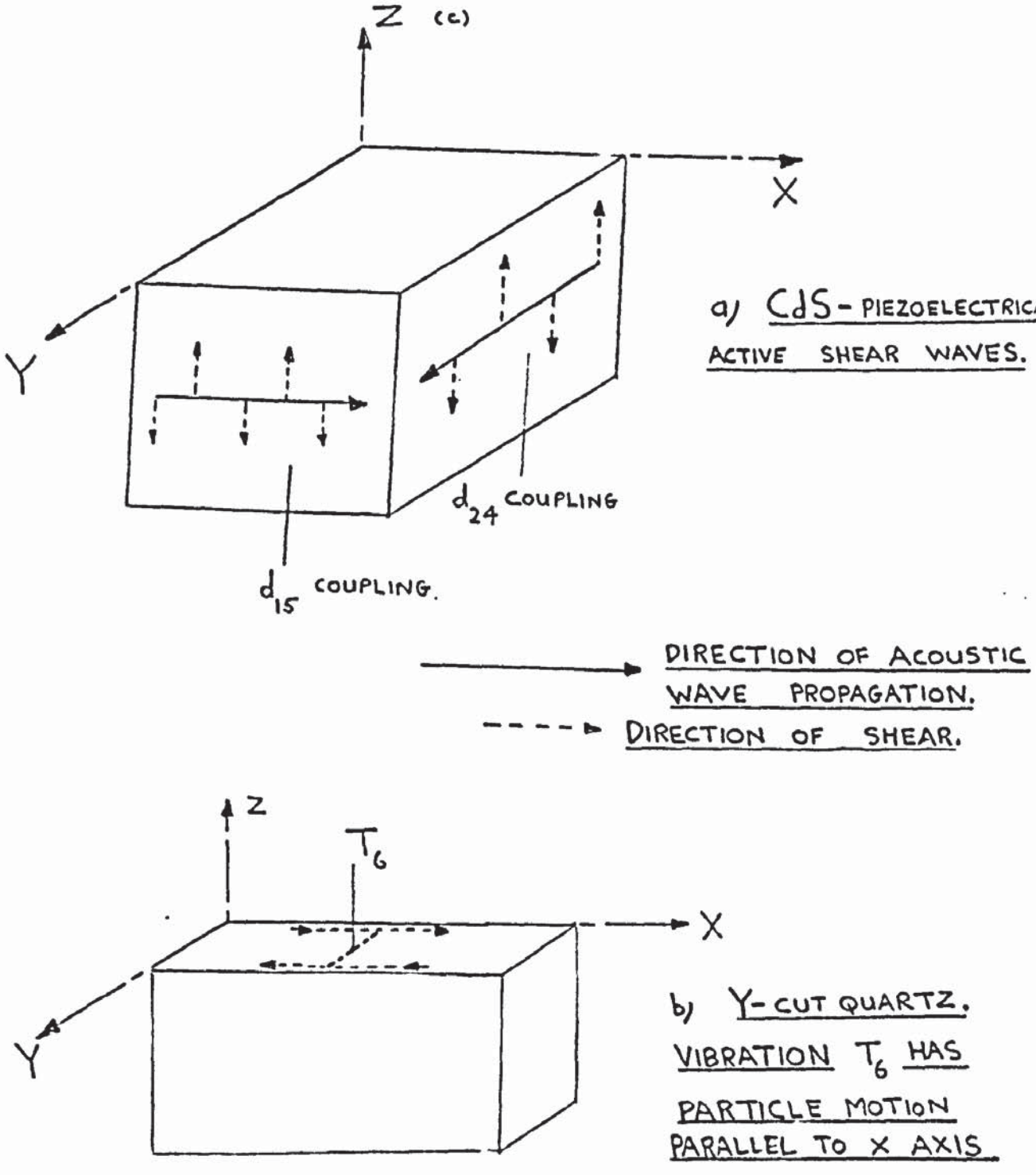

FIG. 3. SHEAR WAVE PROPAGATION IN CdS AND QUARTZ

Jaffe et al[5] and Berlincourt[6] have given the complete piezoelectric constants of CdS. For CdS there are only three independent piezoelectric constants that are non-zero, as follows:

$$d_{31} = d_{32}$$

$$d_{15} = d_{24}$$

$$d_{33}$$

The equations 1.2 simplify to:

$$S_1 = d_{31} E_3 \quad \ldots\ldots\ldots\ldots\ldots\ldots \quad 1.3$$

$$S_2 = d_{32} E_3 \quad \ldots\ldots\ldots\ldots\ldots\ldots \quad 1.4$$

$$S_3 = d_{33} E_3 \quad \ldots\ldots\ldots\ldots\ldots\ldots \quad 1.5$$

$$S_4 = d_{24} E_2 \quad \ldots\ldots\ldots\ldots\ldots\ldots \quad 1.6$$

$$S_5 = d_{15} E_1 \quad \ldots\ldots\ldots\ldots\ldots\ldots \quad 1.7$$

Eqn. 1.5 shows that a longitudinal wave propagating in the 'C' direction is piezoelectrically active. Eqn. 1.6 shows that a shear wave propagating in the Y direction, fig 3(a), with particle motion along the 'C' axis has the electric field along the Y axis. Hence it is piezoelectrically active. Similarly eqn. 1.7 shows the shear wave propagating in the X direction with particle motion parallel to the 'C' axis to be piezoelectrically active. Eqns. 1.3 and 1.4 show that longitudinal waves propagating in the X and Y directions produce components of piezoelectric polarisation in the 'C' direction only and these waves are not piezoelectrically active.

The results of Nine[4], and Nine and Truell[7] are consistent with a piezoelectric mechanism.

FIG. 4. ACOUSTIC AMPLIFIER STRUCTURE (AFTER HUTSON ET AL[10])

FIG. 5. ULTRASONIC ATTENUATION IN CdS (AFTER HUTSON ET AL[10])

1.2.2 Ultrasonic amplification

White [10] suggested that instead of the relatively weak deformation - potential coupling proposed by Weinreich [9], the strong piezoelectric coupling could be used to amplify ultrasonic waves. White realised that the same mechanism which caused positive acoustic attenuation in the absence of electron drift should cause negative attenuation (amplification) when the electron drift velocity exceeded the acoustic wave velocity. Following White's suggestion, Hutson, McFee and White [10] amplified transverse ultrasonics in photoconducting CdS by the application of a d.c. electric field which caused the drift velocity of optically excited electrons to exceed the velocity of sound. The experimental arrangement used is shown in fig. 4. Micro-second pulses of ultrasonics produced at the first transducer propagated through the CdS crystal and were detected at the second transducer. The CdS was orientated for d_{15} coupling. A d.c. voltage pulse of approximately 5μ S. duration was applied between the indium contacts. The acoustic buffers provided electrical insulation between the r.f. and high voltage circuits and a convenient time delay. Fig.5 shows the observed effects of the electron drift velocity on the ultrasonic attenuation as a function of the frequency of the ultrasonics and the crystal resistivity.

At frequencies of 15 and 45 MHz the authors obtained acoustic amplification coefficients of 26 and 54 db $cm.^{-1}$ respectively. The acoustic signal propagated through the CdS maintained in the dark was used as a reference level for calculating the amplification coefficients.

An analysis of the propagation of ultrasonics in piezoelectric semiconductors by Hutson and White [11] was extended by White [12] to cover the case when a d.c. electric field was applied. The theory was developed for the case of plane acoustic waves in a n-type semiconductor such that $k\bar{\ell} << 1$

$k = \frac{2\Pi}{\lambda}$ = propagation constant of the ultrasonics

λ = acoustic wavelength

$\bar{\ell}$ = mean free path of the electrons

A discussion of the theory is given in section 2.1 of this thesis. The absorption coefficient α was obtained as:

$$\alpha = \frac{K^2}{2} \frac{\omega_c}{V_s \gamma} \left[1 + \frac{\omega_c^2}{\gamma^2 \omega^2} \left(1 + \frac{\omega^2}{\omega_c \omega_D} \right)^2 \right]^{-1} \quad \ldots 1.8$$

α = absorption coefficient. Nepers cm^{-1}.

K = electro-mechanical coupling coefficient

$K^2 = \frac{d^2}{\epsilon s}$

d = piezo-electric constant

ϵ = electrical permittivity

s = appropriate elastic constant

ω_c = dielectric relaxation frequency

$= \frac{\sigma}{\epsilon}$

σ = electrical conductivity

V_s = phase velocity of sound

ω_D = diffusion frequency

$= \frac{V_s^2}{fD_n}$

f = fraction of space charge not trapped

D_n = diffusion coefficient

$\gamma = 1 - \frac{f\mu E_o}{V_s}$

μ = electron mobility

E_o = applied d.c. field

ω = angular frequency of sound wave

Fig. 5 includes the theoretical curves for three cases. The agreement between the theoretical curves and the experimental ones is far from perfect. The theoretical curves are symmetrical about the cross-over point ie. the maximum attenuation equals the maximum amplification. However the experimental curves are asymmetric, with the maximum gain less than the maximum attenuation.

White's theory had recognised that there could be a division of the acoustically produced space charge between the conduction band and bound states in the energy gap but he assumed that the bound charge although bound in the sense of not contributing to the conductivity, equilibrates with the conduction band in a time short compared to the frequency of the sound waves ie. the electron trapping relaxation time τ was much less than $\frac{1}{\omega}$. An investigation by Uchida et al[13] showed that when the product of the relaxation time of the electron trapping and the angular frequency of the sound is of the order of unity the phase difference between the charge bunching in the bound states and the charge bunching in the conduction band becomes appreciable and the fraction f takes a complex form. Under this condition the dependence of α on the applied voltage becomes considerably asymmetric about

FIG. 6. EXPERIMENTAL ULTRASONIC AMPLIFICATION IN CdS. (AFTER ISHIGURO ET AL.[14])

FIG. 7. THEORETICAL ULTRASONIC ATTENUATION IN CdS. (AFTER ISHIGURO ET AL[19])

the value of the voltage at which $\alpha = 0$. Further the frequency characteristics of α deviate from the White theory. Uchida et al[13] developed modifications to Whites theory so that the limitation $\tau << \frac{1}{\omega}$ no longer applied. A discussion of the theory is given in section 2.3 of this thesis. The amplification coefficient α' was obtained as:-

$$\alpha' = \frac{-K^2}{2} \frac{\omega}{V_s} \frac{\gamma' \frac{\omega}{\omega_c} + a\left(\frac{\omega^2}{\omega_c \omega'_D} + \frac{\omega}{\omega_c} a\right)}{\left(\gamma' \frac{\omega}{\omega_c} - a\right)^2 + \left(1 + \frac{\omega^2}{\omega_c \omega'_D} + \frac{\omega}{\omega_c} a\right)^2} \quad \ldots 1.9$$

The symbols are the same as eqn. 1.8 except for the following

α' = amplification coefficient

$\gamma' = 1 - \frac{V'_d}{V_s}$

V'_d = modified effective electron drift velocity

$= -bf\mu E_o$

ω'_D = modified diffusion frequency

$= \frac{V_s^2}{bf\, D_n}$

The constants 'a' and 'b' are related to the magnitude of the trapping effects. The values of 'a' and 'b' can vary for different CdS crystals. When a = 0 and b = 1 eqn. 1.9 simplifies to eqn. 1.8.

An experimental investigation by Ishiguro et al [14] showed that when the conductivity of the crystal was low the deviation from White's theory became considerable. Fig.6 shows the experimental results obtained by Ishiguro et al [14] and fig.7 shows the theoretical expectations of White's theory and the trapping theory. Experimentally

the largest gain and the most symmetrical curves corresponded to the highest conductivity. Trapping effects caused the cross-over field to decrease as the carrier concentration increased. The general agreement between experiment and the trapping theory shows that trapping effects can be a significant factor in the electro-acoustic interaction in CdS.

There are some advantages in using shear waves rather than longitudinal waves in electro-acoustic devices. One advantage derives from the velocity of sound for shear waves being less than for longitudinal waves. In CdS $V_s = 1.75 \times 10^5$ cm. sec^{-1} for shear waves and 4.41×10^5 cm. sec^{-1} for longitudinal waves, Bolef et al [15]. Accordingly a smaller drift field, with consequent reduction of ohmic heating, is required to obtain supersonic electron drift. Astrov et al[16] studied the propagation of 10 MHz longitudinal ultrasonics in CdS and observed breakdown of the CdS when applying sufficiently large fields for acoustic amplification.

McFee[17] has reported that when using longitudinal waves the apparent cross-over point on the amplification - voltage curve corresponded to that expected for shear waves. McFee considers that this phenomenon is brought about by the amplification of shear waves whose wave vectors make finite angles with the 'C' axis.

In the experimental work on electro-acoustic devices previously mentioned, both the drift field and the acoustic input were pulsed. The use of a low duty cycle drift field pulse reduces the ohmic heating of the CdS. Wanuga [18] has reported working at 60MHz using continuous drift fields. He restricted the resistivity of the

CdS used to somewhat higher values than is usual in order to minimise ohmic heating. Acoustic gains of 20db and 12db were observed for pulsed r.f. input and continuous r.f. input respectively. The reduced gain with continuous acoustic input is thought to be due to the increased acoustic flux built up as a result of crystal boundary reflections. The term acoustic flux refers to the broadband acoustic spectrum that is produced by amplification of piezoelectrically active lattice waves. McFee [17] and Wang et al [19] have reported that the gain of ultrasonic waves is reduced in the presence of acoustic flux.

A mechanism which is unfavourable for continuous drift field operation was discussed by White [20], who showed theoretically that appreciable distortion of initially plane elastic wavefronts may occur in piezoelectric semiconductors because of heating effects and dispersion. Continuous operation of the d.c. drift field will produce a temperature gradient between the centre and the edges of the crystal. Such distortion of the wavefronts would cause a considerable reduction in response for the usual phase sensitive transducer.

Workers concerned with producing an electronic circuit element from the electro-acoustic amplifier have eliminated buffers from the devices in order to increase net electrical gain. Thus, Ishiguro et al [14] have achieved a net gain of 32 db between the electrical input and output terminals at 105 MHz. Hickernell and Sakiotis [21] have obtained a net electrical gain of 40 db at 60 MHz.

May [22] has evaluated the potential of the device as an amplifier of electronic signals and compared it with existing amplifiers. The noise figures obtained for the CdS acoustic amplifier by Hanlon[23]

indicate that it may not have wide application. However the acoustic amplification process is expected to be utilised in several devices. Hemphill et al[24] has described a CdS ultrasonic delay line with variable round trip loss. White et al [25,26] have described an electro-acoustic oscillator that acts as a source of electrical and acoustic oscillations up to frequencies in excess of 5 GHz. The readiness with which the highly refined CdS samples used by White et al[26] will oscillate means that considerable attention has to be paid to design considerations of an intended C.W. electronic amplifier, May [22].

The acoustic gain possible at frequencies high in the MHz range is predicted to be considerably in excess of 100 db $cm.^{-1}$ by the theory of White. Hanlon [27] has shown that for room temperature operation the maximum possible ultrasonic gain is limited to about 80 decibels due to the build up of acoustic noise flux. The considerable experimental difficulties, and difficulty of obtaining good quality crystals of CdS, have limited the experimental.investigations in this region of the frequency spectrum. White et al [26] have observed the amplification of ultrasonics in CdS at a frequency of 220 MHz. Blotekjaer and Quate [28] have studied ultrasonic amplification in the range 500 - 700 MHz. For some of their experiments the transducers were operated in a re-entrant microwave cavity. The results showed, amongst other discrepencies from theoretical expectations, a lack of a condition of maximum gain in the attenuation-voltage curves.

1.2.3 Further electro-acoustic phenomena

In addition to the enhanced attenuation and amplification

in CdS the strong piezoelectric coupling between electrons and certain acoustic modes produces many manifestations, including the following:

1. Non-linearity and oscillations in current-voltage characteristics.
2. The acousto-electric effect.
3. Harmonic generation.
4. Microwave emission [29]
5. Propagation of collective waves [30, 31]
6. Piezoelectric polaron effects [32]
7. Acoustic after effects [33]

The first three phenomena listed above are directly relevant to the propagation of acoustic waves in CdS and they will be briefly discussed.

Shortly after the first experiments on ultrasonic amplification, Smith [34] observed current saturation in CdS when the electron drift velocity was greater than the velocity of sound. It was observed that when a voltage pulse was applied, producing supersonic electron drift, the current initially equalled its expected Ohm's law value and then underwent an oscillatory decay to a lower value. For photo-conducting CdS the degree of saturation decreased as the crystal resistivity increased until for low illumination levels the current was ohmic. Hutson [35] ascribed the non-ohmic behaviour to the acousto-electric current accompanying a large ultrasonic flux produced by the acoustic amplification process. He showed theoretically that the acousto-electric current flowed with the acoustic wave when

it is being attenuated and against it when the wave is being amplified. Hence when the voltage exceeds the threshold required for acoustic amplification the acousto-electric current which is associated with waves that are being built-up subtracts from the ohmic current. Hutson's theory predicted that harmonic generation played an important part in the non-ohmic behaviour. A detailed experimental study by McFee [17] showed the current decay to be related to the acoustic flux growth and provided support for Hutson's theory. Experiments on current saturation in CdS have been reported by several workers [36-38]. The current saturation phenomena in CdS has not received a wholly satisfactory explanation as yet. Carleton et al [30], have discussed some of the mechanisms proposed. The experimental observation that the current saturation starts when the electron drift velocity equals the sound velocity enables the electron mobility to be estimated. Values obtained for electron mobility in photoconducting CdS by this method have been reported to be anomalous for electron propagation parallel to the 'C' axis, McFee [17] and Hamaguchi et al [39]. The electron mobility measured by this technique is also sensitive to trapping behaviour, Hamaguchi et al [39]. Moore et al [40] have extracted information about the traps by comparing the Hall mobility with the trap influenced mobility.

Okada and Machino [41] observed that when CdS was non-uniformly illuminated, such that the negative end was illuminated more strongly than the rest of the crystal, the oscillatory decay observed by Smith [34] was prolonged. Depending on voltage, level of illumination and uniformity of illumination the oscillation can

have increasing, constant or decreasing amplitudes. Similarly, adjustments to the experimental parameters can alter the period of the oscillations over a wide range. Experiments on oscillations in CdS have been described by several workers [42 - 46]. It has been established that the mechanism of the phenomena is closely related to the acoustic amplification process but the poor quality of the crystals available has hindered comparisons between the numerous theories.

The term acousto-electric effect refers to the appearance of a d.c. electric field along the direction of propagation of an acoustic wave in certain materials. In CdS the acoustic waves and electrons are piezoelectrically coupled. For no electron drift the acoustic waves feed energy into the electron distribution and the forward momentum transferred represents an electron flow in the direction of the acoustic wave. Under amplifying conditions the electrons feed energy into the acoustic wave and the forward momentum lost represents an electron flow which is opposite in direction to the acoustic wave propagation. The first theoretical treatment and naming of the effect was in 1953 by Parmenter [47] who obtained results in strong disagreement with later workers. Weinreich and White [48] experimentally observed the acousto-electric effect in n-type Ge. In 1962 i.e. after acoustic gain had been observed in CdS, Wang [49] detected the acousto-electric field generated in CdS. Working with 33 MHz ultrasonics Wang found that for zero drift voltage and an acoustic input intensity of approximately 1 Watt cm^{-2} an acousto-electric field of 1 v cm^{-1} was obtained.

This field was some six orders of magnitude larger than the acousto-electric fields produced in Ge by the relatively weak deformation potential coupling, using ultrasonic waves of the same intensity. Weinreich [9] had theoretically obtained a relationship showing the acousto-electric field to be proportional to the acoustic attenuation. The Weinreich relationship is:

$$E_{ae} = \frac{2 \alpha I}{n_o q v_s}$$

E_{ae} = acousto-electric field

α = absorption coefficient (positive or negative)

I = acoustic intensity

n_o = electron density

q = electronic charge

v_s = sound velocity

Wang [49] measured the acousto-electric field as a function of drift field. The acousto-electric field was observed to change sign for large drift fields as did the acoustic attenuation. However the measured acousto-electric field was not zero when the acoustic attenuation was zero as would be expected if the Weinreich relationship was strictly obeyed. Southgate and Spector [50] have shown that the observed violation of Weinreich's relationship was due to the effects of electron trapping.

The possibility of achieving large harmonic generation of acoustic waves in piezo-electric semiconductors was first realised by Hutson [35]. Harmonic generation in CdS has been reported by

Tell [51], Kroger [52], Elbaum and Truell [53] and Ishiguro et al [14]. The field produced by the interaction of the electrons with the acoustic wave contains higher harmonics which produce strain at the harmonic frequencies in strongly piezoelectric materials. This electron stimulated non-linearity greatly exceeds the magnitude of the non-linear effects whose origin is lattice anharmonicity. Kroger [52] showed the amplitude of the second harmonic to be proportional to the square of the amplitude of the injected sound wave whereas the amplitude of the detected fundamental was proportional to the amplitude of the injected sound. Kroger carried out experiments in which the amplitude of the second harmonic was obtained as a function of electron density, for a constant input signal and no applied voltage. He also studied the amplitude of the second harmonic as a function of electric field for a constant input signal and electron density. Results of the latter experiment do not agree as well with theory as the former. Tell [51] took data at the cross-over point in the attenuation-voltage curve. At this point the change in the amplitude of the fundamental during propagation down the crystal is due solely to losses to higher harmonics whilst at other drift voltages the fundamental and harmonics are amplified or attenuated at different rates.

Modifications to White's linear theory for ultrasonic amplification, involving the use of Fourier series in the general case are the basis of present theories of harmonic generation in CdS. The complication of electron trapping effects has not yet been added to the theory. The theories of harmonic generation, Tell [51], Kroger [52], are only valid for extremely modest input

acoustic power levels and relate only to the second harmonic and not to higher harmonics.

1.2.4. Crystal quality

CdS was the first piezoelectric semiconductor to be produced in single crystal form of sufficient size, and having suitable electronic parameters for use in electro-acoustic devices. Other materials are now available although their quality is generally regarded as being inferior to CdS. Newell [54] has given a simplified method of evaluating various piezo-electric semiconductors for use in ultrasonic amplifiers.

Midford [55] and Gordon et al [56] have studied ultrasonic amplification in CdSe. Ishiguro [57] has similarly reported ultrasonic amplification in elemental single crystal Te. Hickernell [58] has investigated the electro-acoustic gain interaction in GaAs.

Considerable effort has been expended attempting to produce large single crystals of CdS having suitable electronic properties, eg. large electron mobility, small trapping effects, large piezoelectric constant, convenient resistivity etc., and a high degree of uniformity both with respect to different areas and from crystal to crystal.

A brief outline of the methods available for producing single crystal CdS is given below. The two basic methods for single crystal preparation of CdS are growth from a liquid phase and from a vapour phase. There are many variations within each of the two approaches. Techniques involving growth from a liquid phase can be divided into three groups:

1) Growth from a stoichiometric or near stoichiometric melt.

2) Growth from a non-stoichiometric melt.

3) Growth from a solvent.

Fahrig [59] has described techniques utilising growth from a melt. Rubenstein and Ryan [60] have described the growth of CdS single crystals from metallic solutions. The solvent metals used include cadmium, tin and bismuth.

In the vapour phase growth method the vapour from which the crystallisation occurs is produced in three main ways:

1) By passing H_2S over heated Cd.

2) Sublimation from previously prepared CdS

3) Direct synthesis from the purified elements.

Clark and Woods [61] have described the growth of large single crystals of CdS using vapour phase techniques.

Normally, low resistance crystals are produced by both of the main growth methods and dopants have to be added to obtain suitable electronic properties. Fahrig [59] and White et al [26] have discussed several methods for doping CdS.

Growth from the vapour phase appears the more successful method at present. Lorenz [62] has reviewed the past work in II-VI materials crystallisation research and discussed the limitations of the two basic methods. A brief description of the procedures used to grow and heat treat the CdS crystals used in our research is given in appendix 1 of this thesis.

The lack of uniformity in electronic properties in a given CdS crystal and the variations in properties between crystals are important factors in the development of electro-acoustic devices.

Wilson [63] has studied the variation of electromechanical coupling coefficient in CdS. He found that etching the [0001] face produced etch pits thought to indicate localised reversal of the polar direction of the 'C' axis. The density of etch pits was reduced successively by an annealing process and the electro-mechanical coupling coefficient was found to increase as the etch pit density was reduced.

The following techniques have been used to study the degree of uniformity of electric field strength in CdS crystals:

1. Electrical contact probes.
2. Capacitive probe.
3. Polarised light probe.

Pressure probes were used to measure the electric field distribution in CdS in early photoconducting experiments in order to measure the voltage barriers produced by non-ohmic electrical contacts (Smith [64]). Recent work on the spatial variation of electric field strength in CdS by Haines and Paige [65] utilised movable gallium probes. In their study of high field domains in CdS Haydl and Quate[66] used tungsten probes which were thermally bonded to the surface by a discharge from a capacitor. McFee and Tien [67] have used vacuum deposited indium strips as probes. Twenty or more contacts, .002" wide and separated by .015", were

evenly distributed along the samples.

Ishida et al [68] have used capacitative probes, similar to those of Gunn[69], to follow the potential variations in current oscillating CdS.

Both of the types of probe mentioned above have the disadvantage of being influenced by the surface regions rather than measuring the behaviour in the bulk. However, by using modestly sized crystals and probing all the faces a fairly consistent picture of the crystal uniformity can be obtained. The optical probe developed by Maines [70] has the advantage of probing the bulk of the CdS. The optical probe consisting of plane polarised light of wavelength 6328Å from a He-Ne laser covered an area of about 1m.m. dia. With the CdS crystal orientated for current flow parallel to the 'C' axis the light was introduced along an X axis with the plane of polarisation at 45° to the 'C' axis. The light emerging from the CdS is in general elliptically polarised. The linear electrooptic (Pockels) effect produced changes in the ellipticity parameters of the emergent light. Use of the linear electrooptic coefficients enabled the electric field strength at various points to be measured.

Recent experiments by Parsons and English [71] have shown that the electron mirror microscope can resolve more detail in the crystal resistivity variation than previous techniques and they have investigated the non uniformity produced by various sulphur treatments of low resistivity CdS.

Paige [72] has shown that the absorption of 35 GHz microwaves is sufficiently high in low resistivity CdS for the variation in the

density of free electrons to be observed.

Robertson and Ash [73] have investigated the internal inhomogeneities in resistivity, electro-mechanical coupling constant and electron drift mobility in photoconducting CdS using an optical probe. The probe consisted of a laminar amplitude modulated beam of light projected through the crystals. The information about the crystal inhomogeneities was extracted from the a.c. component of the current and ultrasonic signal.

1.2.5 Conclusion

In the foregoing sections an outline has been given of researches made which have had some relation to the propagation of ultrasonics in piezoelectric semiconductors.

Some of the works were published during the course of the present research, which commenced at the end of 1964, but at that time it seemed that there was a worthwhile field of investigation open and none of the later publications altered this view.

It was decided to carry out measurements on photoconducting CdS because, of the known piezoelectric semiconductors, CdS was most readily available in single crystals of reasonable size.

The field of electro-acoustic interaction in piezoelectric semiconductors was not related to any previous research undertaken at this University. Accordingly it was decided that the initial research would be on a wide front and that experience would be sought of several electro-acoustic phenomena and the supporting techniques. The research programme was later concentrated to bear

on specific cases of interest. In particular some effects were not studied in detail after it became apparent that they were unduly sensitive to variation in crystal quality and that they were not exhibited at all by some crystals. The research programme, as outlined below, was basically to study phenomena exhibited by all CdS crystals of reasonable quality and efforts were made to evaluate the effects of lack of crystal perfection on experimentally observed behaviour.

It was also decided to select what appeared to be the best single crystal available and, because of the time necessary to fabricate a successful amplifier structure, to concentrate the main research onto this selected crystal.

The research programme was one of measurement of acoustic attenuation with applied voltage and crystal resistivity over a frequency range extending to about 350 MHz using harmonic operation of quartz transducers.

In particular the variation with frequency of maximum gain and the electric field needed for maximum gain for given resistivities were measured.

A method was devised for measuring the lack of uniformity of the CdS (voltage phasing experiment) and the effect of crystal non-uniformity on the attenuation-voltage curve and the attenuation-conductivity curve, for no applied voltage, was investigated.

The effects of large input acoustic power levels on ultrasonic propagation were measured. The behaviour of the acoustic

harmonics produced by the electro-acoustic interaction was monitored whilst using large input power levels.

The comparison of acoustic powers at different operating frequencies was made using the acousto-electric effect.

Section 2

Theory

2.1 White's amplification theory

The interaction of acoustic waves with mobile carriers in piezoelectric semiconductors, with no applied d.c. electric field, was discussed theoretically by Hutson and White [11]. Later White [12] extended the theory to cover the case of an applied d.c. electric field. White's theory was developed using the assumption that the condition $k\bar{\ell} \ll 1$ applied.

k = propagation constant of the acoustic wave

$= \frac{2\Pi}{\lambda}$

λ = acoustic wavelength

$\bar{\ell}$ = mean free path of the carriers.

At 300°K $k\bar{\ell} \simeq 1$ in CdS for an acoustic frequency of 30 GHz, McFee[8]. In the present research experiments were performed at room temperature using ultrasonics of frequency between 15 and 350 MHz. Thus the condition that $k\bar{\ell} \ll 1$ was satisfied. Pippard [74] has discussed the amplification process for the case of $k\bar{\ell} \gg 1$ using a quantum-mechanical approach. An outline of White's theory is given below. In particular the phase relationships between the important parameters in the interaction process are explicitly included and used to give some physical insight to the mechanism.

The treatment applies to plane waves in an n-type semiconductor. The acoustic waves of interest are those longitudinal

and shear waves which are accompanied by a longitudinal piezoelectric field. This means the problem is essentially one dimensional. To avoid the encumbrances of a tensor notation the case considered is that of one piezoelectric constant coupling an ultrasonic wave travelling in the x direction to an electric field in the x direction. For a plane acoustic wave propagating in the x direction the strain S is related to the physical displacement in the medium, u, as follows:

$$S = \frac{\partial u}{\partial x}$$

The basic wave equation for an elastic medium is given by:

$$\frac{\partial^2 u}{\partial t^2} = \frac{c}{\rho} \frac{\partial^2 u}{\partial x^2}$$

$$\rho \frac{\partial^2 u}{\partial t^2} = \frac{\partial T}{\partial x} \quad \ldots\ldots 2.1$$

ρ = mass density

t = time

c = elastic constant

T = stress

The basic equations of state which describe a piezoelectric crystal are given below: see for example Blitz [75] p 45.

$$T = cS - eE \quad \ldots\ldots\ldots\ldots\ldots \quad 2.2$$

$$D = eS + \epsilon E \quad \ldots\ldots\ldots\ldots\ldots \quad 2.3$$

T = stress

S = strain

c = elastic constant at constant electric field

e = piezoelectric constant

E = electric field

D = electric displacement

ϵ = dielectric permittivity at constant strain.

Using eqn. 2.2 for the stress, eqn. 2.1 becomes:

$$\rho \frac{\partial^2 u}{\partial t^2} = c \frac{\partial^2 u}{\partial x^2} - e \frac{\partial E}{\partial x} \quad \ldots\ldots\ldots 2.4$$

To solve this wave equation E must be expressed in terms of u. Gauss' equation and the continuity equation are used for this purpose. The Gauss equation for the one dimension case is:

$$\frac{\partial D}{\partial x} = Q \quad \ldots\ldots\ldots\ldots\ldots 2.5$$

Q = space charge

The space charge Q is written as $Q = -q n_s$

q = magnitude of electronic charge

n_s = the number density of electrons required to produce the space charge

Gauss' equation is expressed as:

$$\frac{\partial D}{\partial x} = -q n_s \quad \ldots\ldots\ldots 2.6$$

The continuity equation is:

$$\frac{\partial J}{\partial x} = \frac{-\partial Q}{\partial t} \quad \ldots\ldots\ldots 2.7$$

J = electric current density

The current density J in an n-type semiconductor is given by:

$$J = q (n_o + f n_s) \mu E + q D_n \frac{\partial n_c}{\partial x} \quad \ldots\ldots\ldots 2.8$$

μ = electron mobility

D_n = electron diffusion constant

Now,

$$n_c = n_o + f n_s$$

n_o is the equilibrium density of electrons in the conduction band, without ultrasonic propagation. n_c is the instantaneous local density of electrons in the conduction band. The deviation from equilibrium is the space charge $q n_s$. Some of the space charge may be produced by trapped electrons and these immobile electrons do not participate in conduction. Only the fraction f of the space charge is present in the conduction band and aids the conduction. If there is no trapping, all the space charge is due to conduction electrons and f = 1. The first term in eqn. 2.8 is due to drift caused by the electric field and the second to diffusion caused by the concentration gradient. Using equations 2.6, 2.7, 2.8 to eliminate J, n_s and n_c we get:

$$\frac{-\partial^2 D}{\partial x \partial t} = \mu \frac{\partial}{\partial x} \left\{ \left(q n_o - f \frac{\partial D}{\partial x} \right) E \right\} - f D_n \frac{\partial^3 D}{\partial x^3} \quad \ldots\ldots 2.9$$

In general the parameters which have space and time dependence are not in phase and we can write:

$$E = E_o + E_1 \exp j (kx - \omega t + \theta_1) \quad \ldots\ldots 2.10$$

$$D = D_o + D_1 \exp j (kx - \omega t + \theta_2) \quad \ldots\ldots 2.11$$

$$u = u_o \exp j (kx - \omega t + \theta_3) \quad \ldots\ldots 2.12$$

$$S = S_o \exp j (kx - \omega t)$$

$$J = J_o \exp j (kx - \omega t + \theta_4)$$

$$n_s = n_{so} \exp j (kx - \omega t + \theta_5)$$

The various phase angles are taken with respect to the strain S.

For convenience we write $\tilde{E}_1 = E_1 \exp j\ (kx-\omega t+\theta_1)$

$$\tilde{D}_1 = D_1 \exp j\ (kx-\omega t+\theta_2)$$

E_o = external d.c. electric field applied parallel to the x axis.

$\tilde{E}_1$ = the alternating electric field due to the ultrasonic wave propagating in a piezoelectric medium.

ω = angular frequency of the ultrasonics = $2\Pi\nu$

ν = cyclic frequency of the ultrasonics.

The parameters u, S, J, n_s, $\tilde{E}_1$, $\tilde{D}_1$ are alternating vector quantities. E_o and D_o, representing the applied electric field and the resulting electric displacement respectively, are fixed vectors that are constant both spatially and temporally.

Using eqns. 2.3, 2.10, 2.11 D is eliminated from eqn.2.9 A linear small signal theory is obtained by neglecting the terms containing the product of two wave amplitudes. The only such term obtained when working on equation 2.9 is due to the product $n_s E_1$ To neglect this term is a valid approximation if n_{so} is small compared to n_o. E_1 is thus obtained as:

$$E_1 \exp j\ (\theta_1 - \theta_3) = \frac{-j\ keu_o}{\epsilon}\left\{1 + \frac{j\sigma}{\epsilon\omega}\left[1+f\mu E_o \frac{k}{\omega}+jD_n f\omega\left(\frac{k}{\omega}\right)^2\right]^{-1}\right\}^{-1} \quad (2.13)$$

σ = electrical conductivity = $n_o q \mu$

Using eqn. 2.13 for E in the wave equation 2.4 we get:

$$\rho\omega^2 = c^1 k^2$$

The modified elastic constant c' is given by:

$$c' = c\left\{ 1 + \frac{e^2}{\epsilon c}\left[1 + \frac{j\sigma}{\epsilon\omega}\left\{1 + f\mu E_o \frac{k}{\omega} + jD_n f\omega \left(\frac{k}{\omega}\right)^2\right\}^{-1}\right]^{-1}\right\} \quad . . \quad (2.14)$$

Including attenuation the ultrasonic wave is described by the following equation:

$$u = u_o \exp(-\alpha x) \exp j(kx - \omega t + \theta_3)$$

α = absorption coefficient (Nepers $cm.^{-1}$)

$$u = u_o \exp j([k + j\alpha]x - \omega t + \theta_3)$$

The modified propagation constant k' becomes

$$k' = j\alpha + \frac{\omega}{V_s} \quad . . . . . \quad (2.15)$$

The coupling between the acoustic wave and the electrons is small in an absolute sense even in such a strongly piezoelectric material as CdS for which $K^2 = .036$ for piezoelectrically active shear waves, Berlincourt[6]. K, the electromechanical coupling coefficient, is given by:

$$k^2 = \frac{e^2}{\epsilon c}$$

It is convenient to put $\omega_c = \frac{\sigma}{\epsilon}$, $\omega_D = \frac{V_s^2}{fD_n}$ and $\gamma = 1 + \frac{f\mu E_o}{V_s}$

ω_c is the dielectric relaxation frequency

ω_D is the diffusion frequency

γ is a comparison of the rate of electron drift, V_d with the velocity of sound.

For electrons $V_d = -f\mu E_o$

Hence $\gamma = 1 - \frac{V_d}{V_s}$

Equation 2.14 becomes:

$$c' = c\left\{1 + K^2\left[1 + j\frac{\omega_c}{\omega}\left\{\gamma + j\frac{\omega}{\omega_D}\right\}^{-1}\right]^{-1}\right\} \quad \ldots \quad (2.16)$$

For acoustic propagation in a passive material, the velocity of sound, V_o is given by:

$$V_o = \left(\frac{c}{\rho}\right)^{\frac{1}{2}}$$

The propagation constant $k = \frac{2\Pi}{\lambda}$

$$= \frac{\omega}{V_o}$$

$$\therefore \quad k = \omega\left(\frac{\rho}{c}\right)^{\frac{1}{2}}$$

For a piezoelectrically active material k becomes k', equation 2.15, and c becomes c', equation 2.16, and the velocity of sound is V_s.

$$\text{ie.} \quad j\alpha + \frac{\omega}{V_s} = \omega\left(\frac{\rho}{c'}\right)^{\frac{1}{2}}$$

Equating real parts $\frac{\omega}{V_s} = R\ \omega\left(\frac{\rho}{c'}\right)^{\frac{1}{2}}$

$$V_s = R\left(\frac{c'}{\rho}\right)^{\frac{1}{2}}$$

$$= R\, V_o\left(\frac{c'}{c}\right)^{\frac{1}{2}} \quad \ldots \ldots \quad (2.17)$$

Equating imaginary parts $\alpha = I\,\omega\left(\frac{\rho}{c'}\right)^{\frac{1}{2}}$

$$= I\,\frac{\omega}{V_o}\left(\frac{c}{c'}\right)^{\frac{1}{2}} \quad \ldots \ldots \quad (2.18)$$

Equation 2.18 becomes:

$$\alpha = \frac{K^2}{2}\,\frac{\omega_c}{V_s\gamma}\left[1 + \frac{\omega_c^2}{\gamma^2\omega^2}\left(1 + \frac{\omega^2}{\omega_c\omega_D}\right)^2\right]^{-1} \quad \ldots \quad (2.19)$$

Equation 2.17 becomes :

$$V_s = \left(\frac{c}{\rho}\right)^{\frac{1}{2}}\left[1 + \frac{K^2}{2}\left(\frac{1 + \frac{\omega_c}{\gamma^2\omega_D} + \frac{\omega^2}{\gamma^2\omega^2_D}}{1 + \frac{\omega^2_c}{\gamma^2\omega^2}\left(1 + \frac{\omega^2}{\omega_c\omega_D}\right)^2}\right)\right] \quad \ldots (2.20)$$

The equations for α and V_s will be discussed later in this section. It is necessary to obtain equations relating $\tilde{E}_1$, J, S and n_s in order to gain some physical insight into the electro-acoustic interaction.

Using the relationships given for material displacement, u, and strain, S, we obtain the following relationship:

$$S_o = u_o jk \exp j\theta_3$$

Thus equation 2.13 becomes

$$E_1 \exp j\theta_1 = -\frac{e}{\epsilon}\,\frac{[\gamma + j\frac{\omega}{\omega_D}]\,S_o}{[\gamma + j\left(\frac{\omega}{\omega_D} + \frac{\omega_c}{\omega}\right)]}$$

Multipliction by exp j (kx- ωt) to both sides yields:

$$\tilde{E}_1 = -\frac{e}{\epsilon}\,\frac{[\gamma + j\frac{\omega}{\omega_D}]\,S}{[\gamma + j\left(\frac{\omega}{\omega_D} + \frac{\omega_c}{\omega}\right)]} \quad \ldots\ldots (2.21)$$

Using equations 2.9 - 11 we get:

$$\tilde{D}_1 \exp j(\theta_2 - \theta_1) = \frac{-j\left(\frac{\sigma}{\omega}\right)E_1}{\gamma + j\frac{\omega}{\omega_D}}$$

Thus

$$\tilde{D}_1 = \frac{-j\left(\frac{\sigma}{\omega}\right)\tilde{E}_1}{\gamma + j\frac{\omega}{\omega_D}} \quad \ldots\ldots\ldots\ldots (2.22)$$

Fig. 8. Acoustic velocity as a function of electron drift parameter γ in a piezoelectric material (After McFee[8])

Combination of equations 2.5 and 2.7 gives

$$\frac{\partial^2 D}{\partial x \partial t} = - \frac{\partial J}{\partial x}$$

This equation enables the alternating current density J to be obtained by using equation 2.22.

$$J = \frac{\sigma \tilde{E}_1}{\gamma + j \frac{\omega}{\omega_D}} \quad \ldots\ldots\ldots\ldots 2.23$$

Also,

$$J = - \frac{\sigma e}{\epsilon} \frac{S}{\gamma + j \left(\frac{\omega}{\omega_D} + \frac{\omega_c}{\omega}\right)} \quad \ldots\ldots\ldots 2.24$$

To obtain the space charge density, n_s, we use equations 2.6 and 2.22

$$n_s = - \frac{\sigma}{q V_s} \frac{\tilde{E}_1}{\left[\gamma + j \frac{\omega}{\omega_D}\right]} \quad \ldots\ldots\ldots 2.25$$

$$= \frac{\sigma e S}{q V_s \epsilon \left[\gamma + j \left\{\frac{\omega_c}{\omega} + \frac{\omega}{\omega_D}\right\}\right]} \quad \ldots\ldots\ldots 2.26$$

For $V_d > V_s$, γ is negative and the attenuation is negative. Fig. 5 shows the dependence of the attenuation constant on the applied electric field.

Fig. 8 shows the variation of V_s with the electron drift parameter γ. The acoustic wave velocity has a minimum value of approximately V_o at $\gamma = o$ and asymptotically approaches the value of $V_o \left(1 + \frac{K^2}{2}\right)$ for $|\gamma| >> |$. When $\gamma = o$ the relative velocity of the drifting electrons and acoustic wave is zero and the electron

distribution can almost completely equilibrate with the acoustic wave. The field of the bunched electrons almost cancels out the longitudinal piezoelectric field of the acoustic wave and the sound velocity is almost identical to that in a passive material having the same values of c and ρ.

From equation 2.26 we have

$$n_s = \frac{\sigma e S}{q V_s \epsilon} \left(\frac{\left[\gamma - j \left(\frac{\omega_c}{\omega} + \frac{\omega}{\omega_D} \right) \right]}{\left[\gamma^2 + \left(\frac{\omega_c}{\omega} + \frac{\omega}{\omega_D} \right)^2 \right]} \right)$$

and

$$n_s^* = \frac{\sigma e s}{q V_s \epsilon} \left(\frac{\left[\gamma + j \left(\frac{\omega_c}{\omega} + \frac{\omega}{\omega_D} \right) \right]}{\left[\gamma^2 + \left(\frac{\omega_c}{\omega} + \frac{\omega}{\omega_D} \right)^2 \right]} \right)$$

A quantity indicated with an asterisk is the complex conjugate of that quantity.

$$|n_s| = n_{so} = \frac{\sigma e S_o}{q V_s \epsilon \left[\gamma^2 + \left(\frac{\omega_c}{\omega} + \frac{\omega}{\omega_D} \right)^2 \right]^{\frac{1}{2}}}$$

Differentiation with respect to γ, holding all other parameters constant gives :

$$\frac{\partial n_{so}}{\partial \gamma} = - \frac{\sigma e S_o \gamma}{q V_s \epsilon \left[\gamma^2 + \left(\frac{\omega_c}{\omega} + \frac{\omega}{\omega_D} \right)^2 \right]^{3/2}}$$

$= o$ at turning points of n_{so} and $\gamma = o$ corresponds to a maximum in n_{so}.

At the synchronous velocity the electron bunching is

larger than for other electron velocities.

For large $|\gamma|$ the velocity of the electrons relative to the acoustic wave is high and the electron distribution cannot respond to the acoustic wave so that negligible bunching occurs. The longitudinal piezoelectric field is then present in full strength so that the material is piezoelectrically stiffened as discussed by Kyame [76]. In this case V_s is greater than V_o. In CdS the maximum fractional velocity variation $\frac{V_s - V_o}{V_o}$ is 1.8% for K_{15} coupling. For very high ultrasonic frequencies the electron distribution cannot respond fully to the acoustic wave even for $\gamma = o$ so that the material is partially piezoelectrically stiffened for all γ.

By considering the acousto-electric effect it can be shown that the amplification coefficient α is particularly related to the vectors J and $\tilde{E}_1$ and we now outline the steps involved.

In deriving the equations of the small signal amplification theory the term $q\mu n_s \tilde{E}_1$, contained in the current density equation, was neglected. This approximation is valid if the condition $n_{so} < n_o$ holds. The term $q\mu n_s \tilde{E}_1$ can be calculated to a first approximation by using the expressions for n_s and $\tilde{E}_1$ given by Whites' theory.

The double periodicity contained by the term $q\mu n_s \tilde{E}_1$ does not average to zero over an acoustic period and the d.c. current produced is called the acousto electric current J_{ae}.

$$J_{ae} = \frac{q\mu}{2\Pi} \int_{0}^{\theta = 2\Pi} n_s \tilde{E}_1 \, d\theta = n_s \cdot \tilde{E}_1 \left(\frac{q\mu}{2} \right)$$

Using equations 2.21 and 2.26 it can be shown that:

$$n_s \cdot \tilde{E}_1 = \frac{-K^2 \omega_c S_o^2 c}{q V_s \gamma \left[1 + \frac{\omega_c^2}{\gamma^2 \omega^2} \left(1 + \frac{\omega^2}{\omega_c \omega_D} \right)^2 \right]}$$

By comparison with the equation for the attenuation coefficient, 2.19, we obtain:

$$n_s \cdot \tilde{E}_1 = \frac{-2\alpha c S_o^2}{q} \quad \ldots\ldots\ldots\ldots\ldots\ldots\ldots\ldots 2.27$$

$$\text{hence } J_{ae} = -\mu c S_o^2 \alpha$$

The acoustic intensity I is given by the following relationship: see for example Blitz [75], p 15.

$$I = \tfrac{1}{2} \rho V_s^3 S_o^2$$

$$= \tfrac{1}{2} c V_s S_o^2 \quad \ldots\ldots\ldots\ldots\ldots\ldots 2.28$$

$$\therefore J_{ae} = \frac{-\mu I 2\alpha}{V_s}$$

The acousto-electric field E_{ae} is related to J_{ae} by the equation:

$$E_{ae} = -\frac{J_{ae}}{\sigma} = -\frac{J_{ae}}{n_o q \mu}$$

$$\therefore E_{ae} = \frac{2\alpha I}{n_o q V_s} \quad \ldots\ldots\ldots\ldots 2.29$$

This is the Weinreich relationship. It is discussed in section 2.2 of this Thesis.

In deriving an expression for E_{ae} it was apparent that α was related to $[n_s \cdot \tilde{E}_1]$. We now further investigate this relationship by combining equation 2.27 and 2.28:

$$2\alpha = -q \frac{V_s}{2I} \quad n_s \cdot \tilde{E}_1$$

From equations 2.24 and 2.26 we have:

$$J = -q V_s n_s$$

ie. J and n_s are identical vectors except for the scalar term $-q V_s$

hence

$$n_s \cdot \tilde{E}_1 = - \frac{J \cdot \tilde{E}_1}{q V_s}$$

and

$$2\alpha = \frac{1}{2} \frac{J \cdot \tilde{E}_1}{I}$$

The term $\frac{J \cdot \tilde{E}_1}{2}$ represents the average power per unit volume dissipated by the a.c. field.

Using equations 2.21, 2.24 and 2.26 we can obtain the relative phases of the acoustic strain S, alternating field $\tilde{E}_1$, a.c. current J, and the electron bunching density n_s. Fig.9a shows the relative phases of these quantities on a rotating vector diagram for the case of $\gamma = o$.

The following simplified expressions were obtained from the three mentioned above and were used to determine the phase angles shown in fig.9. $J = -a_1 [\gamma - j (\frac{\omega_c}{\omega} + \frac{\omega}{\omega_D})] S$

$$\tilde{E}_1 = -a_2 (a_3 - j\gamma a_4) S$$

$$n_s = a_5 [\gamma - j (\frac{\omega_c}{\omega} + \frac{\omega}{\omega_D})] S$$

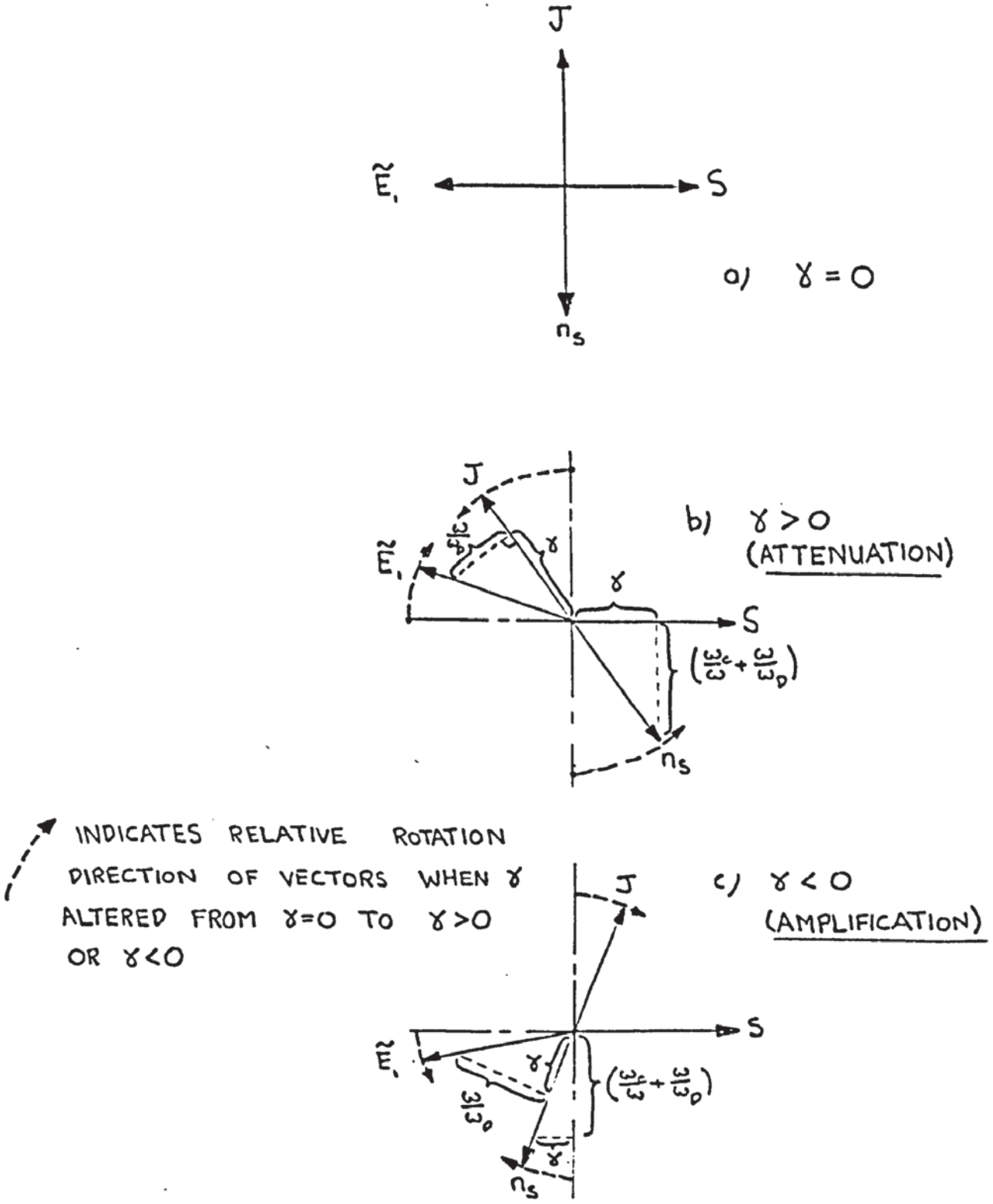

FIG. 9. PHASE RELATIONSHIPS BETWEEN J, $\tilde{E}_1$, S, n_s.

a_1 to a_5 are positive real constants.

Figs. 9(b, c) show the relative phases of S, J, $\tilde{E}_1$ and n_s for attenuating ($\gamma > 0$) and amplifying ($\gamma < 0$) conditions respectively. The following simplification of equation 2.23 was used to obtain the phase angle between J and $\tilde{E}_1$.

$$J = a_6 \left(\gamma - j \frac{\omega}{\omega_D}\right) \tilde{E}_1$$

a_6 is a positive real constant.

J and n_s are exactly 180° out of phase under all conditions.

The attenuation coefficient α is proportional to $J.\tilde{E}_1$. Under conditions such that $\gamma > 0$ the phase angle ϕ between J and $\tilde{E}_1$ is always less than 90°. $J.\tilde{E}_1$ is positive under these conditions indicating an acoustic power loss.

Under conditions of $\gamma < 0$ the phase angle ϕ is within the limits $90^\circ < \phi < 180^\circ$ and the power loss is negative ie. the acoustic wave gains energy from the electrons.

When $\gamma = 0$ ϕ equals 90° so that the acoustic attenuation is zero even if $\tilde{E}_1$ is not completely shorted out.

For small diffusion effects, so that $\frac{\omega}{\omega_D} << 1$, J and $\tilde{E}_1$ are almost exactly in phase for $\gamma > 0$ and almost exactly out of phase for $\gamma < 0$. Diffusion effects increase the acute angle between J and $\tilde{E}_1$ and thus reduce $|\alpha|$.

The sinusoidal electric field due to an acoustic wave propagating in a piezoelectric semiconductor causes current to flow and the current accumulates space charge which is described by equation 2.26. The term electron bunches is used to describe the localised space charge.

This production of electron bunches is illustrated in

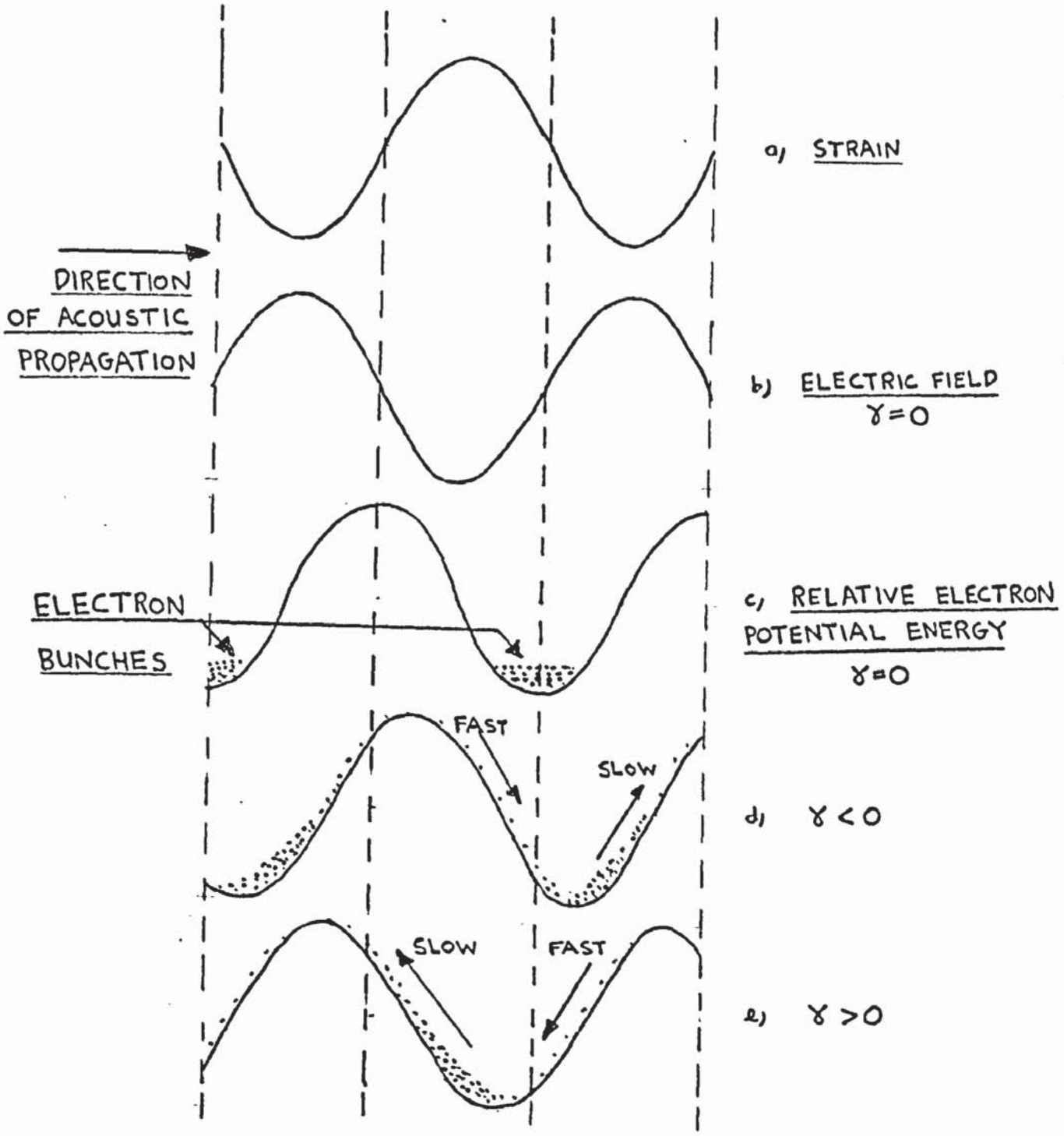

FIG. 10. ELECTRO-ACOUSTIC INTERACTION

fig. 10c for the case of $\gamma = 0$. For $\gamma < 0$ the electrons are overtaking the acoustic wave. The electrons move more slowly in the regions where the electric field of piezoelectric origin opposes the applied electric field and more electrons are found in these regions. The electrons preferentially populate the rising slope of the potential energy curve and amplification results, fig. 10d. The converse is true for the case of $\gamma > 0$, fig. 10e.

The localised electron bunches produce a periodic change in the conductivity of the material.

The acoustic gain depends on the conductivity being modulated and if for example part of the space charge is trapped ie. f is not unity, then the gain is not as large as it is in the absence of trapping effects. The effects of trapping on the performance of an electro-acoustic device can be considerable and this topic is discussed in section 2.3.

2.2. The acousto-electric effect

The Weinreich relationship [9], relating the acousto-electric field E_{ae} to the attenuation coefficient, was derived in section 2.1. using White's amplification theory.

It can also be obtained by equating the average force on the electron distribution to the rate of change of momentum of the acoustic wave.

The acousto-electric force F_{ae} on an electron is given by the expression:

$$F_{ae} = - E_{ae} q$$

E_{ae} is the acousto-electric field

q is charge of the electron.

The total force on n_o electrons is $n_o F_{ae}$.

The rate of momentum loss per unit volume from the acoustic wave is given by the expression

$$\frac{2\alpha I}{V_s}$$

This term is obtained by using the definition of the attenuation coefficient to determine the acoustic intensity and hence energy density at two planes in the acoustic beam. The change in energy density represents a momentum loss per unit volume and the average rate of this momentum loss is obtained as the term above.

Hence $$n_o E_{ae} q = \frac{2\alpha I}{V_s}$$

and $$E_{ae} = \frac{2\alpha I}{n_o q V_s}$$

This is the Weinreich relationship. The acousto-electric field is proportional to the attenuation coefficient α and the direction of electron flow represented by E_{ae} reverses when the sign of α is changed eg. by a suitable applied electric field. As mentioned in section 1.2.3 it has been experimentally observed that the acousto-electric field is not zero when the attenuation coefficient is zero. The above treatment assumed f = 1 and if trapping effects are present f is complex. Spector and Southgate[50] allowed a complex value of f in deriving an expression for the acousto-electric field and showed that when trapping occured the values of the applied drift fields at which the acousto-electric

field and the attenuation coefficient are zero are different.

As discussed in section 4.3.4, the acousto-electric effect is useful for comparing experimentally the acoustic intensity that enters the CdS crystal when the r.f. input is applied to each transducer in turn. It can also compare the acoustic intensities entering the CdS for operation at several frequencies.

2.3. Amplification theory including trapping effects.

Hutson and White [11] realised that the acoustic wave disturbs the equilibrium population of electrons trapped in energy levels inside the energy gap. They considered the case of the trapped electrons equilibrating with the conduction band in times that were short compared to the period of the acoustic wave ie. $\tau << \frac{1}{\omega}$.

τ = relaxation time of electron trapping.

ω = angular frequency of the acoustic wave. For this case charge bunching in the traps is in phase with the acoustic wave and f, the fraction of the acoustically produced space charge that is mobile, is a real number between o and 1. For higher frequency ultrasonics it is possible that $\tau \sim \frac{1}{\omega}$. In this case there is an appreciable phase difference between the trapped electron bunches and the acoustic wave and f becomes complex. For even higher frequencies, such that $\tau >> \frac{1}{\omega}$ electron trapping effects are not produced. In this case f may approach unity. Uchida et al [13] extended the treatment of Hutson and White by assuming an arbitrary trapping relaxation time. A brief outline

of their theory is given below.

For the sake of simplicity it was assumed that only one kind of electron trapping centre existed in a CdS crystal. For frequencies such that $\frac{1}{\omega} >> \tau$ (Whites [12] assumption) the following symbols are used.

f = fraction of space charge mobile.

n_s = total concentration of bunched electrons .

n_1 = concentration of bunched free electrons.

n_2 = concentration of bunched trapped electrons.

The symbols f_o, n_{s1}, n_3 and n_4 refer to the respective quantities listed above, for the condition $\frac{1}{\omega} \hat{<<} \tau$

We have $n_{s1} = n_3 + n_4$

$n_3 = f_o n_{s1}$

$n_4 = n_{s1} (1-f_o)$

and

$n_s = n_1 + n_2 = n_{s1}$

$n_1 = f\ n_s$

$n_2 = n_s (1-f)$

The localised concentration of trapped electrons in the low frequency case is n_2 whilst it is n_4 for the high frequency case. The deviation in density in the high frequency case from the low frequency case is n_4-n_2. This deviation relaxes with a time constant τ

so $$\frac{\partial n_4}{\partial t} = - \frac{(n_4-n_2)}{\tau} \quad \ldots\ldots\ldots (2.30)$$

The use of $-j\omega$ for the operator $\frac{\partial}{\partial t}$ is consistent for waves of the type exp j $(kx-\omega t)$

Equation 2.30 becomes:

$$-j\omega n_4 \tau = -(n_4 - n_2)$$

$$f_o = \frac{f - j\omega\tau}{1 - j\omega\tau}$$

The imaginary part of f_o has a maximum when $\omega\tau = 1$. For convenience in calculating the amplification factor, f_o is rewritten as:

$$f_o = \frac{bf}{1 + ja}$$

where $a = \dfrac{(1-f)\omega\tau}{f+(\omega\tau)^2}$

$$bf = \frac{f^2 + (\omega\tau)^2}{f + (\omega\tau)^2}$$

The constants 'a' and 'b' vary with different CdS crystals depending on the number and type of trapping centre. Both 'a' and 'b' are frequency dependent. The constant 'a' is numerically equal to the ratio of the imaginary to the real part of f_o and $(\tan^{-1} a)$ gives the phase difference between the mobile and total space charge. The constant 'b' affects parameters that include f_o eg. the electron drift parameter γ and the diffusion frequency ω_D.

The modified trapping parameter $f_o = \dfrac{bf}{1 + ja}$

is substituted into the equations used by White, beginning with the current density equation, 2.8, and modified equations for α, n_s etc. are obtained. The following substitutions are made:

The electron drift velocity $V'_d = -bf\mu E_o$

$$\gamma' = 1 - \frac{V'_d}{V_s}$$

$$= 1 + \frac{bf\mu E_o}{V_s}$$

$$\omega'_D = \frac{V_s^2}{bfD_n}$$

Uchida et al[13] used a propagation constant of $k'_1 = \frac{\omega}{V_s} - j\alpha'$

where α' is the amplification coefficient. α' has the opposite sign to the α of White's theory. The amplification coefficient is obtained as:

$$\alpha' = -\frac{K^2\omega}{2V_s} \frac{\gamma' \frac{\omega}{\omega_c} + a\left(\frac{\omega^2}{\omega_c\omega'_D} + \frac{\omega}{\omega_c} a\right)}{\left(\gamma' \frac{\omega}{\omega_c} - a\right)^2 + \left(1 + \frac{\omega^2}{\omega_c\omega'_D} + \frac{\omega}{\omega_c} a\right)^2} \quad \ldots . \quad (2.31)$$

If a = o, b = 1 then $\omega'_D = \omega_D$ and $\gamma' = \gamma$ and equation 2.31 simplifies to equation 2.19 given by Whites' theory. To obtain the values of γ' at which α' is a maximum and minimum, equation 2.31 is differentiated with respect to γ' and $\frac{\partial\alpha'}{\partial\gamma'}$ is set equal to zero. This procedure gives:

$$\gamma'_{max} = -\left(\sqrt{1 + a^2} + a\right)\left(\frac{\omega_c}{\omega} + \frac{\omega}{\omega'_D} + a\right) + a\frac{\omega_c}{\omega} \quad . . \quad (2.32)$$

$$\gamma'_{min} = \left(\sqrt{1 + a^2} - a\right)\left(\frac{\omega_c}{\omega} + \frac{\omega}{\omega'_D} + a\right) + a\frac{\omega_c}{\omega} \quad . . \quad (2.33)$$

γ'_{max} = the value of γ' at which α' is a maximum.

Substitution of these values for γ' into equation 2.31 gives the maximum and minimum values of α' which are:

$$\alpha'_{max} = \frac{K^2\omega}{4V_s} \quad \frac{1}{(\sqrt{1+a^2}+a)\left(1+\frac{\omega^2}{\omega_c\omega'_D}+\frac{\omega}{\omega_c}a\right)} \qquad \ldots\ldots\ldots\ldots (2.34)$$

$$\alpha'_{min} = -\frac{K^2\omega}{4V_s} \quad \frac{1}{(\sqrt{1+a^2}-a)\left(1+\frac{\omega^2}{\omega_c\omega'_D}+\frac{\omega}{\omega_c}a\right)} \qquad \ldots\ldots\ldots\ldots (2.35)$$

(α'_{max}) is the maximum value of the amplification coefficient.

(α'_{min}) represents minimum amplification ie. maximum attenuation.

For comparison, the White theory yields the following values for $[\gamma_{max}]$ and $[\alpha_{max}]$:

$$\gamma = \pm\left\{\frac{\omega_c}{\omega}+\frac{\omega}{\omega_D}\right\}$$

ie. $\gamma_{max} = -\gamma_{min}$

$$\alpha_{max} = -\alpha_{min} = \frac{K^2\omega}{4V_s} \quad \frac{1}{\left(1+\frac{\omega^2}{\omega_c\omega_D}\right)}$$

In White's theory $[\alpha_{min}]$ represents minimum attenuation ie. maximum amplification, and $[\alpha_{max}]$ represents maximum attenuation.

The amplification-voltage curve given by the modified

theory is asymmetric for $a \neq o$. The measure of the asymmetry is given by

$$\left| \frac{\alpha'_{max}}{\alpha'_{min}} \right| = \frac{\sqrt{1 + a^2} - a}{\sqrt{1 + a^2} + a} \quad \ldots\ldots\ldots 2.36$$

The value of γ' at which α' is zero is obtained from equation 2.31 as:

$$\gamma' = -a \left(\frac{\omega}{\omega'_D} + a \right)$$

hence

$$E_o = - \frac{V_s}{bf\,\mu} \left[1 + a \left(\frac{\omega}{\omega\tau_D} + a \right) \right]$$

The drift field at which $\alpha' = o$ varies according to the crystal trapping parameters and the operating conditions eg. crystal resistivity and ultrasonic frequency. Fig.6 gives experimental results showing the asymmetry behaviour and the shift in the cross-over point in the α' versus γ' curve. The modified equations for $\tilde{D}_1$, $\tilde{E}_1$, J, S and n_{s1} are given below:

$$\tilde{D}_1 = \frac{-j \frac{\sigma}{\omega} (1 + ja) \tilde{E}_1}{\gamma' + j \frac{\omega}{\omega\tau_D} + ja}$$

$$J = \frac{\sigma (1 + ja) \tilde{E}_1}{\gamma' + j \frac{\omega}{\omega\tau_D} + ja} \quad \ldots\ldots\ldots\ldots (2.37)$$

$$\tilde{E}_1 = - \frac{eS}{\epsilon} \frac{(\gamma' + j \frac{\omega}{\omega'_D} + ja)}{\left\{ (\gamma' - \frac{\omega_c}{\omega} a) + j (\frac{\omega}{\omega'_D} + a + \frac{\omega_c}{\omega}) \right\}}$$

$$n_{s1} = \frac{- \sigma (1 + j a) \tilde{E}_1}{q V_s \left\{ \gamma' + j \frac{\omega}{\omega'_D} + j a \right\}}$$

$$= \frac{\sigma e}{q V_s \epsilon} \frac{(1 + ja) S}{\left\{ \gamma' - \frac{\omega_c}{\omega} a \right\} + j \left\{ \frac{\omega}{\omega'_D} + a + \frac{\omega_c}{\omega} \right\}} \quad . . (2.38)$$

The constant 'a', which numerically equals the ratio of the imaginary to the real part of f_o, appears in equation 2.37 which relates J to $\tilde{E}_1$. The resulting phase shift between J and $\tilde{E}_1$ reduces the amplification and attenuation coefficients. The term $q f n_s E_o$ contained in the current density equation, 2.8, indicates that the out-of-phase current component is proportional to the drift field. Accordingly the trapping effects reduce the maximum amplification more than the maximum attenuation.

The term n_{s1} for the case $\omega\tau \gtrsim 1$ is analogous to n_s in the $\omega\tau \ll 1$ case ie. it contains the space and time dependence and phase information. The value of n_{s1} under a condition of maximum amplification is denoted $n_{s1(\alpha' max)}$ and is given by the following equation.

$$n_{s1} \ (\alpha' max) = \frac{- \sigma eS}{q V_s \epsilon} \frac{(1 + ja)}{(\frac{\omega_c}{\omega} + \frac{\omega}{\omega'_D} + a)(\sqrt{1+a^2}+a-j)}$$

. . . . . (2.39)

Equation 2.39 was obtained by substituting the value of (γ'_{max}) given by eqn. 2.32 into eqn. 2.38. The numerical value of $n_{s_1}\ (\alpha' max)$ is denoted $|n_{s_1}\ (\alpha' max)|$ and is obtained as:

$$|n_{s_1}\ (\alpha' max)| = \frac{\sigma e S_o}{q V_s \epsilon} \quad \frac{1}{\left(\frac{\omega_c}{\omega} + \frac{\omega}{\omega_D'} + a\right)} \quad \frac{(1 + a^2)^{\frac{1}{2}}}{[\sqrt{1+a^2}+a)^2+1]^{\frac{1}{2}}}$$

. . . . . 2.40

When a = o, b = 1 eqn. 2.40 simplifies to the equation for $|n_s\ (\alpha\ min)|$ given by the White theory:

$$|n_s(\alpha\ min)| = \frac{1}{\sqrt{2}} \quad \frac{\sigma e S_o}{q V_s \epsilon} \quad \frac{1}{\left(\frac{\omega_c}{\omega} + \frac{\omega}{\omega_D}\right)}$$

It has been shown in this section that the theory of acoustic amplification that includes trapping behaviour predicts markedly different amplification behaviour to the White theory.

The reasonable agreement of the modified theory of ultrasonic amplification, incorporating trapping considerations, with the experimental results previously referred to indicates that trapping effects can adversely affect the performance of electro-acoustic devices.

SECTION 3.

PREPARATIVE TECHNIQUES

3.1 Introduction

The acoustic amplifier structure used in the present research incorporated acoustic buffers and was based on that used by Hutson, McFee and White [10]. It was felt that the operating convenience offered by the physical separation of the r.f. terminals and the H.T. leads considerably outweighed the relatively small increase in overall acoustic transmission obtained with a buffer-less structure, as used by Ishiguro et al [14].

In this section the preparation of an acoustic amplifier device is described. The initial procedure involved the orientation, cutting and polishing of CdS crystals. Subsequently large area ohmic contacts were made to the CdS. After a description of the preparation of transducers and acoustic buffers the method of fabricating an amplifier assembly is outlined.

3.2 Crystal preparation

3.2.1 Orientation

Irregularly shaped single crystals of CdS were obtained [77] and subsequently orientated and shaped to allow the propagation of piezo-electrically active shear waves. As discussed in section 1.2.1 this required the wave direction to be perpendicular to the 'C' axis and the particle displacement to be parallel to the 'C' axis. The most convenient faces to prepare were the principal

faces $\{11\bar{2}0\}$ and $\{10\bar{1}0\}$. Fig. 2 shows the inclination of these faces to the crystal axes. There were three steps in the initial orientation procedure, as follows:

1. Preliminary examination.
2. Examination in polarised light.
3. Orientation using X-rays.

A visual examination sometimes helped in finding the approximate direction of the 'C' axis. The crystals were generally elongated in this direction and often striations parallel to the 'C' axis were visible on cleavage surfaces. Such preliminary assessment as was thus possible shortened the subsequent examinations.

The examination in polarised light was based on the optical anistropy of CdS; the principal refractive indices being 2.506 and 2.529. The crystal was examined between crossed polaroids using light of 5800$\mathring{A}$ wave length. Light of this wavelength is weakly absorbed; the absorption coefficient has the typical value of 2.9 $cm.^{-1}$ (section 4.1).

In general a complete rotation of the crystal about the normal to the plane of the polaroids produced four maxima and four minima in the transmitted light intensity. Only when the light travels parallel to the 'C' direction does rotation not affect the light intensity. This technique enabled the 'C' axes to be located directly for many crystals. For some crystals it was initially not possible to locate the 'C' axis directly because of their irregular shape. For such crystals two small faces were ground perpendicular to the direction of elongation.

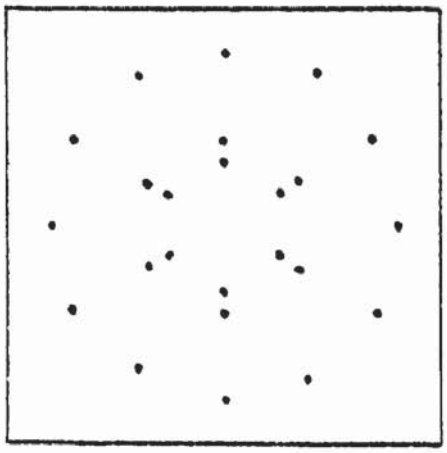

a/ X-RAY BEAM PARALLEL TO 'c' AXIS

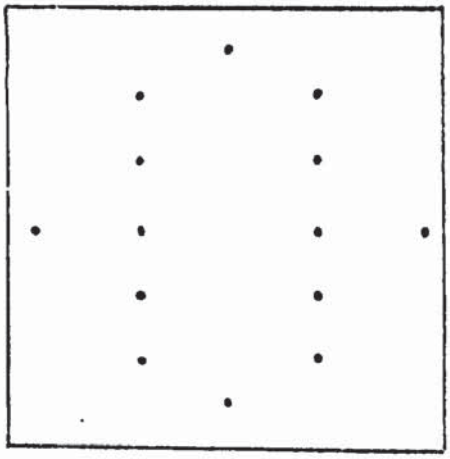

'c' AXIS

b/ X-RAY BEAM PERPENDICULAR TO [11$\bar{2}$0] PLANE

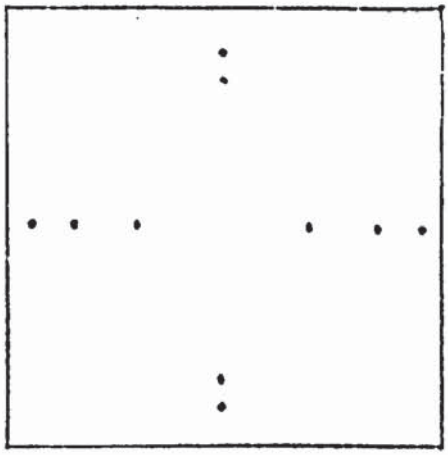

'c' AXIS

c/ X-RAY BEAM PERPENDICULAR TO [T100] PLANE

FIG. 11. LAUE X-RAY DIFFRACTION PATTERNS FOR CdS

This enabled the 'C' axis to be observed directly. The location of the 'C' axis using polarised light could be carried out quickly and reduced the number of X-ray exposures required.

For the X-ray orientation the crystal was mounted with wax onto a small platform designed to fit on top of a Phillips goniometer head. The head was fitted to the slide of an X-ray machine. The head was adjusted so that the 'C' axis, as determined using polarised light, was approximately parallel to the X-ray beam. Using the unfiltered radiation from a copper target tube (to reduce exposure time) a Laue back-reflection photograph was taken. Measurement of the diffraction pattern enabled the magnitude and direction of the angular movement of the crystal to be calculated in order to achieve two conditions:

1. To centralise the diffraction pattern - which shows hexagonal symmetry.
2. To rotate the inner hexagon of images so that a line drawn through two opposite images lay either vertically or horizontally.

Fig.11 (a) shows the appearance of the diffraction pattern for reflection from the [0001] plane. As discussed in Appendix 2 the 'C' axis is parallel to the incident X-ray beam when the pattern shows hexagonal symmetry and that when a diameter of the inner hexagon of images is vertical a plane of the group $\{11\bar{2}0\}$ is vertical and a plane of the $\{\bar{1}100\}$ group is horizontal.

A maximum of three exposures enabled the 'C' axes to be made parallel to the X-ray beam to within $\pm 1^{\circ}$ and a diameter of

the inner hexagon of images to be vertical or horizontal within $\pm 1^{\circ}$. The sample-film distance was initially made small, about 3 cm., in order to collect as large an angular spread of reflected X-rays as possible.

The position of the axes with respect to the major faces on the crystal was recorded. The crystal was transferred to the cutting table of a diamond saw and cut so that the $\{0001\}$ faces were exposed ie. two cuts perpendicular to the 'C' axis. It was then placed on a $\{0001\}$ face and cut four times, with 90° rotation about the 'C' axis between cuts, to expose the principal faces $\{10\bar{1}0\}$ and $\{11\bar{2}0\}$.

To orientate the crystal more accurately a combined orientation-grinding device was used. This device is described in more detail in section 3.2.3. The crystal was waxed onto the central stem so that a principal face, as cut on the diamond saw, was against the flat end of the stem. The assembly was placed on the slide of the X-ray machine so that back reflection photographs could be taken. The sample-film distance was made larger than that used during the initial X-ray alignment in order to increase the sensitivity of the diffraction pattern to angular movements of the crystal. The adjusting screws were altered between exposures to centralise the diffraction pattern. A maximum of three exposures enabled the face to be orientated to better than 30 minutes of arc. Figs. 11 (b,c) show the appearance of the diffraction patterns from the $[11\bar{2}0]$ and $[\bar{1}100]$ planes respectively. The face was ground and polished without removal from the jig.

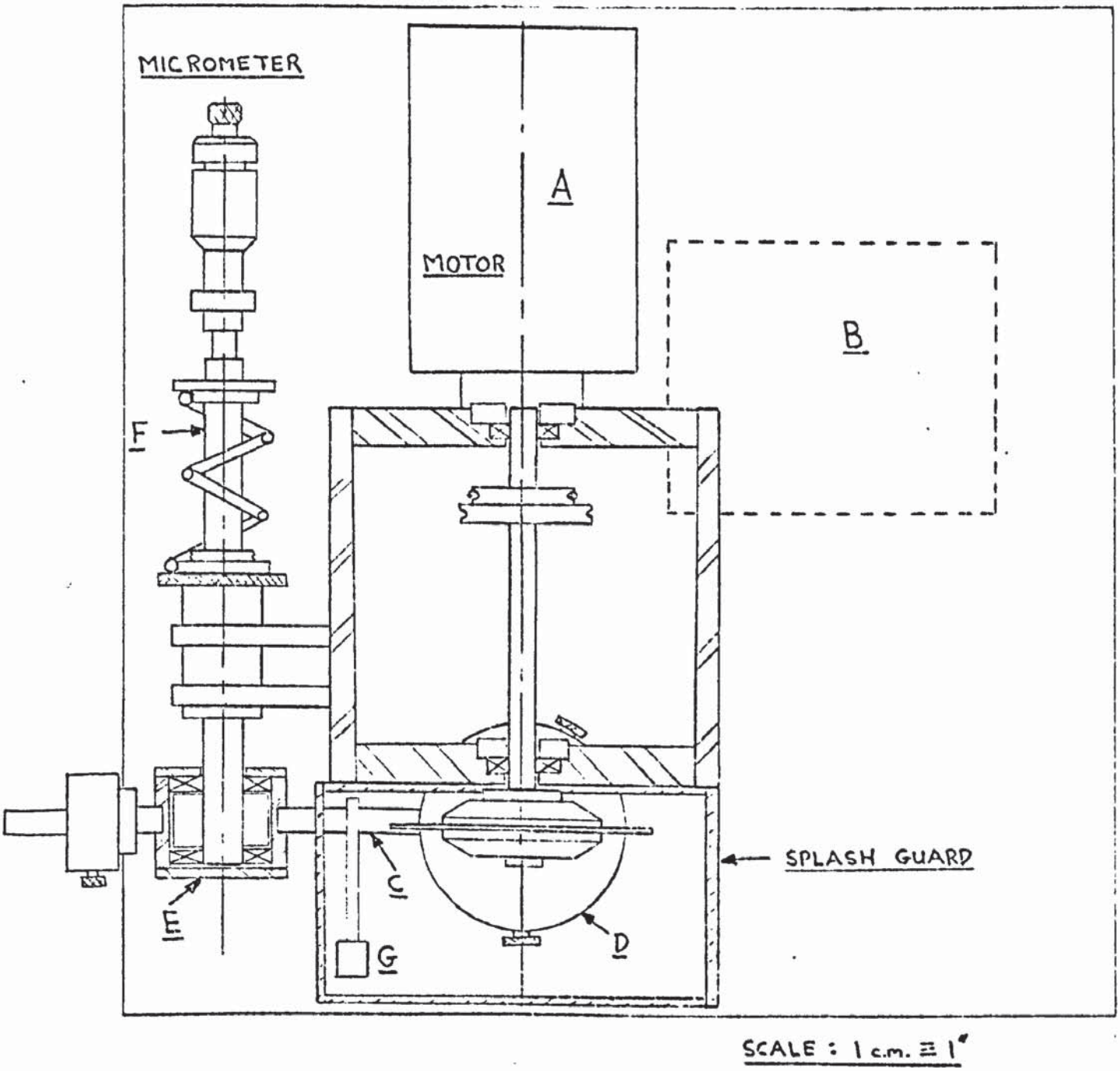

FIG. 12. DIAGRAM OF DIAMOND SLITTING SAW.

The opposite face was prepared by a similar procedure.

3.2.2. Cutting

Although CdS is a fairly soft material, having a Knoop hardness of 122, it is brittle and if it is not cut carefully it fractures and cleaves, particularly parallel to the 'C' axis. A slow running precision diamond slitting saw was built for cutting the crystals. It was based on a design by Fynn and Powell [78]. The saw satisfied the following four conditions:

1. True running of saw blade.
2. Optimum cutting speed.
3. Optimum cutting pressure.
4. Suitable lubricant.

A diagram of the saw appears in fig.12. The 80 watt motor was of the repulsion induction type and the speed could be varied continuously from 50 to 2800 r.p.m. The available torque and uniformity of running were increased if the motor was run from 1000 - 2800 r.p.m. and reduction gear used. Two methods for reducing the speed of the blade were used. With the motor in position A, fig.12, the double pulley blocks on the upper shaft and motor axle gave reductions of 4, 3.5, 2 and 1.75 to 1. For lower speeds a 9:1 reduction gear was fitted to the motor which was then operated in position B. The blade used was a 4" O.D. x .015" thick metal bonded diamond wheel. The arm C on which the work table D was fitted moved in the plane of the saw blade. Adjustments at the head E enabled this condition to be fulfilled. The rod F around which the head rotated was spring loaded against a micrometer

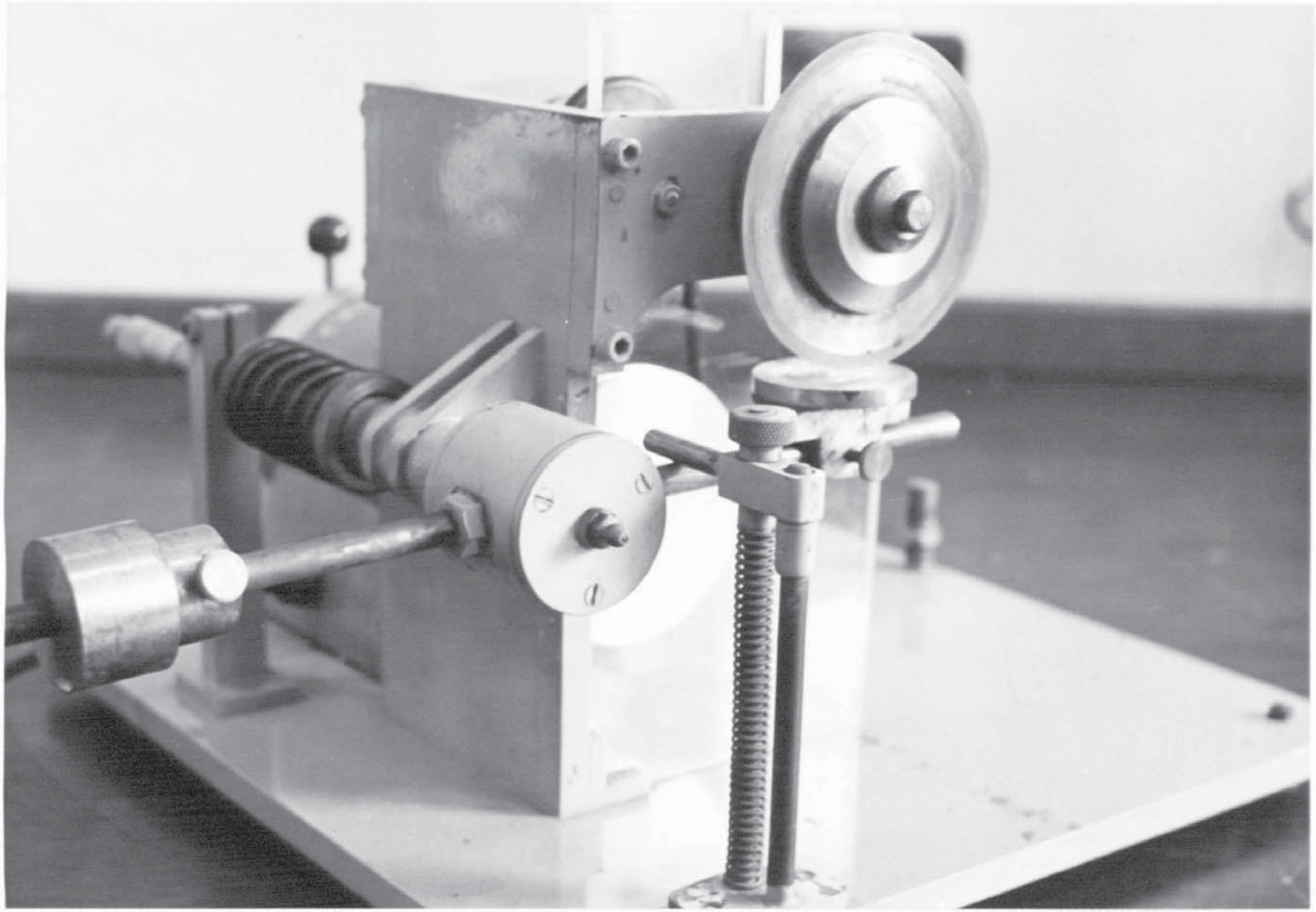

FIG. 13. DIAMOND SLITTING SAW

so that the work table could be advanced by known amounts between cuts. The device G limited the depth of the cut. The cutting pressure was controlled by movement of the counterweight.

To eliminate intermittent contact between the blade and the crystal the head contained a damping arrangement. The head was a closed cylinder with a spacer between the two ballraces such that the cavity within the cylinder was reduced to a .003" radial gap. The cylinder was filled with oil of S.A.E. 30 to provide the damping. The work table could be rotated about the vertical axis in fig.12 and about the arm C and locked in position to an angular positional accuracy of about 1^{o}. To avoid sawing into the work table the crystals were mounted on glass slides which were in turn mounted on the platform. Water was used as a lubricant and it was fed in just in advance of the sample. A perspex guard was fitted to stop the lubricant spraying out.

The saw was successfully used to cut a wide range of materials including sapphire, fused silica, spinels, ferrites and barium titanate.

For typical sized specimens of CdS cutting speeds of 500-700 r.p.m. (on a 4" O.D. wheel) with cutting pressures of 20-30 grams produced a good surface finish with negligible edge-chipping. This performance made the subsequent lapping and polishing far less tedious.

Fig.13 shows the overall appearance of the diamond slitting saw.

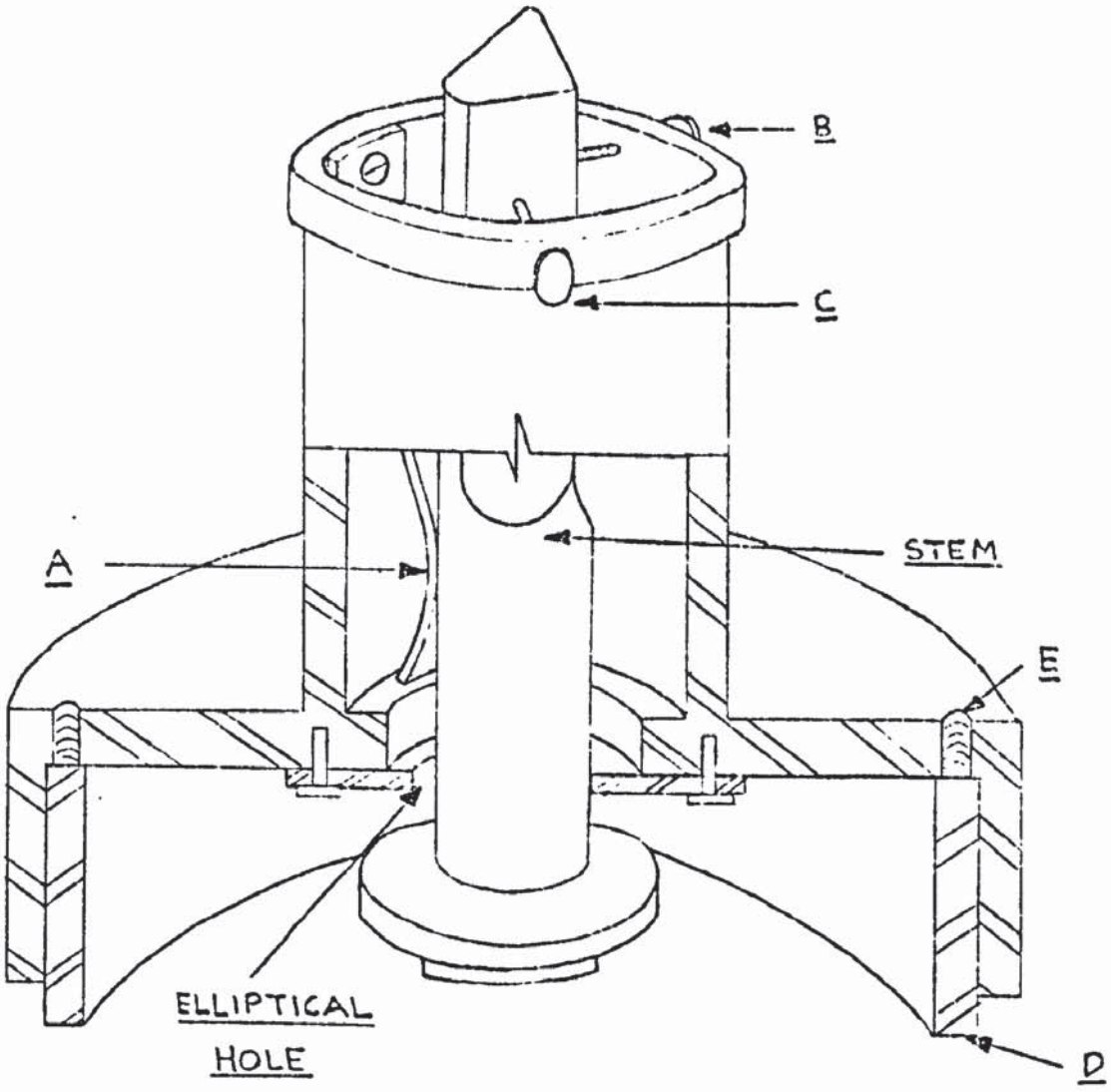

FIG. 14. SECTIONED VIEW OF ORIENTATION-GRINDING JIG

3.2.3. Grinding and polishing

After a crystal had been cut to expose the appropriate faces it was waxed onto a combined orientation-grinding device. This enabled faces that were initially within $\pm 5^{\circ}$ of proper orientation to be orientated to better than 20 minutes of arc and ground and polished without removal from the device. The device was based on a design by Bond [79].

A spring A, fig.14, pressed one end of the stem into the small end of an elliptical hole. Two perpendicular screws, B and C, were in contact with the other end of the stem and enabled the angular inclination to be altered. The ring D was of hardened chrome steel and was a force fit into the base of the device. It could be removed by inserting screws into the tapped holes E. The device could be clamped to a Vee-block mount and the assembly placed on the slide of the X-ray machine.

Usually a guard ring of a soft material was waxed on with the crystal to prevent edge chipping and a turned down edge resulting from the polishing process. The guard ring was a circular piece of brass, covered with wax, having the same thickness as the crystal to be polished. The guard ring had a large number of diametral cuts in its exposed face in order to reduce the area in contact with the polishing agent and hence decrease its effective hardness.

When a crystal had been suitably aligned in the orientation-grinding device the stem was pushed forward slightly so that the crystal projected beyond the steel ring. The crystal

holder was then moved about on a sheet of 600 grade silicon carbide paper resting on a sheet of plate glass. Water was used as a lubricant. The stem was gradually advanced forward until the face was satisfactorily ground. The crystal holder was initially moved in a figure of eight path with the long axis of the figure gradually rotating. For the final few strokes the crystal holder was moved across the grinding agent in a single straight line. These final strokes ensured that the surface of the crystal showed a series of fine grinding lines in one direction. The holder and crystal were carefully washed to remove all particles of silicon carbide before polishing began.

The crystals were polished by hand operation. Generally the polishing was carried out on a thin polishing paper using levigated aluminas of different grades for fast, slow and very fine polishing. The polishing movement was as described above and the polishing with each grade of alumina was continued until the parallel marks of the previous stage were erased.

Having prepared one face the time for orientation of the opposite face was reduced considerably by the following procedure. The crystal was removed from the polishing jig and the inclination of the stem was adjusted to make its face parallel to the outer rim. The face of the stem was lightly ground and polished, using the jig as a holder, in order to accurately produce a surface parallel to the outer rim. The crystal was waxed to the stem with its polished face adjacent to the prepared face of the stem, and after one X-ray photograph to confirm the orientation the polishing

process was commenced. This technique was shown to produce a higher standard of parallelism than was obtained by independently orientating the two surfaces involved.

This polishing technique produced satisfactory surface finishes for the majority of the experiments. Polishing was done on pitch laps when an exceptional surface finish was required, for example when it was required to introduce light into the crystal with a minimum of scattering due to surface irregularities. The techniques used to prepare and use the pitch laps are now briefly outlined.

The polishing pitch was composed of coal tar, pine tar, beeswax and Venice turpentine. The amount of turpentine added determined the hardness of the pitch. A lap consisting of a disc of pitch 8" diameter and ½" thick on top of a brass plate was prepared. The procedure used was to pour the molten pitch into a container consisting of the brass plate with a circumferential side wall of gummed paper tape (with the dry glue facing inward). When the pitch had set the paper was removed and the pitch was channeled by cutting it with a hot knife so that the surface was divided into a system of square facets of ¾" side separated by channels 1/16" wide. The face of the lap was trimmed up to remove all raised edges, using a razor blade.

To obtain a flat surface on the lap it was immersed in water at about 45°C for some time and then pressed onto a sheet of plate glass with a weight of about 5 Kg for 15 minutes. A solution of sodium oleate in glycerine was used as a lubricant to

ensure the lap did not stick to the plate glass. Using levigated alumina as a polishing agent the lap was worked in using only the outer ring of the polishing jig before introducing the crystal. A different lap was required for each grade of alumina used. The techniques used to prepare and use the pitch laps were based on those described by Ingalls [80] and Strong [81].

3.3. Measurement of parallelism and surface finish

In an acoustic amplifier consisting of a CdS crystal and two buffers there are six surfaces that the ultrasonics traverse in addition to four bonds. To propagate and detect plane waves required that the surfaces were flat and parallel and the bonds uniform to a high degree, preferably better cumulatively than to a quarter of the shortest acoustic wavelength used. This section describes the techniques used to monitor the dimensional accuracy of amplifier components.

The optical anisotropy of CdS provided a convenient means of checking the parallelism of the end faces of prepared crystals. The method consisted of placing the crystal between crossed polaroids such that the light travelled perpendicularly to the $\{11\bar{2}0\}$ or $\{10\bar{1}0\}$ faces. The crystal was rotated so that the transmission azimuth of the first polariser made an angle of 45° to the 'C' axis. Using monochromatic light of 5800A° wavelength a series of parallel fringes were observed if the two faces being viewed were individually plane but not parallel. The measurement of the fringe spacing enabled the wedge angle to be calculated. As shown in fig.15a the incident plane polarised light can be

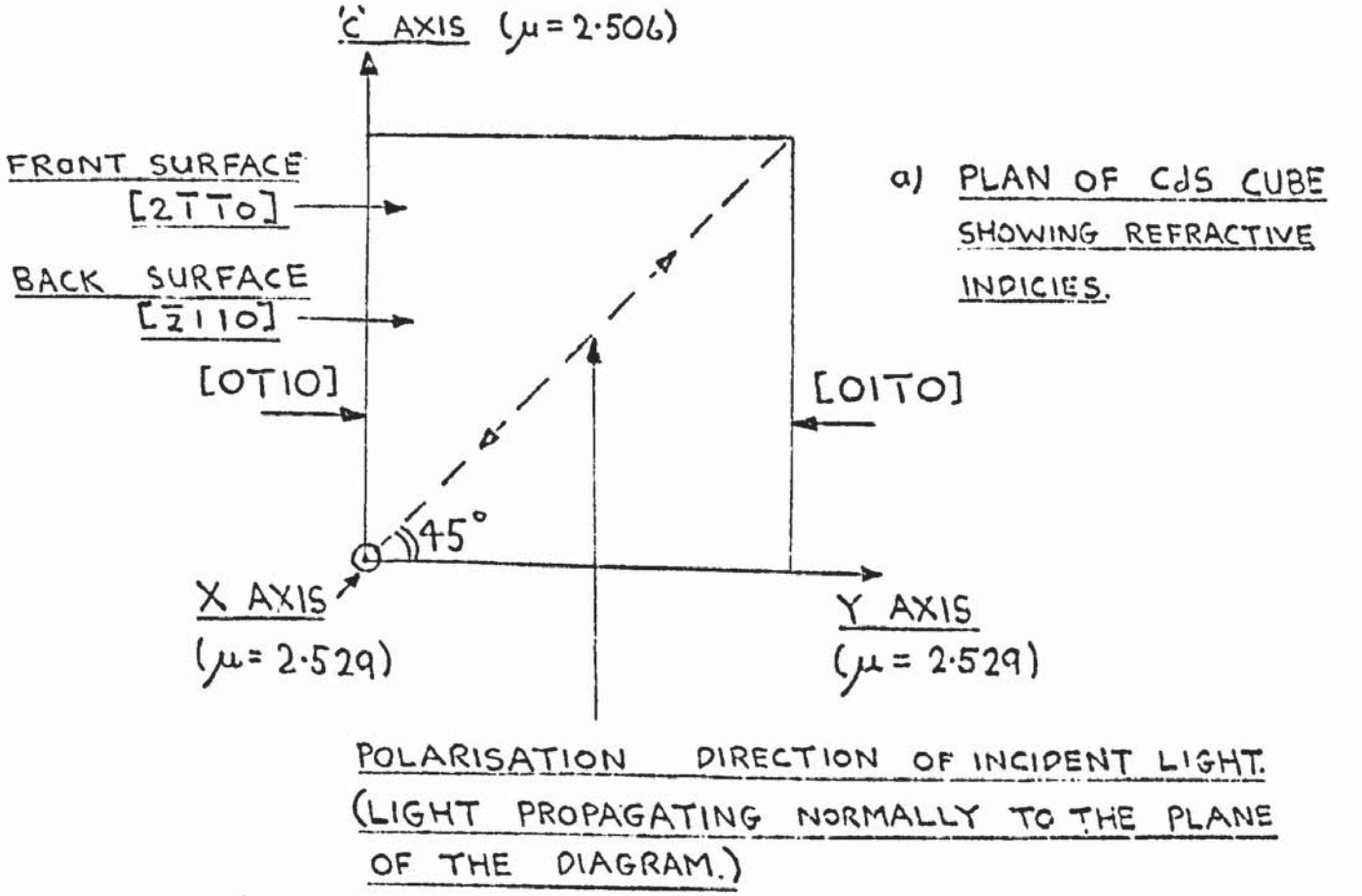

a) PLAN OF CdS CUBE SHOWING REFRACTIVE INDICIES.

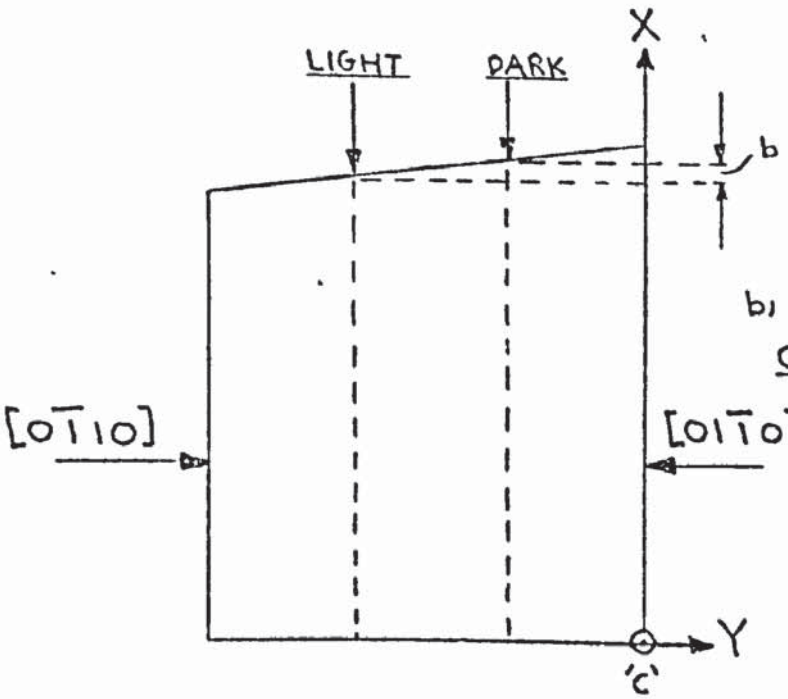

b) SIDE ELEVATION OF A THICKNESS WEDGE

FIG. 15. REFRACTIVE INDICIES OF CdS.

resolved into components parallel and perpendicular to the 'C' axis. For a crystal 'd' cm. thick the effective path difference (δL) between the components on emergence is given by:

$$\delta L = d\,(2.529 - 2.506)$$
$$= d\,(.023)$$

Now,

$$\delta L = \frac{(2n+1)}{2}\lambda \quad \text{where } n = o,\ 1,\ 2 \text{ etc.}$$

for destructive interference of the components and $\delta L = n\lambda$ for constructive interference.

In going from a dark fringe to a light fringe, fig.15b, the difference in thickness 'b' is given by:

$$b = \frac{5800 \times 10^{-8}}{2 \times .023} = 1.26 \times 10^{-3} \text{ cm.}$$

For example if the fringe spacing was 0.25 cm. the wedge angle α is given by:

$$\alpha = \frac{1.26 \times 10^{-3}}{.25} = .3^{o}$$

For a 1 cm. cube the minimum wedge angle that can be measured by this method is approximately 10 minutes of arc. If the crystal faces were convex then circular fringes would be seen.

For crystals and buffers with faces larger than 8 m.m. diameter an apparatus for mechanically checking parallelism was

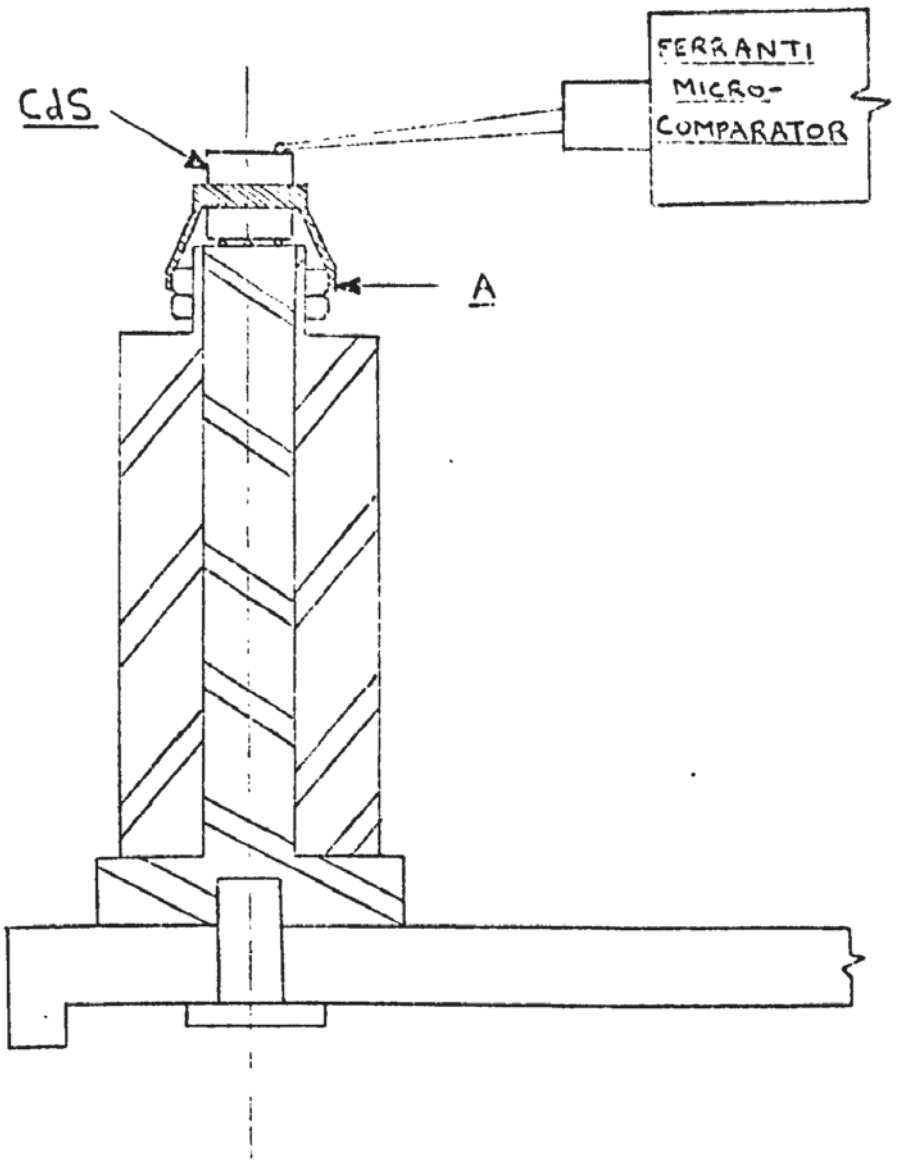

FIG. 16. SECTIONED VIEW OF PARALLELISM CHECKING INSTRUMENT

built. The crystal was rotated about a three point bearing and a Ferranti micro-comparator was used to measure the variation in height of circles of different radii on the top face. The specimen was held by an elastic collar, fig.16. Three guy-lines attached to the rotating sleeve A held the crystal lightly against the three ball bearings of 1 m.m. dia. On the Ferranti micro-comparator the scale can be read to better than one small division which corresponds to 0.00001 c.m.

For example if the difference between the high and low points on a 8 m.m. dia. circle (180° of rotation apart) was .00002 c.m. the wedge angle α is given by:

$$\alpha = \frac{2.0 \times 10^{-5}}{.8} = 5 \text{ secs of arc.}$$

Because of flexure in the experimental instrument the reliable sensitivity was about 10 secs of arc.

A lens brush was used to remove any dust from the crystal and bearings prior to useage. The probe arm of the micro-comparator had a spherical end of 2 m.m. diameter. The pressure on the upper crystal surface from the probe arm and the pressure on the lower surface from the three point bearing were low enough not to cause any significant surface blemish.

A Taylor-Hobson "Talysurf" metrology machine was used to monitor the profile of individual faces and the quality of the surface finish. With this instrument the sample is held stationary whilst a diamond stylus is moved in a straight line across the

surface. The movement of the stylus is monitored electrically and a profile of the surface is produced on a chart whilst a meter reading gives the average surface roughness. The diamond stylus which had a .010" radius and a load of approximately 2 grams caused a single fine scratch on the surface of CdS. For surfaces that had received careful polishing on a pitch lap the surface topography was observed using the Newton's rings technique.

3.4. Electrical contacts to CdS

CdS is essentially an n-type material. Spear and Mort [82] have reported that the electron mobility is about twenty times as large as the hole mobility.

Many commonly used contact materials such as silver, gold, copper, carbon, platinum etc., do not make good electrical contacts to CdS when deposited in the normal way ie. evaporation, electro-plating, thermo-setting paste etc. With these contact materials the current-voltage characteristic is non-linear for low voltages and potential barriers are formed at each end of the crystal.

There are two basically different methods for producing ohmic contacts to CdS. One method, based on the work of Buttler and Muscheid [83] uses a noble gas discharge immediately prior to deposition of the contact material. Using this technique the choice of metal for the contact is not critical and ohmic contacts are obtained with most metals. This is thought to be partially because the highly disordered CdS region near the surface acts as an electrical intermediary between the metal and the single crystal CdS. Page et al [84] consider that the process of ion

FIG. 17. THE CONTACT BETWEEN A METAL AND A SEMICONDUCTOR. (AFTER SMITH[85])

bombardment ejects the volatile sulphur atoms from the surface layer. The resulting surface layer is cadmium rich and is strongly n-type. The ohmic quality of the contacts is rapidly reduced for ambient temperatures of more than 100°C and this process occurs less rapidly at room temperatures.

The second method, based on the work of Smith [85], is to diffuse a tri-valent metal into the CdS. This acts as a donor and is a source of conduction electrons. Metals with low work functions are the most suitable. The metals generally used are indium and gallium. Fig. 17 illustrates simple contact between CdS and metals with high and low work functions. Metals having a work function much higher than CdS are expected to produce rectifying contacts whilst metals with a work function approximately equal to that of CdS should produce ohmic contacts. It is generally found that there is a poor correlation between the degree of rectification and the work function of the metal making contact to a semiconductor and several models have been proposed to account for this lack of correlation eg. Kroger [86]. Smith [85] concludes that the barrier height of the CdS - indium interface is less than or equal to 0.1 eV. Contact materials such as In and Ga will diffuse into the crystal, particularly for operating temperatures of more than 100°C, and eventually changes the nature of the crystal for a considerable depth. The use of aluminium as a contact material as suggested by Spitzer and Mead [87] and Goodman [88] has been developed by Boer and Hall [89]. In order to avoid a film of insulating Al_2O_3 on the crystal surface a

multi-layer technique was developed. Contacts fabricated in this way will retain their ohmic nature up to 350°C.

Electrical contact materials used in acoustic amplifiers must produce ohmic contacts to the CdS and also enable attachment of buffers or transducers to the CdS such that the transmission loss through the device is small. The fraction of an incident acoustic beam transmitted from one medium into another medium separated by a bond of a third medium is a function of the specific acoustic impedances of the media, the bond thickness and the acoustic frequency. (See, for example, Kinsler and Frey [90], p 152). For shear waves the specific acoustic impedance of CdS, fused silica, and indium are comparable. For operation in the MHz frequency range indium bonds are expected to have a high acoustic transmission coefficient.

In the present research ohmic contacts were produced by evaporation of indium. The crystals were etched in dilute chromic acid after polishing. The chromic acid was prepared by dissolving 700 grms of chromium trioxide in 2L of distilled water and adding 100 mL of concentrated sulphuric acid. After the solution had cooled it was diluted three times. With the etching solution at 70°C the crystals were immersed for three minutes. The crystals were thoroughly rinsed in distilled water, followed by pure ethyl alcohol and finally air dried. Rather than lift the etched crystal through a possible surface skin of contamination the etch was first diluted using distilled water.

The CdS crystal was placed in a jig (fig.18) in a high

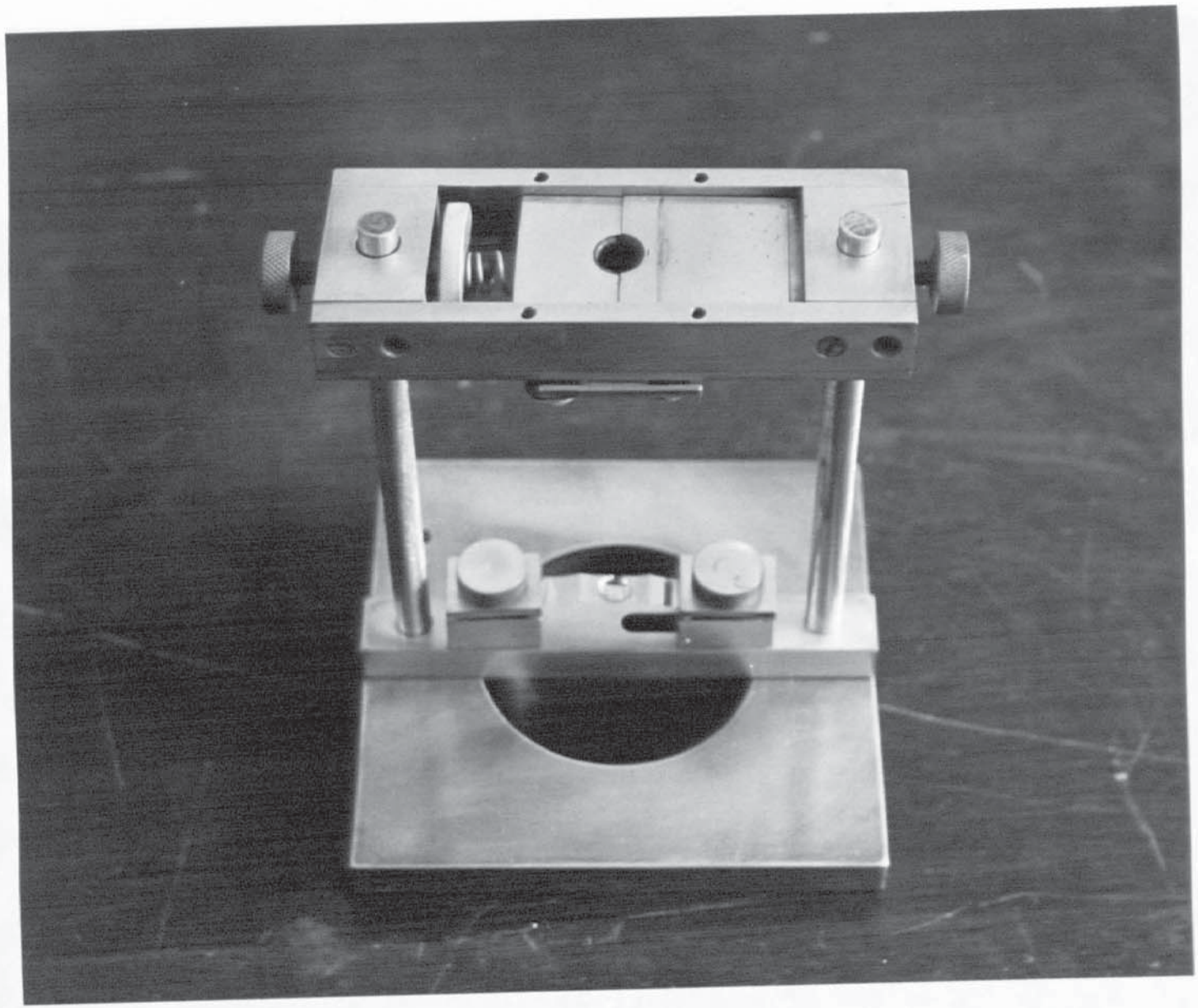

FIG. 18. EVAPORATION JIG

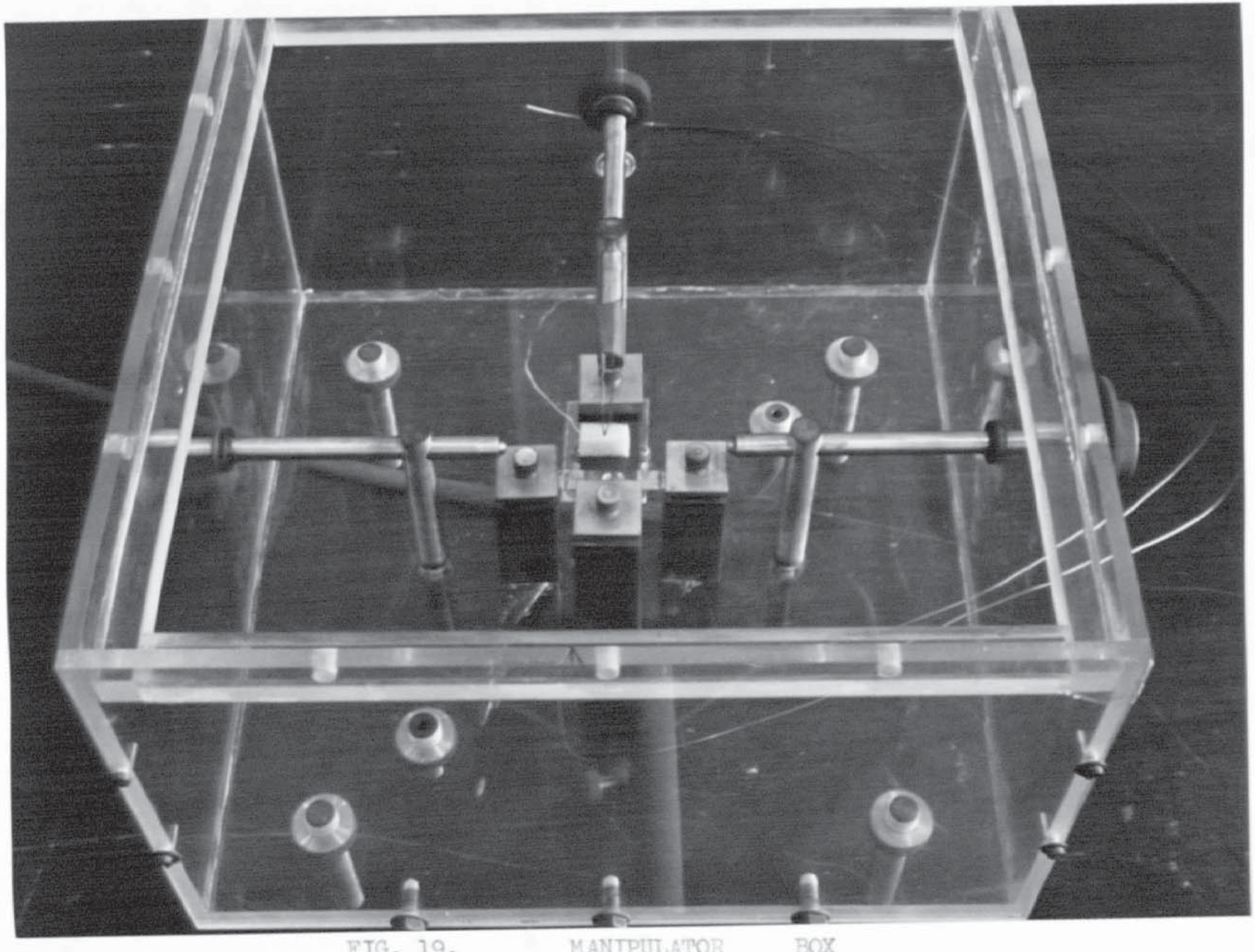

FIG. 19. MANIPULATOR BOX

vacuum system incorporating an Edwards ES 50 rotary pump, Edwards E04 diffusion pump and a liquid nitrogen trap. The jig shielded all the sides of the crystal from the evaporant except the contact area which was defined by a copper mask. The indium was evaporated from a molybdenum strip heater. The pressure in the chamber was generally 1×10^{-7} torr before evaporation, rising two to five times during evaporation.

Measures were taken to minimize any possible surface contamination by hydrocarbons by the use of Viton gaskets, absence of vacuum grease on gaskets, low backstreaming rate diffusion pump fluid and minimum exposure of the experimental chamber to the rotary pump.

The charge of indium, consisting of 2-3 cm. of 1.6 m.m. dia. hyper-pure wire, produced a film about 1μ thick, calculated from geometric considerations and assuming a unity sticking factor. The evaporation process was halted before the charge of indium was fully used in order not to evaporate the slight amount of slag which was usually observed during an evaporation.

After evaporation the crystal was placed in a perspex manipulation box, based on that described by Clark and Woods [91]. The box, shown in fig. 19 was flushed with pure nitrogen while the crystal was radiatively heated, from a molybdenum strip heater, so that its temperature slowly rose to 170°C (melting point of indium is 156°C). This procedure ensured that the evaporated indium wet the surface and diffused slightly into the crystal. To attach wires to the contacts two freshly cut pellets of indium

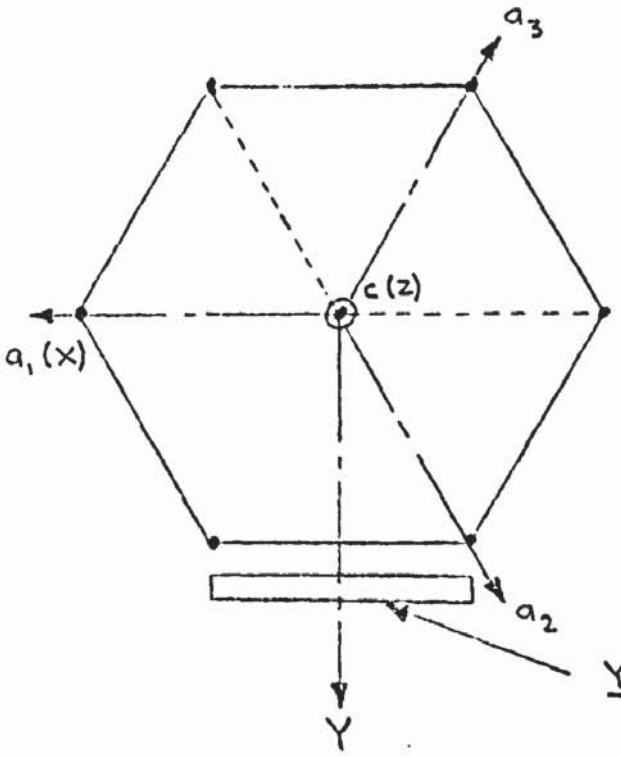

a) PLAN OF UNIT CELL ON 'c' AXIS.

• Si ATOMS

Y-CUT SLAB

b) SHEAR STRESS IN Y-CUT PLATES FOR ELECTRIC FIELD APPLIED ACROSS Y FACES.

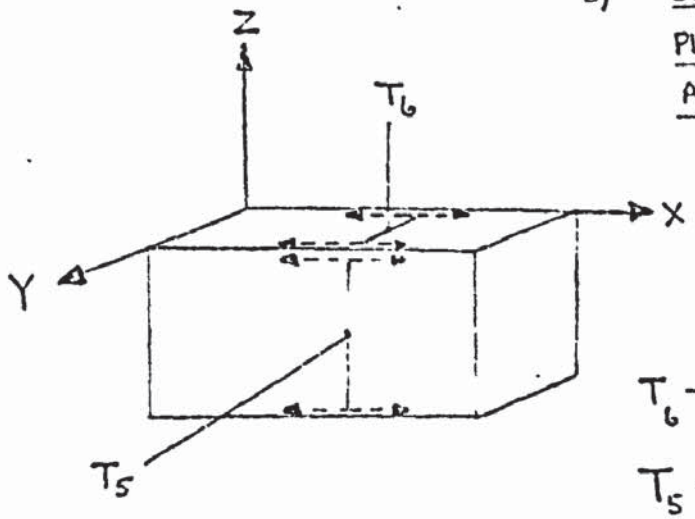

T_6 — THICKNESS SHEAR.

T_5 - FACE SHEAR (NOT USUALLY IN RESONANCE.)

FIG. 20. Y-CUT α-QUARTZ.

were pressed onto the evaporated films. Pressure was applied using a jig incorporating a spring loaded piston. The faces pressing the pellets were mica covered to ensure that the pellets did not adhere to them. The crystal was again radiatively heated to 170°C and lengths of copper wire held in the chucks were pushed into the body of the hemispherical pools of indium.

The contact fabrication procedure had the feature that the indium was heated only when in a vacuum or a gas with which it did not react. Also the heat to melt the indium films and dots was conducted from within the crystal rather than down a soldering iron. In early experiments using commercial purity nitrogen a thin blue film was built up on the inside of the perspex manipulator box. X-ray analysis showed this deposit to be "moly-blue", a hydrated mixed oxide of molybdenum. The subsequent use of pure nitrogen ("white spot") eliminated this source of contamination.

The electrical quality of the contacts was judged from the linearity of the current-voltage characteristics particularly at low voltages.

3.5. Preparation of acoustic amplifier components

3.5.1 Transducer preparation

Ultra-sonic transducers of Y-cut α-quartz were obtained.[92] Fig.20 shows the orientation of the Y-cut plates and the directions of shear stress for applied electrical fields. The transducers were 7-10 m.m. dia. and of 15 MHz fundamental frequency. The transducers had an electrode of gold-chromium entirely covering one face. Two operations were carried out on the transducers:

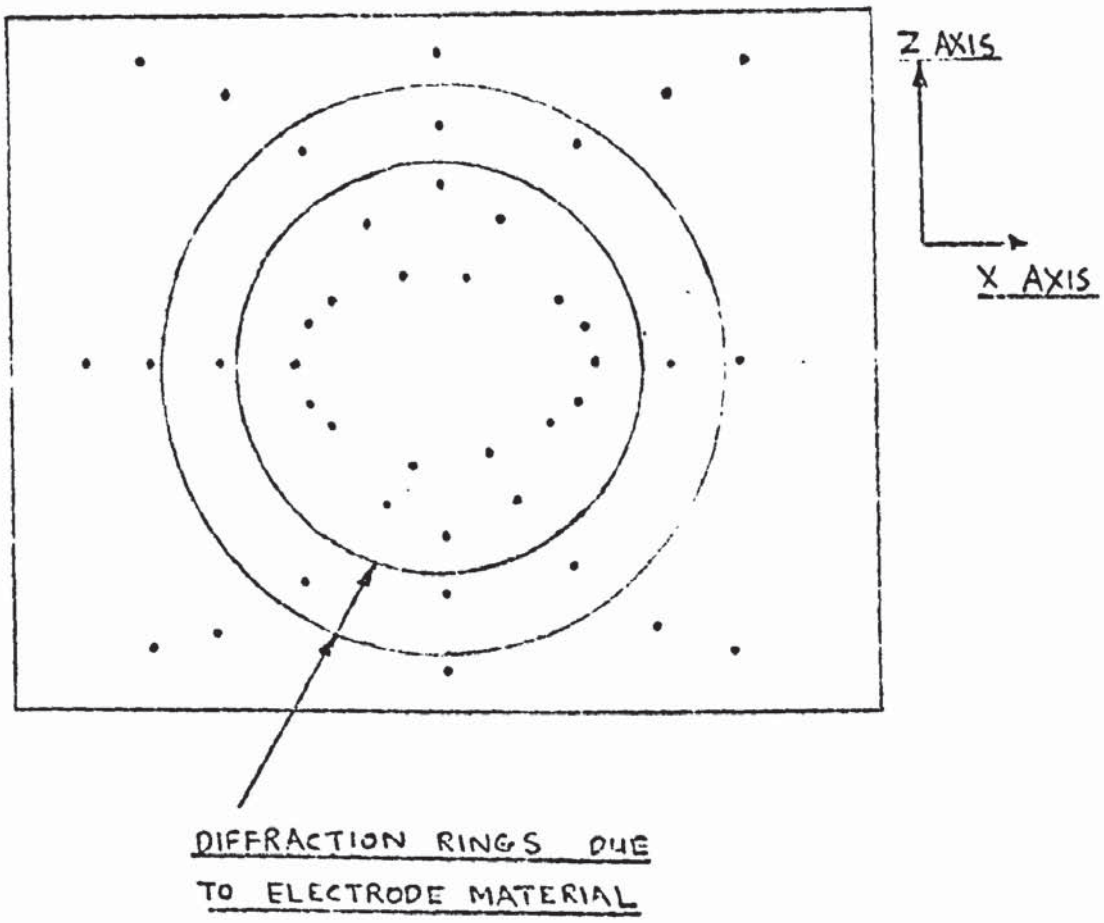

FIG. 21. TRANSMISSION X-RAY DIFFRACTION PATTERN FOR Y-CUT α-QUARTZ

1. The position of the X axis was determined by X-ray analysis and marked on the transducer face.

2. An electrode and wire were attached to the unplated face.

A chord was scribed on the fully plated face of the transducer. The line was not continuous but dashed in order not to separate electrically the two portions of the plating. The transducer was mounted on top of an X-ray goniometer such that the scribed line was vertical and the plane of the transducer perpendicular to the X-ray beam. To facilitate the setting up of the transducer a telescope with a graticule was mounted on a stand which fitted the slide of the X-ray machine. Using copper K_α radiation a transmission photograph was taken. The diffraction pattern, which had a symmetrical array of points from the quartz and a set of concentric rings from the polycrystalline plating, enabled the direction of the X axis to be determined. Fig.21 shows the diffraction pattern obtained. The angle and sense of the X axis in relation to the scribed line was noted for each transducer. At a later date it became possible to obtain transducers with a small flat ground parallel to the X-axis. For these transducers the orientation of the flat with respect to the X axis was checked using the techniques described above.

Acoustic diffraction considerations involving the frequency of operation, the length of the CdS crystal and buffers, and the number of sonic transits to be used determined the diameter of the electrode that was applied to the transducer.

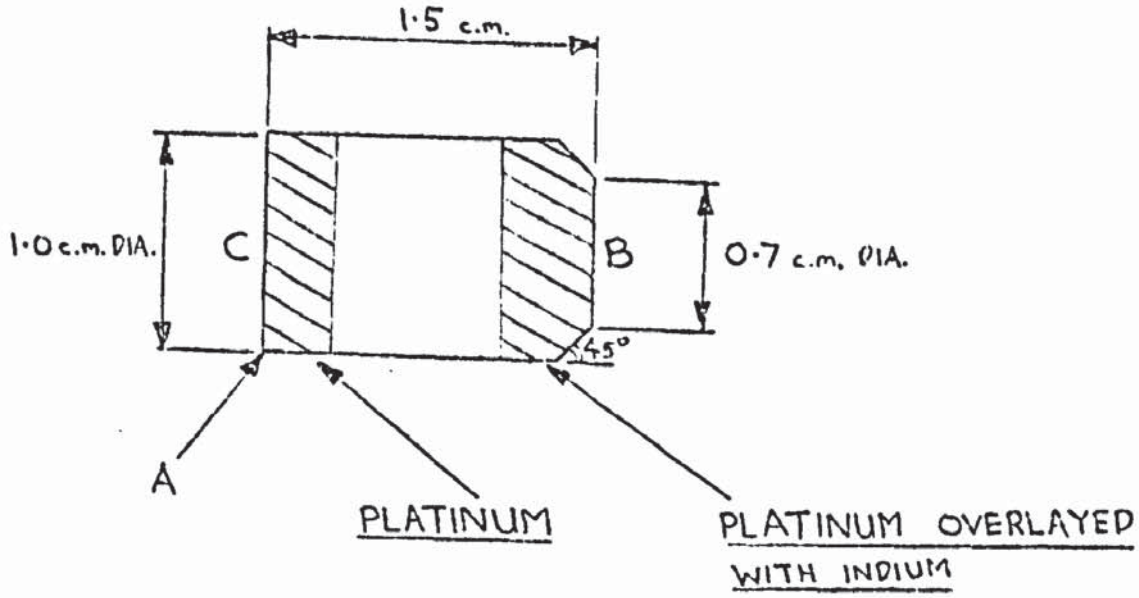

FIG. 22. ACOUSTIC BUFFER SHOWING BEVELLING AND PLATING

The Fresnel length 'd' (over which the acoustic beam is sensibly non-divergent) is given by [93]:

$$d = \frac{a^2}{\lambda}$$

a = dia. of active region of transducer

λ = acoustic wavelength

Using a proprietary silver paste a spot about 1.0 m.m. dia. was fired onto the transducer. Care was taken to keep the firing temperature in the range 520-540°C to avoid any possibility of change over into β-quartz (which occurs at 573°C) and resultant electrical twinning. A coating of platinum of the required diameter was similarly fired on using a proprietary preparation. Using a silver bearing tin-lead solder and a resin base flux, a copper wire was soldered onto the central silver spot. A Variac in the electrical supply to the soldering iron was adjusted so that the temperature of the bit was just sufficient to melt the solder. This kept the solder saturated with silver and prevented the solder dissolving silver from the fired spot. The transducer was warmed to 180-200°C on a hot plate to avoid thermal shock.

3.5.2. Preparation of buffers

Fused silica acoustic buffers were obtained [92]. They were cylinders 1 cm. dia., 1.5 cm. long having the end faces parallel and flat to optical standards. Two operations were carried out on the buffers:

1. They were shaped.
2. Platings of platinum and indium were applied.

The buffers were tapered at one end in order to make the diameter of the smaller end face equal to that of the electrical contact areas of particular CdS crystals. The buffers were mounted in a hole in a cylindrical block of brass using thermo-setting wax such that half their length protruded. With the block rotating in a lathe a 45° bevel, as shown in fig. 22, was ground using 600 grade silicon carbide paper. Wax covered the face B to prevent the optically polished surface being scored. The buffer was reversed and the corner A was rounded slightly.

A coating of a proprietary platinum preparation was applied to the end faces B and C and the shaded cylindrical surfaces in fig. 22. The edge A was rounded because surface tension effects produced extremely thin coverings on sharp edges. In order to get films that adhered well to the fused silica and were uniform it was necessary to use very thin coatings and use two successive applications and firings. To prepare end C with the buffer standing on face B and repeat the procedure for the other end involved four firings which adversely affected the quality of the films. A jig, constructed in stainless steel, was used to hold the buffer whilst painting on the platinum preparation and during the firing. This reduced the number of firings to two. When the platinum films had been successfully fired-on a film of indium was evaporated onto the area at the end B of the buffer.

3.6. The complete acoustic amplifier.

3.6.1. Assembly of acoustic amplifier

The basic acoustic amplifier was assembled from a CdS

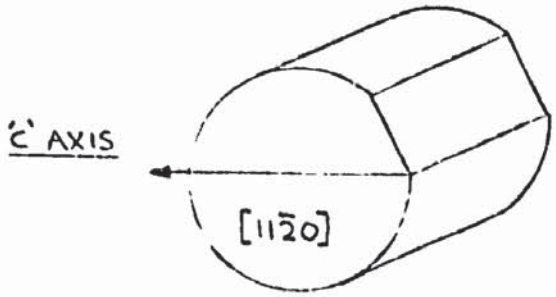

a) CYLINDRICAL CRYSTAL OF CdS.

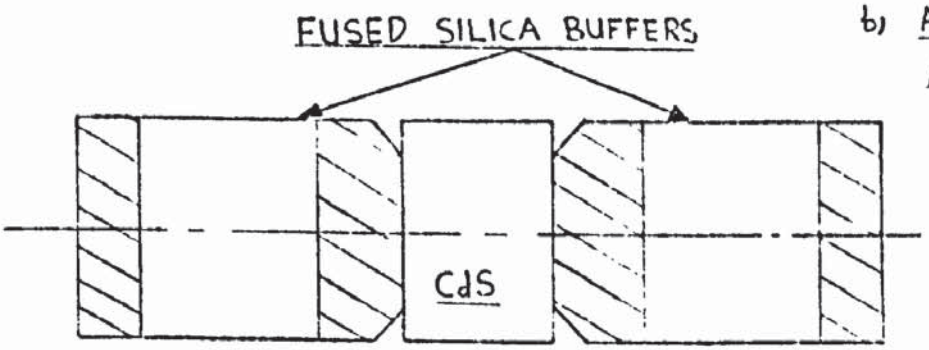

b) ACOUSTIC BUFFER ATTACHMENT.

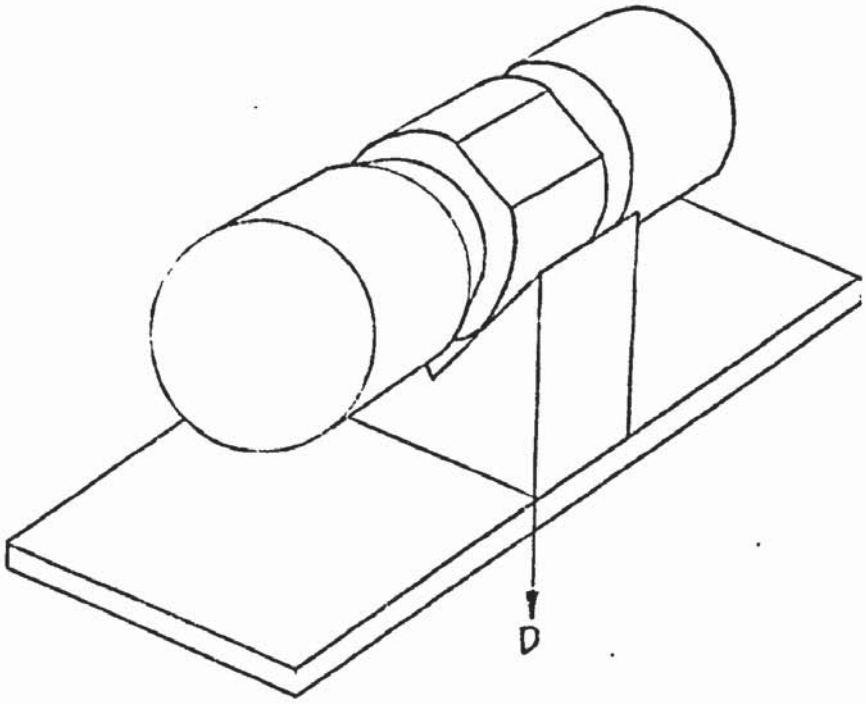

c) JIG FOR TRANSDUCER ALIGNMENT.

FIG. 23. ASSEMBLY OF ACOUSTIC AMPLIFIER.

crystal, two buffers and two transducers. Several irregularly shaped CdS crystals were orientated and shaped by the procedures previously described. In addition two rough-cut cylinders of CdS were prepared. Measurement of the photoconducting and current-voltage characteristics of these specimens showed that one of the prepared cylinders was most suitable for operation in an electro-acoustic amplifier. The procedure used for fabricating an amplifier is described below and it applies particularly to a 1 cm. dia. cylindrical crystal, fig. 23a. A flat having a known orientation to the 'C' axis was ground on the crystal. The crystal had indium contact areas 7 m.m. dia. The buffers had indium coatings on the 'B' end faces, fig. 22. The buffers were bonded to the CdS by a cold welding process utilising the appreciable self diffusion rate of indium.

The indium surfaces on the buffers and CdS crystal were produced within as short a time as possible to avoid gross contamination. The indium surfaces were cleaned and slightly roughened by wiping them with a swab of lint free tissue. Immediately upon being swabbed the specimens were layed in a Veegroove and contacted with manual pressure so that they adhered to each other, as shown in fig. 23b. The assembly was mounted in a jig and a pressure of 250-300 p.s.i. was applied. The apparatus was placed in an oven and maintained at a temperature of 125°C for 24 hours. Experiments using oven temperatures above the melting point of indium, 156°C, failed to produce good bonds - probably due to the metal oxidising rapidly above this

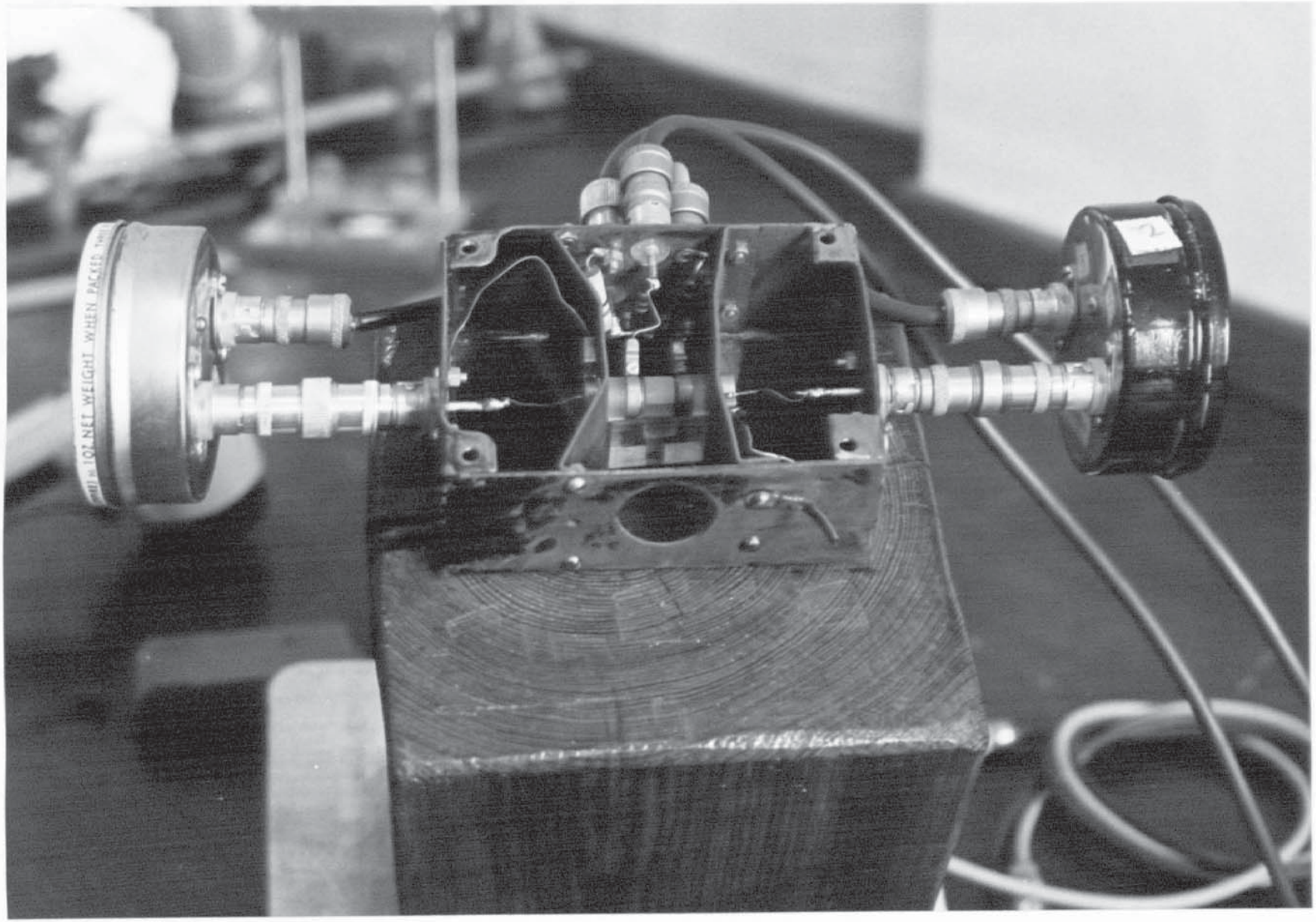

FIG. 24. ACOUSTIC AMPLIFIER

temperature. Arenberg[94] and Brew [95] have described indium bonding techniques as used to fabricate ultrasonic delay lines.

The assembly was placed in a Vee block, as shown in fig.23 (c). The CdS was held to the Vee block by two rubber bands. The crystal was rotated until the 'C' axis was parallel to direction D using a template against the flat on the crystal and the side of the Vee block. The whole assembly was then placed in a vertical plane. A small quantity of molten salol (phenyl salicylate) was put on the face C of the upper buffer. The transducer, with wire attached, was floated on the salol and rotated until the X axis was parallel to the D direction using the scribed line on the transducer against a template. The transducer was pressed against the buffer to reduce the thickness of the salol bond and the excess salol was absorbed in a piece of lint free tissue. If the super-cooled salol did not solidify within a minute it was seeded. A transducer was attached to the other buffer by the same method. The technique enabled the transducers and CdS to be lined up to within $\pm 2^{\circ}$.

Circlips were added to each end of the buffers and the amplifier assembly was mounted in a metal box with three shielded compartments, fig.24.

3.6.2 Processing of organic bonds.

With the acoustic amplifier assembly mounted vertically the salol bonds were processed in order to give optimum performance ie. large amplitude signals due to shear wave transmission with minimal spurious signals. The salol bond at one end was melted

using a stream of warm air. The appropriate transducer was operated whilst the molten salol bond was seeded at one end of the shear axis. Kapustin [96] has shown that the presence of ultrasonics produces crystallisation rates in phenyl salicylate some several hundred times faster than in the absence of ultrasonics. The re-crystallisation procedure sometimes had to be carried out several times in order to produce the optimum detected signal at the other transducer. The procedure of seeding along the X-axis during transducer operation produced on average a better bond than if the ultrasonic vibrations were absent.

When a salol bond was molten it transmitted an ultrasonic signal due to its visco-elasticity. Under these conditions it was observed that for each r.f. pulse applied to the input transducer the output transducer received several small ultrasonic pulses each with a different transit time. The times of propagation of these signals through the amplifier structure indicated that the level of shear waves transmitted by the molten bond was small compared to that of longitudinal waves. The times of propagation were those expected for a longitudinal wave traversing the acoustic amplifier and producing shear waves by mode conversion at the three bonds encountered. During the crystallisation process the level of the spurious signals fell whilst there was a considerable increase in the level of the photosensitive shear mode having a transit time corresponding to shear wave propagation through the full length of the acoustic amplifier structure. The reason why longitudinal waves are propagated into the acoustic buffer beneath

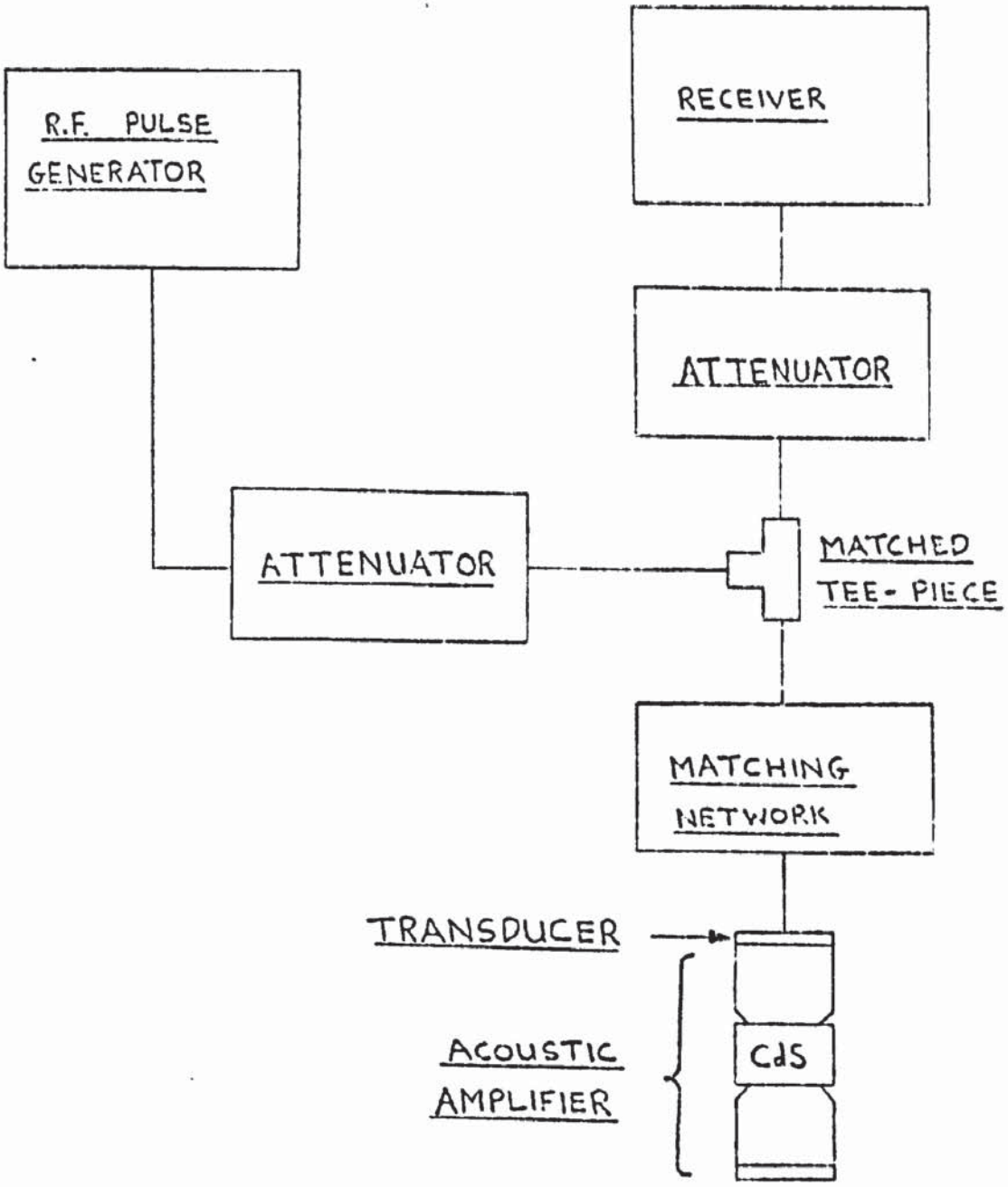

FIG. 25. BLOCK DIAGRAM OF SINGLE-ENDED OPERATION OF AN ACOUSTIC DEVICE.

the molten salol bond is not clear.

Observation of salol crystallisation between glass slides showed that the bond can crystallise with several types of appearance including; uniform consistency, fibrous appearance and a mosaic of intersecting single crystals. The variation of received signal with different salol bonds is believed to depend on the nature and uniformity of the crystallised solid.

The overall loss between the electrical input and output terminals of an acoustic amplifier was found to increase when the amplifier had been operated for a period in excess of one year. This effect was found to be due to deterioration of the salol bonds and when they were renewed the overall loss reverted to its earlier value. By using each transducer individually in single-ended operation, fig.25, both before and after renewing the salol bonds it was determined that both bonds were equally in need of treatment. Because one transducer had been used primarily as a transmitter and one as a receiver these findings suggested that the ageing effect was not due to the amplitude of the ultrasonics traversing the bond. It was observed that if the original salol bonds (ie. the deteriorated ones) were melted and allowed to solidify then no improvement in transmission was achieved. The bonds were restored to their former efficiency by melting and removing the old salol and renewing with fresh salol. During this procedure it was observed that the amount of salol between the transducer and the buffer had considerably diminished during the course of operation. The reduction in the overall transmission through the acoustic

amplifier is thus considered to be due to a reduction in the area of overlap of the effective transmitting and receiving portions of the two transducers caused by loss of bonding material, possibly by evaporation.

SECTION 4

EXPERIMENTAL TECHNIQUES

In this section a description is given of the techniques used to operate an acoustic amplifier.

4.1 Crystal illumination

The resistivity of the CdS was varied by altering the illumination intensity. Using a suitable optical system the CdS was illuminated by a sensibly parallel beam of light such that the illumination was made uniform over the crystal face. In order to achieve a reasonably uniform distribution of photo-electrons throughout the volume of the crystal it was necessary to use weakly absorbed light.

Fig.26 shows the optical absorbance of a plate of CdS plotted as a function of wavenumber. The optical absorbance (A) is related to the percentage transmission (T) by the formula:

$$A = 2 - \log_{10} T$$

The absorption curve was obtained using a Unicam SP 800 spectrophotometer. The CdS sample used to obtain the spectral absorption curve was smaller in height than the 14 m.m. high slit used on the SP 800 therefore the crystal was mounted on a masking slit to ensure that the detected light had travelled through it. Accordingly the absorbance figures initially obtained were not absolute values. The instrument has both reference and specimen light beams and will present absolute values of absorbance if an identical mask is placed in the reference

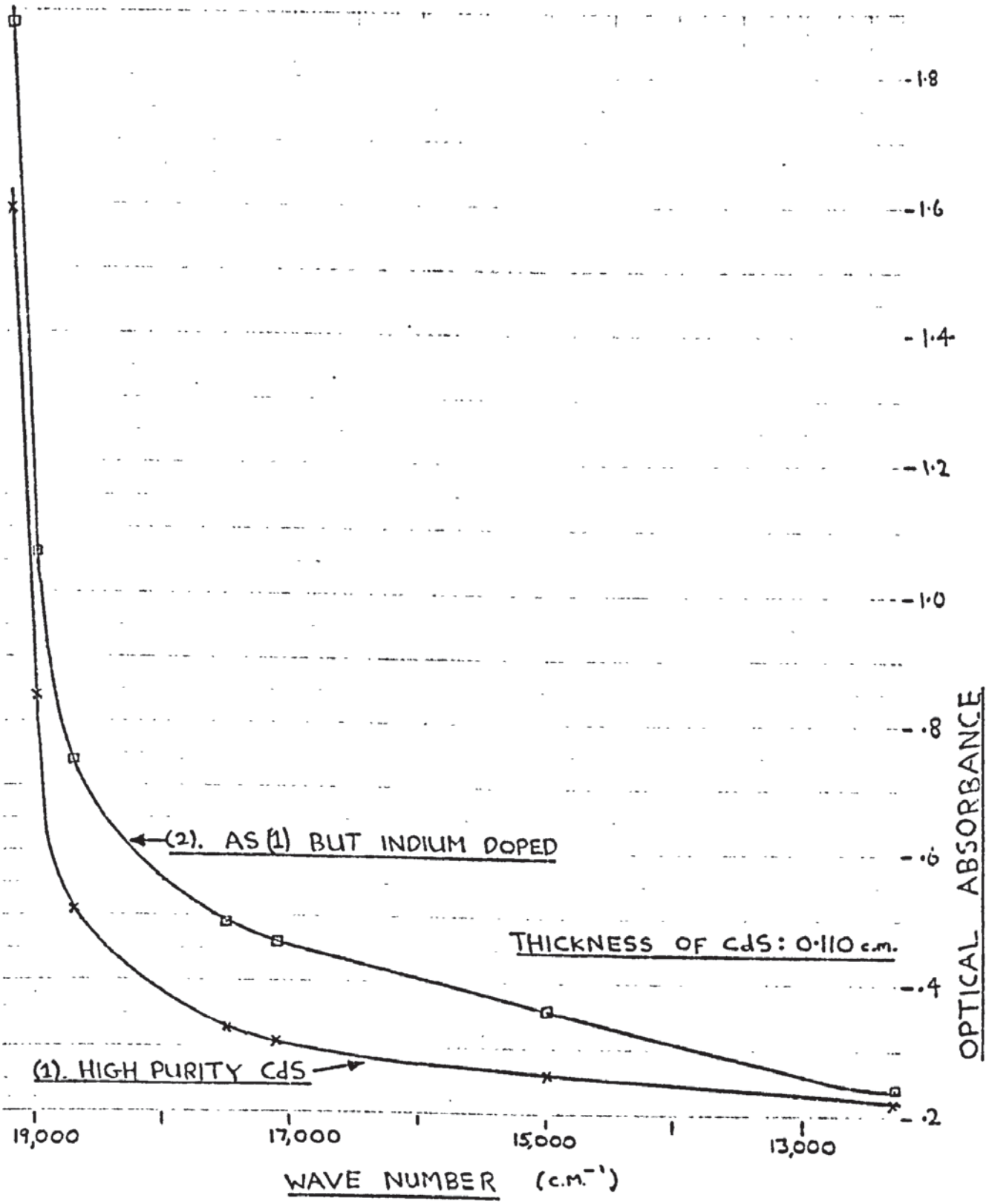

FIG. 26. OPTICAL ABSORBANCE VERSUS WAVE NUMBER FOR CdS.

beam. In practice it was found more convenient to measure the optical absorbance at a fixed wavelength using a silicon photocell. A parallel beam of light of wavelength 5800Å was projected onto a silicon photocell (Mullard BPY 10). The change in short-circuit current as read on a microammeter when a piece of CdS was placed just in front of the photocell enabled the optical absorbance to be calculated. At a given wavelength the value of absorbance obtained using the photo-cell differed from that obtained with the spectrophotometer because the masking slit used in the latter reduced the area of transmission by a factor 'n'

If for the photocell technique we have:

$$A = 2 - \log_{10} T$$

A = absorbance

T = percentage transmission

Then for the spectrophotometer we have

$$A' = 2 - \log_{10} Tn$$

$$\text{ie. } A' = A - \log_{10} n \qquad (n \text{ is } < 1.0)$$

A' = observed absorbance due to modified transmission Tn.

The effect of the area reduction is to shift the spectrophotometer absorbance curve as a whole to increased values of absorbance and preserve its shape. Thus the calibration of the whole spectrophotometer absorbance curve was effected using the photocell readings at one wavelength.

The photocell was shown to have a linear response to the intensity of the light by means of neutral density filters. The CdS specimen used had plane and parallel faces with a high quality surface finish. The geometry of the arrangement, using the photocell, minimised any error due to light scattering. There was no observable difference in the absorption of plane polarised light travelling perpendicular to the 'C' axis with polarisation azimuths parallel or perpendicular to the 'C' axis.

Fig.26 shows that light having a wavelength of less than about 5200Å is strongly absorbed in CdS. This wavelength corresponds to photon energies sufficient to transfer an electron from the valence band to the conduction band, the band gap corresponding to 2.42 eV. The absorbance reaches a minimum, in the spectral region investigated, at about 8100Å wavelength and for longer wavelengths it shows a local maximum at about 1μ wavelength. This is due to the same traps that cause infra red quenching and negative photoconductivity.

Table 1 gives the observed values of optical absorption coefficient as a function of wavelength for a specimen of high purity CdS.

TABLE 1

Wavelength $\overset{o}{A}$	Optical Absorption Coefficient $cm.^{-1}$
8130	1.0
6670	1.8
5710	3.5
5350	6.6
5260	14.8
5205	29.7

The optical absorption coefficient k is defined by Lambert's law which states that the intensity I of a wave that has traversed a thickness x of material with absorption coefficient k is:

$$I = I_o e^{-kx}$$

I_o = original intensity

The effect of boundary reflections of light has to be taken into account in calculating k from experimentally determined values of transmission coefficient. The intensity reflection coefficient R for a electro-magnetic wave traversing normally the boundary between two media is given by the Fresnel equation:

$$R = \left(\frac{n_2 - n_1}{n_2 + n_1} \right)^2$$

n_2 , n_1 are the refractive indicies of the two media. CdS has $n_2 \sim 2.5$ and air has $n_1 \sim 1.0$ giving R a value of .18 for the CdS-air interface.

Fig. 27 shows a light beam incident on a slab of CdS. Only two reflections are considered.

Fig 27. Optical transmission through CdS

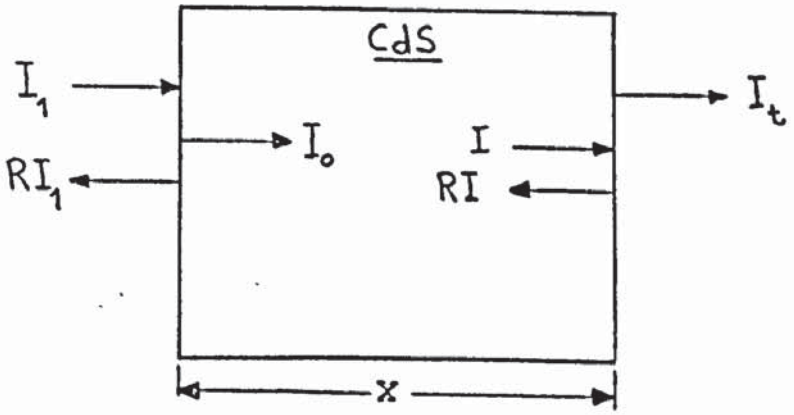

I_1 = total incident light intensity

I_t = transmitted light intensity

$$I_o = I_1 \quad (1 - R)$$

$$I = I_t \quad (1 - R)^{-1}$$

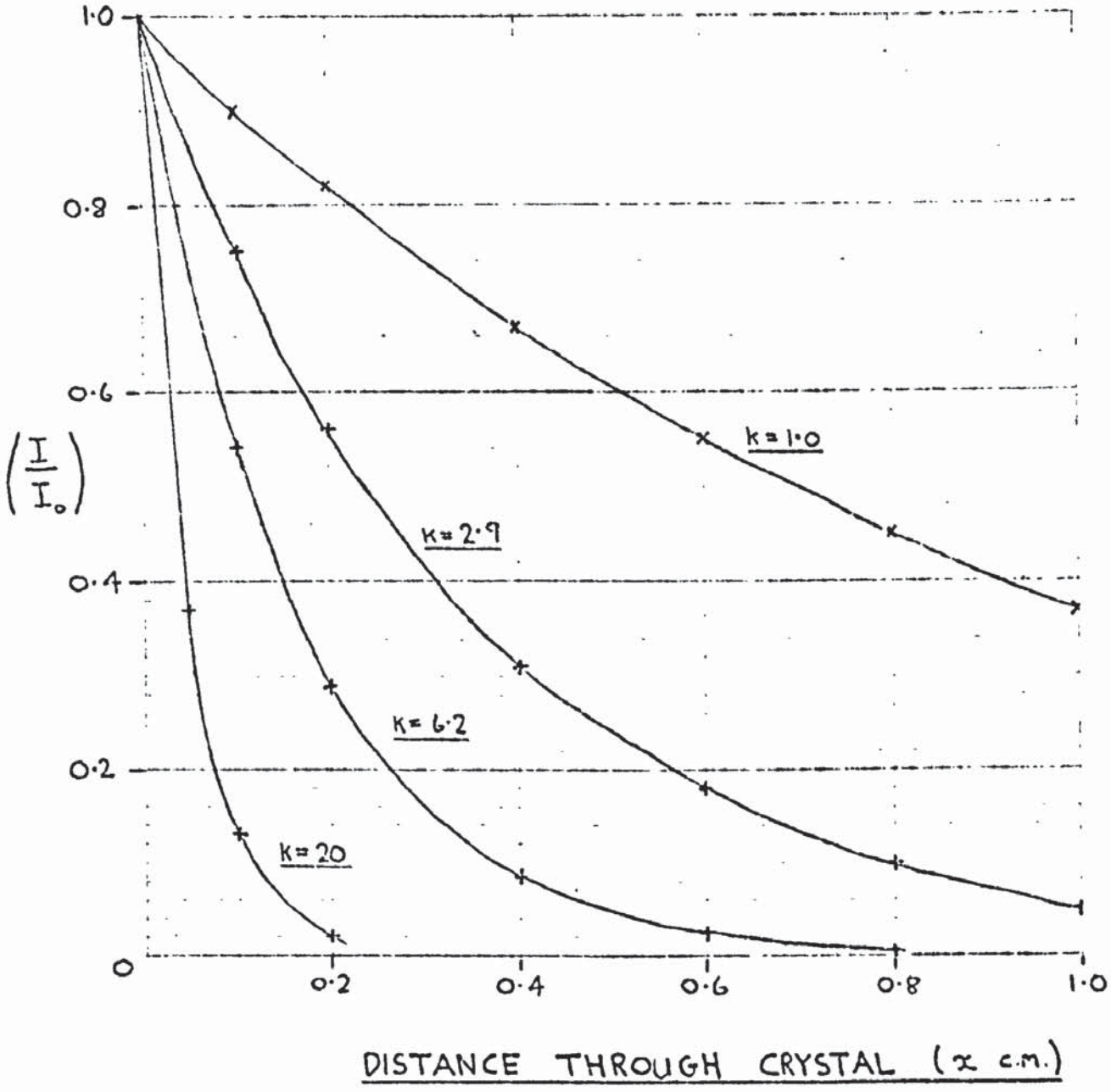

FIG. 28. OPTICAL ABSORPTION IN CdS

$$\text{ie.} \quad \frac{I}{I_o} = \frac{I_t}{I_1 (1-R)^2} = e^{-kx}$$

The experimentally determined values of $\frac{I_t}{I_1}$ and a knowledge of R and x enabled k to be calculated, as table 1.

Lambert's Law was used to calculate the light intensity against distance travelled in a piece of CdS, fig.28. Even for light having an absorption coefficient of 2.9 $cm.^{-1}$ there is a considerable transverse non-uniformity in resistivity over the central 3 m.m. of the crystal through which the ultrasonics pass. The uniformity of the crystal resistivity can be improved by using various ambient temperatures to achieve the required resistivity. Truell et al[97] have investigated the ultrasonic attenuation in CdS (for no applied voltage) as a function of resistivity using a CdS crystal having a resistivity of 10^{10} ohm-cm. at 20°C falling to 10^4 ohm-cm. at 400°C. Lord and Truell [98] have similarly used a CdS crystal whose resistivity was 10^2 ohm-cm. at 20°C increasing to 10^6 ohm-cm. at liquid helium temperatures. Both of these investigations of ultrasonic attenuation avoided problems associated with bonds to transducers by using the CdS crystal as a self transducer. There are considerable technical problems in constructing an acoustic amplifier structure for temperature cycling, particularly associated with the ohmic contacts and bonds.

Davis and Drews [99] have calculated the effects of transverse and longitudinal variation in crystal resistivity on ultrasonic propagation. For the geometry they chose (electrical

contact areas and acoustic beam covering the entire cross-sectional area of the crystal) the predicted effects of transverse non-uniformity on the ultrasonic attenuation-conductivity curves were considerable for strongly absorbed light. The predicted effects are in general agreement with Harnik and Yasar [100].

Using filters to select various spectral regions the author observed that electro-acoustic effects such as ultrasonic attenuation and amplification were not noticeably dependent on the spectral composition of the illumination provided the crystal resistance was kept constant. The acoustic amplifier used to make these observations had a 3 m.m. dia. beam of ultrasonics propagating along the central axis of a 1 cm. dia. CdS crystal. A typical experiment is now briefly described. Using interference filters, having a bandwidth of about 80Å, a CdS acoustic amplifier was successively illuminated with light having wave lengths centred on 4540, 4960, 5470 and 5800Å. In each case the light intensity was adjusted so that the crystal resistance was 1.12×10^5 ohms and the attenuation of 46.8 MHz shear ultrasonics was noted (no drift field was applied to the CdS). The ultrasonic attenuation was found to be $4.50 \pm .25$ db for each case. It was concluded from experiments of this type, including several with large applied fields, that for the acoustic amplifier used, the effect of transverse non-uniformity in crystal resistivity on the attenuation and amplification of ultrasonics was negligible and that measures to reduce the non-uniformity (for example by illuminating crystals with light beams into two opposite faces) were not necessary.

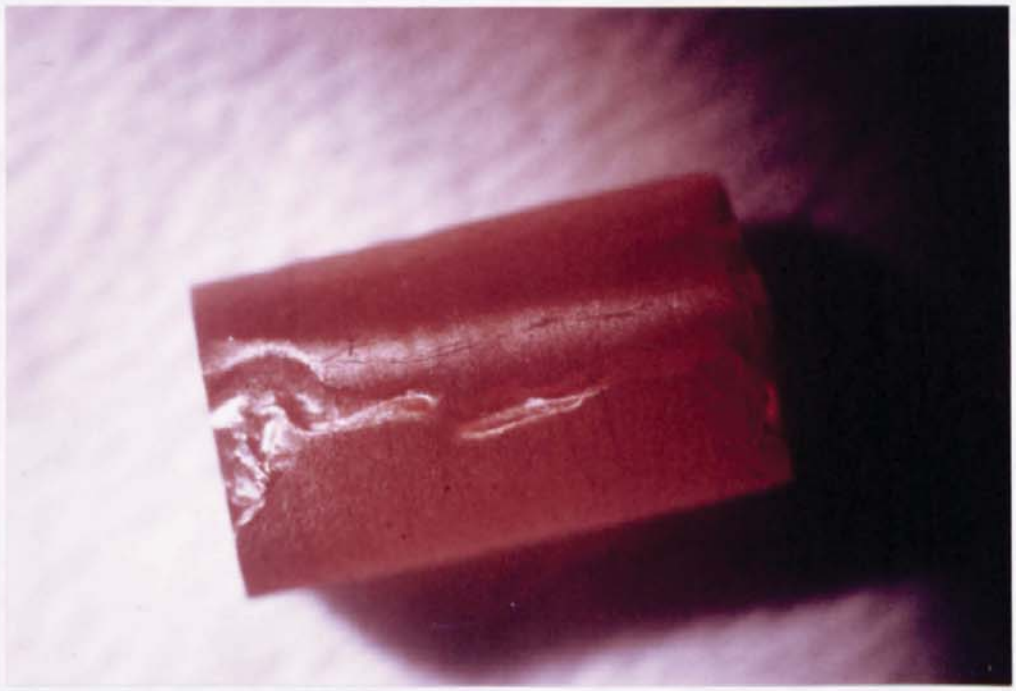

FIG. 29. ELECTRICAL BREAKDOWN OF A CdS CRYSTAL

During preliminary experimentation, using unfiltered light from an incandescent filament lamp, two crystal breakdowns were experienced on the front surface of CdS crystals. These breakdowns, one of which is shown in fig.29, were attributed to the high current density carried in the region near the front surface. In order to prevent such crystal breakdown the resistivity of the CdS was controlled by varying the intensity of weakly absorbed illumination. The radiation from a 100w incandescent filament lamp was passed through a set of three filters, as listed below, before illuminating the CdS.

Filters used:

1. 3 m.m. thick Chance HA1 - to remove all infra-red radiation.
2. Interference filter centred on 5800$\mathring{A}$ - 80$\mathring{A}$ bandwidth.
3. Wratten 23A filter - to reduce short wavelength tail of the interference filter.

4.2. Acoustic amplifier circuitry

For reasons discussed in section 1.2.2 both the drift field and the acoustic input were pulsed. In particular the use of a low duty cycle drift field pulse reduced the ohmic heating of the CdS. A block diagram of the acoustic amplifier circuit is given in fig.30. The Advance pulse generator was triggered externally at 50 or 100 pps or internally at 15 - 500 pps. It gave a pre-pulse that was used to trigger the oscilloscope. Within 0.2μS it also delivered a positive going flat topped pulse of up to 50v and 0.8 - 2μS duration to the r.f. pulse generator. This

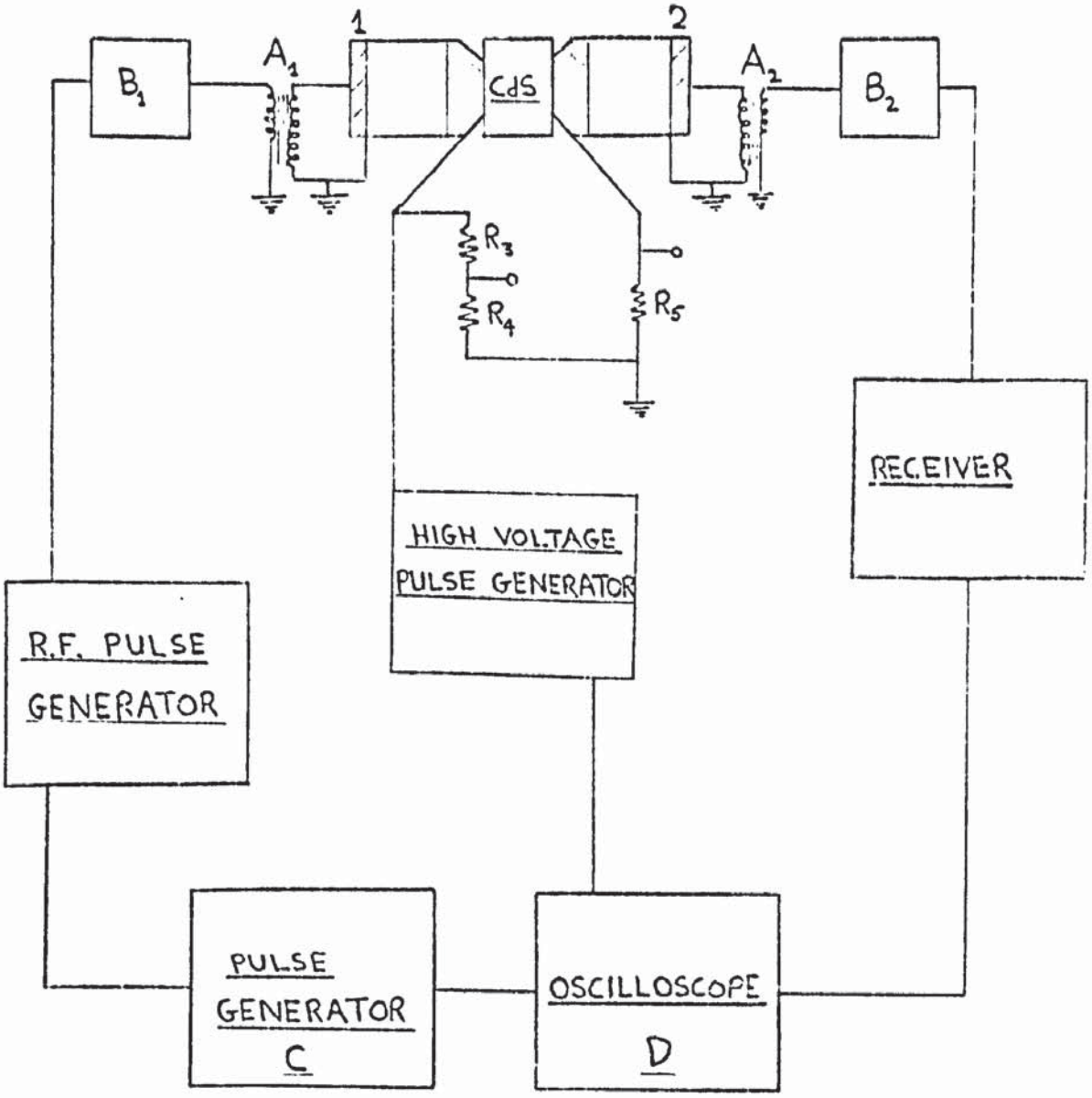

A : MATCHING TRANSFORMERS.

B : CALIBRATED V.H.F. ATTENUATORS

C : ADVANCE PG 5002D

D : TEKTRONIX 547

FIG. 30. BLOCK DIAGRAM OF ACOUSTIC AMPLIFIER CIRCUITRY.

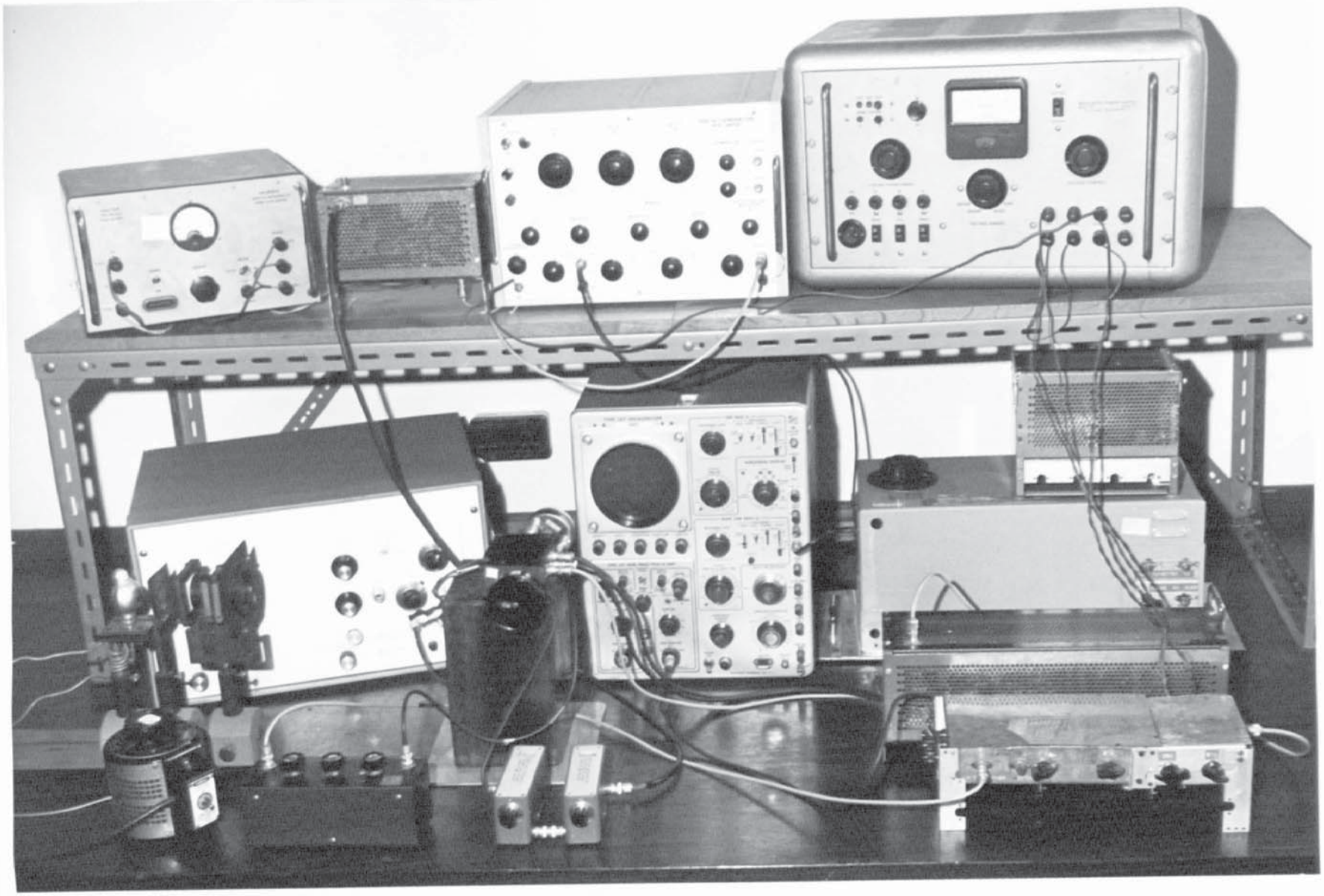

FIG. 31. EXPERIMENTAL ARRANGEMENT

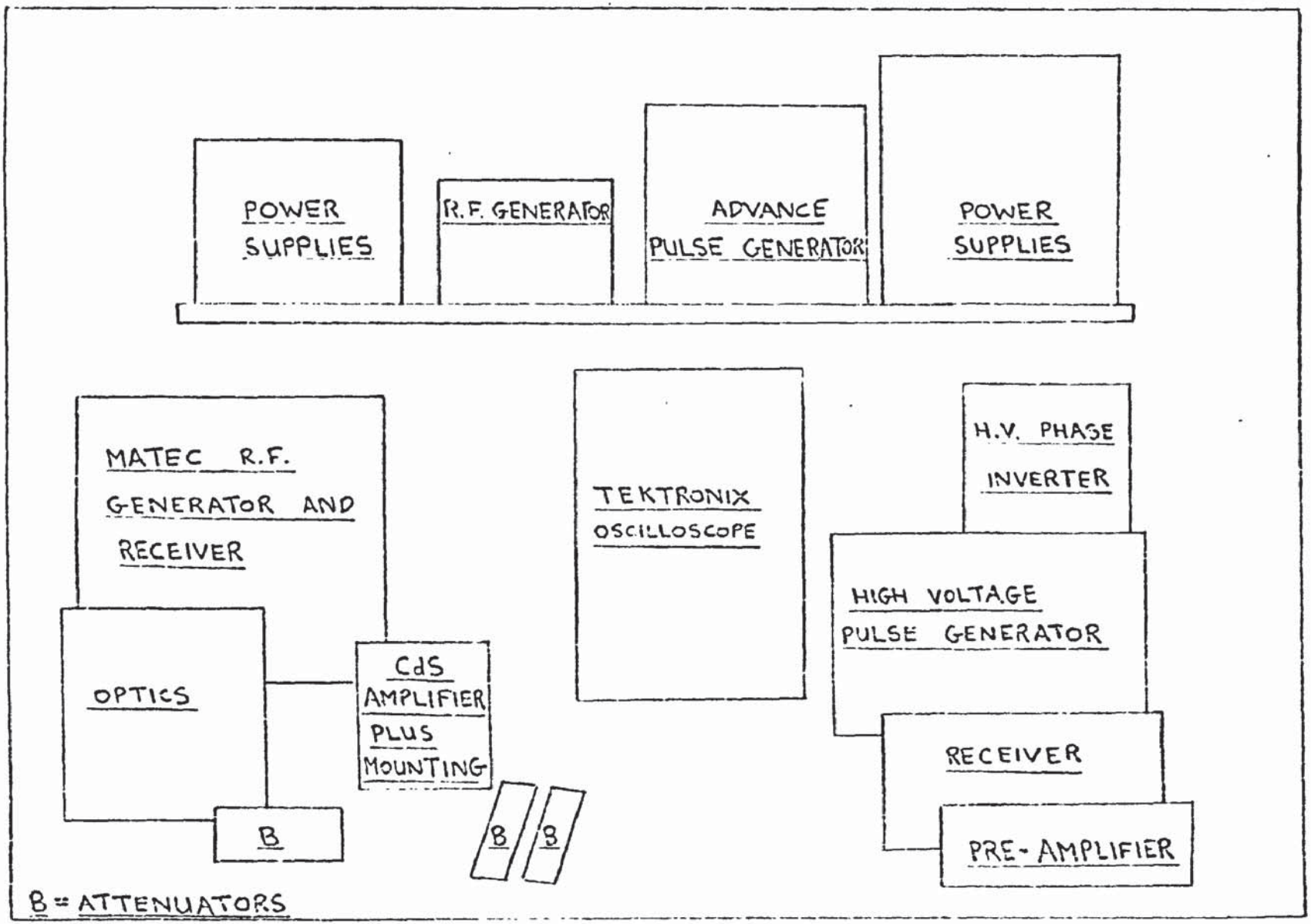

FIG. 32. KEY TO EXPERIMENTAL ARRANGEMENT.

switched the oscillator and an r.f. pulse was delivered to the first transducer. The ultrasonics generated were propagated in a fused silica buffer for approximately 4 μS before reaching the CdS. Gate A of the oscilloscope delivered a flat topped pulse of about 20v. This pulse, whose width could be varied continuously from 1 to 50 μS, was delayed 1 - 50 μS from the pre-pulse. The 20v pulse was fed to the high voltage pulse generator thereby initiating the d.c. voltage pulse. The second transducer received the transmitted ultrasonics and the superheterodyne receiver provided the amplification and detection necessary for a display on the oscilloscope. The fused silica buffers of the acoustic amplifier provided both electrical insulation between the high voltage and r.f. circuits and a convenient time delay. Some details of the r.f. and high voltage pulse generators and the r.f. receiver are given in sections 4.2.1 to 4.2.3. An ultrasonic frequency of about 45 MHz was chosen as a starting point in the present research and r.f. equipment was constructed for operation at this frequency. This frequency was chosen because it was within the bandwidth of the oscilloscopes available, whilst the ultrasonic gain predicted by White's amplification theory was considerable. Subsequently the behaviour of ultrasonics having other frequencies was investigated using a Matec ultrasonic pulse generator and receiver. Fig.31 shows the general view of the experimental arrangement (Fig.32 provides a key to fig.31.)

4.2.1. High voltage pulse generator

The principal purpose of the high voltage pulse generator

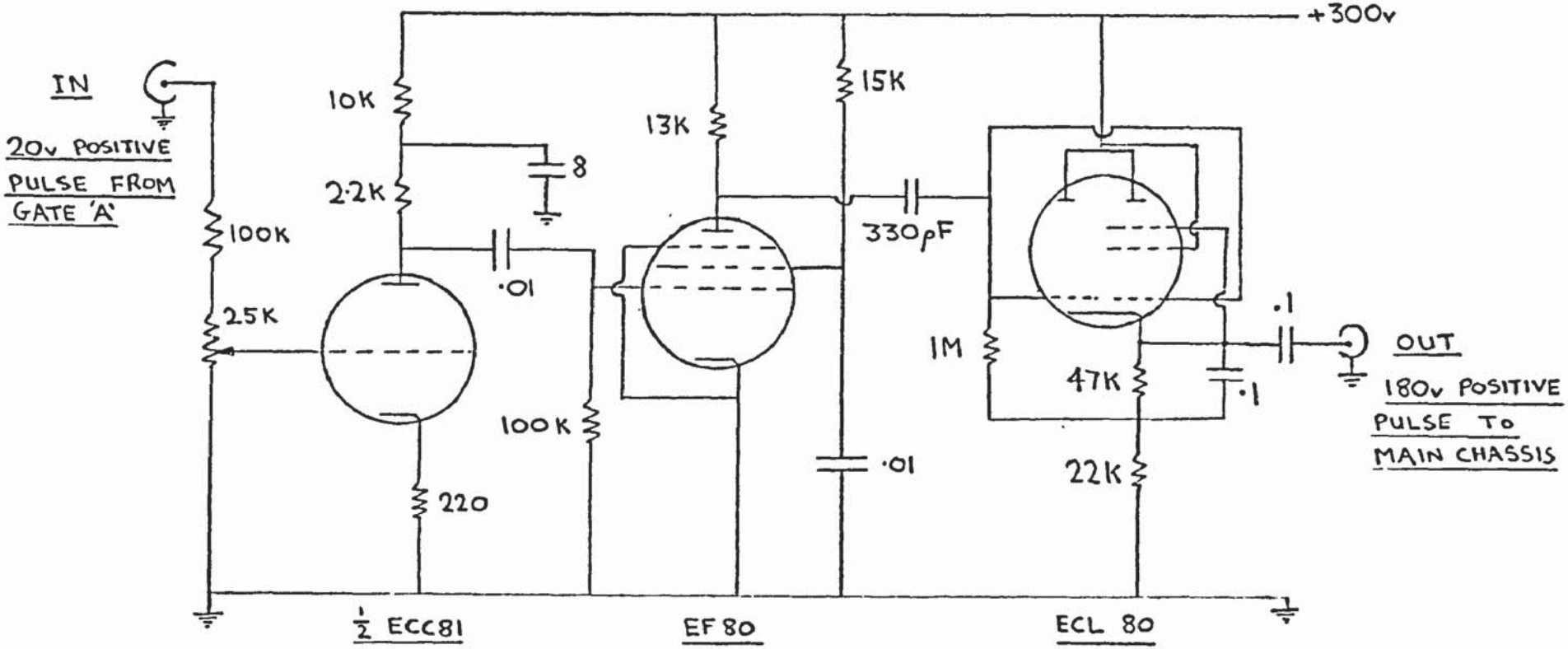

RESISTANCES IN OHMS

CAPACITANCES IN μF UNLESS OTHERWISE STATED

FIG. 33. CIRCUIT OF HIGH VOLTAGE PULSE GENERATOR. PRE-AMPLIFIER STAGE.

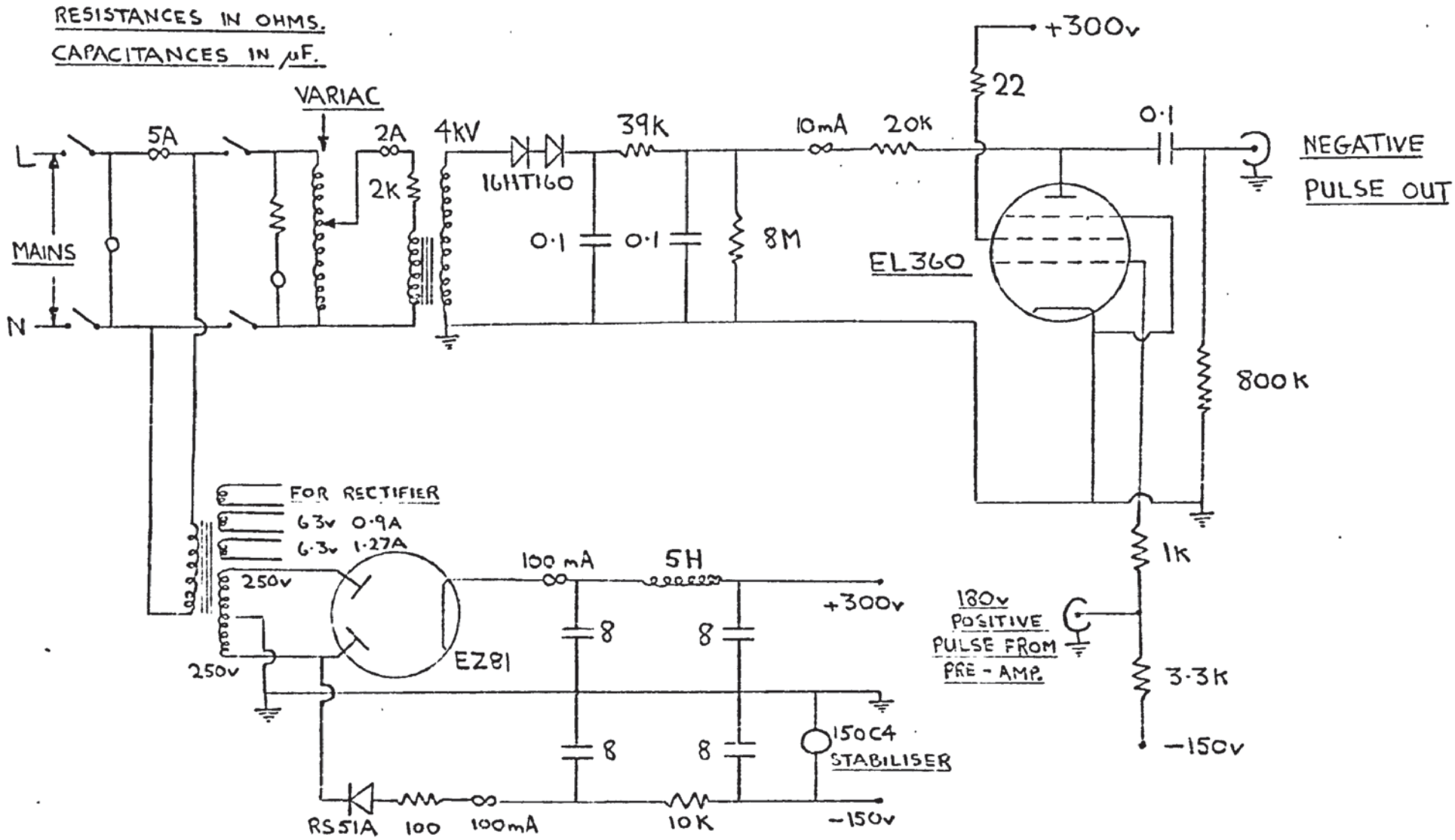

FIG. 34. CIRCUIT OF HIGH VOLTAGE PULSE GENERATOR – MAIN CHASSIS.

RESISTANCES IN OHMS

CAPACITANCES IN μF

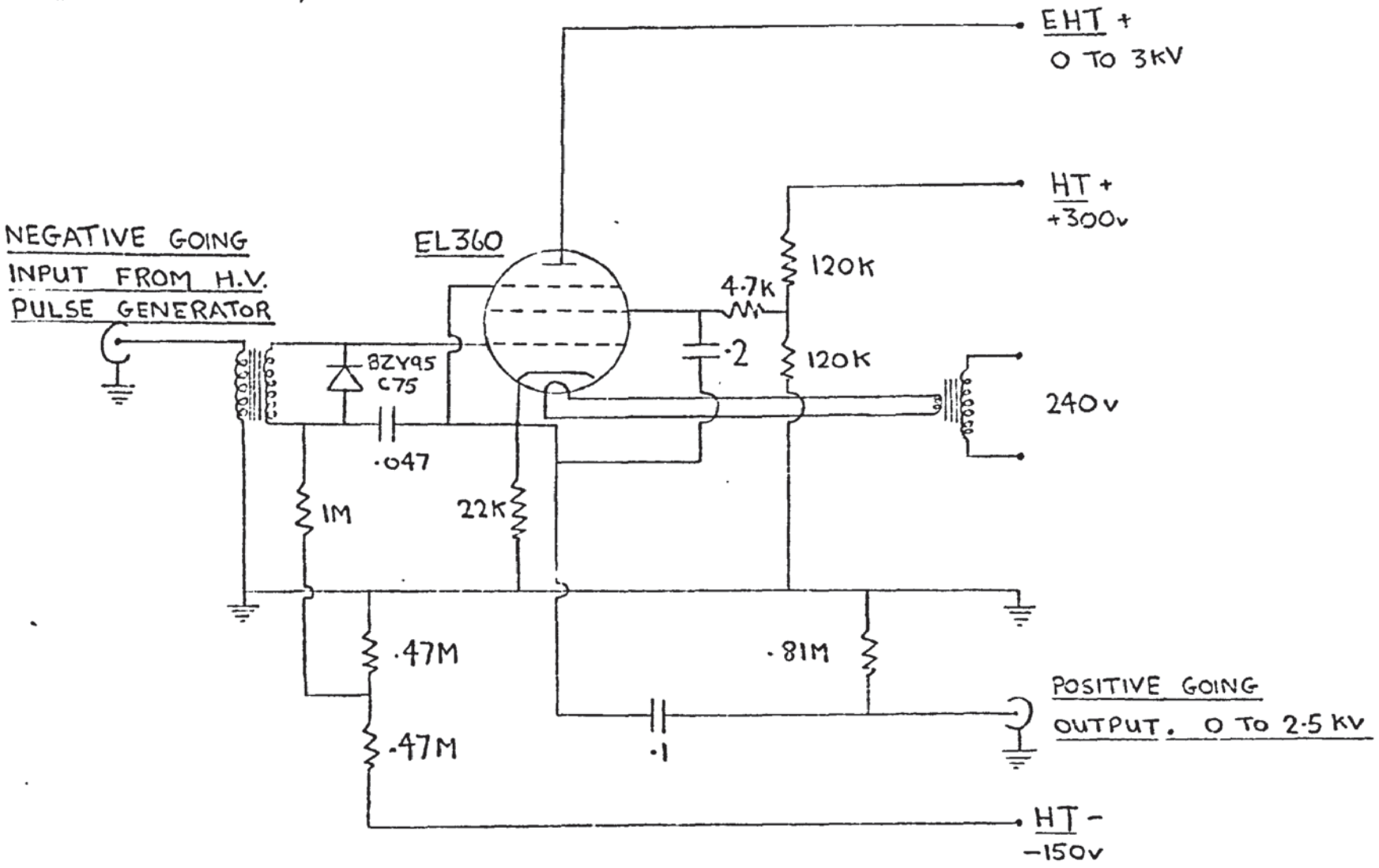

FIG. 35. CIRCUIT OF HIGH VOLTAGE PULSE GENERATOR PHASE INVERTER

was to produce the d.c. drift field across the CdS. The basic high voltage pulse generator gave negative-going flat topped pulses that were continuously variable in height from 200v to 4 kv. The width of the pulses, which was controlled by the input from gate A of the oscilloscope, was variable from 1 to 50μS. The output components of the circuit were of sufficient capacity to supply the appropriate current to crystals having a resistance of 7 kΩ or more for pulse repetition rates of 15-100 per second. The rise time of the pulses were typically 0.3μS. The circuit of the negative-going high voltage pulse generator is given in figs.33 and 34.

The positive going 20v pulse from gate A, fig.33, was introduced to the pre-amplifier via a voltage dividing network and amplified to a 180v positive going pulse. The pulse was fed to the output valve on the main chassis, fig.34. The valve, which had been held off by the negative grid potential, was turned on by the positive pulse. The current flow reduced the potential of the anode and produced a negative going pulse. The chassis included circuits for generating the +300v and -150v H.T. used.

When positive going pulses were required a high voltage pulse generator phase inverter was attached to the main pulse generator. The circuit is given in fig.35. The valve was held off by its negative voltage supply until the negative going pulse was introduced. The transformer produced a positive going pulse, which was limited in amplitude by the zener diode, and this turned the valve on. The output was taken from the cathode. The heater supplies were from a transformer, and the screen voltage was

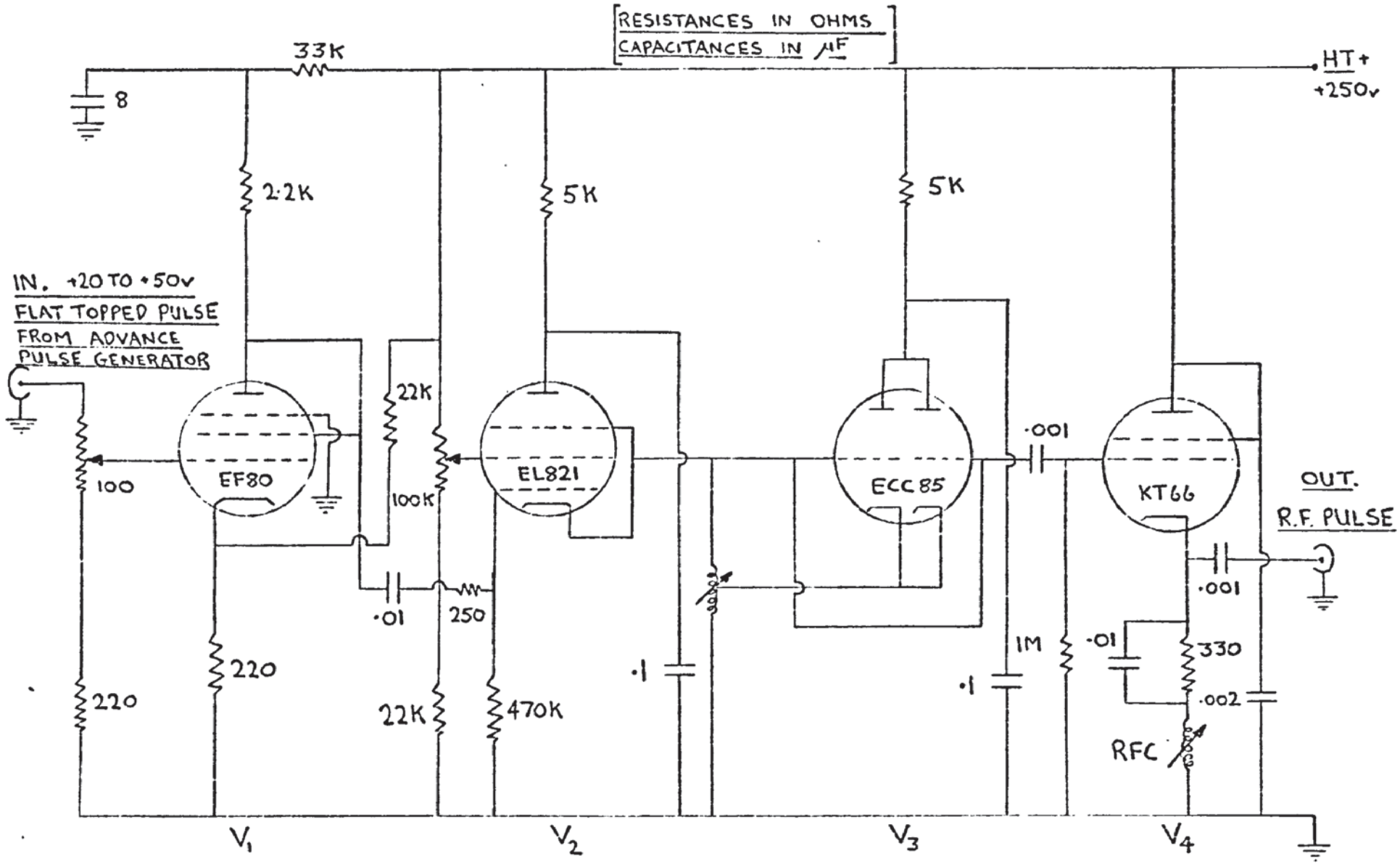

FIG. 36. PULSED R.F. GENERATOR

arranged to move in sympathy with the cathode.

4.2.2. Pulsed r.f. generator

The pulsed r.f. generator was driven by a positive going pulse from the Advance pulse generator. The circuit is given in fig.36. The V_1 stage amplified and inverted the input pulse and applied it to valve V_2 which had been operating and effectively short-circuiting the oscillator circuit of valve V_3. The pulse applied to valve V_2 turned it off and the r.f. oscillations from the Hartley oscillator circuit of V_3 were brought to the output via the cathode follower circuit of valve V_4. The cessation of the input pulse caused valve V_2 to conduct again and quench the oscillations. The frequency of oscillation was tuneable over the range 45 ± 5 MHz. The unit delivered an r.f. pulse of about 38v peak to peak into a 50 Ω termination. The rise and fall times were 0.3μS. The pulse width could be varied from less than 1μS to more than 20μS.

4.2.3. Receiver

To detect and display on the oscilloscope the small r.f. signals from the receiving transducer a superheterodyne receiver was used. The circuit of the 45 MHz receiver is shown in fig.37. The input was fed via the transformer to the grid of valve V_1. This valve mixed the input r.f. with a signal of higher frequency and the difference frequency of 30 MHz was amplified through a three stage tuned amplifier arrangement (for convenience in presentation valve V_3 and its associated circuitry which is identical to the valve V_2 stage, is omitted from the

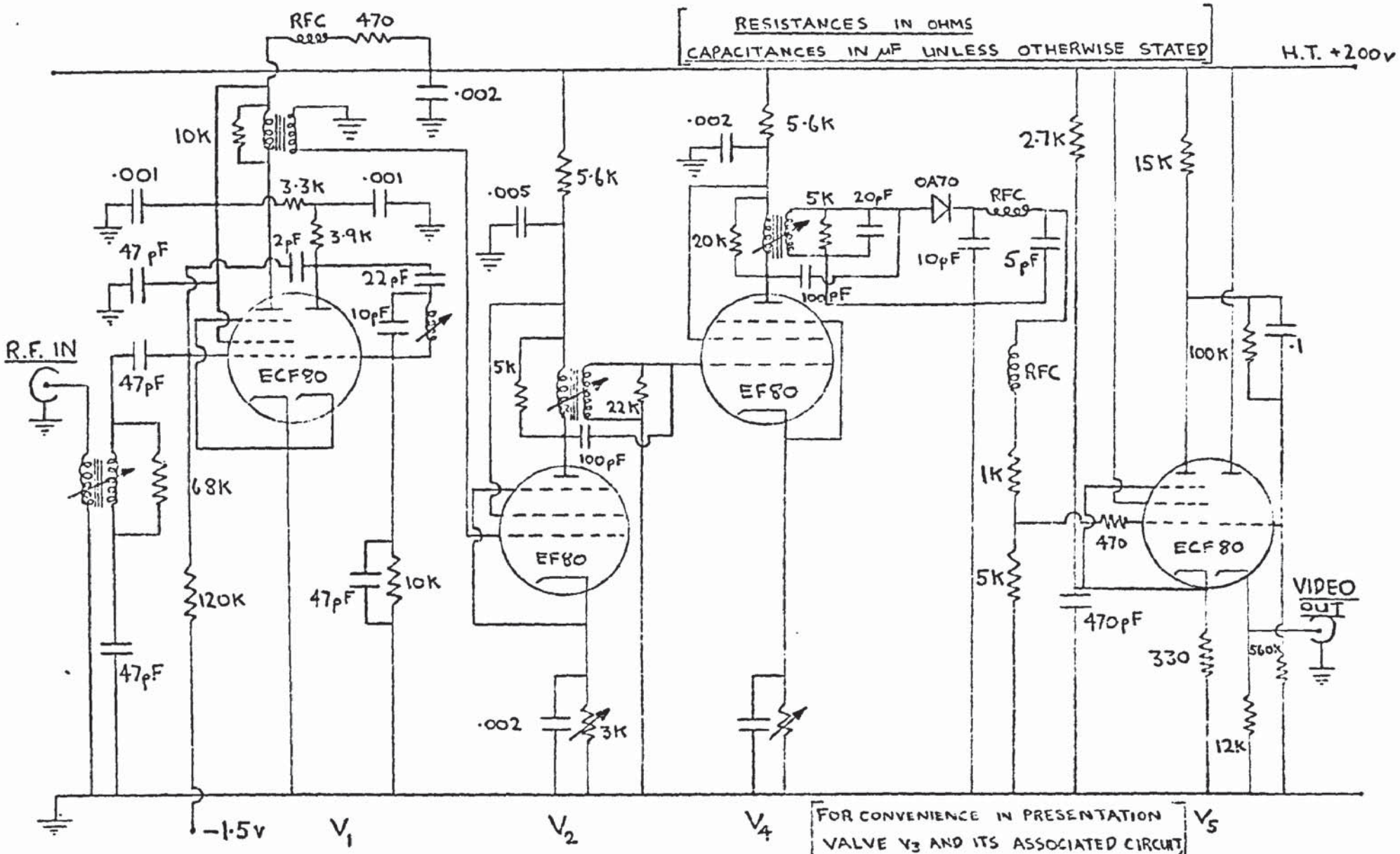

FIG. 37. RECEIVER.

FOR CONVENIENCE IN PRESENTATION VALVE V_3 AND ITS ASSOCIATED CIRCUIT, WHICH IS IDENTICAL TO THE VALVE V_2 STAGE, IS OMITTED FROM THE CIRCUIT DETAILS.

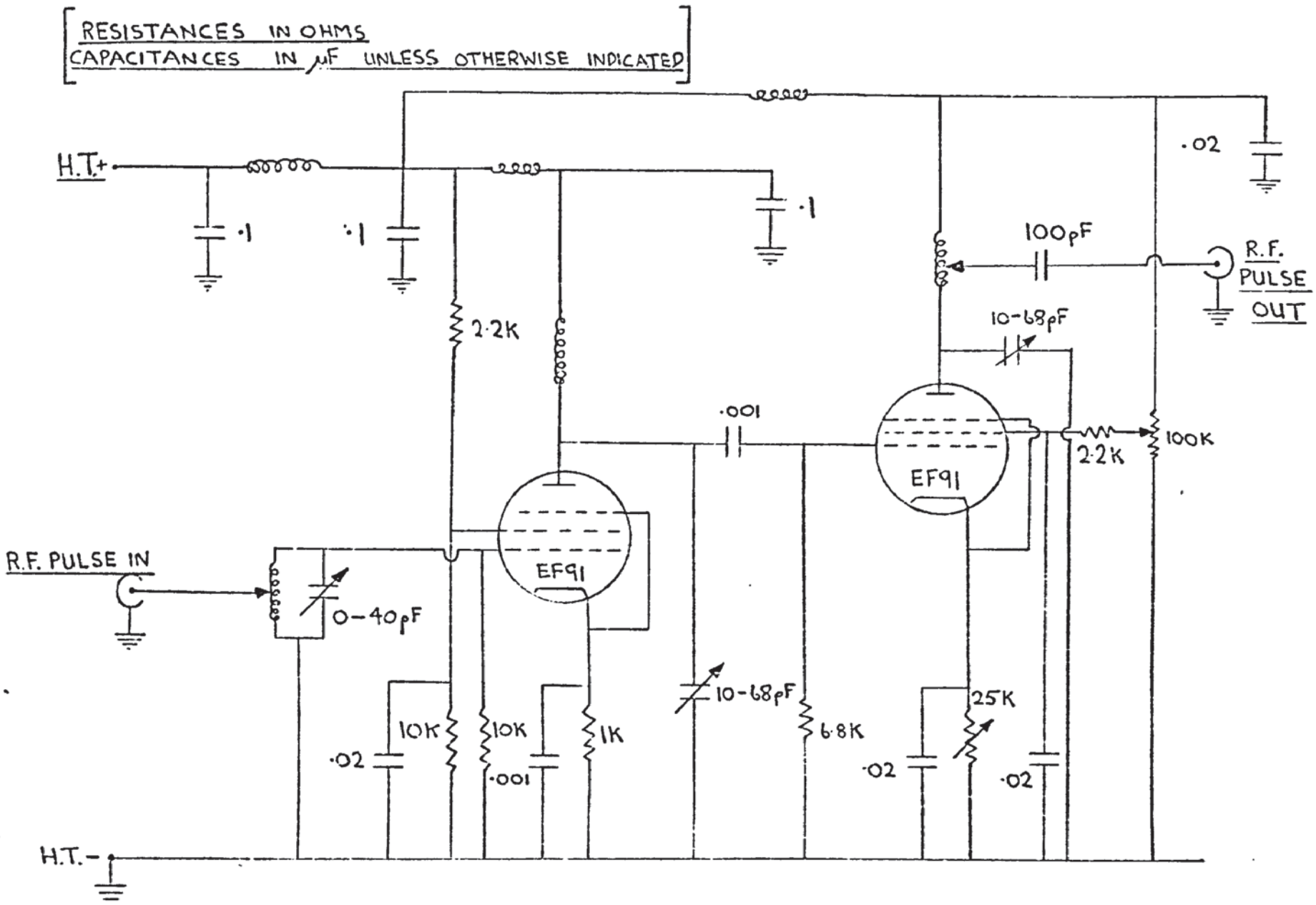

FIG. 38. CIRCUIT OF TUNED PRE-AMPLIFIER (PEAKED AT 45 MH3)

circuit drawing). After the envelope of the pulse was detected by a diode circuit a final amplification stage was used, with a cathode follower output. The output saturated at 120v. The gain available was in excess of 80 db, with a low noise level. On occasions when it was desirable to have more gain a tuned pre-amplifier was used. The circuit is shown in fig.38. The small amount of noise present in the output of the superheterodyne receiver was thought to be largely generated in the mixer stage. The use of the tuned pre-amplifier before the mixer stage enabled an additional gain of 20-25 db to be obtained without noticeably increasing the noise level. A similar receiver was constructed for use at 75 MHz.

4.3. Electrical measurements

In the following sub sections a description is given of the methods used to measure the operating parameters of a CdS acoustic amplifier.

4.3.1. Voltage and current

The value of the current flowing in the CdS crystal was obtained by measuring on an oscilloscope the voltage developed across a small resistor in series with the CdS, fig.30. The voltage applied across the crystal was similarly measured using a voltage dividing chain in parallel with the crystal. The crystal resistivity was controlled by varying the illumination intensity.

The measurements of current and voltage were accurate to $\pm$ 3% individually. The crystal resistance was measured with an accuracy of $\pm$ 6% by using current and voltage readings obtained

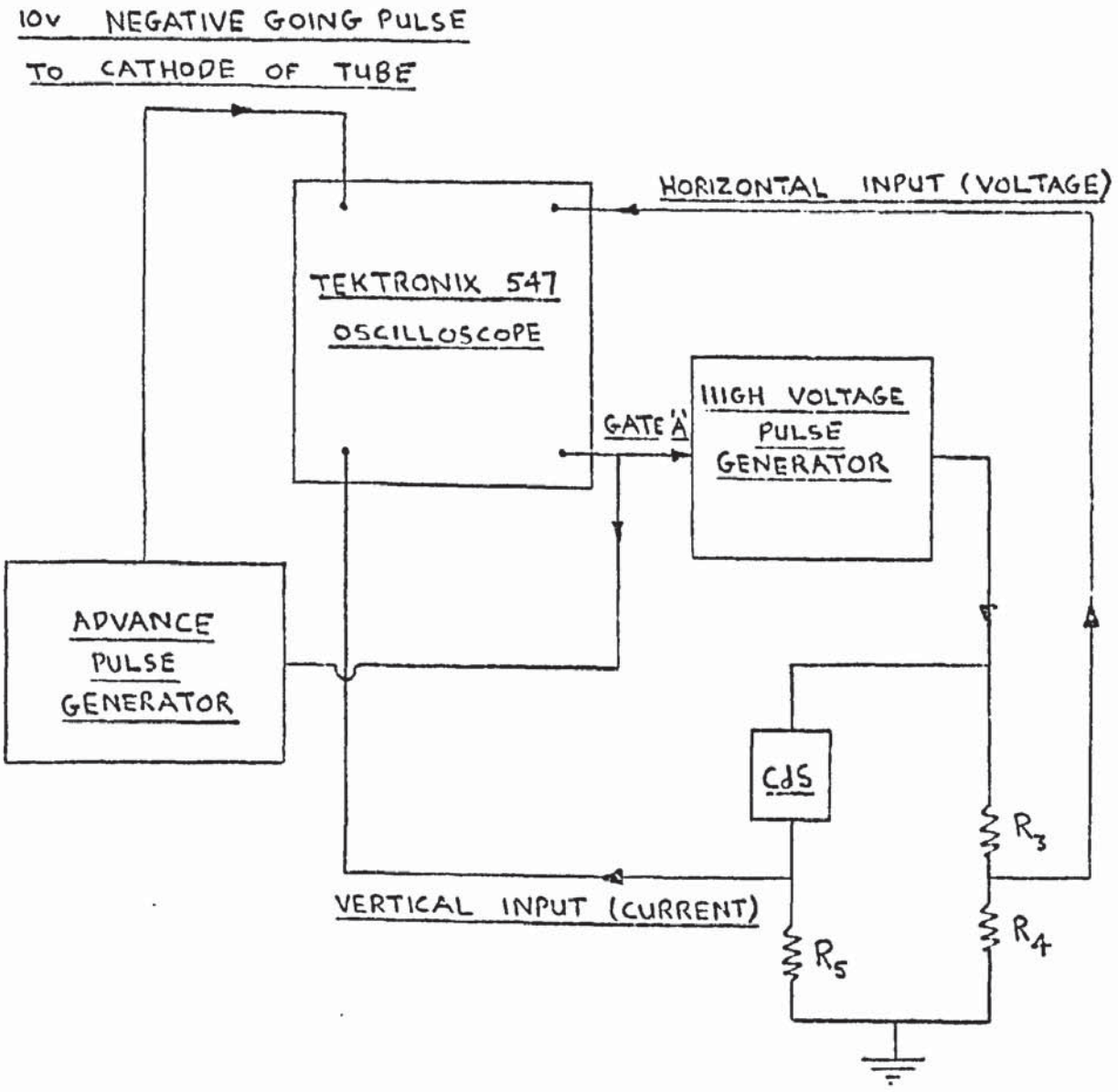

FIG. 39. BLOCK DIAGRAM OF CIRCUIT USED FOR CURRENT-VOLTAGE CHARACTERISTICS

during pulsed operation.

The high voltage pulse generator produced flat topped pulses when it was controlled by gate A of the oscilloscope. The resistance network used in conjunction with the CdS crystal enabled the current and voltage to be monitored and displayed on the dual trace plug-in of the oscilloscope. To obtain the current-voltage characteristics directly the high voltage pulse generator was controlled by sweep A of the oscilloscope, so that a ramp output was obtained, and the current monitoring lead was fed into the vertical input whilst the voltage monitoring lead was fed into the horizontal input. This simple method for obtaining the current-voltage characteristics was not suitable for voltages producing supersonic electron drift in the CdS because of the time delay in the production of a large internal acoustic flux which often involved several sonic transits in the CdS. The arrangement used for obtaining current-voltage characteristics under these conditions is shown in fig.39. The pulse applied to the cathode of the oscilloscope tube was variable in width and could be delayed with respect to the gate A output. The current and voltage traces were brightened and the relationship of current to voltage was displayed after giving the acoustic flux time to build up, if appropriate drift voltages were used. The current-voltage characteristic was traced out point by point as the voltage was increased.

4.3.2 Ultrasonic frequency

The ultrasonics were produced by applying r.f. signals to quartz transducers having a nominal fundamental frequency of

TABLE 2

Transducer harmonic	nominal resonant frequency MHz	measured resonant frequency* MHz
1	15	15.6
3	45	46.8
5	75	78.0
7	105	109.2
9	135	140.4
11	165	171.6
13	195	202.8
15	225	234.0
17	255	265.2
19	285	296.4
21	315	327.6
23	345	358.8

* Extrapolated values after the 7th harmonic

15 MHz. Ultrasonics of higher frequency were obtained by operation at odd harmonics of the fundamental, up to the 23rd harmonic. The resonant frequency of the transducers was measured by altering the frequency of the r.f. input until the maximum signal was propagated through the amplifier structure, with the CdS in the dark. The frequency of the input r.f. signal was measured for the 1st, 3rd, 5th and 7th harmonics using a calibrated Tektronix 547 oscilloscope. The measurement of frequency was accurate to $\pm$ 1%. The results, which showed consistent behaviour, have been extrapolated to the 23rd harmonic and are given in Table 2. For convenience the nominal frequency of operation eg. 15, 45, 75 MHz is referred to in the following sections. The bandwidth of the transducers was about 2 MHz for the third harmonic.

4.3.3. Ultrasonic attenuation

Calibrated step attenuators were used to control the magnitude of the r.f. input to the transmitting transducer and the input to the receiver. The attenuation of the ultrasonics propagated through CdS under various operating conditions was compared to the standard condition of the CdS in the dark with no applied voltage by using the attenuators to maintain a constant input level to the receiver. In this way problems associated with receiver non-linearity and ageing were eliminated. The attenuators consisted of switched networks such that the input and output impedances were sensibly constant for all dial settings. The calibration of the attenuators was accurate only if the impedences

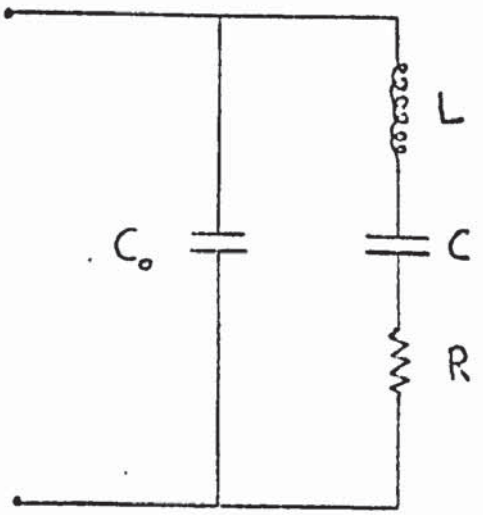

a) EQUIVALENT ELECTRICAL CIRCUIT FOR A PIEZOELECTRIC TRANSDUCER.

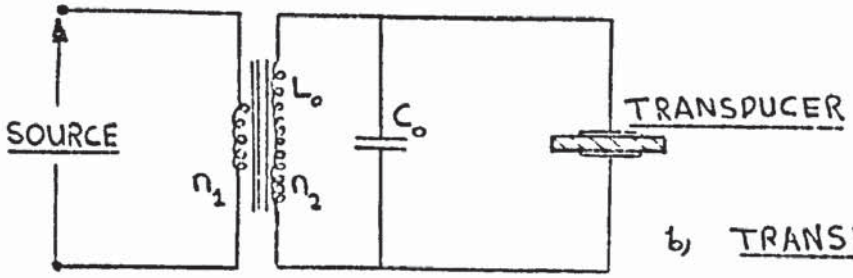

b) TRANSFORMER FOR MATCHING A PIEZOELECTRIC TRANSDUCER

FIG. 40 TRANSDUCER CIRCUITS.

presented to them at either end were the same as their characteristic impedance. In order to correctly terminate the attenuators the effective impedance of the transducers was matched to the attenuators by a transformer. The equivalent electrical circuit for a piezoelectric transducer is shown in fig.40a (from Blitz [75], p 50). The symbols used are given below:

C_o = capacitance between electrodes

inductance $L = \frac{M}{\alpha^2_T}$ M = transducer mass

capacitance $C = \frac{\alpha^2_T}{Cm}$ Cm = mechanical compliance

resistance $R = \frac{R_m}{\alpha^2_T}$ R_m = mechanical resistance

α^2_T is called the transformation factor and is related to the velocity of the transducer surface. The values of L, C and R depend particularly on the mounting of the transducer and during the present research the optimum values of the transformer matching arrangement, fig.40 b, were obtained empirically.

The transformers were mounted in an earthed box that was fitted directly onto the acoustic amplifier housing. They were tuneable by means of a ferrite core and a capacitor across the secondary.

The output impedance of the r.f. pulse generator was equal to the characteristic impedance of the attenuators. The attenuators were matched to the pre-amplifier and receiver by means of transformers.

To calibrate the attenuator B_1, fig.30, the output from

transformer A_2 was fed directly into channel 1 of the measuring oscilloscope. Channel 2 displayed the output from the r.f. pulse generator. The transformer A_1 was tuned so that the output of the r.f. pulse generator did not vary when the attenuator B_1 was switched from zero inserted db to an attenuation setting of say 10db. When this condition was achieved the input transducer was adequately matched. The voltages indicated on channel 1 for various settings of B_1, under constant input conditions, were used to calculate the actual values of the attenuation settings.

For the purpose of adjusting transformer A_2 to present the correct impedance to attenuator B_2 the attenuator was connected to the r.f. pulse generator instead of the receiving equipment and the output from transformer A_1 was fed directly into channel 1 of the oscilloscope. Transformer A_2 was adjusted until it presented the correct impedance to B_2 using the technique previously described for transformer A_1. Having matched the transducer to the attenuator B_2 by using the transducer to transmit ultrasonics into the CdS the circuitry was arranged as fig.30 ie. the output from attenuator B_2 was fed into the receiver. A tap-off between A_2 and B_2 was fed into channel 1 of the oscilloscope. The input transformer of the receiver was tuned until the signal on channel 1 did not vary when the attenuator B_2 was switched from zero inserted db to an attenuation setting of say 10db. When this condition was achieved the attenuator B_2 was adequately matched.

A sensitive check on the matching and accuracy of the attenuators was made by operating the system as fig.30 with initially

0 db in B_1 and for example 50 db in B_2 . The CdS was maintained in the dark to prevent electro-acoustic effects causing non-linearity. The magnitude of the receiver signal was noted. As the attenuation in B_1 was increased in steps the corresponding values of B_2 necessary to maintain the signal at a constant level were noted. At all settings the sum of the attenuation in B_1 and B_2 was very close to 50 db for correct matching.

The measurements of attenuation caused by electro-acoustic effects were made by altering the attenuators so as to restore the receiver output to a constant value. This method was found to be more accurate and convenient than a method based on calibration of the receiver sensitivity.

The procedure used to measure attenuation changes in the CdS is described below using the example of the variation of attenuation with applied voltage. Preliminary work necessary in this experiment was to match the attenuators carefully, measure the ultrasonic frequency and ensure that the drift field pulse had a suitable time duration and was correctly phased with respect to the entry of the pulse of ultrasonics into the CdS. With the crystal in the dark the attenuators B_1 and B_2 were set with enough attenuation in the circuit to give a reasonable signal from the receiver. It was desirable that the signal from the receiver produced an oscilloscope trace whose height could be accurately measured. The crystal was then illuminated and the crystal resistivity was measured until a steady value was obtained. The attenuators were adjusted to produce the standard receiver signal.

The voltage across the crystal was raised in steps to a maximum whilst the attenuator settings to give the standard signal were noted. The readings were repeated as the voltage was reduced to zero in steps. The crystal resistivity was checked to see if any change had occured during the experiment. Finally the attenuator settings for the dark condition were checked. This procedure was found to give reproducible results to better than $\pm$ .5 db.

4.3.4. Ultrasonic power level

Ishiguro et al [14] observed that a CdS ultrasonic amplifier which strongly amplified small signals showed a saturated output when large input signals were applied. In the present research the behaviour of large amplitude ultrasonic signals in CdS was investigated for a wide range of operating conditions and a measure of the acoustic power level in the CdS was required in order to analyse the results.

The peak acoustic power level present in a pulse of ultrasonics as it entered the CdS was measured by an insertion loss technique at 45 MHz. Using the methods described in section 4.3.3. the attenuators were accurately matched to the circuit shown in fig.30. The second attenuator (B_2) and the receiver were then removed and the output of the transformer A_2 was fed directly into the oscilloscope, which was terminated by the appropriate impedance. The arrangement at this time is shown in fig.41. Using the full output of the r.f. generator, and a known pulse length, the maximum peak to peak height (A)

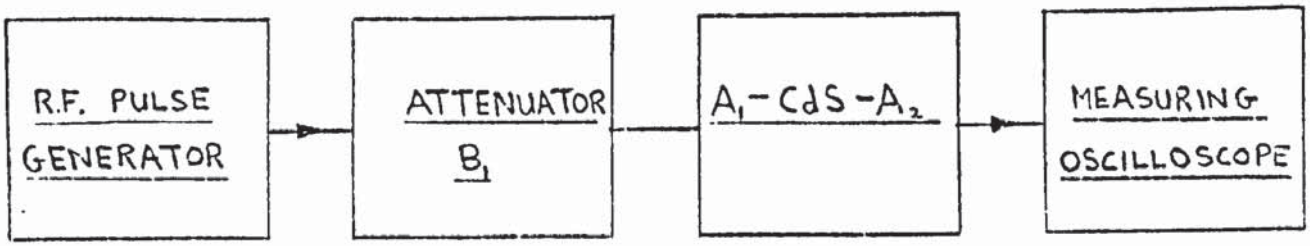

FIG. 41. BLOCK DIAGRAM OF INSERTION-LOSS MEASUREMENT CIRCUITRY

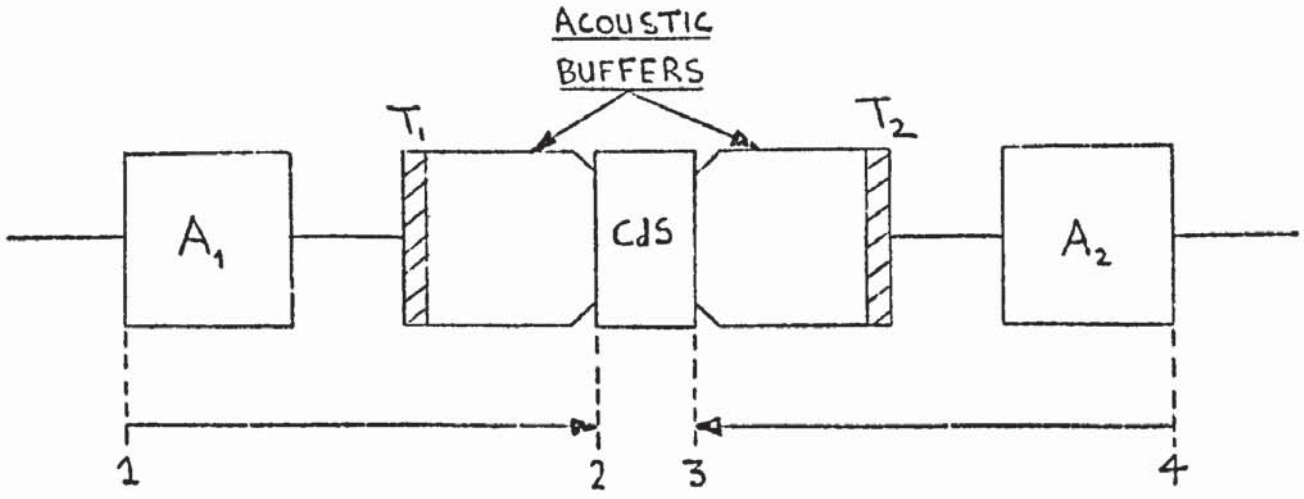

A_1, A_2 - TRANSFORMERS.

T_1, T_2 - TRANSDUCERS.

FIG. 42. SIGNAL LOSSES IN THE ACOUSTIC AMPLIFIER ASSEMBLY.

of the r.f. pulse displayed on the oscilloscope was noted for a known setting of the attenuator. During this measurement the CdS was kept in the dark. The CdS housing, with both transformers, was then removed and the attenuator was fed directly to the oscilloscope which was terminated by the appropriate impedance. The in-circuit attenuation was adjusted until the oscilloscope displayed a signal of height A (on the same oscilloscope setting as before). In this way the total attenuation (insertion loss) due to the two transformers and the CdS amplifier structure was measured without having to correct for the oscilloscope bandwidth. The maximum peak to peak voltage of the r.f. generator was measured, using a convenient number of decibels in the attenuator, and if necessary a correction was made for the fall off of oscilloscope sensitivity due to its bandwidth. Hence the maximum electrical power produced by the r.f. pulse generator could be calculated.

McFee and Bateman [101] have measured the non-electronic contribution to the ultrasonic attenuation in CdS (ie. the dark attenuation) and found it to be small eg. less than 0.1 db $cm.^{-1}$ at 45 MHz. The small acoustic loss in the CdS under these conditions means that it is the regions 1 to 2 and 3 to 4 of the acoustic amplifier, fig.42, that produce the measured insertion loss. Region 1 to 2 includes transformer A_1, transducer T_1, salol bond, buffer and one indium bond. If it was established that the loss incurred in region 1-2 was W dbs less than that in region 3-4 then we can calculate the maximum acoustic power incident into the CdS in the following manner.

total loss in the acoustic amplifier structure

(db) = X + Y = Z

X = loss in section 1-2

Y = loss in section 3-4

Y-X = W

$$\therefore \quad X = \frac{Z-W}{2}$$

The peak acoustic power level entering the CdS (Q'_{max}) is thus $\frac{Z-W}{2}$ dbs down on the measured maximum electrical power produced by the r.f. pulse generator. Finally the maximum acoustic intensity I entering the CdS was obtained by dividing Q'_{max} by the cross-sectional area of the acoustic beam. The peak acoustic strain incident into the CdS is given by the following equation:

$$I = \tfrac{1}{2} \rho V_s^3 S^2$$

S = strain

V_s = acoustic velocity

ρ = density

In the present research the difference between X and Y was determined using the acousto-electric effect. The ratio of the acousto-electric voltages obtained for a given input into each end of the amplifier structure in turn was measured with the CdS illuminated. This ratio, expressed in terms of decibels, provided the value of Y-X used to calculate the maximum acoustic intensity entering the CdS.

In determining acoustic power by the insertion loss technique it was necessary to consider the effect of acoustic

diffraction on the measured loss.

The acoustic wave radiated from an extended source has not, in general, the symmetric spherical radiation pattern characteristic of a point source. The acoustic pressure produced at any point by an extended source is the sum of the pressures that would be produced by an equivalent assembly of point sources. When the radius of the active region of the transducer is large compared to the acoustic wavelength the radiation pattern has many side lobes and the angular width of the main lobe is small. The acoustic intensity along the axis of a circular transducer is known to undergo wide variations with increasing distance from the transducer (Kinsler and Frey [90], p 175). This intensity variation shows a series of maxima of constant amplitude and intervening nulls. The axial intensity has its last maximum at a distance given by

$$d = \frac{a^2}{\lambda}$$

d = distance from transducer.

a = radius of active region of transducer.

λ = acoustic wavelength.

The region extending a distance $\frac{a^2}{\lambda}$ in front of a transducer is known as the Fresnel zone and in this zone the radiated sound may be thought of as being confined within a cylinder of radius 'a'. The region further away from the transducer than the Fresnel zone is known as the Frauhofer zone. For distances such that $d > \frac{3a^2}{\lambda}$ the beam shows at least approximately spherical divergence. The maximum half angle of divergence

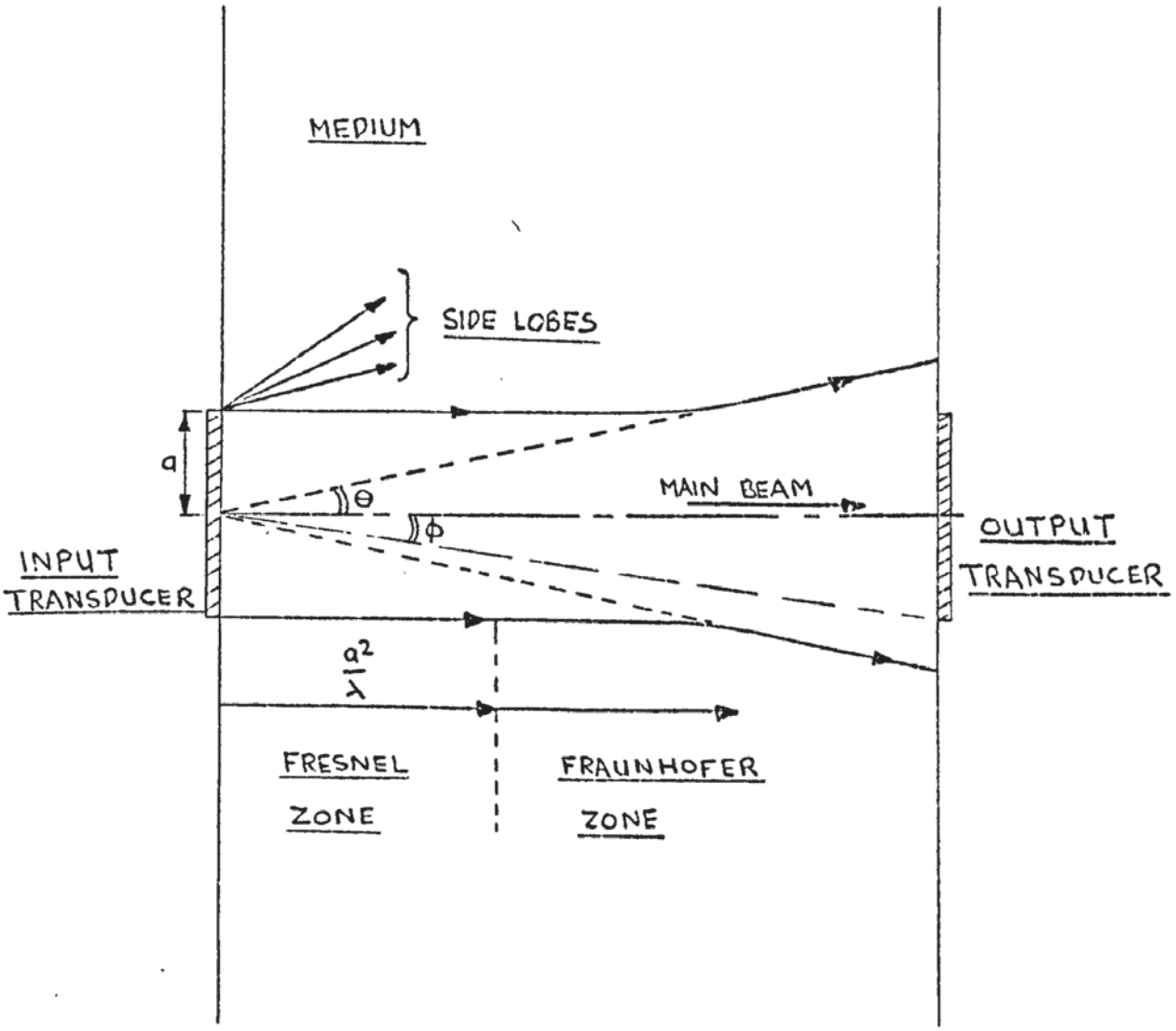

θ = FRESNEL ANGLE

ϕ = ACCEPTANCE ANGLE OF OUTPUT TRANSDUCER

FIG. 43 ACOUSTIC BEAM FROM A TRANSDUCER

FIG. 44. ACOUSTIC ATTENUATION DUE TO DIFFRACTION (AFTER SEKI ET AL.[103])

is given by the equation

$$\text{Sin } \theta = \frac{0.61\lambda}{a}$$

Fig.43 shows the beam of sound in front of a transducer.

Considerable mathematical difficulties are encountered in showing how the measured acoustic intensity varies with distance from the circular transducer, as integrated over the receiving area, and various expressions and approximation schemes have been developed, for example Williams [102], Seki et al [103], Papadakin [104], and Bass [105]. It is generally accepted that the apparent attenuation caused by diffraction effects alone amounts to about 1 db per distance of $\frac{a^2}{\lambda}$. Fig.44 shows the apparent loss in db caused by diffraction effects as a function of $\frac{a^2}{\lambda}$ (from Seki et al [103]). The curve was computed for ka = 100 and within 2% it is correct for all values of ka between 100 and 1000.

$$k = \text{propagation constant}$$
$$= \frac{2\Pi}{\lambda}$$

The transducers used had an active region of diameter 0.318 cm. The velocity of shear waves in CdS is 1.75×10^5 cm. sec^{-1}. The corresponding value for fused silica [106] is 3.76×10^5 cm. sec^{-1}. Table 3 gives the Fresnel lengths and angles (θ) in CdS and fused silica for operations at three frequencies.

TABLE 3.

Frequency (MHz)	$\frac{a^2}{\lambda}$ (cm.)		θ Fused Silica	θ CdS
	fused silica	CdS		
15.6	1.04	2.25	$5^\circ\ 24'$	$2^\circ\ 28'$
46.8	3.12	6.75	$1^\circ\ 43'$	$0^\circ\ 50'$
78.0	5.20	11.25	$1^\circ\ 5'$	$0^\circ\ 30'$

The acoustic amplifier structure used was fabricated with a .74 cm. long piece of CdS sandwiched by two 1.50 cm. long fused silica buffers.

To estimate the attenuation caused by diffraction at various planes in the acoustic amplifier structure the appropriate cumulative values of $\frac{a^2}{\lambda}$ were used in conjunction with fig. 44. Table 4 shows the diffraction loss incurred during the acoustic transit to three planes in the amplifier structure.

TABLE 4.

Frequency (MHz)	Cumulative diffraction loss (db) Input transducer to:		
	1. Silica/CdS interface	2. CdS/ silica interface	3. Output transducer
15.6	2.5	2.6	2.9
46.8	1.3	1.6	1.9
78.0	1.1	1.2	1.5

For operation at 46.8 MHz the losses caused by diffraction are only 1.9 db for acoustic propagation through the whole amplifier assembly. When the acoustic beam enters the CdS 1.3 db of this loss has already occurred. At this frequency the effective length of the amplifier structure is equivalent to $1.07 \frac{a^2}{\lambda}$ and the received acoustic wavefront is sensibly plane. For operation at 78 MHz the attenuation caused by diffraction is less than for 46.8 MHz operation. At 15.6 MHz the diffraction attenuation was 2.9 db for propagation thrcugh the whole amplifier, of which 2.5 db had occured during the transit to the first CdS - fused silica interface. At this frequency the diffraction effects meant that the receiving transducer had spherically diverging waves of large radius of curvature incident on it. The phase change across the .318 cm. dia. active region of the transducer corresponded to

only 13% of the acoustic wavelength in Y-cut quartz. Thus the wavefront curvature was negligible. Using the figures quoted in Table 4 the determined values of acoustic power entering the CdS for operation at three frequencies were corrected for diffraction effects.

The error in the insertion loss measurement of acoustic power at 46.8 MHz was estimated to be about $\pm$ 2 db. The input acoustic powers entering the CdS for operation at 15.6, 46.8, and 78 MHz were compared using the acousto-electric effect. This comparison was estimated to be accurate to about $\pm$ 1 db.

SECTION 5

EXPERIMENTAL RESULTS

5.1 Introduction

In sections 3 and 4 a description was given of the preparation of an acoustic amplifier structure and the techniques used to operate it.

In this section specific experiments are described and the results are presented under the following sub-headings :

5.2 Current-voltage characteristics of CdS under various operating conditions.

5.3 Attenuation and amplification of ultrasonic waves of small amplitude.

5.4 Acousto-electric effect.

5.5 Effects of phasing and length of drift field pulse.

5.6 Experiments with large amplitude waves.

All the experiments were performed at room temperature. Full discussion of the results and their inter-relationships forms the content of section 6.

5.2 Current-voltage characteristics of CdS

After a CdS crystal had been orientated and shaped, indium contact areas were produced on the two end faces and the current-voltage characteristics were investigated. The ohmic quality of the contacts was judged to be satisfactory if the current-voltage characteristics were linear for small applied

voltages.

An investigation of the current-voltage characteristics provided information about several properties of the crystal that were important if the crystal was to operate successfully in an acoustic amplifier structure. The resistance of the crystal was measured for a wide range of illumination intensities down to zero. The desirable range of crystal resistivity (ρ) was $\rho > 10^7$ ohm-cm. with the crystal in the dark, falling to $\rho < 10^4$ ohm-cm. for high illumination levels. As described in section 1.2.3 CdS crystals can show departures from Ohmic behaviour for applied voltages large enough to produce supersonic electron drift. The value of the voltage at which departures from Ohm's law occurred was used to estimate the electron mobility.

The quality of commercially available single crystal CdS is known to vary considerably. The information provided by the observation of the current-voltage characteristics prevented the inconvenience of fabricating an acoustic amplifier structure with a particularly unsuitable crystal.

Some observations of the current-voltage characteristics of CdS, for various operating conditions, are presented in sections 5.2.1 to 5.2.3.

5.2.1 Current-voltage characteristics for uniform illumination

The results described in this section relate to a CdS crystal produced by Koch-light Ltd. The crystal was originally cylindrical in shape, being 7.5 m.m. long and 5.0 m.m. dia. A flat surface 3.0 m.m. wide was ground along its length and indium

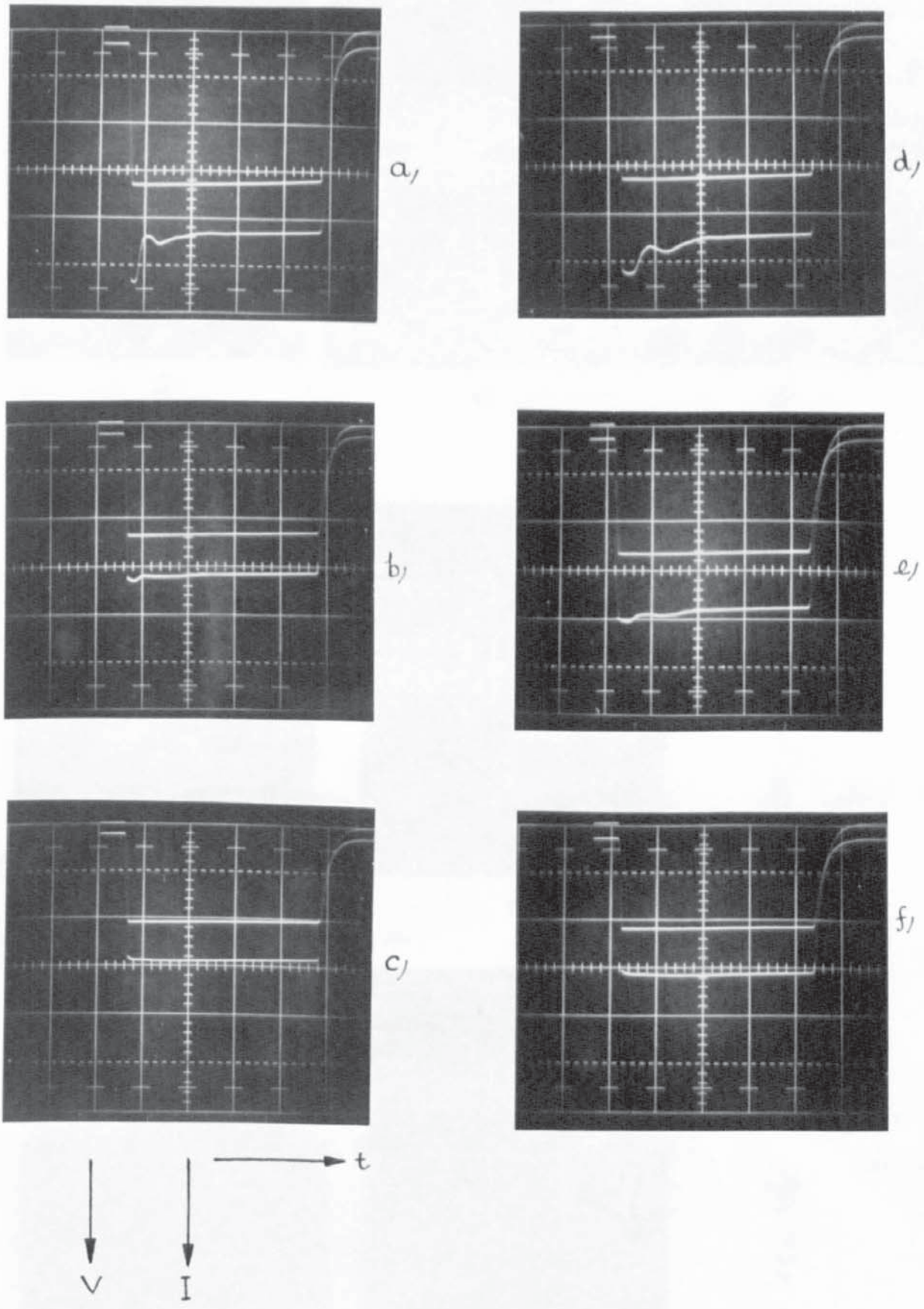

FIG. 45. PULSED VOLTAGE AND CURRENT TRACES FOR CdS.
OPERATING DETAILS GIVEN IN TABLE 5.

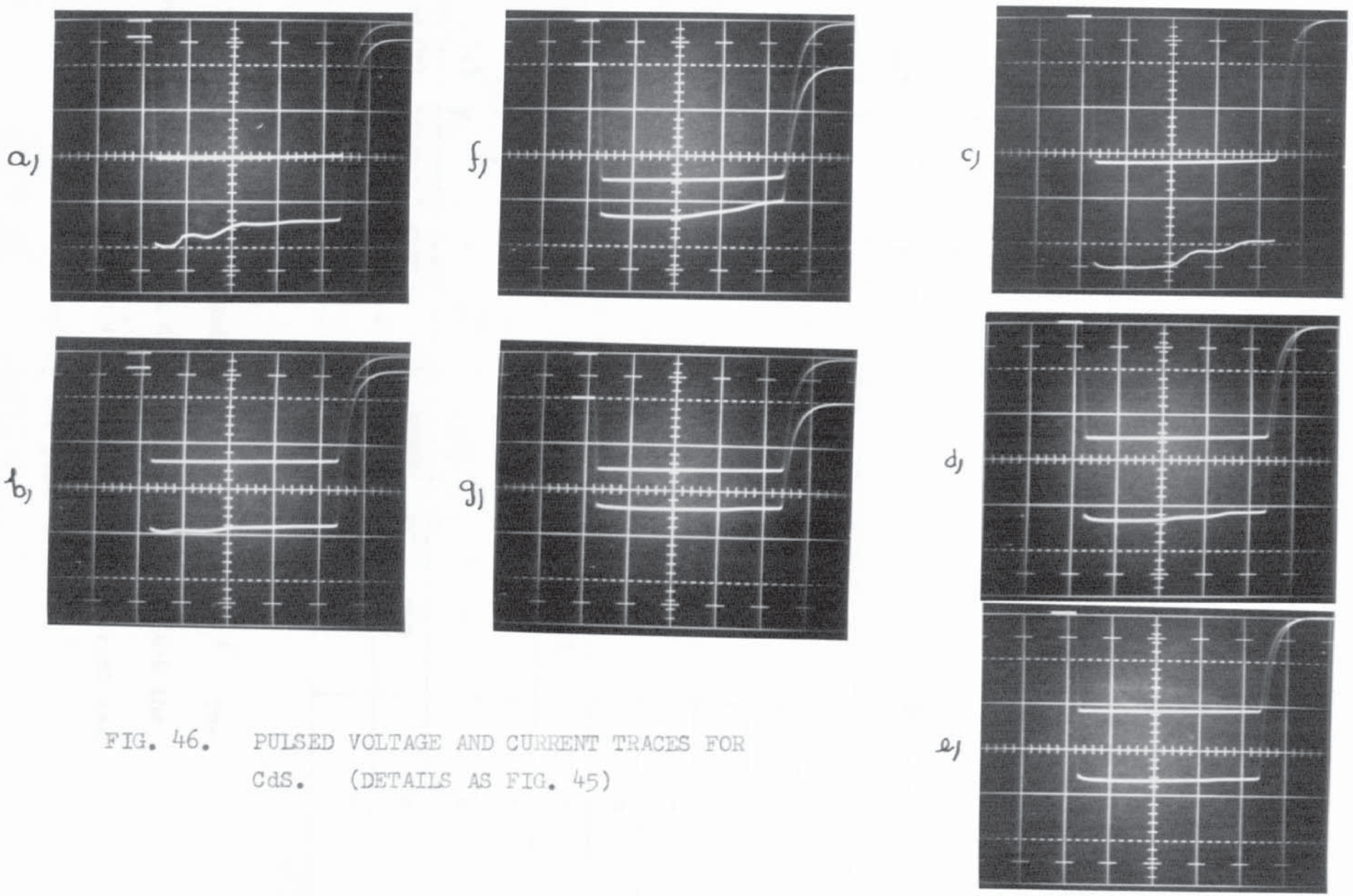

FIG. 46. PULSED VOLTAGE AND CURRENT TRACES FOR CdS. (DETAILS AS FIG. 45)

TABLE 5.

Fig.no.	Crystal Resistance ohms x 10^4	Field applied to CdS V $cm.^{-1}$	Oscilloscope calibrations. (Values represented by 1cm. of graticule)	
			Current (A)	Volts $cm.^{-1}$ on CdS
45(a)	1.1	1800	.0275	600
" (b)	"	1240	"	"
" (c)	"	1080	"	"
" (d)	2.25	1800	.0135	"
" (e)	"	1440	"	"
" (f)	"	1140	"	"
46(a)	3.3	1800	.010	"
" (b)	"	1410	"	"
" (c)	4.8	1920	.0060	"
" (d)	"	1500	"	"
" (e)	"	1396	"	"
" (f)	5.5	2100	.010	"
" (g)	"	1540	"	"

The time scale of the oscilloscope was 5μS $cm.^{-1}$ The position of the current trace was adjusted so that the section of the trace representing the pulse current was below the trace representing the pulse voltage.

contact areas of 3.0 m.m. dia. were produced on the end faces of the crystal. The orientation of the crystal was such that the 'C' axis lay in the plane of the end faces and the electron flow was perpendicular to the 'C' axis i.e. the orientation was suitable for d_{15} coupling (as described in section 1.2.1)

Flat topped voltage pulses of 20μS duration at a pulse repetition rate of 20 p.p.s. were applied to the crystal for a wide range of crystal resistivities (produced by uniform illumination). The voltage and current were monitored by a resistance network, as fig. 30. No ultrasonic signal was injected into the CdS. Figs. 45 and 46 show the voltage and current traces as observed on an oscilloscope. Table 5 details the operating conditions for each case.

By applying voltage pulses to the CdS crystal and noting the values of voltage and current at a time 18μS after the application of the voltage pulse a series of current-voltage characteristics were obtained for crystal resistances between 7.0×10^3 ohms to 8.9×10^4 ohms, fig. 47.

For crystal resistances greater than 8.9×10^4 ohms the characteristics were linear. Decreasing the crystal resistance from this value gave increasing degrees of non-linearity, as shown by table 6.

The values of crystal resistance quoted in Table 5 were those pertaining to the first linear region, before the kink in the current-voltage characteristics.

The considerable effort needed to produce graphs of

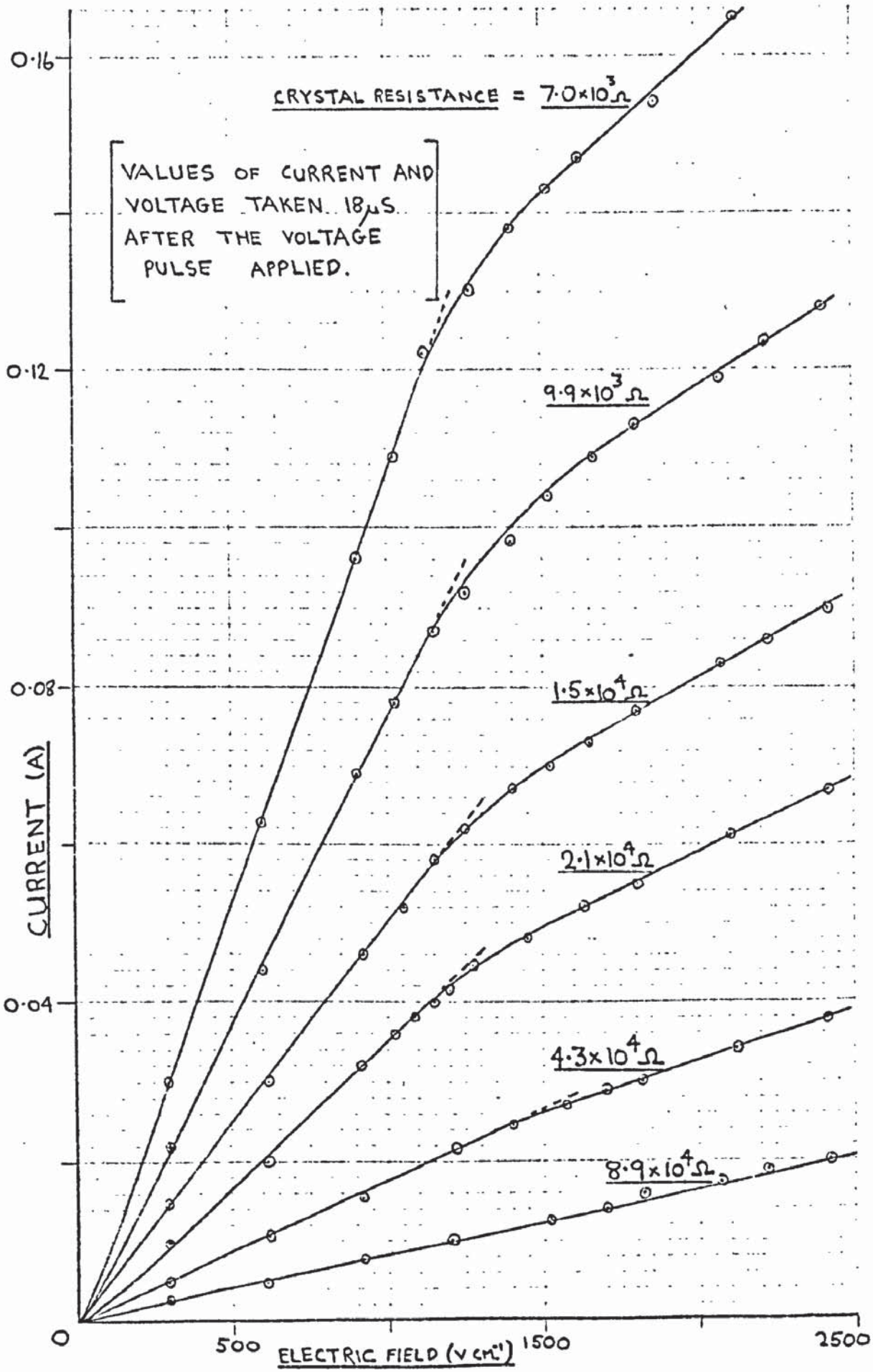

FIG. 47. CURRENT-VOLTAGE CHARACTERISTICS FOR CdS

TABLE 6

Slope resistances of CdS from fig.47

Slope resistance (ohms)		Ratio of $\frac{R_2}{R_1}$
In 1st linear region R_1	In 2nd linear region R_2	
7.0×10^3	2.09×10^4	3.0
9.9×10^3	2.90×10^4	2.93
1.5×10^4	3.35×10^4	2.23
2.1×10^4	4.0×10^4	1.90
4.3×10^4	5.8×10^4	1.35
8.9×10^4	8.9×10^4	1.0

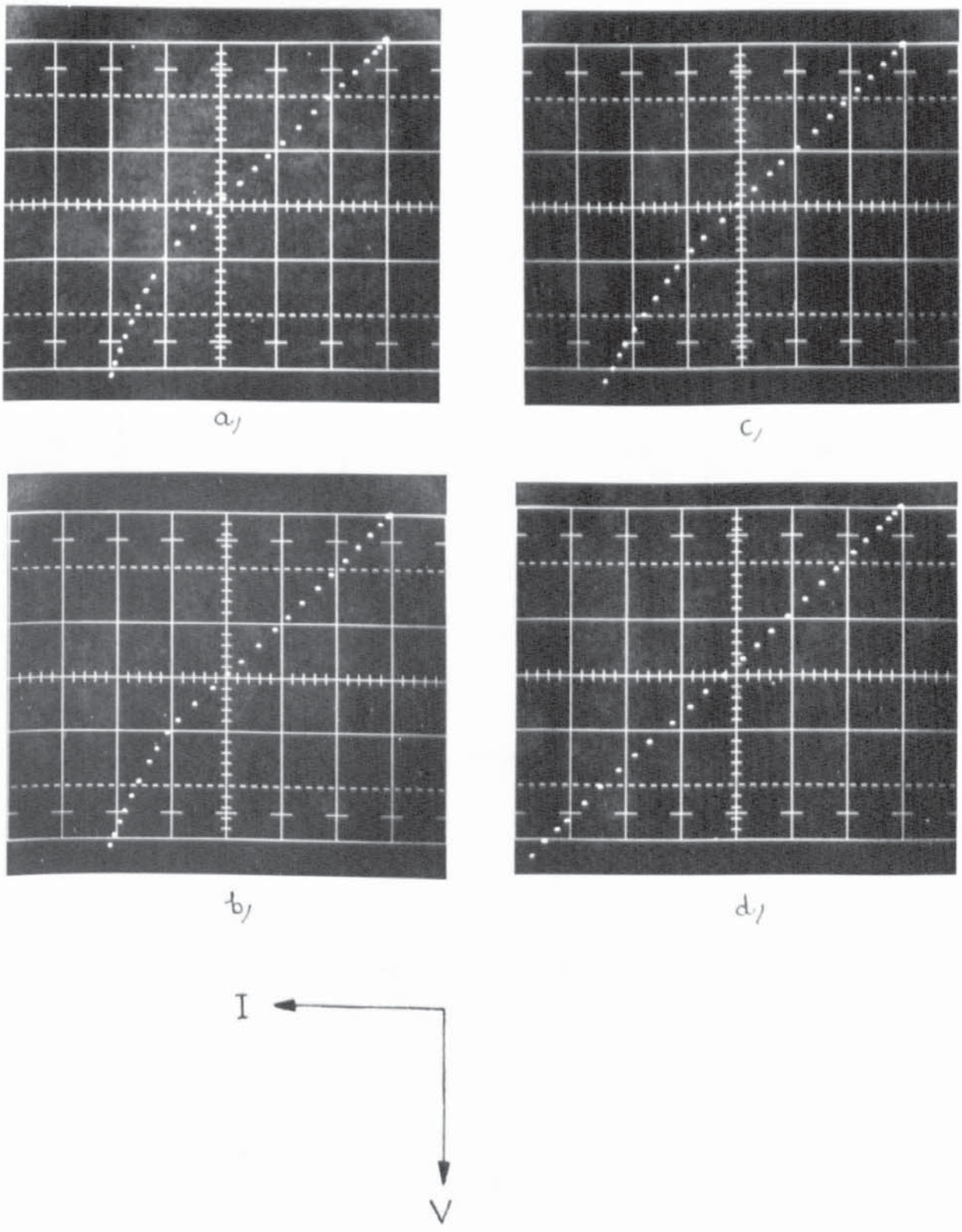

FIG. 48. CURRENT-VOLTAGE CHARACTERISTICS.
OPERATING DETAILS GIVEN IN TABLE 7.

TABLE 7

Current-voltage characteristics for CdS

Key to fig. 48.

Fig.No. 48	Crystal resistance ohms	Oscilloscope calibrations (values represented by 1 cm. of graticule	
		Volts $cm.^{-1}$ on CdS	Current (A)
a	9.9×10^{3}	300	.0442
b	1.3×10^{4}	"	.035
c	2.6×10^{4}	"	.0177
d	5.3×10^{4}	"	.00805

current-voltage by noting individual values when a certain time had elapsed was reduced by using the circuit shown in fig.39, as described in section 4.3.1. With this technique the relationship of current to voltage was plotted for a fixed time delay whilst the voltage was increased in steps. Fig.48 shows the current-voltage characteristics obtained by this method for several values of crystal resistance. The voltage pulse repetition rate was 15 p.p.s. The traces were made bright (to produce a single dot on the photograph) for 1.5μS, starting at a time 16.5μS after pulse initiation, by the application of a 10v negative going voltage pulse to the cathode of the CRT. As the applied voltage was increased in steps the trace was built up by giving the film 25 exposures of 1/5th sec. The scale of the current axis was adjusted to make the slope of the trace approximately 45° for moderate voltages. Table 7 gives the details of the oscilloscope traces shown in fig.48.

5.2.2 The acoustic flux-current relationship

Under suitable conditions of orientation and illumination intensity the current carried by a CdS crystal was observed to decay from its initial value when the applied voltage pulse was large enough to produce supersonic electron drift, for example figs.45 and 46. No ultrasonics were injected into the crystal. The observed current decay was caused by the production of a large acoustic flux that was produced by the amplification of piezo-electrically active lattice waves. By adding a suitably orientated transducer to a CdS crystal the close inter-relationship of the

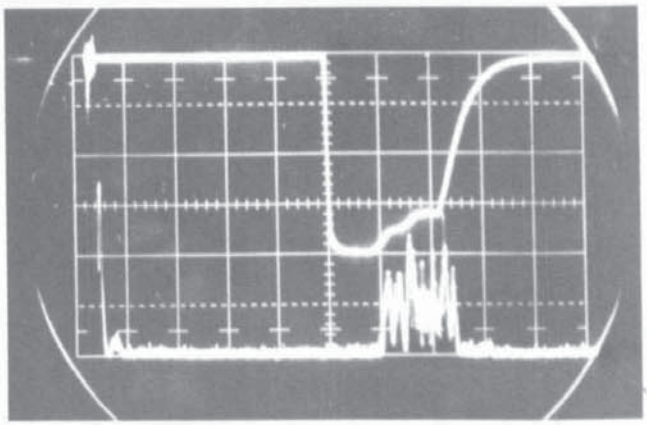

FIG. 49 CURRENT DECAY-FLUX BUILD UP.

FIELD: 1070 V $cm.^{-1}$ on CdS.

CRYSTAL RESISTIVITY: 3.7×10^4 ohm-cm

ULTRASONICS DETECTED AT 45 MHz.

TIME SCALE: 10 μS $cm.^{-1}$ (HORIZONTALLY).

CURRENT TRACE (UPPER TRACE): 5 mA $cm.^{-1}$

LOWER TRACE: AMPLIFIED AND RECTIFIED TRANSDUCER OUTPUT.

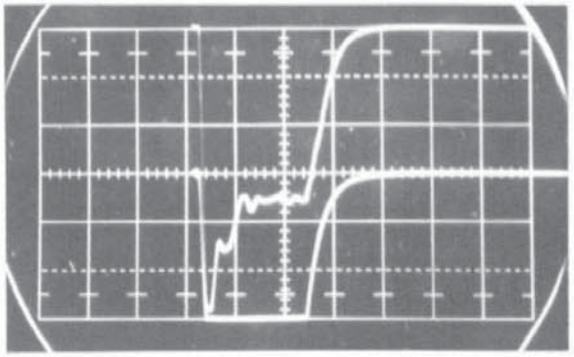

a/

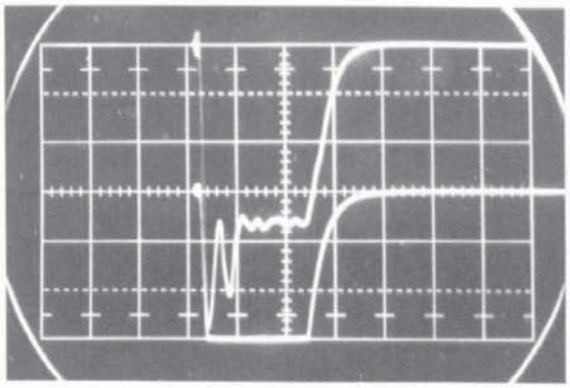

b/

FIG. 50 OSCILLATORY CURRENT DECAY:

a) NO INJECTED ULTRASONICS

b) INJECTED ULTRASONICS

TIME SCALE; $10\mu S$ $cm.^{-1}$ (HORIZONTALLY)

CURRENT TRACE (UPPER TRACE): 10mA $cm.^{-1}$

VOLTAGE TRACE: 1 cm. ON GRATICULE EQUIVALENT TO 400V ON CdS

CRYSTAL RESISTIVITY: 9.1×10^3 ohm-cm

ULTRASONIC FREQUENCY: 45 MHz

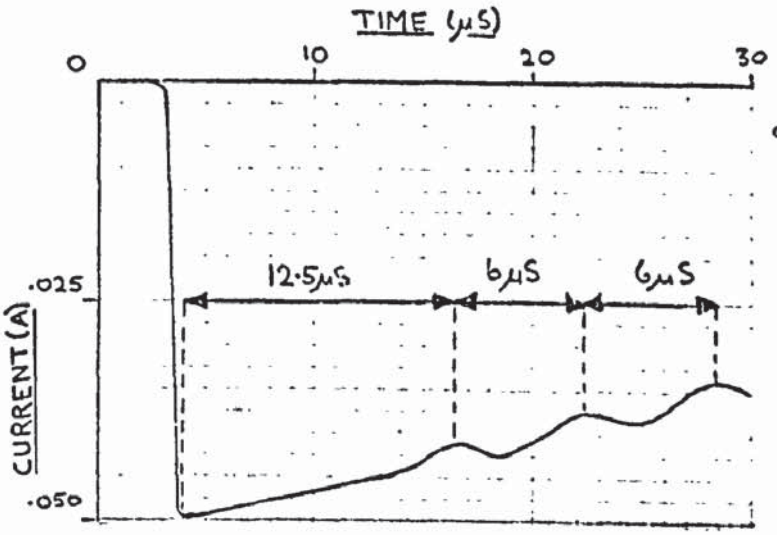

a/ ELECTRIC FIELD : 2000 V CM.$^{-1}$

CRYSTAL RESISTANCE :
$3{\cdot}0 \times 10^4\ \Omega$

NEGATIVE END OF CdS STRONGLY ILLUMINATED

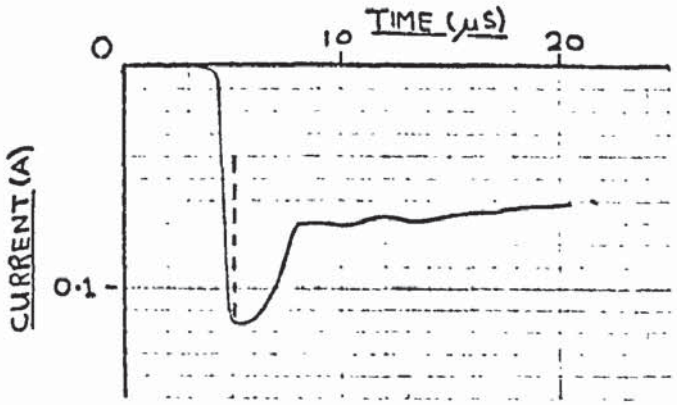

b/

ELECTRIC FIELD : 3050 V CM.$^{-1}$

CRYSTAL RESISTANCE :
$1{\cdot}95 \times 10^4\ \Omega$

POSITIVE END OF CdS STRONGLY ILLUMINATED

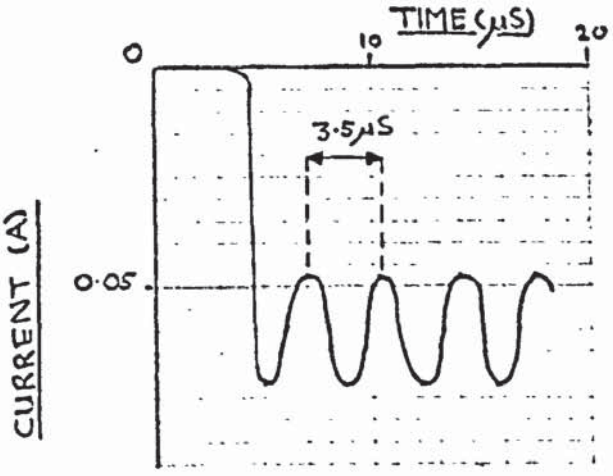

c/

ELECTRIC FIELD : 2070 V CM.$^{-1}$

CRYSTAL RESISTANCE :
$2{\cdot}1 \times 10^4\ \Omega$

NEGATIVE END OF CdS STRONGLY ILLUMINATED.

[ILLUMINATION NOT SO LOCALISED AS (a)]

FIG. 51. CURRENT OSCILLATIONS IN CdS: NON-UNIFORM ILLUMINATION

flux build-up to the current decay was demonstrated, fig.49. The same transducer was used to transmit a pulse of ultrasonics into the CdS whilst a large voltage pulse was applied. The resulting current trace is shown in fig.50a. The current trace obtained for identical values of crystal resistance and applied voltage but no signal injection is shown in fig.50b. The acousto-electric voltage produced by the injected ultrasonic pulse altered the initial portion of the oscillatory decay of the current.

5.2.3 Current-voltage characteristics for non-uniform illumination

In sections 5.2.1 and 5.2.2 the experimental results were obtained with the CdS uniformly illuminated across its width. By illuminating the CdS non-uniformly, for example by interposing a neutral density filter across half of the crystal width, the oscillatory decay of the current was observed to be considerably modified. The current decay obtained with uniform illumination often showed a damped oscillatory decay eg. fig.45a. By varying the applied voltage and the illumination intensity and distribution the oscillations in the current trace were variable in form from an oscillatory decay to constant amplitude oscillations and even increasing amplitude oscillations. In addition the period of the oscillations was variable. Fig.51 shows the current traces obtained for several operating conditions. By adjusting the operating conditions, particularly the illumination distribution and intensity, the period of the oscillations was variable over the range 3.5 to 6.0μS. The time for a shear wave to complete a round trip in the CdS was calculated to be 8.5μS. The shape

of the current decay was very sensitive to changes in the operating conditions.

5.3 Attenuation and amplification of ultrasonics

The attenuation of ultrasonics in CdS was observed for a wide range of experimental conditions. The results presented in this section relate to three basic experiments namely the measurement of ultrasonic attenuation in CdS as a function of:

1) Crystal resistivity.

2) Ultrasonic frequency.

3) Applied voltages of both polarity.

The attenuation was measured relative to the dark value using the techniques described in section 4.3.3. The results described in this section relate to a CdS crystal produced by Eagle-Picher Co. The crystal was originally cylindrical in shape, being .74 cm. long and 1.0 cm. dia. A flat surface .40 cm. wide was ground along its length. The crystal was orientated for d_{15} coupling. The dark resistivity of the crystal was greater than 5×10^9 ohm-cm. falling to less than 5×10^3 ohm - c.m. in strong filtered illumination. The indium contact areas were of .70 c.m. diameter. The arrangement of the acoustic amplifier structure is shown in fig. 24.

The results described in this section have been taken under small signal conditions - in particular this has required the use of sensitive receiving equipment, as described in section 4.2.3.

Figures 52 - 54 give the observed values of attenuation for ultrasonics having frequencies of 15, 45 and 75 MHz respectively as a function of electric field, up to +2000 v cm^{-1}. The polarity of the voltage pulses was such that electrons drifted in the direction of acoustic propagation. Figs. 55 - 57 give the observed values of attenuation for the same frequencies but with voltage pulses of the opposite polarity. Each curve is an average of between 3 and 5 separate experimental runs. As described in section 4.3.3 the experimental readings of ultrasonic attenuation were taken both whilst the voltage was increased in steps to a maximum and whilst it was being reduced and an average value taken. For fields greater than about +1100 v $cm.^{-1}$ the ultrasonics were amplified i.e. the attenuation coefficient became negative. Figs. 58 - 62 give the observed values of attenuation, for fields sufficiently large to produce acoustic amplification, for ultrasonics of frequency from 105 to 345 MHz. For convenience the nominal values of ultrasonic frequency are referred to: table 2 gives the precise values. On figs. 58 - 62 the values of crystal resistivity used are quoted. On figures 52 - 57 the crystal resistivity is represented by $(\frac{\omega_c}{\omega})$. ω_c is the dielectric relaxation frequency

$$\omega_c = \frac{\sigma}{\epsilon}$$

σ = crystal conductivity. ohm^{-1} $cm.^{-1}$

ϵ = dielectric constant. F. $cm.^{-1}$

ω = ultrasonic angular frequency. $sec.^{-1}$

Table 8 gives the values of $\frac{\omega_c}{\omega}$ for frequencies of 15, 45 and 75 MHz for convenient values of crystal resistivity.

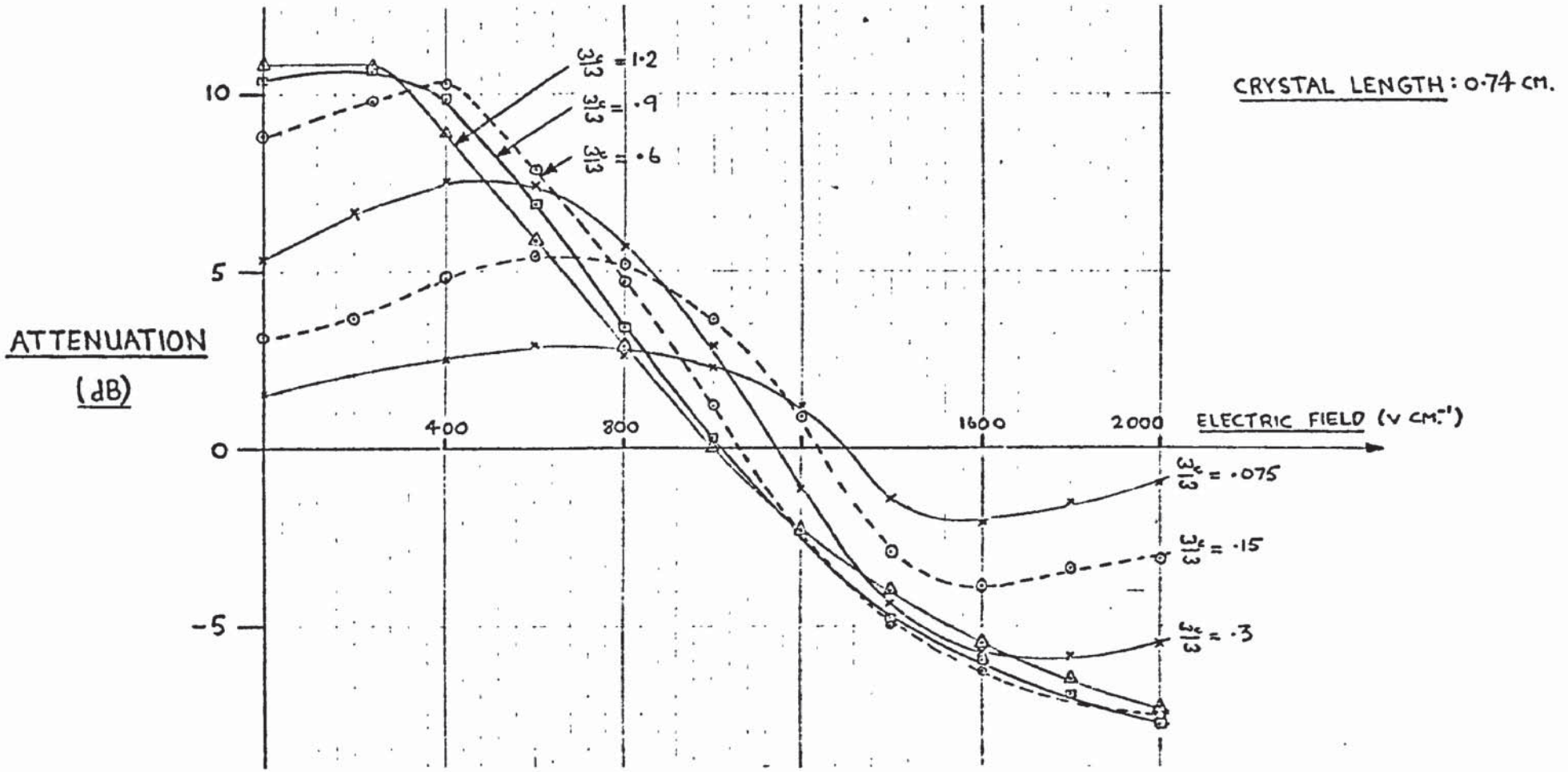

FIG. 52. ULTRASONIC ATTENUATION v. DRIFT FIELD AT 15 MH$_3$.

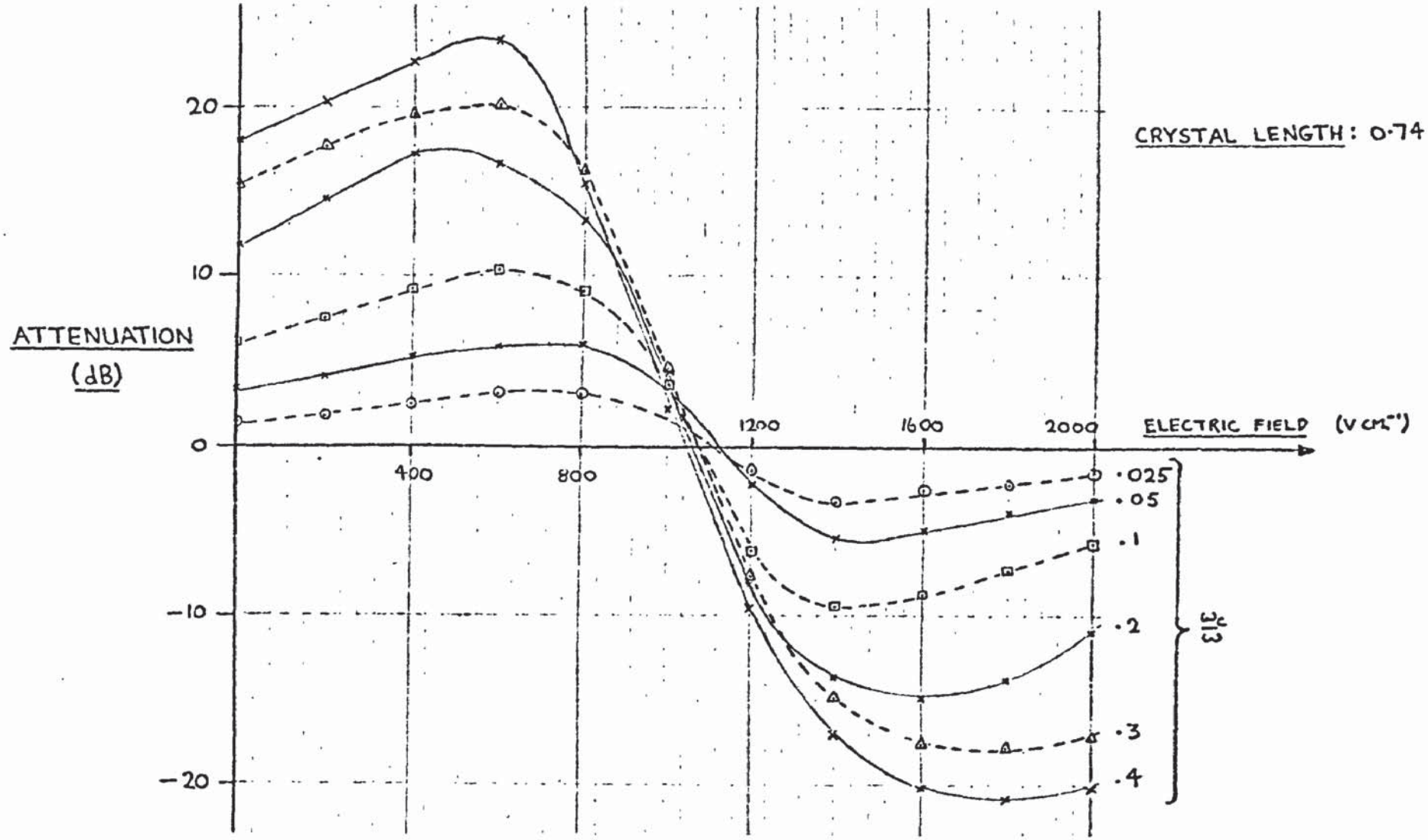

FIG. 53. ULTRASONIC ATTENUATION v. DRIFT FIELD AT 45 MH$_3$

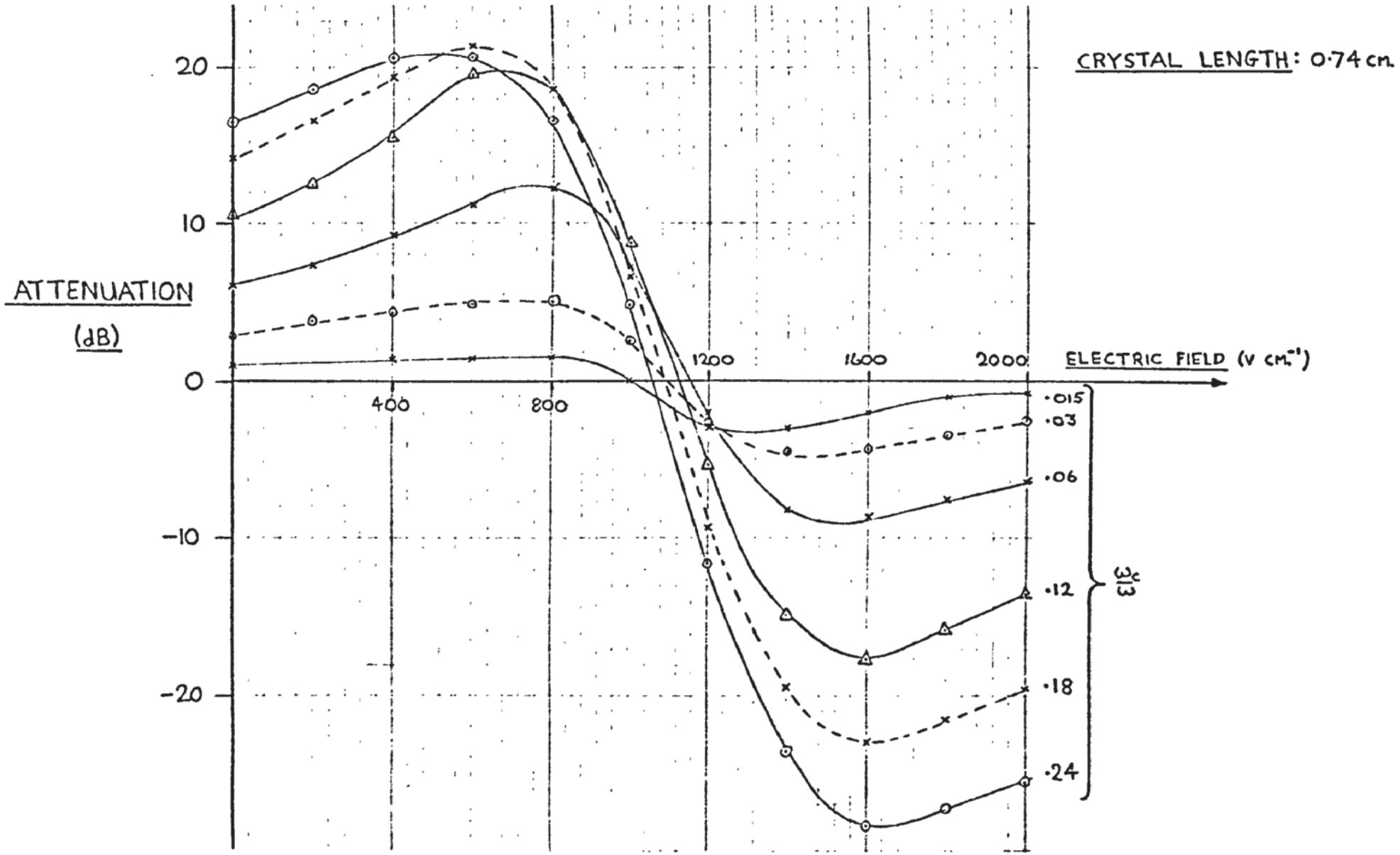

FIG. 54. ULTRASONIC ATTENUATION v. DRIFT FIELD AT 75 MH_3

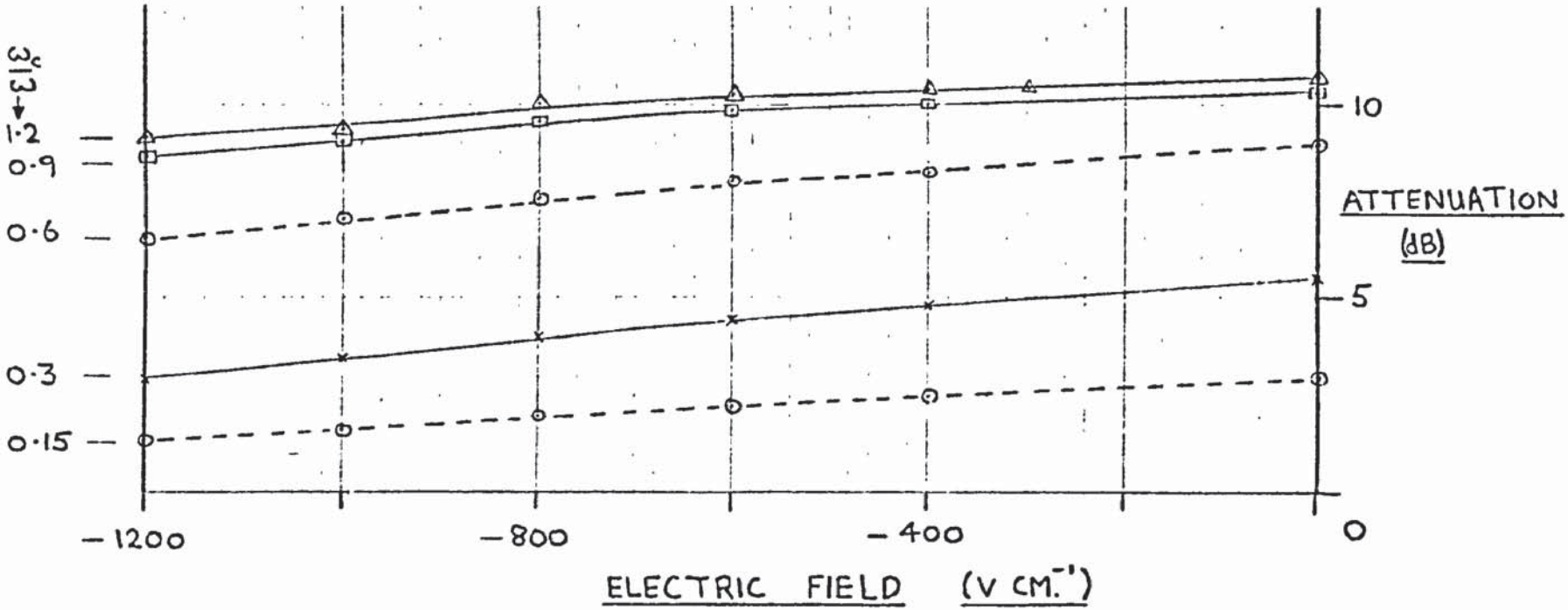

FIG. 55 ATTENUATION OF 15 MH$_3$ ULTRASONICS IN CdS. (NEGATIVE FIELDS)

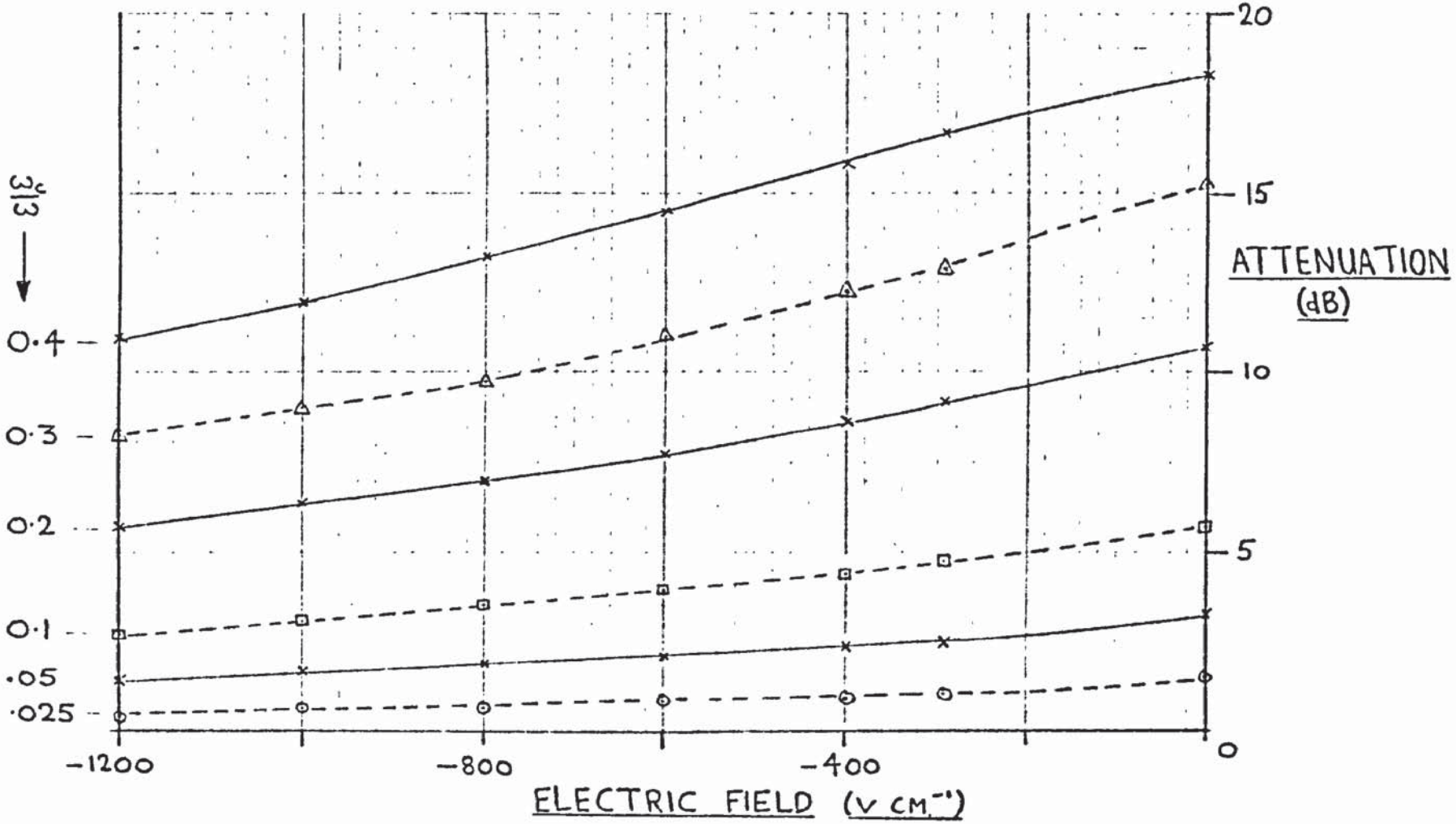

FIG. 56. ATTENUATION OF 45 MH$_3$ ULTRASONICS IN CdS. (NEGATIVE FIELDS)

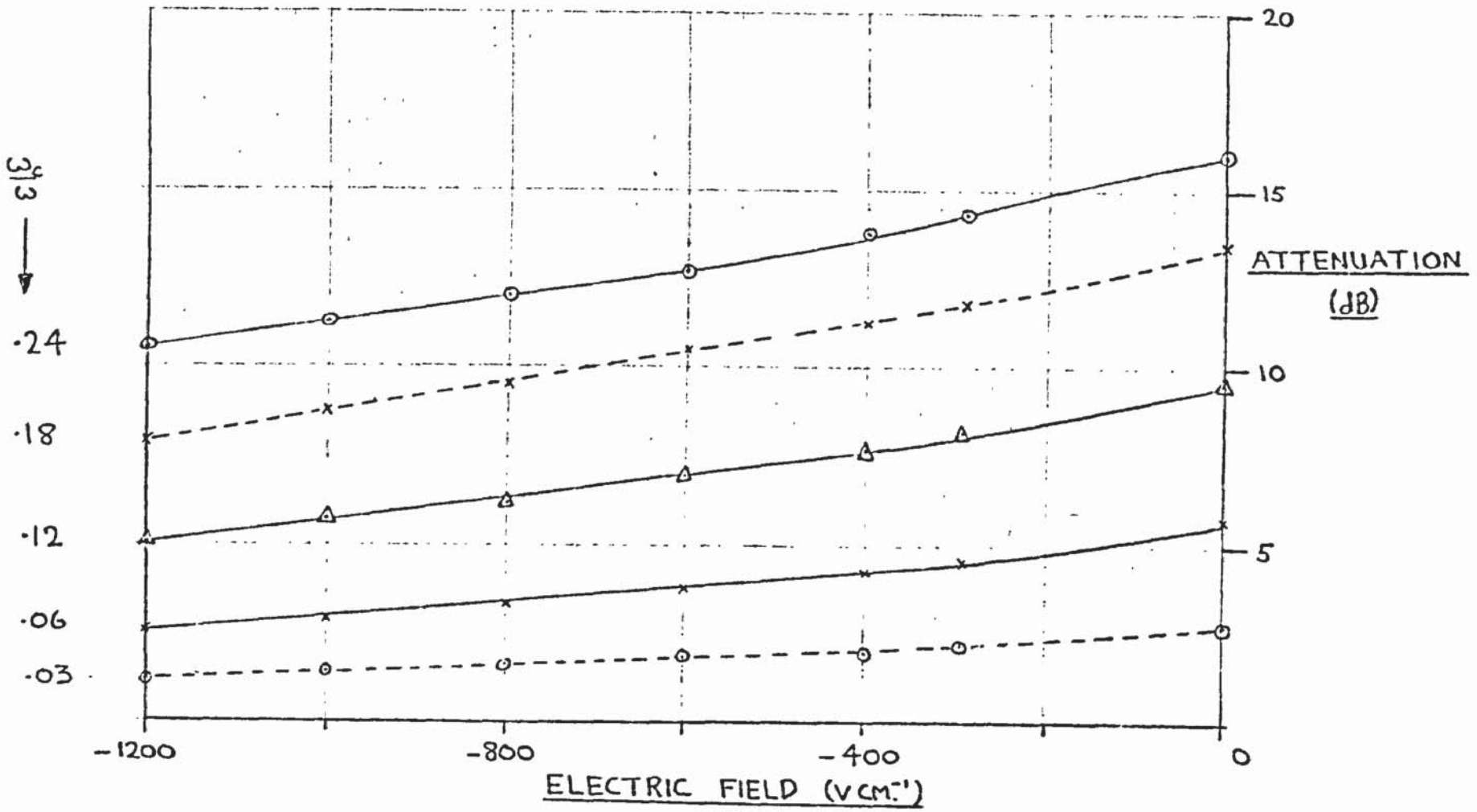

FIG. 57. ATTENUATION OF 75 MH$_3$ ULTRASONICS IN CdS. (NEGATIVE FIELDS)

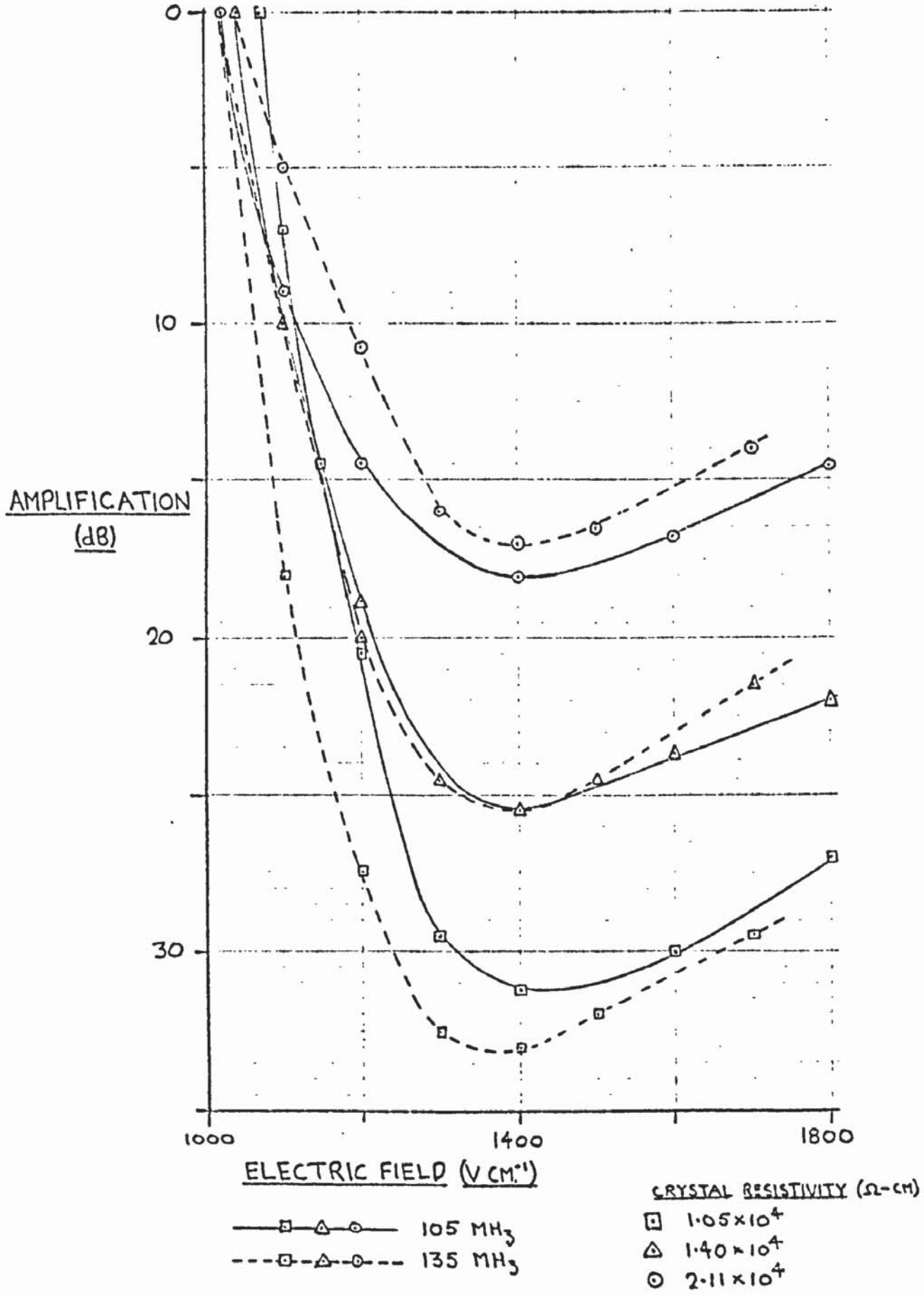

FIG. 58. AMPLIFICATION OF 105 & 135 MH₃ ULTRASONICS.

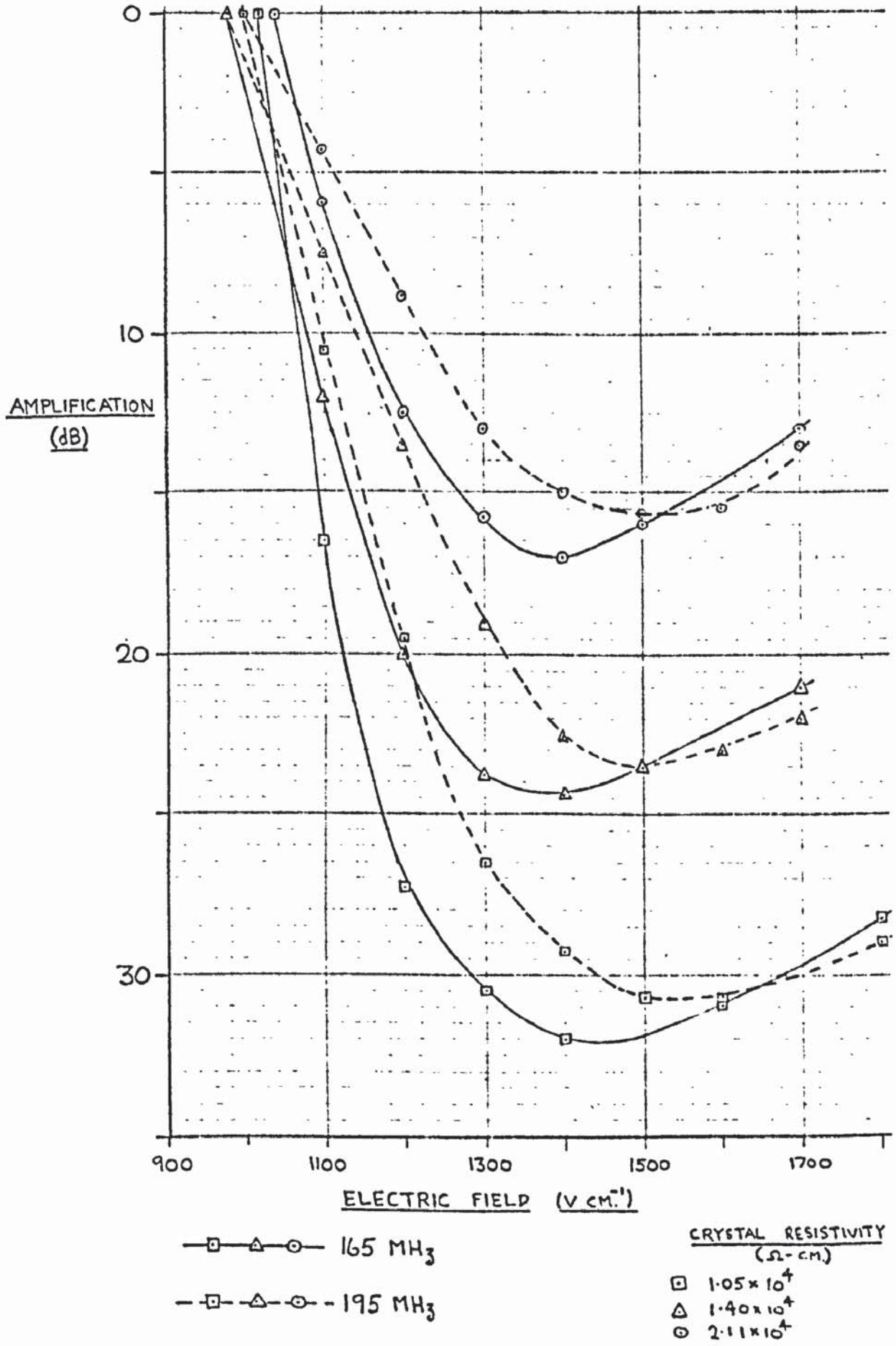

FIG. 59. AMPLIFICATION OF 165 & 195 MH_3 ULTRASONICS

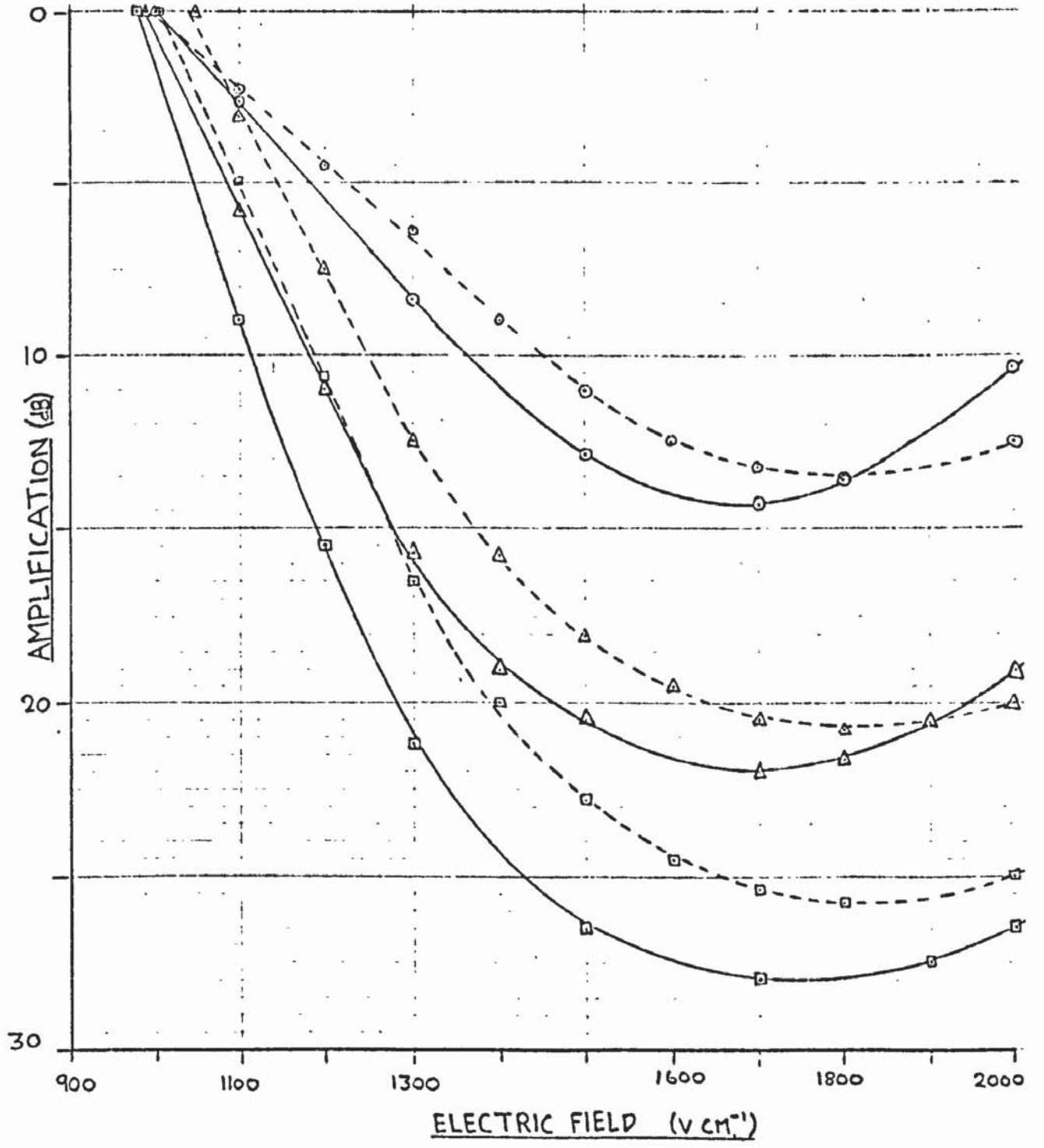

FIG. 60. AMPLIFICATION OF 225 & 255 MH_3 ULTRASONICS

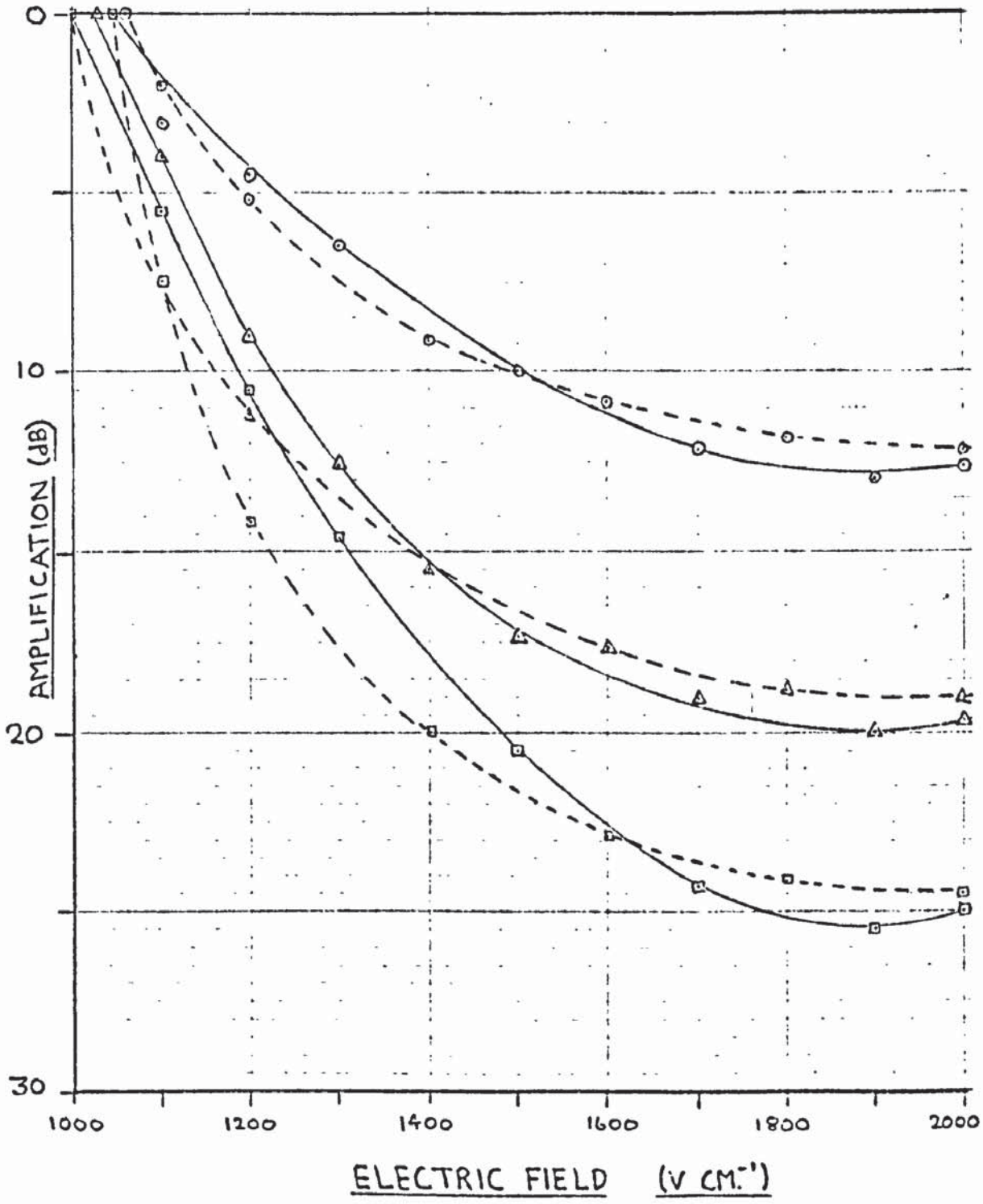

FIG. 61. AMPLIFICATION OF 285 & 315 MH_3 ULTRASONICS

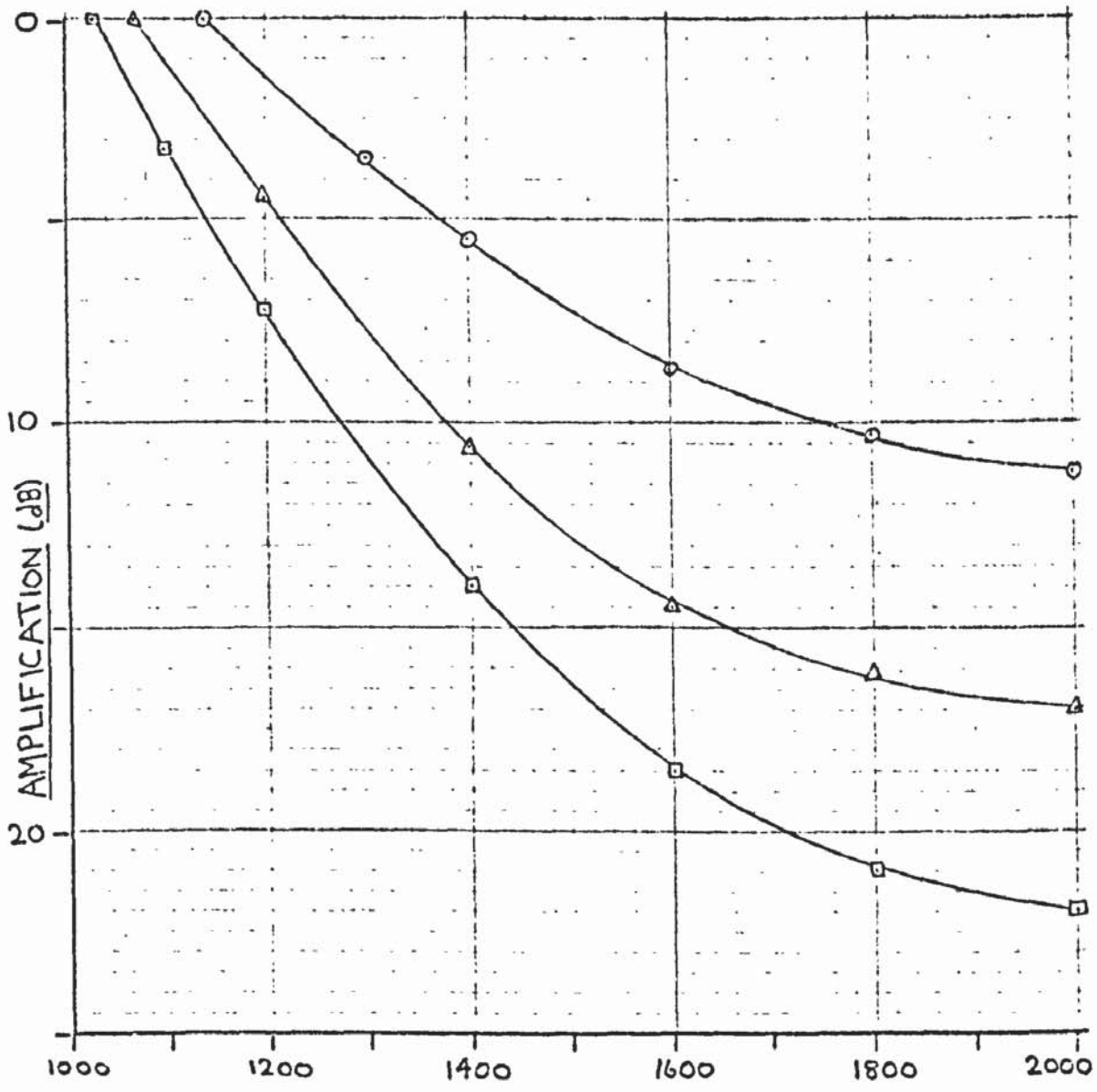

FIG. 62. AMPLIFICATION OF 345 MH$_3$ ULTRASONICS

TABLE 8

Values of $\frac{\omega_c}{\omega}$ for frequencies of 15, 45 and 75 MHz

ρ ohm-cm. x 10^4	σ $ohm^{-1}cm.^{-1}$ x 10^{-5}	$\frac{\omega_c}{\omega}$ Frequency (MHz)		
		15	45	75
16.9	.59	.075	.025	.015
8.44	1.2	.15	.050	.030
4.22	2.4	.30	.10	.060
2.11	4.7	.60	.20	.12
1.41	7.1	.90	.30	.18
1.05	9.5	1.20	.40	.24

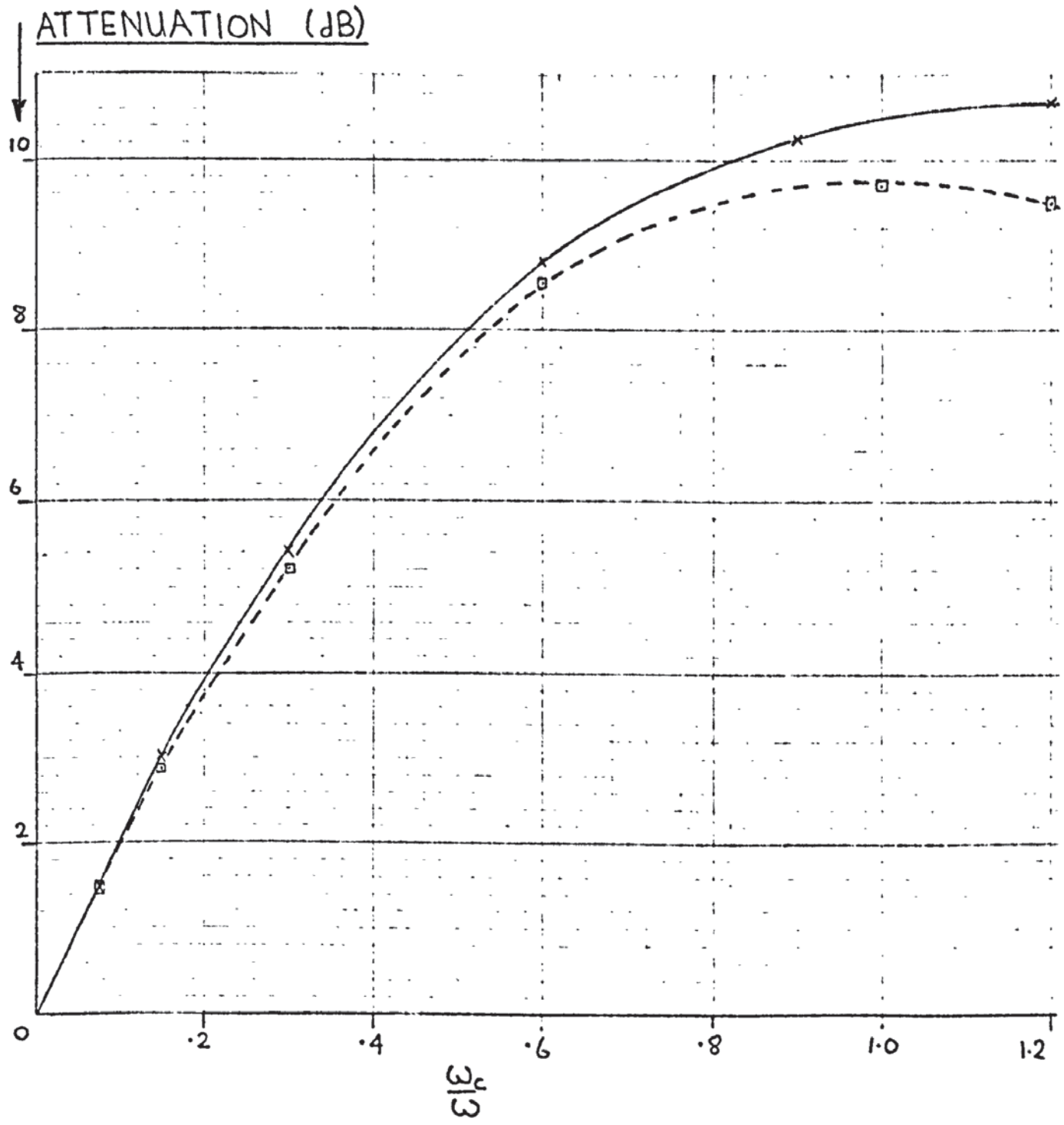

FIG. 63. ATTENUATION OF 15 MH$_3$ ULTRASONICS. NO APPLIED FIELD.

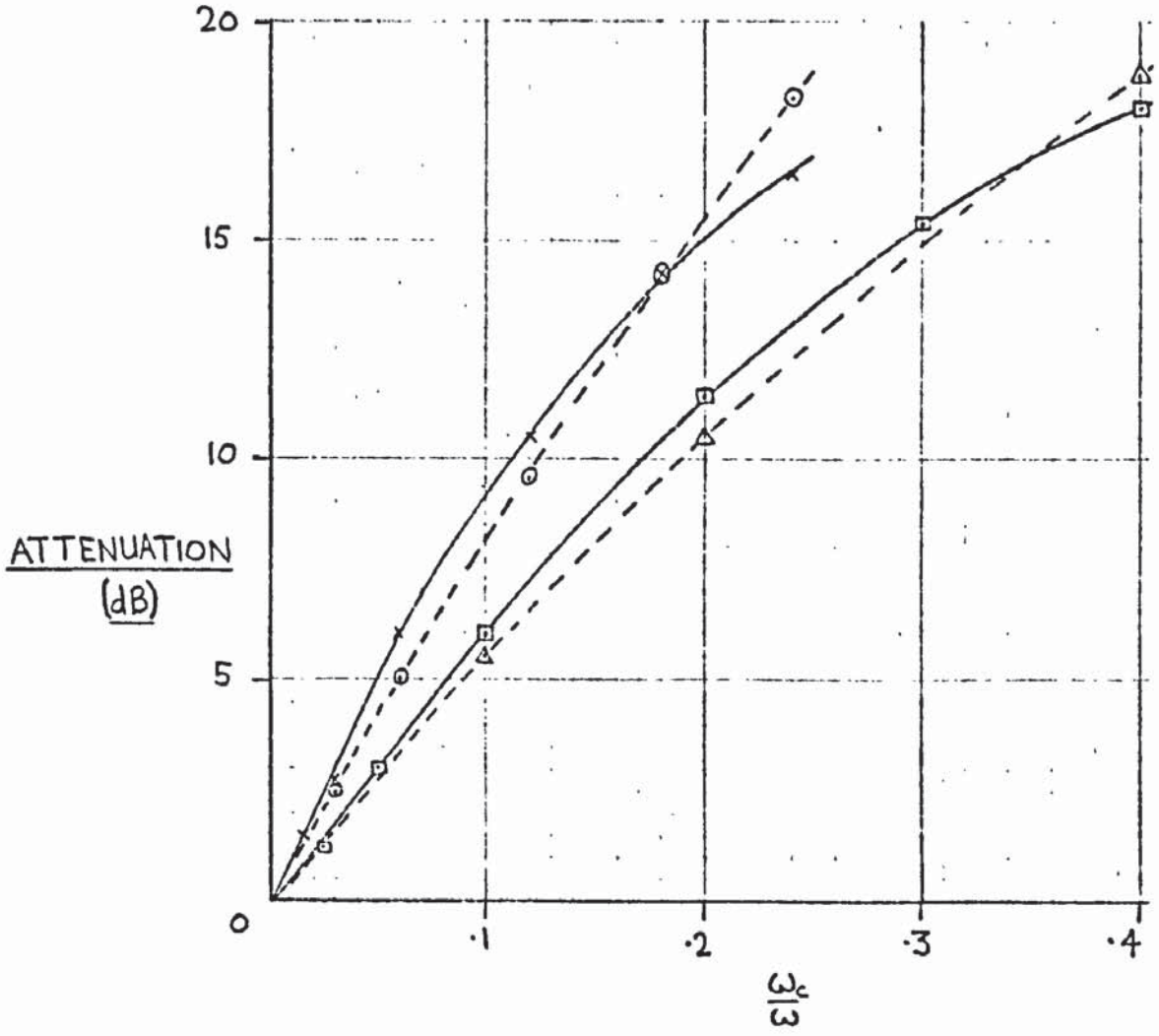

FIG. 64. ATTENUATION OF 45 & 75 MH_3 ULTRASONICS.

NO APPLIED FIELD.

The variation of ultrasonic attenuation with $\frac{\omega_c}{\omega}$ for 15, 45 and 75 MHz and no applied voltage is shown in figs. 63 and 64.

The voltage pulse was applied to the CdS shortly before the ultrasonic pulse entered the crystal and the voltage remained constant until the ultrasonic pulse left the crystal.

The typical appearance of the oscilloscope trace displaying the amplified and rectified output of the receiving transducer is shown in fig. 74 for various operating conditions, explained more fully in section 5.5.1.

Using input r.f. pulses of half height widths between 0.6 and 1.8 μS it was observed that the attenuation-voltage curves obtained were not sensitive to variations in pulse width.

An experimental determination of the attenuation-voltage curves for a given illumination using ultrasonics of 45.8, 46.8 and 47.8 MHz showed that within the limits of experimental error the curves were identical.

The dimensional tolerance of the CdS crystal and the acoustic buffers ensured that across the 0.318 c.m. dia. active region of the transducers the path lengths through the amplifier structure were within a quarter of an acoustic wavelength in Y-cut quartz for operation at all the experimentally used frequencies.

5.4. Measurement of acousto-electric voltage

For the measurements described in this section the CdS acoustic amplifier structure was used. The acousto-electric voltages produced across the CdS by the attenuation of pulses of

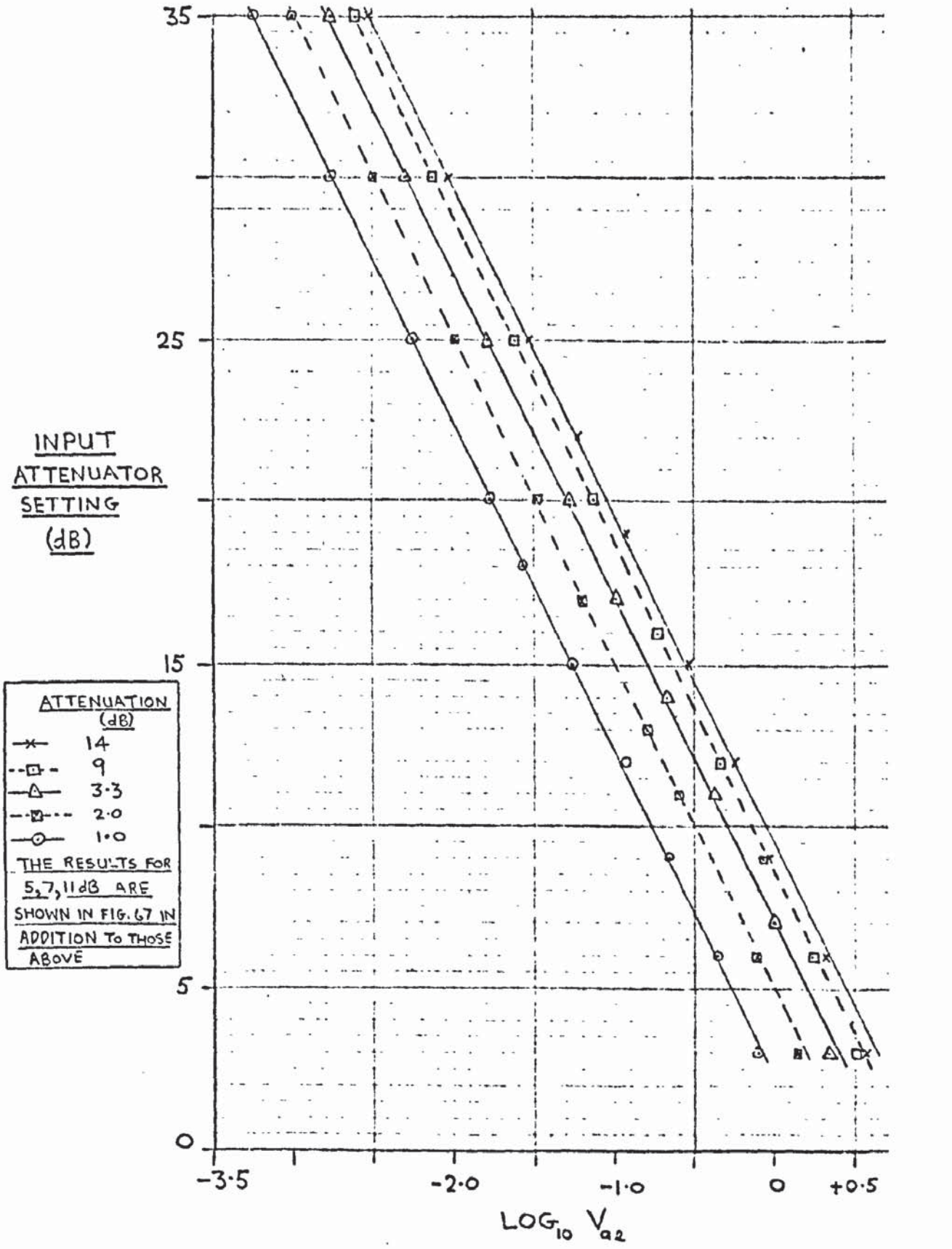

FIG. 65. ACOUSTO-ELECTRIC VOLTAGE v. ACOUSTIC INTENSITY AT 45 MH3

ultrasonics were measured using the contacts, at each end of the crystal, generally used to apply drift field voltages. The acousto-electric voltage was always measured for no applied voltage to the CdS.

Fig.65 shows the variation of the measured acousto-electric voltage with the input acoustic power to the CdS. The acousto-electric voltage was measured by feeding the output from the CdS into the oscilloscope via the measuring network shown in fig.66.

FIG. 66. MEASUREMENT OF ACOUSTO-ELECTRIC VOLTAGE.

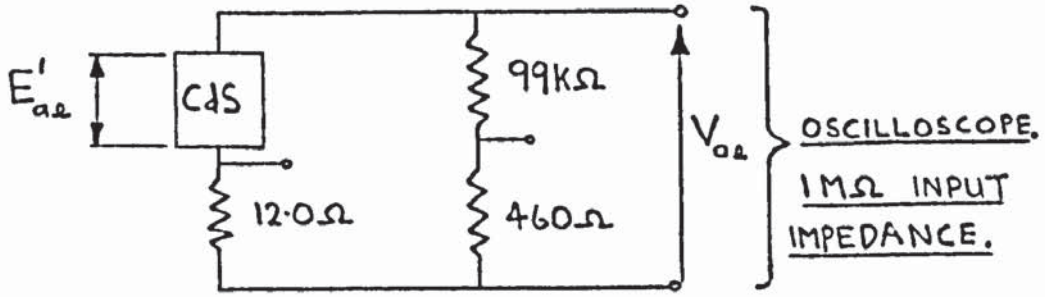

The input acoustic power was controlled by varying the input step attenuator. The ultrasonic frequency was 45MHz and the half height pulse width was 1.4 μS. The variation of acousto-electric voltage with input acoustic power was measured for 8 different crystal resistivities. On fig.65 the value of the no-applied voltage acoustic attenuation of 45 MHz ultrasonics is quoted rather than crystal resistivity. Figs.63 and 64 have given the observed relationships between crystal resistivity (expressed in terms of $\frac{\omega_c}{\omega}$) and ultrasonic attenuation at 15, 45 and 75 MHz (for no applied voltage). Fig.67 shows the variation of acousto-

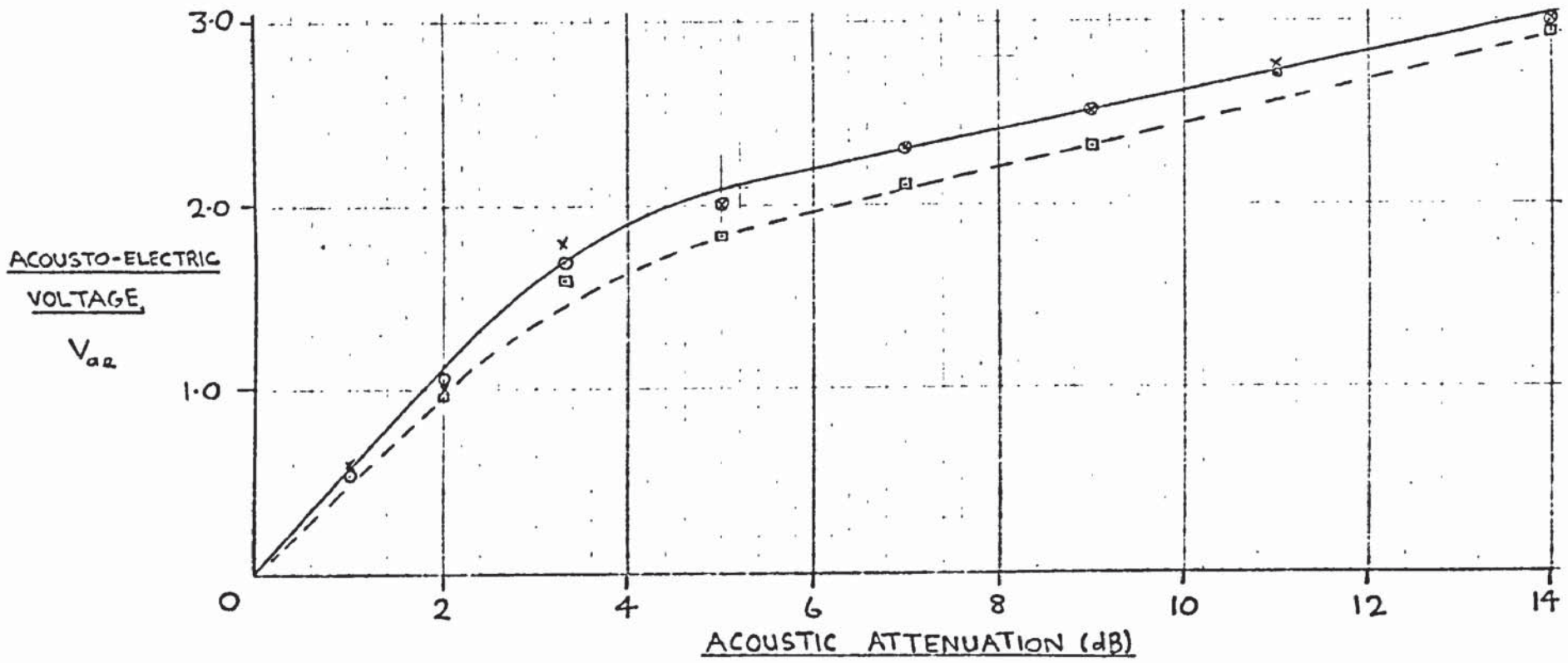

—×— 35 dB IN INPUT ATTENUATOR. SCALE: V_{ae} OF 1·0 ≡ ·001v

—⊙— 25 dB IN INPUT ATTENUATOR. SCALE: V_{ae} OF 1·0 ≡ ·01v

--⊡-- 15 dB IN INPUT ATTENUATOR. SCALE: V_{ae} OF 1·0 ≡ ·1v

FIG. 67. ACOUSTO-ELECTRIC VOLTAGE v. ACOUSTIC ATTENUATION AT 45 MH$_3$.

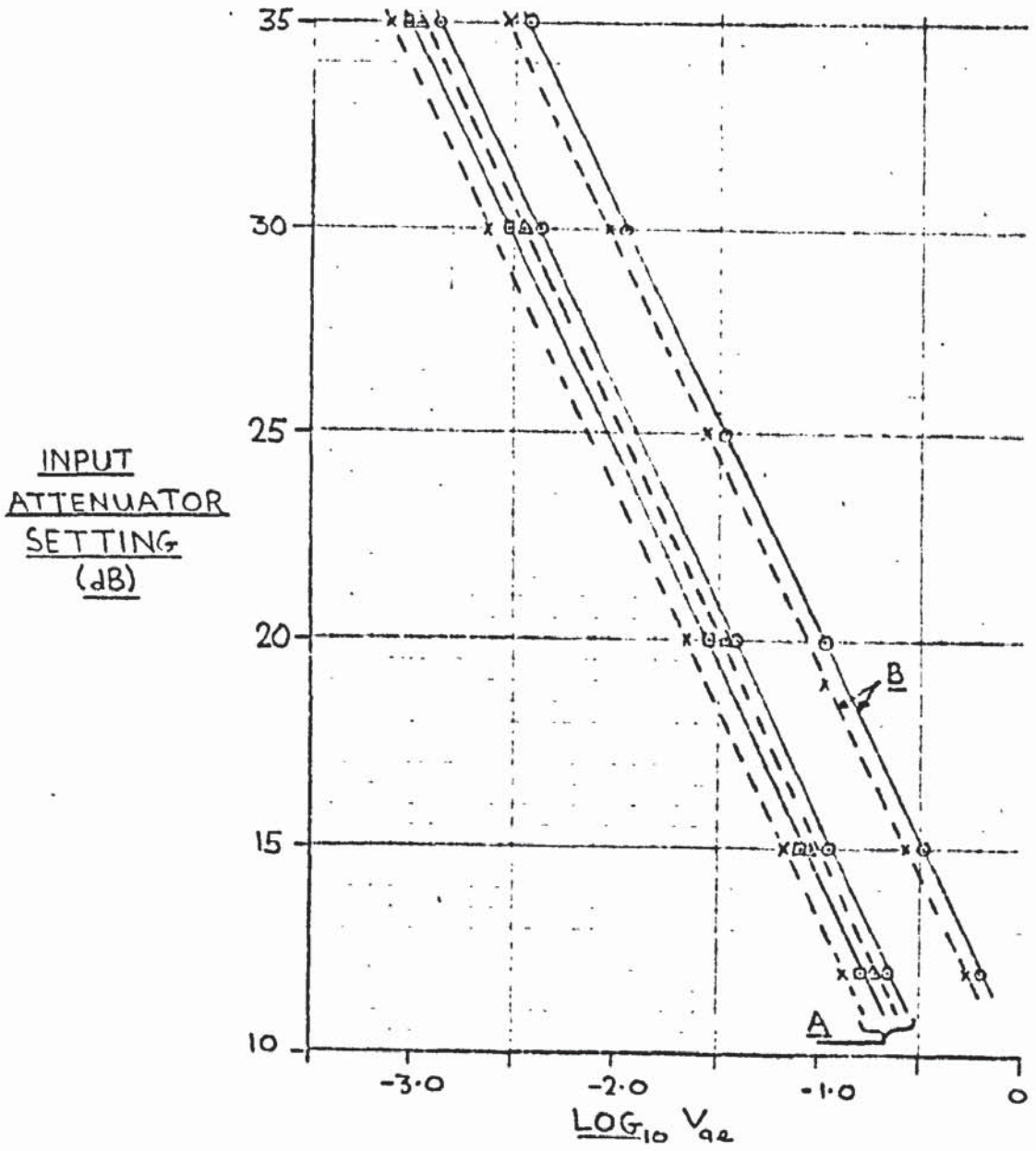

A :- V_{ae} MEASURED ACROSS 4·3kΩ

B :- V_{ae} MEASURED ACROSS 1MΩ

ATTENUATION (dB)

× 9

⊡ 12 } NOT PLOTTED FOR THE 'B' CASE FOR REASONS OF CLARITY.

△ 15 }

⊙ 17·8

FIG. 68. ACOUSTO-ELECTRIC VOLTAGE v. ACOUSTIC INTENSITY AT 45MHz

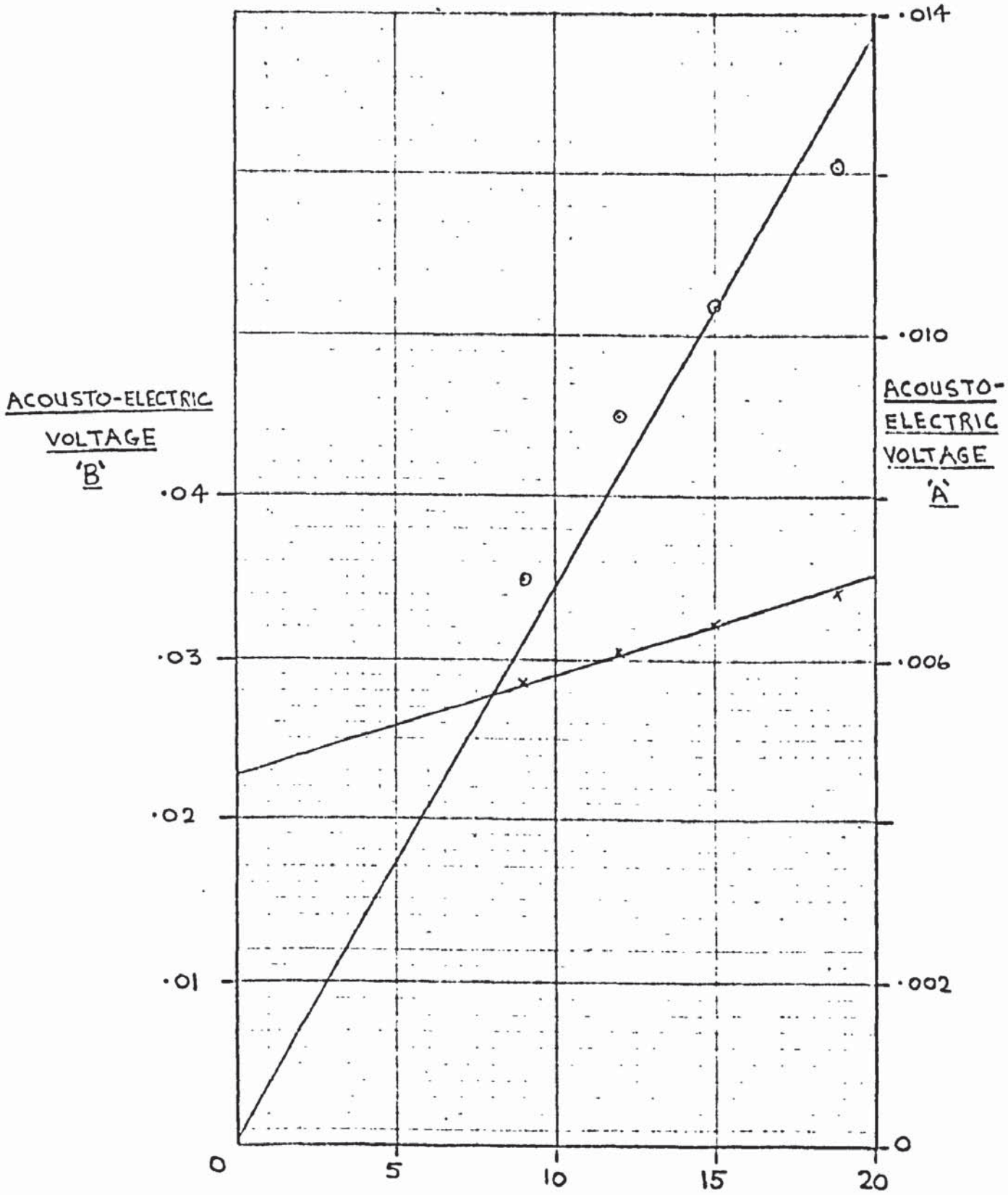

FIG. 69. ACOUSTO-ELECTRIC VOLTAGE v. ACOUSTIC ATTENUATION AT 45 MH$_3$

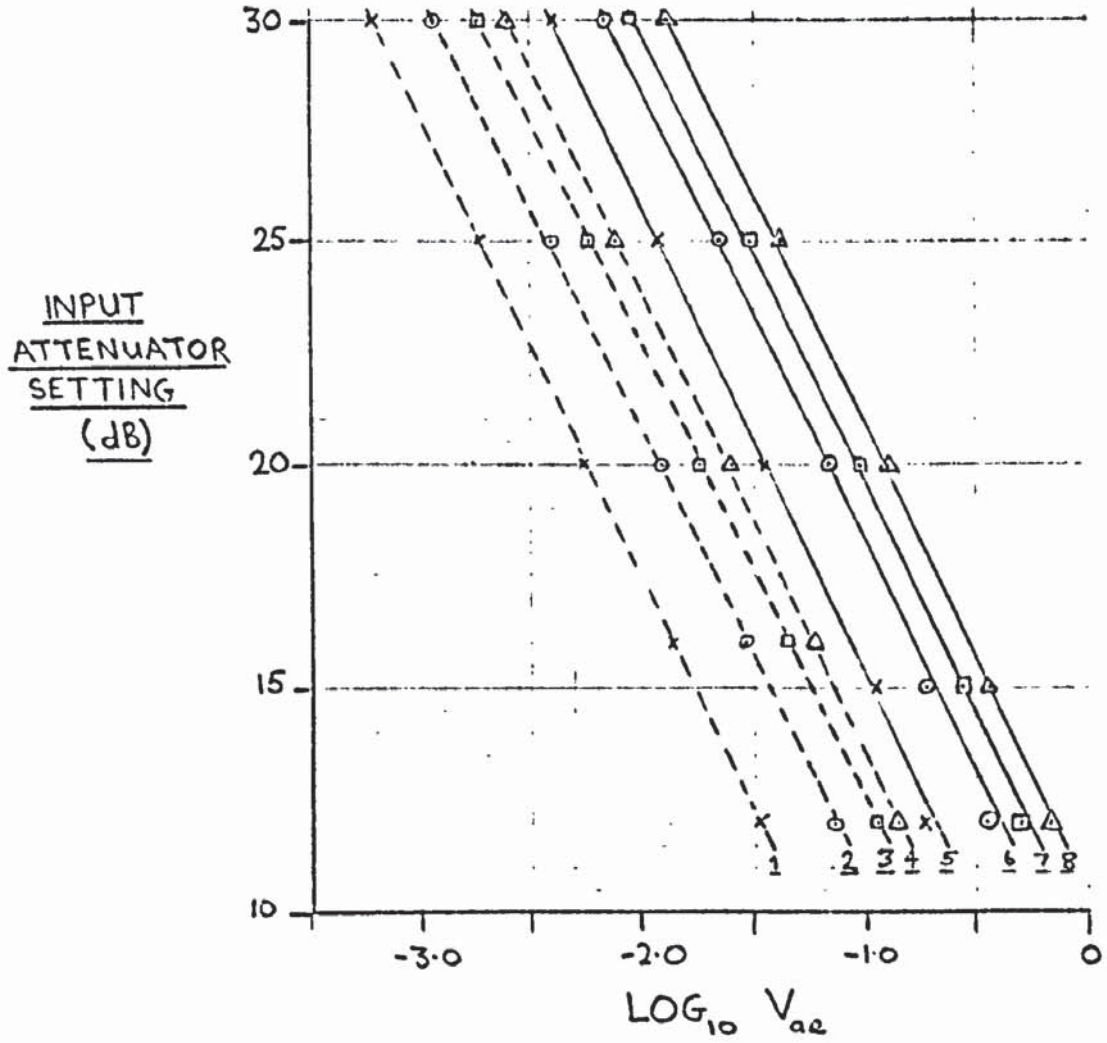

V_{ae} MEASURED ACROSS 4·3 KΩ

45 MH_3 : PLOTS 1–4

15 MH_3 : PLOTS 5–8

PLOT	ATTENUATION (dB)
1	2·0
2	4·3
3	6
4	8·5
5	2·0
6	4·0
7	6
8	8·8

FIG. 70 ACOUSTO-ELECTRIC VOLTAGE v. ACOUSTIC INTENSITY AT 15 & 45 MH_3.

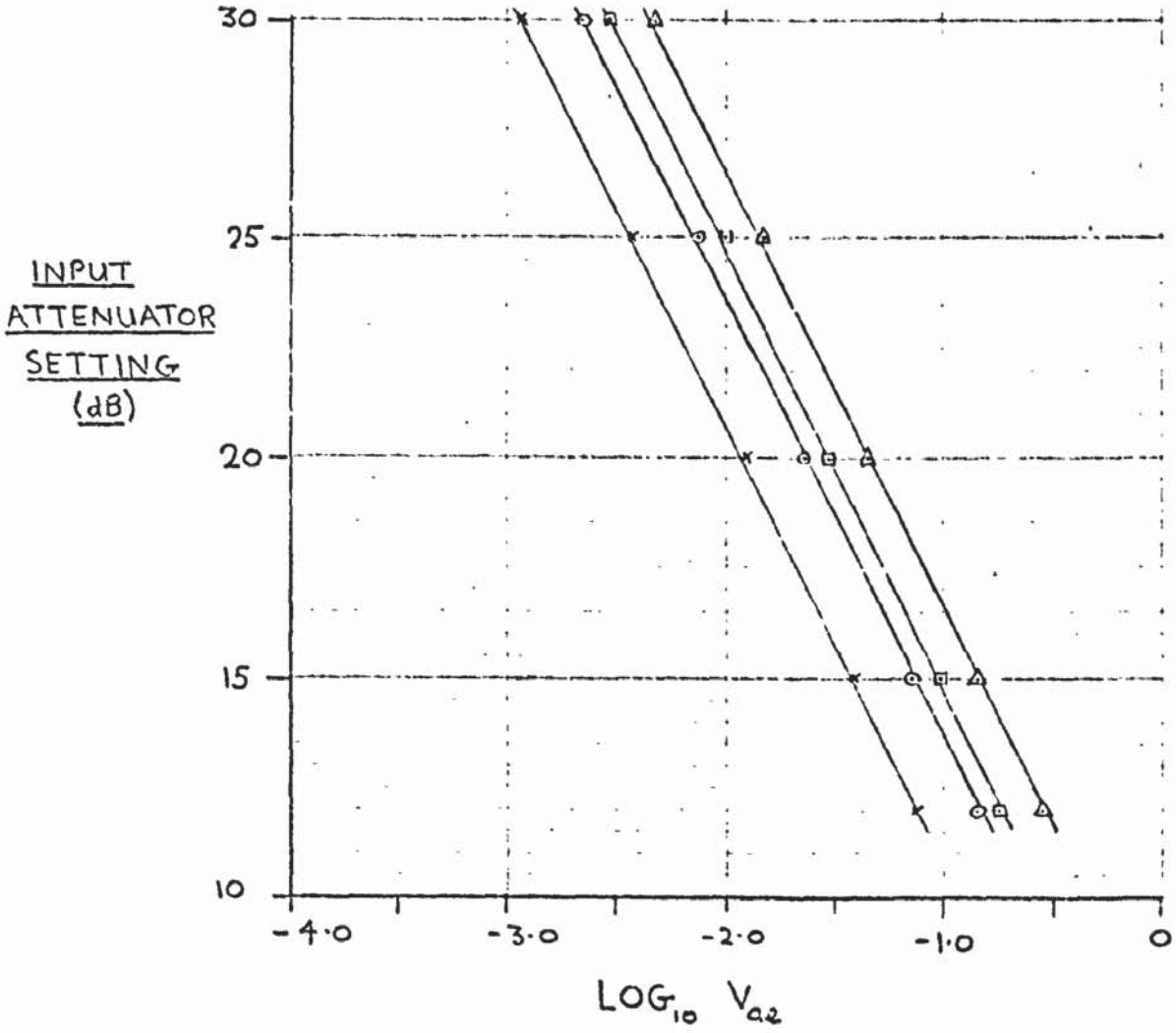

V_{ac} MEASURED ACROSS 4·3 KΩ

ATTENUATION (dB)

× 2·0
⊙ 4·0
⊡ 5·8
△ 9

FIG. 71. ACOUSTO-ELECTRIC VOLTAGE v. ACOUSTIC INTENSITY AT 75 MH$_3$

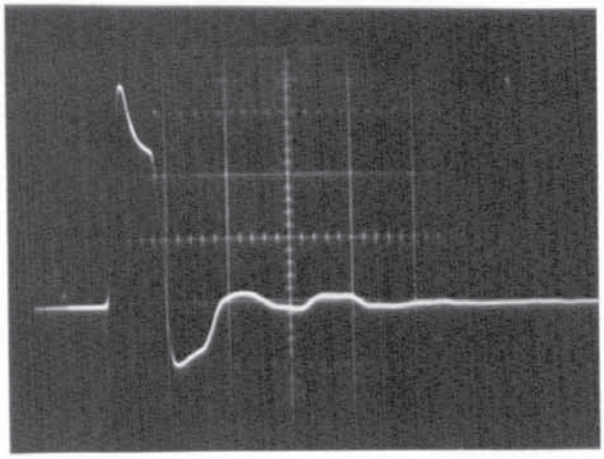

FIG. 73. ACOUSTO-ELECTRIC VOLTAGE PRODUCED BY AN ULTRASONIC PULSE IN CdS.

CRYSTAL LENGTH: 0.74 cm.

ULTRASONIC FREQUENCY: 45 MHz

OSCILLOSCOPE TERMINATED BY 700 ohms

NO-VOLTAGE ACOUSTIC ATTENUATION: 2.5 db PER CRYSTAL LENGTH

OSCILLOSCOPE SETTINGS:

HORIZONTAL, $5\,\mu S\ cm.^{-1}$

VERTICAL, .005 $V\ cm.^{-1}$

electric voltage with the no-voltage attenuation for several values of input acoustic power. This graph was obtained from fig. 65.

As discussed in section 6.3 the variation of the acousto-electric voltage with no-voltage attenuation shown in fig. 67 can be explained using Weinreich's relationship. To test the correctness of the explanation given the acousto-electric voltage was measured as a function of input acoustic power and no-voltage attenuation with the oscilloscope terminated by 4.3kΩ and also with the output from the CdS going directly into the oscilloscope i.e. the 100 kΩ resistor chain of fig. 66 was removed. The results are shown in figs. 68 and 69.

Experiments were carried out in which the acousto-electric voltage was measured as a function of input acoustic power and no-voltage attenuation for ultrasonics of frequency 15, 45 and 75 MHz. The results are shown in figs. 70 and 71. The half height width of the ultrasonic pulses was set at 1.4μS for each frequency of operation. The r.f. pulse generator was triggered at 50 p.p.s. The no-voltage attenuation and the crystal resistance were measured for each case. The variation of the measured acousto-electric voltage with no-voltage attenuation for given attenuator settings at each ultrasonic frequency used is shown in fig. 72. These results enabled the input acoustic power entering the CdS for the three operating frequencies to be compared.

Fig. 73 shows an acousto-electric wave-form as the ultrasonic pulse was reflected backwards and forwards in the

acoustic amplifier structure.

5.5. Experiments involving phasing the applied voltage pulse.

5.5.1 Ultrasonic amplification during first acoustic transit and subsequent transits.

When an r.f. pulse was applied to the input transducer a pulse of ultrasonics was produced which travelled through the amplifier structure. Fig.74a shows the oscilloscope trace of the amplified and rectified receiver transducer output. The ultrasonics were of 45 MHz. The CdS was maintained in the dark and no voltage was applied. The largest peak was due to the transit of the ultrasonic pulse through the amplifier structure. The peaks 8.0, 16.0 and 24.0μS delayed with respect to the first transit were caused by reflections at the interfaces in the amplifier structure. The time delays of the three main echoes corresponded to those expected for 1, 2 and 3 round trips in the acoustic buffers, as shown in fig.76. Fig.74b shows on 11 db reduction in the received first transit due to illumination of the crystal. As shown on fig.74C a field of 1050 v c.m.$^{-1}$ restored the first transit to its dark level. The 6μS long voltage pulse was applied 9μS before the first transit was received i.e. it was applied just before the ultrasonic pulse entered the CdS. When the voltage pulse was applied only 2μS before the first transit was received, as fig.75a, the second peak was amplified. The amplification was received by the component of the second peak due to path 2, fig.76. For this condition the first transit was of the same height as the illumination only case, fig.74b.

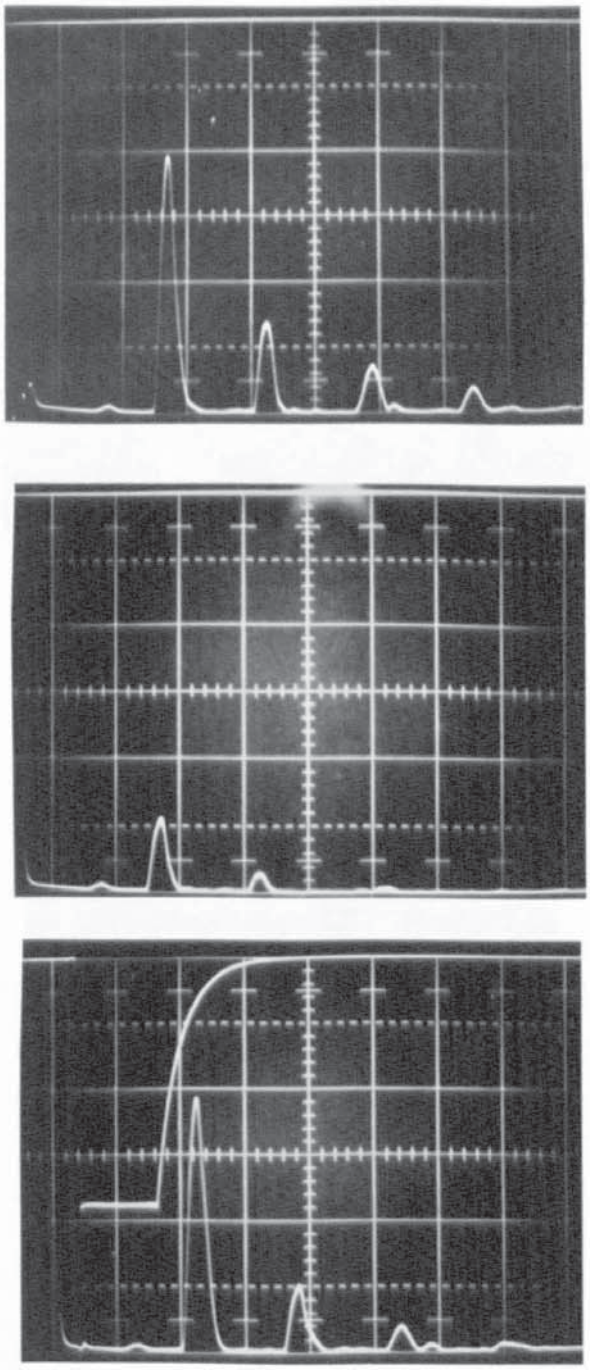

a/

b/

c/

FIG. 74. OSCILLOSCOPE TRACES FOR AMPLIFICATION OF ULTRASONICS:

ULTRASONIC FREQUENCY: 45 MHz

TIME SCALE: 5 μS $cm.^{-1}$

APPLIED FIELD: 286 v $cm.^{-1}$ ON CdS

FOR 1 cm. OF GRATICULE

RECEIVER OUTPUT LINEAR

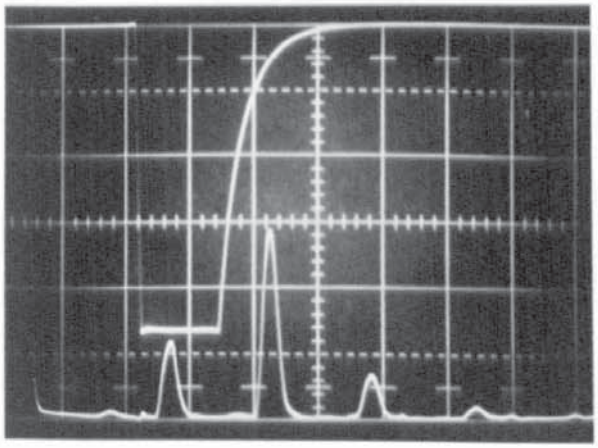

a/

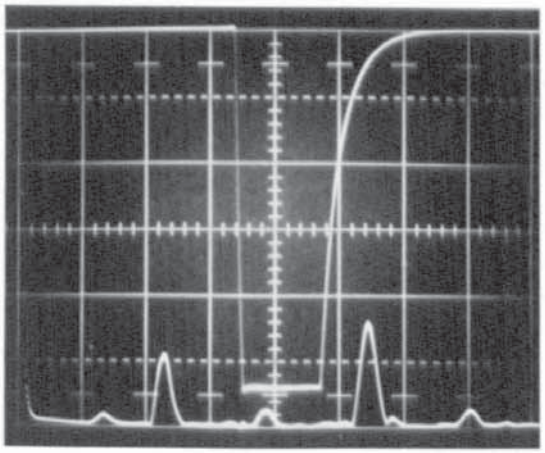

b/

FIG. 75. OSCILLOSCOPE TRACES FOR AMPLIFICATION OF ULTRASONICS.

DETAILS AS FIG.74.

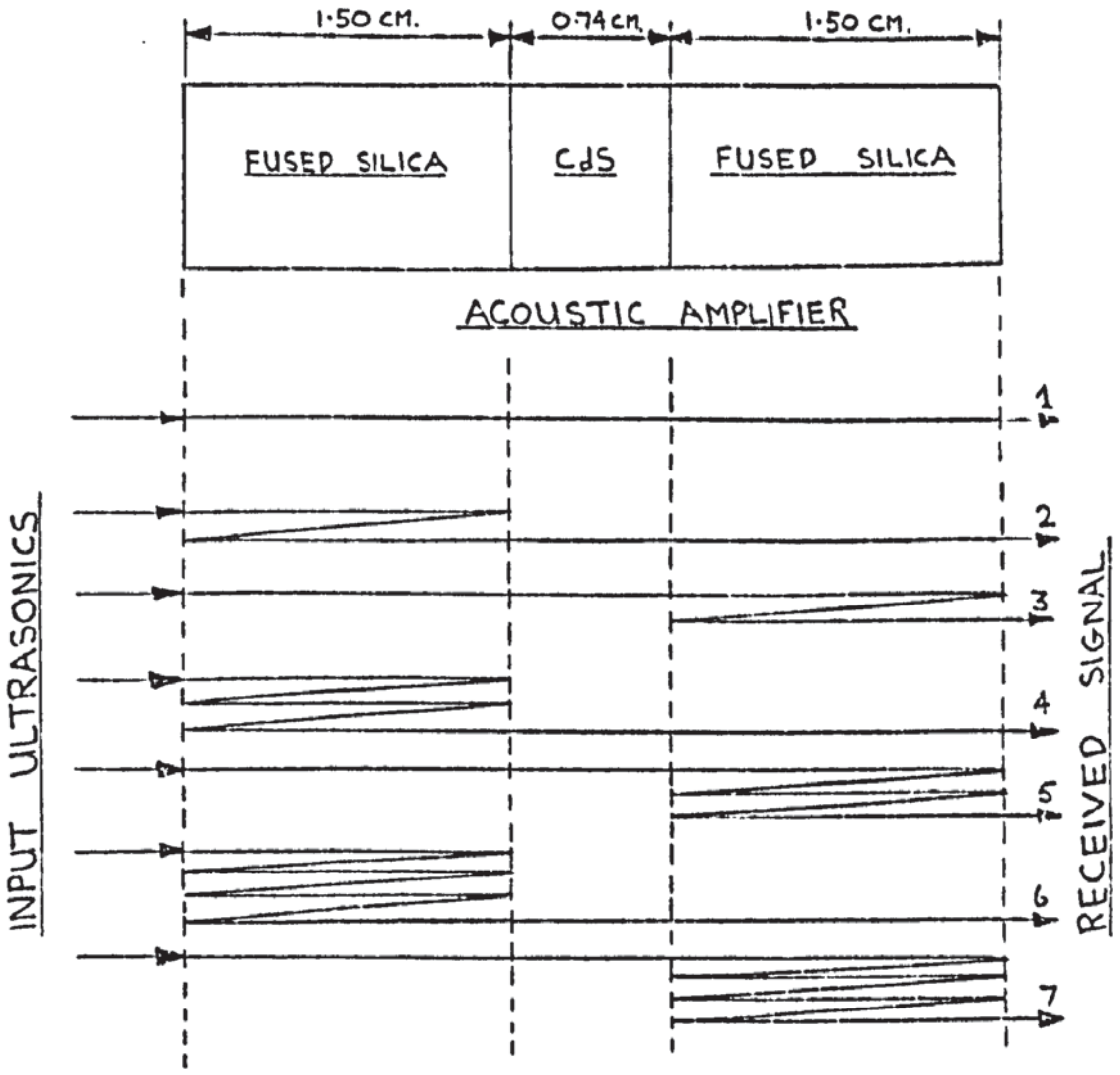

PATH 1 CORRESPONDS TO 1ST MAIN PEAK DETECTED

PATHS 2&3 CORRESPOND TO 2ND MAIN PEAK DETECTED

PATHS 4&5 CORRESPOND TO 3RD MAIN PEAK DETECTED

PATHS 6&7 CORRESPOND TO 4TH MAIN PEAK DETECTED

SHEAR WAVE TRANSIT TIMES:

FUSED SILICA, 3·95 μS.

CdS, 4·2 μS.

FIG. 76. ULTRASONIC REFLECTIONS IN AN ACOUSTIC AMPLIFIER STRUCTURE

When the voltage pulse was applied 6μS after the first transit was received the third peak was amplified. The amplification was received by the component of the third peak due to path 4, fig.76. For this voltage phasing condition the heights of the first and second peaks were the same as the illumination only case.

5.5.2 Voltage phasing for first acoustic transit

In an effort to ascertain if the ultrasonic amplification property of a CdS crystal was uniform throughout its length the effects of voltage phasing on the propagation of the first acoustic transit were investigated.

Fig.77 shows the attenuation required in the input attenuator in order to maintain a constant output level of the first acoustic transit whilst the voltage pulse was applied at various times with respect to the entry of ultrasonics into the CdS. The experiment was carried out for voltage pulses ranging in time duration from 2.0 to 8.5μ S. Ultrasonics of 45 MHz frequency were used. Fields of 1200 v cm^{-1} were used in each case. The half height width of the ultrasonic pulse was 1.2μS.

5.5.3 Specialised voltage phasing

The experiment described above was modified in order to gain more information about the uniformity of the CdS. The width of the applied voltage pulse was maintained at 8.0μ S. The half height width of the ultrasonic pulse was made 0.5μS. The Matec receiver was used to amplify the output from the receiving transducer for display on the oscilloscope. The height of the receiver output was recorded as the phase of the voltage pulse

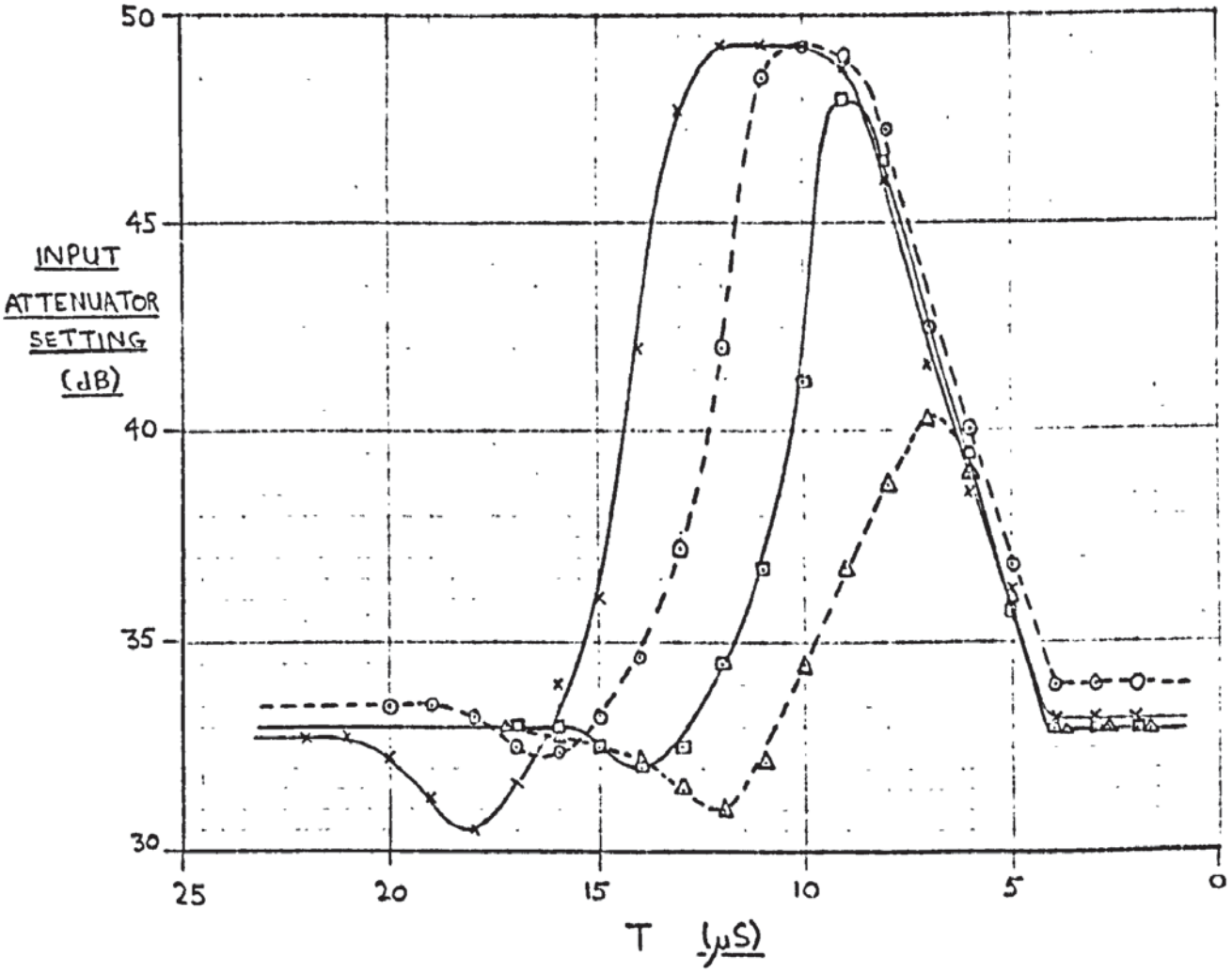

T = TIME INTERVAL BY WHICH RISING EDGE OF VOLTAGE PULSE PRECEDES RECEIVED ULTRASONIC SIGNAL

VOLTAGE PULSE LENGTH (μS)

—×— 8·5
--⊙-- 6·0
—□— 4·0
---△-- 2·0

OPERATING CONDITIONS

$\frac{s}{\lambda}$ = ·18

ELECTRIC FIELD : 1200 V CM.$^{-1}$

FIG. 77. EFFECTS OF VOLTAGE PULSE PHASING ON ACOUSTIC AMPLIFICATION AT 45 MH$_3$.

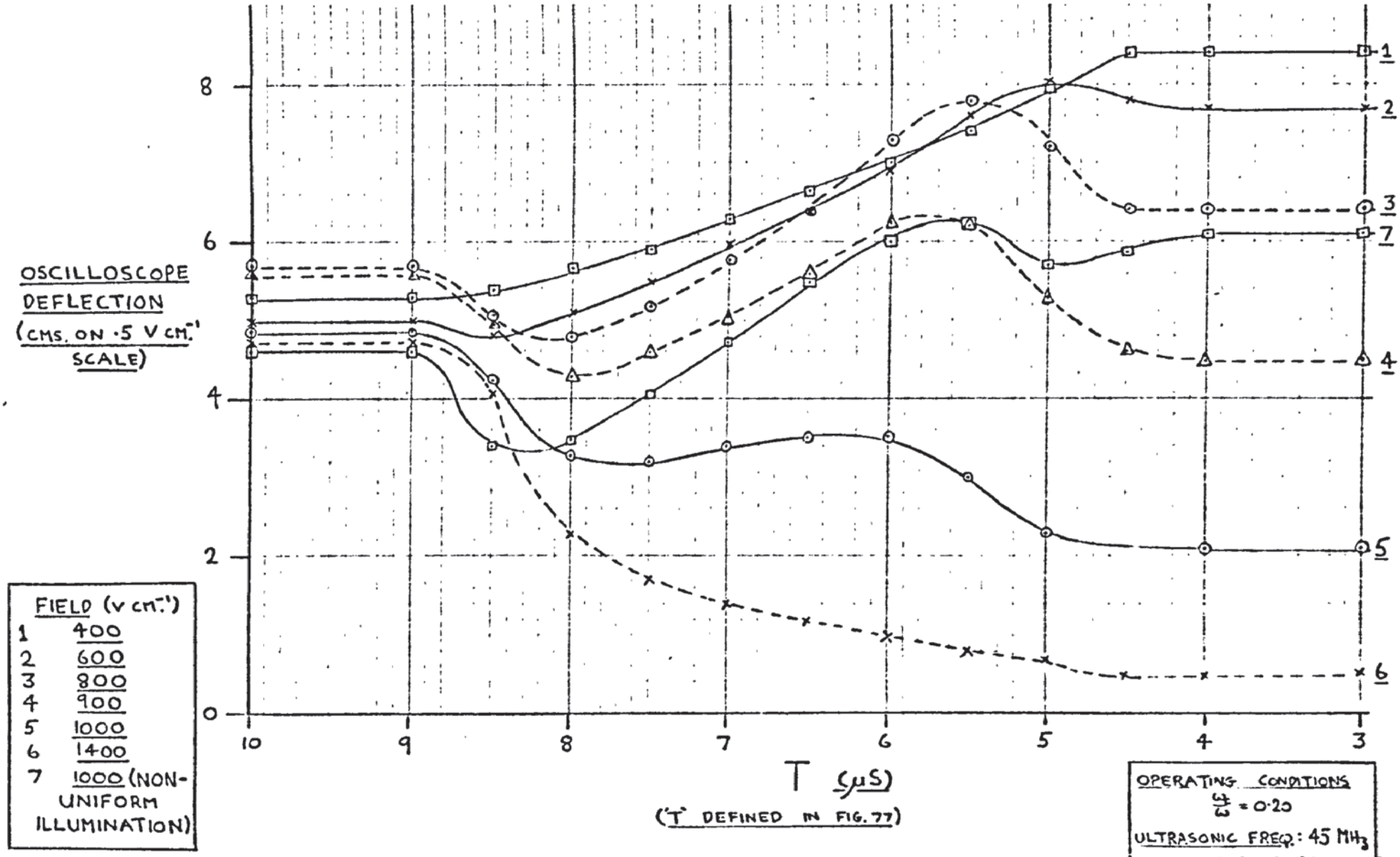

FIG. 78. VOLTAGE PHASING EXPERIMENT.

was altered in 0.5 μS steps relative to the time of arrival of the first transit. The experiment was repeated for several values of applied voltage. Fig.78 shows typical results obtained. The receiver was calibrated and found to be accurately linear over the range used. In this experiment the changes in acoustic attenuation were somewhat smaller than most of the experiments reported in this thesis, and for this reason it was more convenient in this case to record the receiver output rather than maintain it at a constant level by the use of attenuators. Identical results were obtained when the ultrasonics were injected into the CdS in the opposite direction provided the polarity of the voltage pulse was reversed also.

5.6. Experiments involving large amplitude ultrasonics.

5.6.1 Input-output acoustic characteristics.

In order to study electro-acoustic effects in CdS for large amplitude ultrasonic signals a series of input-output acoustic characteristics were taken. In this type of experiment the CdS was maintained in a given operating condition, for example moderate illumination and an amplifying voltage, and initially the input attenuator placed a large amount of attenuation in the circuit whilst the output attenuator placed zero attenuation in the circuit. The word circuit in this context is used to mean the link, by r.f. signals and ultrasonics, between the r.f. generator and receiver. Whilst the in-circuit attenuation of the input attenuator was reduced in steps the attenuation in the output attenuator was adjusted so as to maintain a constant receiver output.

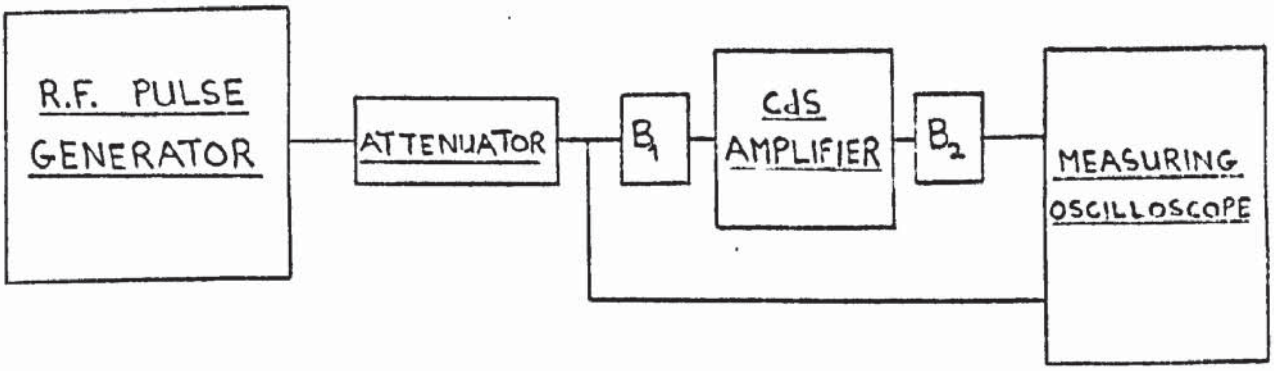

B_1 , B_2 = MATCHING TRANSFORMERS

FIG. 79 DIRECT MEASUREMENT OF LINEARITY OF CdS ACOUSTIC AMPLIFIER

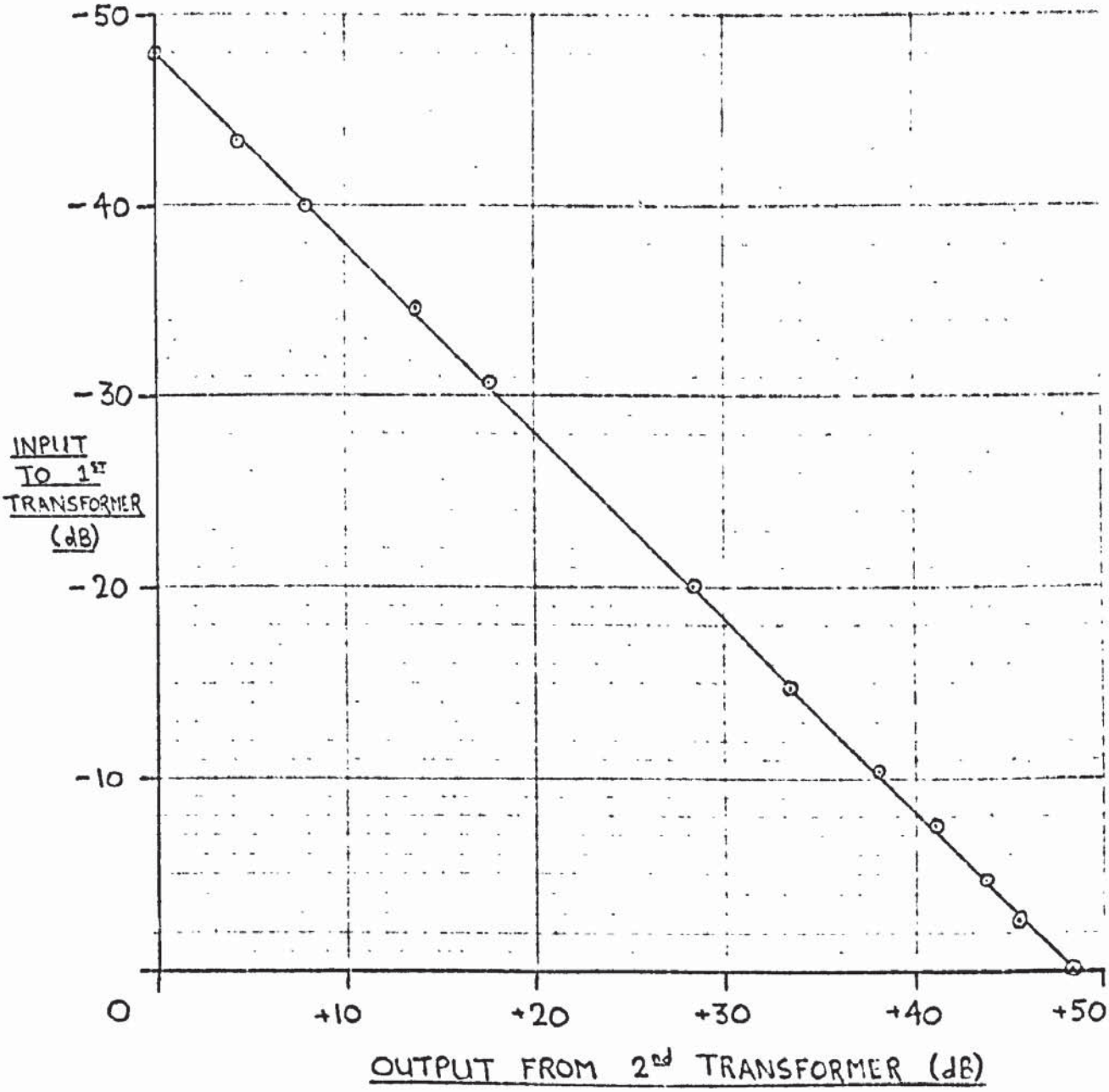

INPUT AND OUTPUT VOLTAGES WERE COMPARED WITH THEIR MAXIMUM VALUES USING THE dB COMPARISON.

DIRECT MEASUREMENT USING ARRANGEMENT OF FIG. 79.

ULTRASONIC FREQUENCY : 45 MH$_3$

NO APPLIED VOLTAGE.

FIG. 80. INPUT - OUTPUT CHARACTERISTIC FOR CdS MAINTAINED IN THE DARK.

In these experiments the input-output curve obtained with the CdS maintained in the dark was used as a reference curve. The linearity of the CdS acoustic amplifier, with the CdS maintained in the dark, was investigated using the arrangement shown in fig.79.

Ultrasonics of 45 MHz frequency were used. The input attenuator was used to vary the acoustic power input to the CdS.

The peak r.f. voltage of the attenuator output was measured directly on the oscilloscope. The output of the receiver transformer was similarly fed directly into the oscilloscope. The values of the input and output voltage were obtained for a wide range of attenuator settings. The results, expressed in decibels, are shown in fig.80. The Matec r.f. pulse generator was used in the experiments described in this section.

When observing input-output acoustic characteristics the usual circuit incorporating input and output attenuators was used, fig.30. When the input and output attenuators were carefully matched to their appropriate transducers by means of transformers the observed input-output characteristics were linear when the CdS was maintained in the dark. In practice the observed input-output characteristic for the dark condition was often not exactly linear due to the attenuators not being exactly matched to the circuit. The observed electro-acoustic non-linearity was small when the CdS was illuminated and either no drift voltage was applied or an attenuating voltage was applied. For these cases the slight non-linearity of the dark-condition

characteristic prevented the electro-acoustic non-linearity from being accurately measured. This problem was overcome by producing a dark-condition input-output characteristic with the initial attenuator settings exactly the same as for the input-output characteristic with the CdS in an attenuating condition. This reference dark-condition input-output characteristic was produced by reducing the receiver gain. For example the dark-condition input-output characteristic may have been commenced with 55 db indicated in the input attenuator and 0 db in the output attenuator, for a certain receiver output.

The input-output characteristic for the CdS in an attenuating state may have commenced with 42 and 0 db in the input and output attenuators respectively, for the same receiver output. To produce the reference characteristic the receiver gain was reduced until the input and output attenuators placed 42 and 0 db in circuit respectively whilst the receiver output was at the standard level. Then the reference characteristic was taken. Any deviation between the reference characteristic and the input-output characteristic for CdS operation was attributed to electro-acoustic non-linearity. Experimental input-output characteristics, with dark-level reference characteristics obtained by the receiver turn-down technique, are presented later in this section. A technique now to be described was sometimes used to avoid having to produce a reference characteristic for each experimental characteristic. If for example a series of experimental runs were performed with various amounts of acoustic

attenuation in the CdS then the input-output characteristic corresponding to the greatest attenuation was taken first. For all subsequent experimental runs, involving less attenuation, the receiver gain was reduced to make the initial values of the attenuator settings equal to those of the first run, for a fixed receiver output. In this way a single dark-condition calibration run sufficed for all the experimental conditions. Input-output characteristics produced in this manner are referred to as normalised characteristics. The normalising technique was applied to determine input-output characteristics for amplifying conditions also. The normalising technique was convenient for determining the extent of non-linearity with minimal effort but it did not provide all the information provided by the individual calibration method. In particular characteristics obtained by the latter method showed the basic values of input and output attenuator settings which enabled the amount of acoustic attenuation to be calculated by reference to the basic dark-condition characteristic.

The very large number of experimental results obtained whilst studying input-output characteristics renders a complete presentation impractical. Instead typical results are presented for the four main operating conditions, namely no applied field, attenuating, cross-over and amplifying fields, at two frequencies. The input-output characteristics presented are detailed in table 9.

Experiments to determine the absolute values of acoustic power entering the CdS corresponding to the settings of the input attenuator are described in section 5.6.4.

TABLE 9.

List of input-output characteristics

Operating frequency MHz	Operating condition of CdS	Measurement technique	Figure no.
15	zero applied field	normalized (N)	81
"	"	individual calibration (IC)	82
"	"	N & I.C. (comparison)	83
"	600 V $cm.^{-1}$	N	84
"	"	I.C.	85
"	"	N & I.C. (comparison)	86
"	cross-over and amplifying fields	I.C.	87
"	amplifying fields	N	88
45	cross-over and amplifying fields $\frac{\omega_c}{\omega}$ =.3	I.C.	89
"	" (.2)	"	90
"	" (.1)	"	91
"	" (.05)	"	92

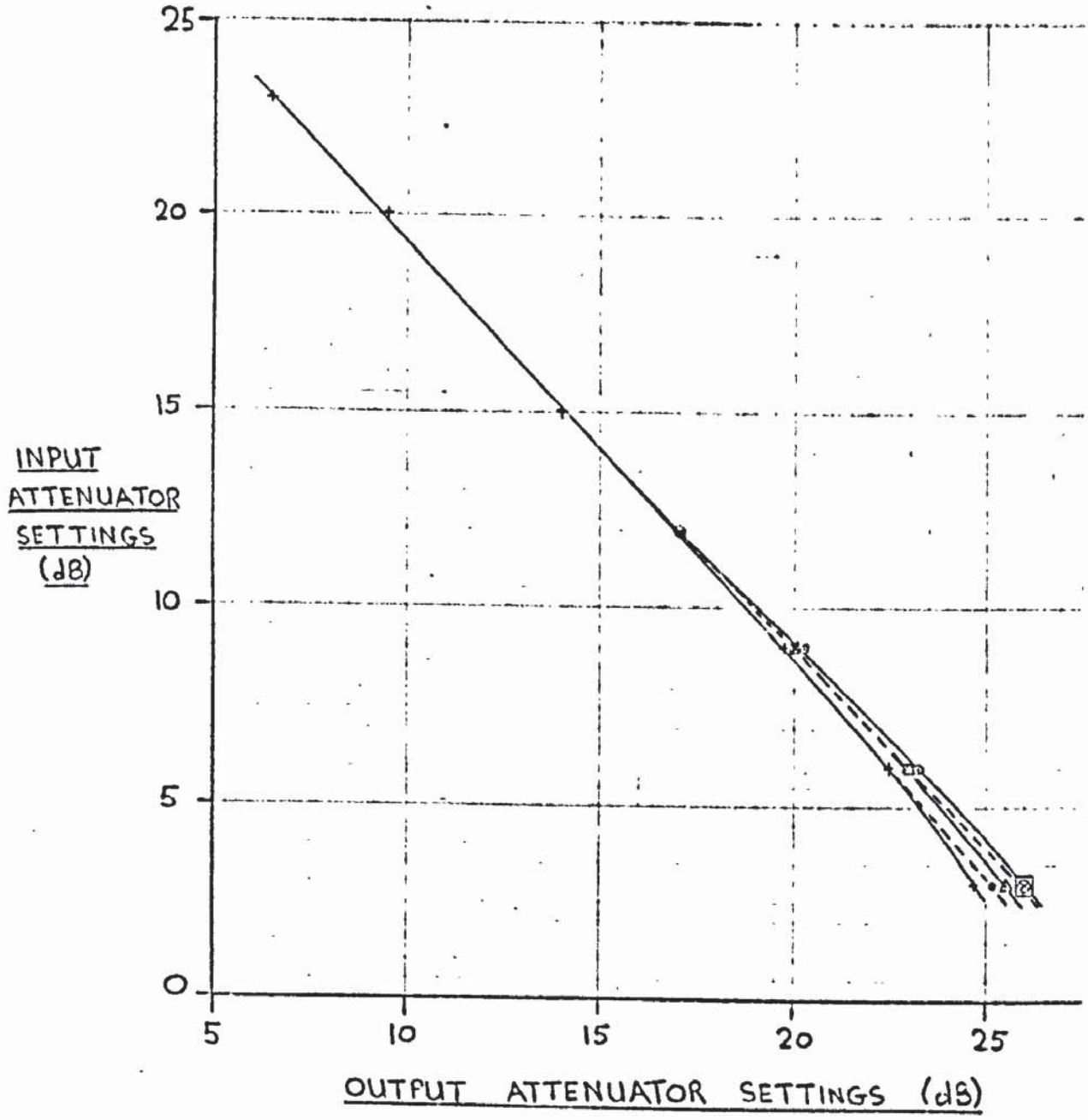

FIG. 81. INPUT-OUTPUT CHARACTERISTICS AT 15 MH$_3$ (NORMALISED)

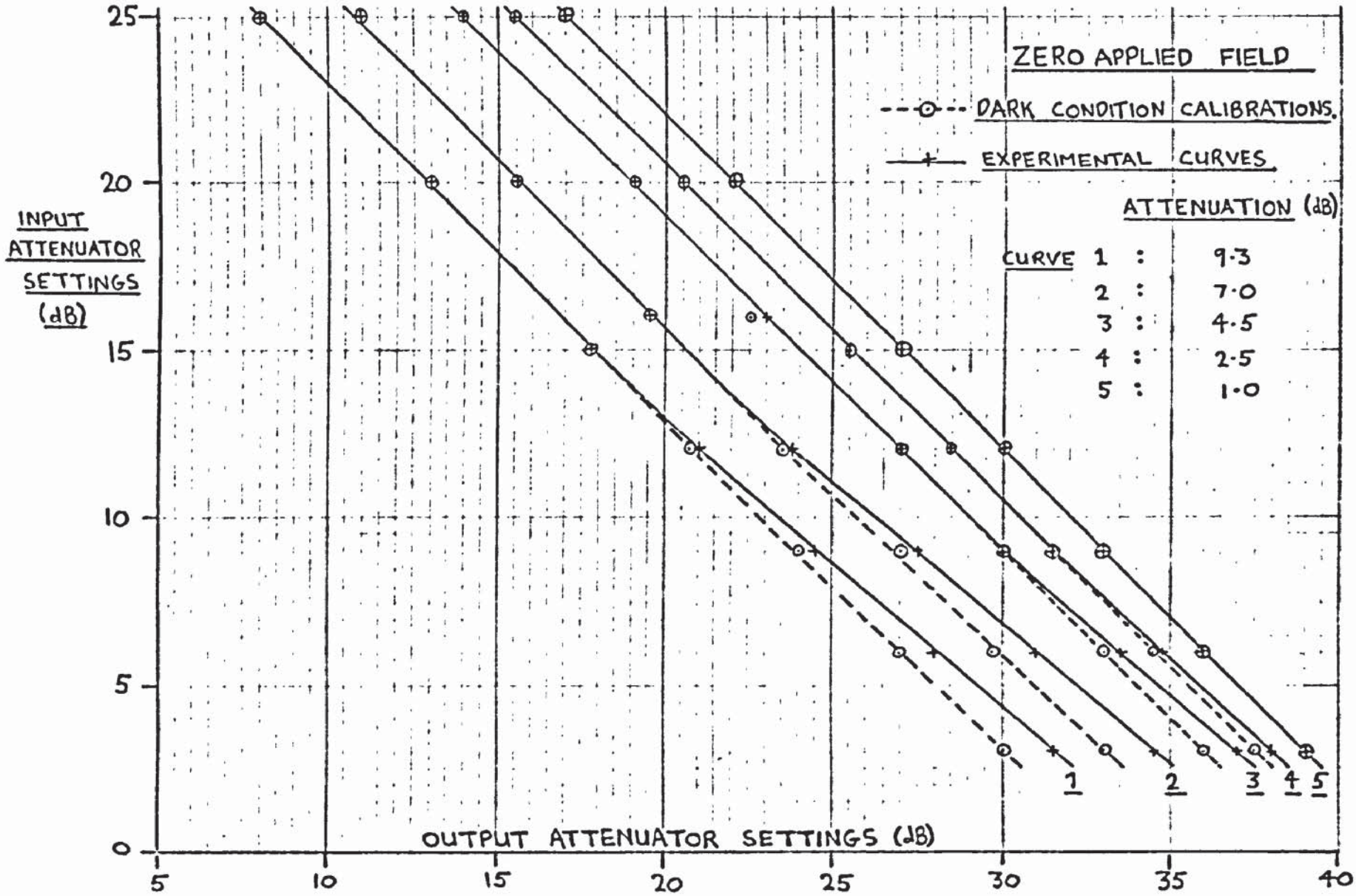

FIG. 82. INPUT-OUTPUT CHARACTERISTICS AT 15 MH$_3$.

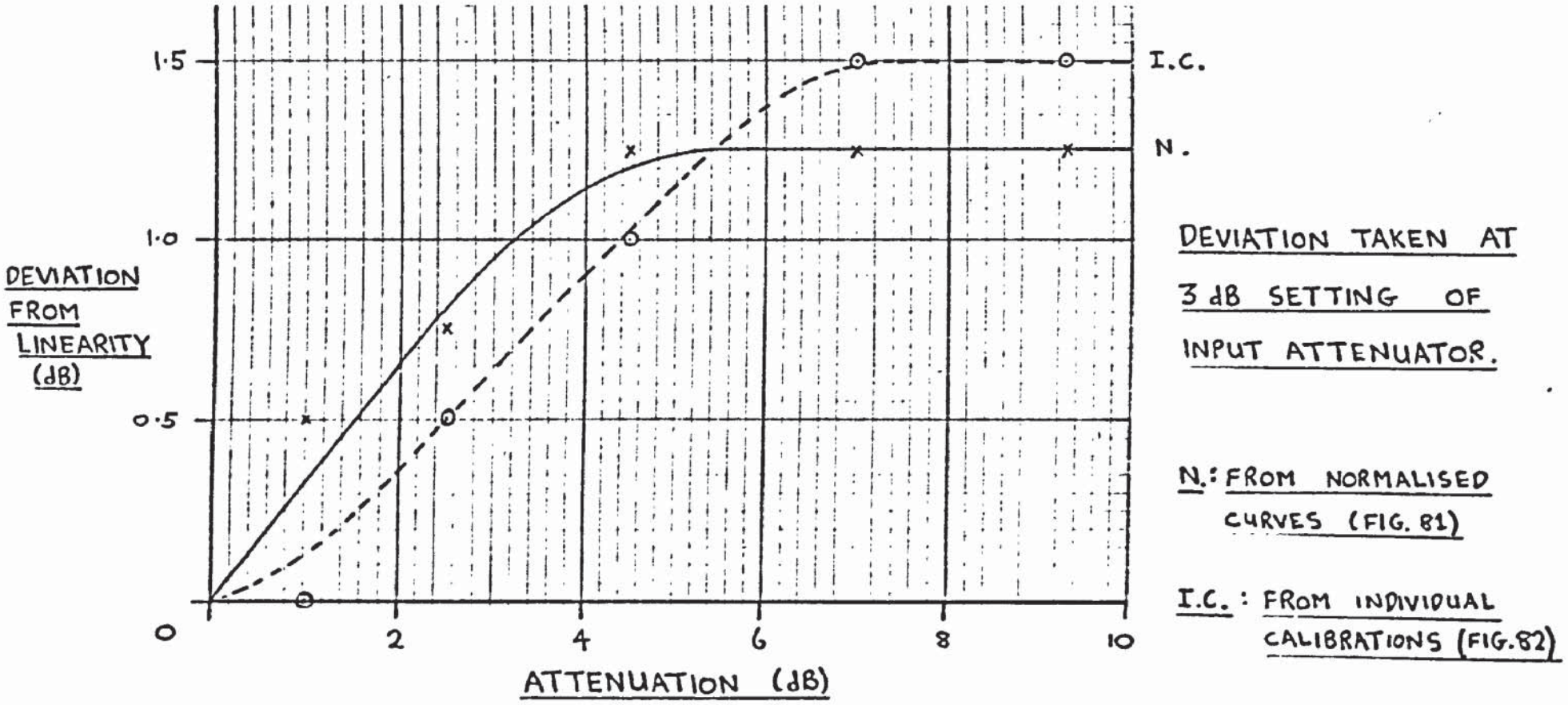

FIG. 83. COMPARISON OF DEVIATION FROM LINEARITY.

(FOR 15 MH_3, ZERO APPLIED FIELD CASE)

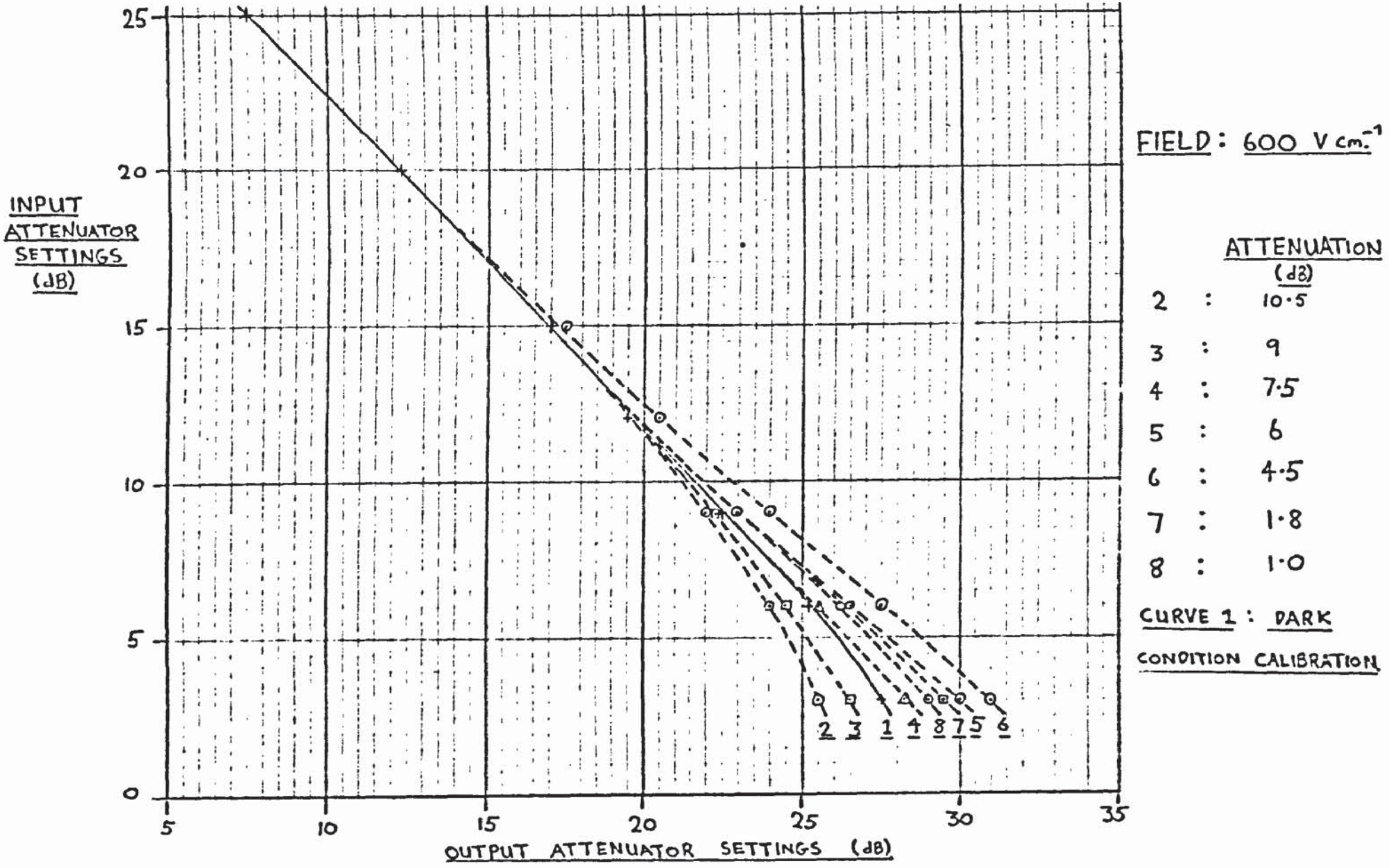

FIG. 84. INPUT-OUTPUT CHARACTERISTICS AT 15 MH$_3$. (NORMALISED)

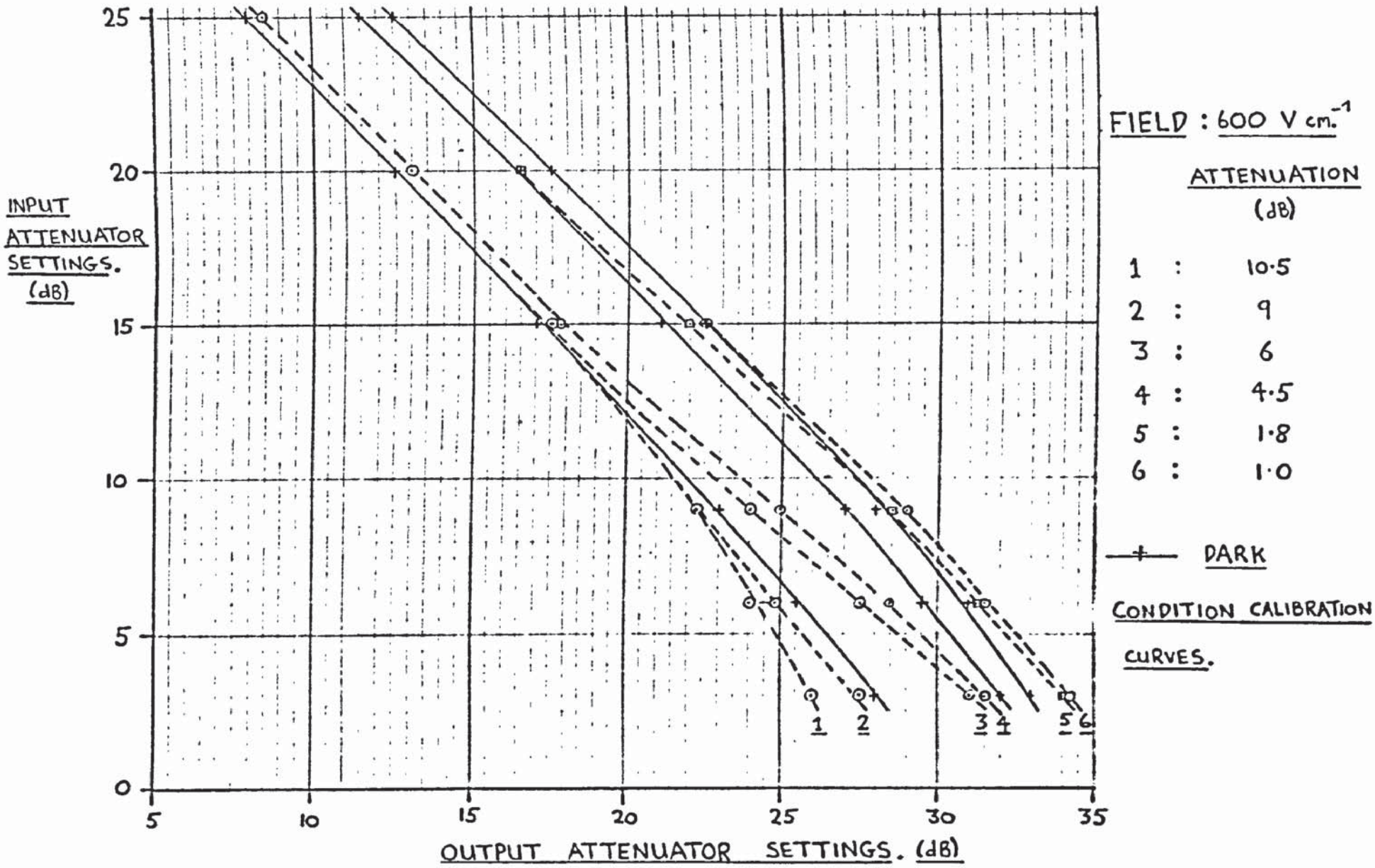

FIG. 85. INPUT-OUTPUT CHARACTERISTICS AT 15 MHz.

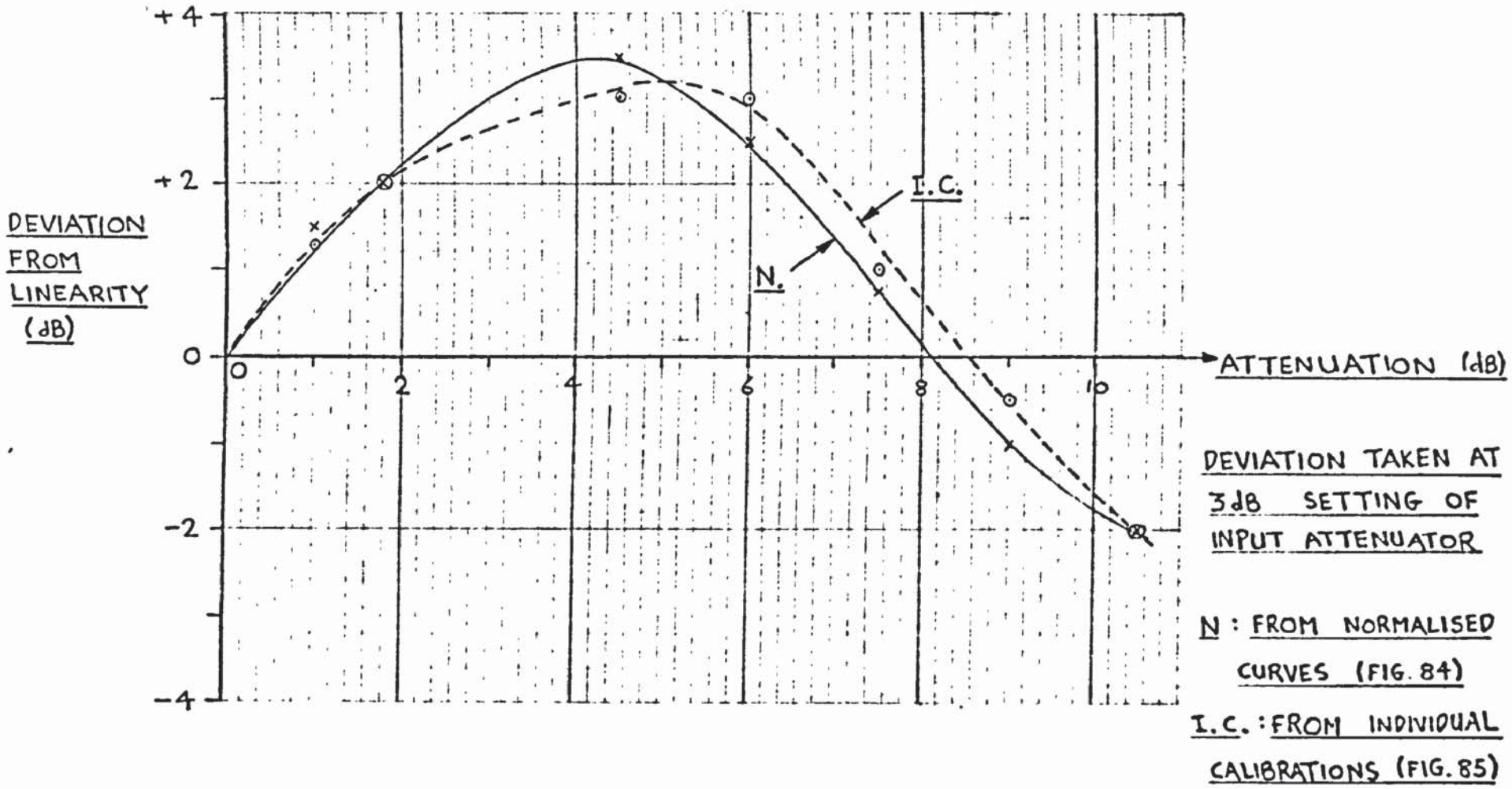

FIG. 86. COMPARISON OF DEVIATION FROM LINEARITY.

(FOR 15 MH_3 , 600 V $cm.^{-1}$ CASE)

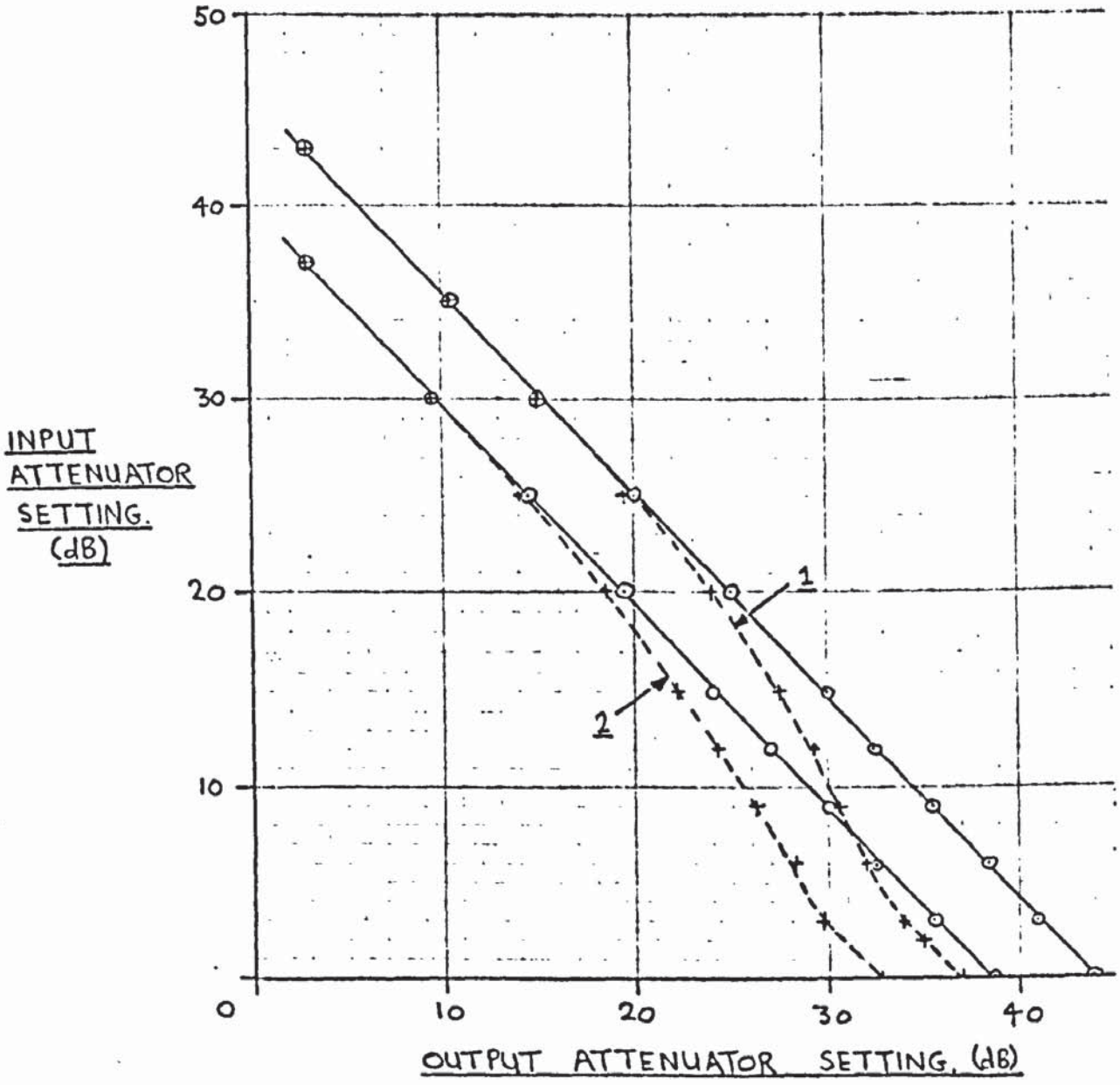

$\frac{3^{c}}{3} = 0.60$

—⊙— DARK CONDITION CALIBRATIONS

CURVE 1 : 1600 V $cm.^{-1}$

CURVE 2 : SMALL SIGNAL CROSS-OVER FIELD

FIG. 87. INPUT-OUTPUT CHARACTERISTICS AT 15 MHz.

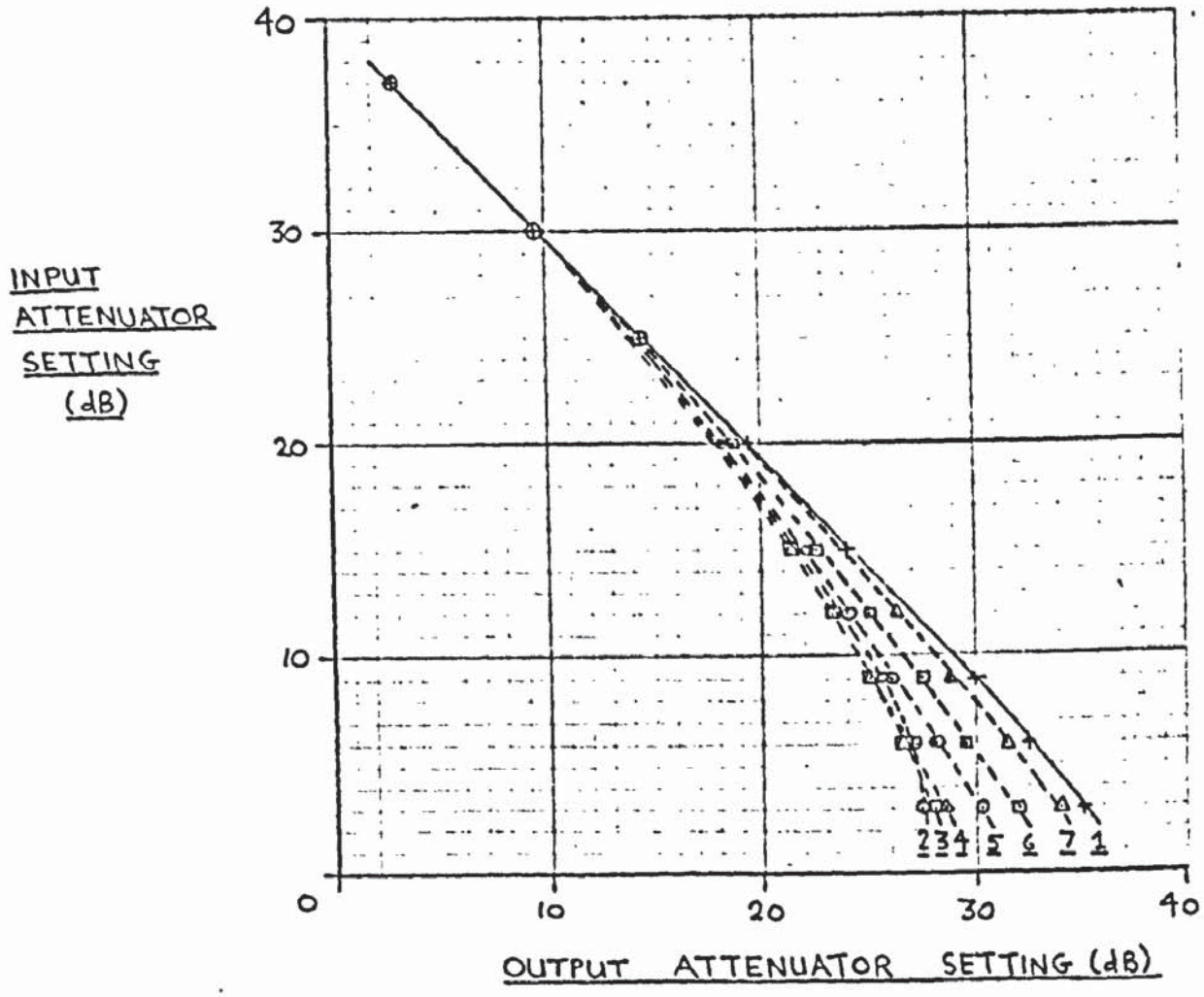

FIELD : 1400 V $cm.^{-1}$

CURVE 1 : DARK CONDITION CALIBRATION.

	ATTENUATION (dB)
2 :	10
3 :	7
4 :	5
5 :	3·0
6 :	2·0
7 :	1·0

FIG. 88. INPUT-OUTPUT CHARACTERISTICS AT 15 MHz. (NORMALISED)

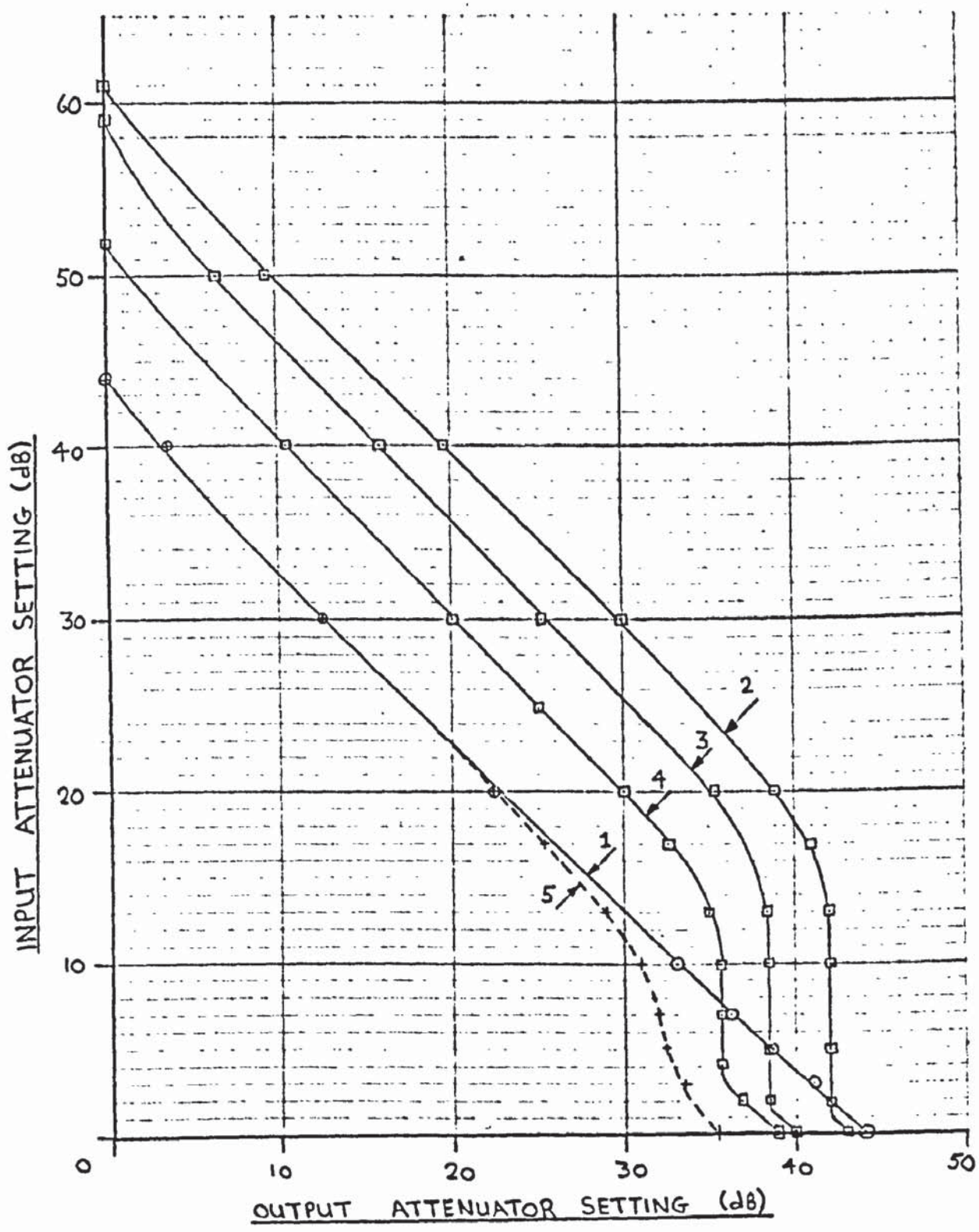

$\frac{3f}{3} = \cdot 3$

FIELD (V cm.$^{-1}$)

2 : 1600

3 : 1400

4 : 1200

5 : SMALL SIGNAL CROSS-OVER FIELD.

CURVE 1 : DARK CONDITION CALIBRATION.

FIG. 89. INPUT-OUTPUT CHARACTERISTICS AT 45 MHz.

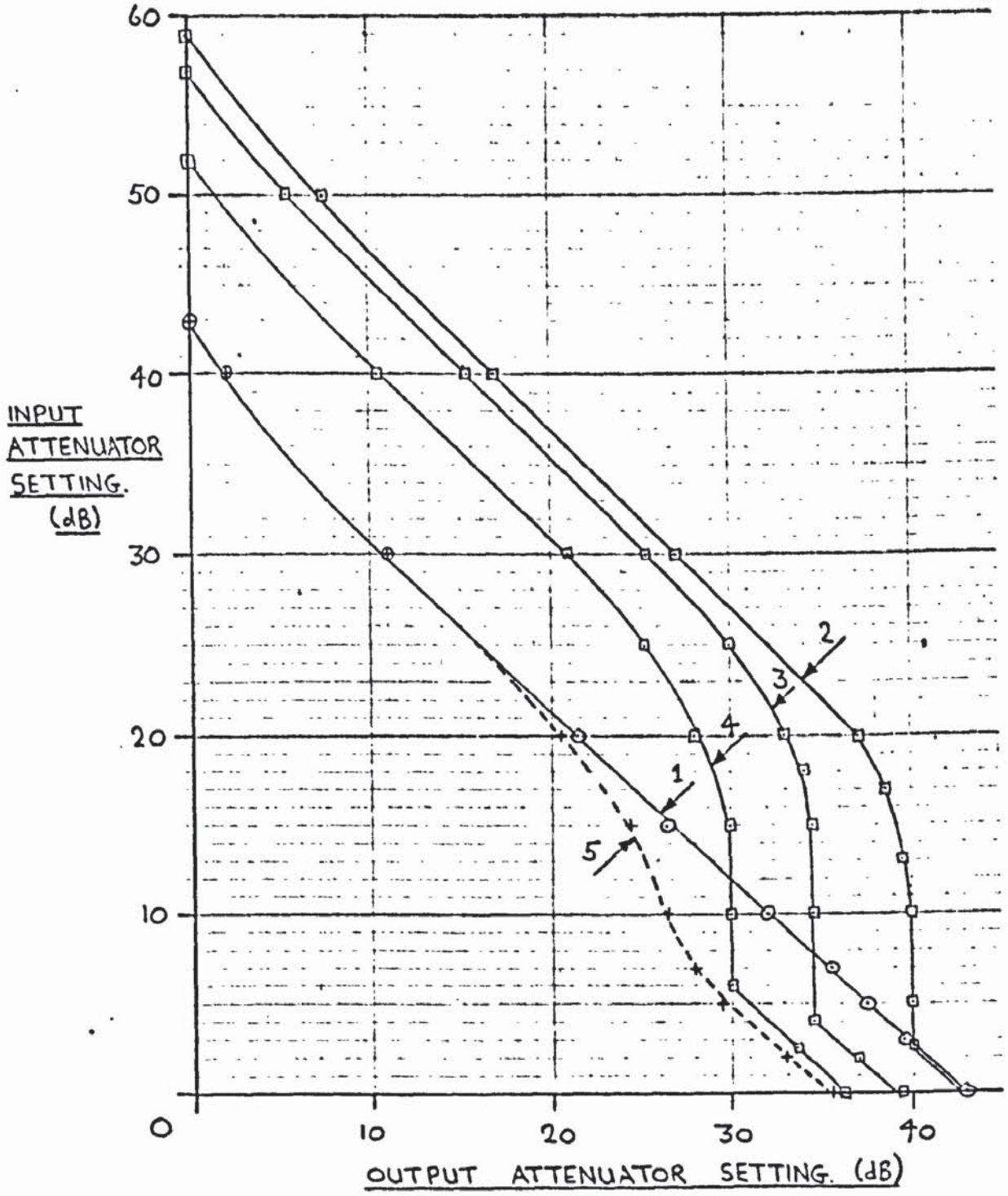

$\frac{\omega_c}{\omega} = \cdot 2$

CURVE 1: DARK CONDITION CALIBRATION

FIELD ($v\ cm.^{-1}$)

2 : 1600
3 : 1400
4 : 1200
5 : SMALL SIGNAL CROSS-OVER FIELD.

FIG. 90. INPUT-OUTPUT CHARACTERISTICS AT 45 MHz.

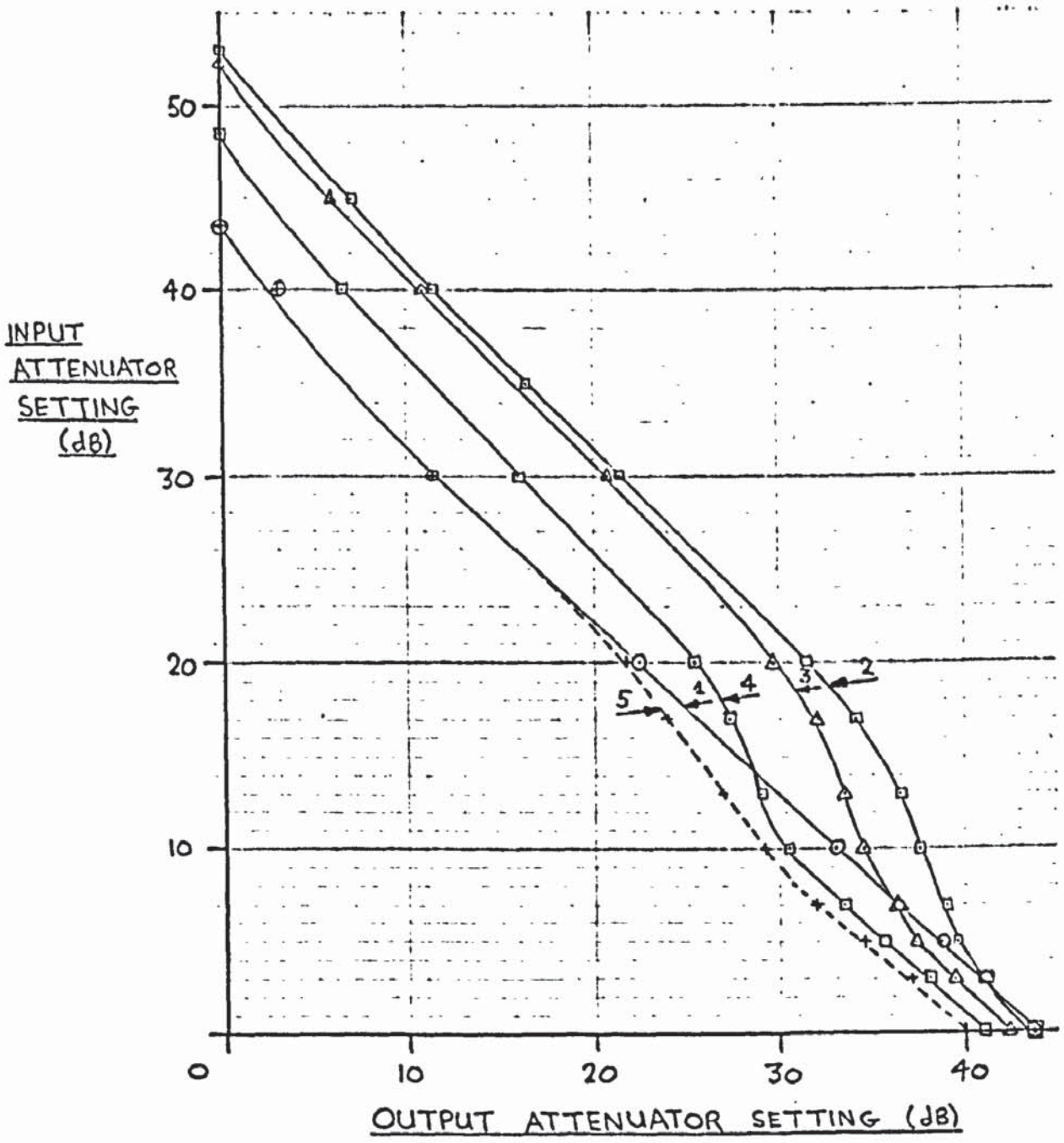

$\frac{\omega_c}{\omega} = \cdot 1$

FIELD ($v\ cm.^{-1}$)

2 : 1600

3 : 1400

4 : 1200

5 : SMALL SIGNAL CROSS-OVER FIELD.

CURVE 1 : DARK CONDITION CALIBRATION.

FIG. 91. INPUT-OUTPUT CHARACTERISTICS AT 45 MHz.

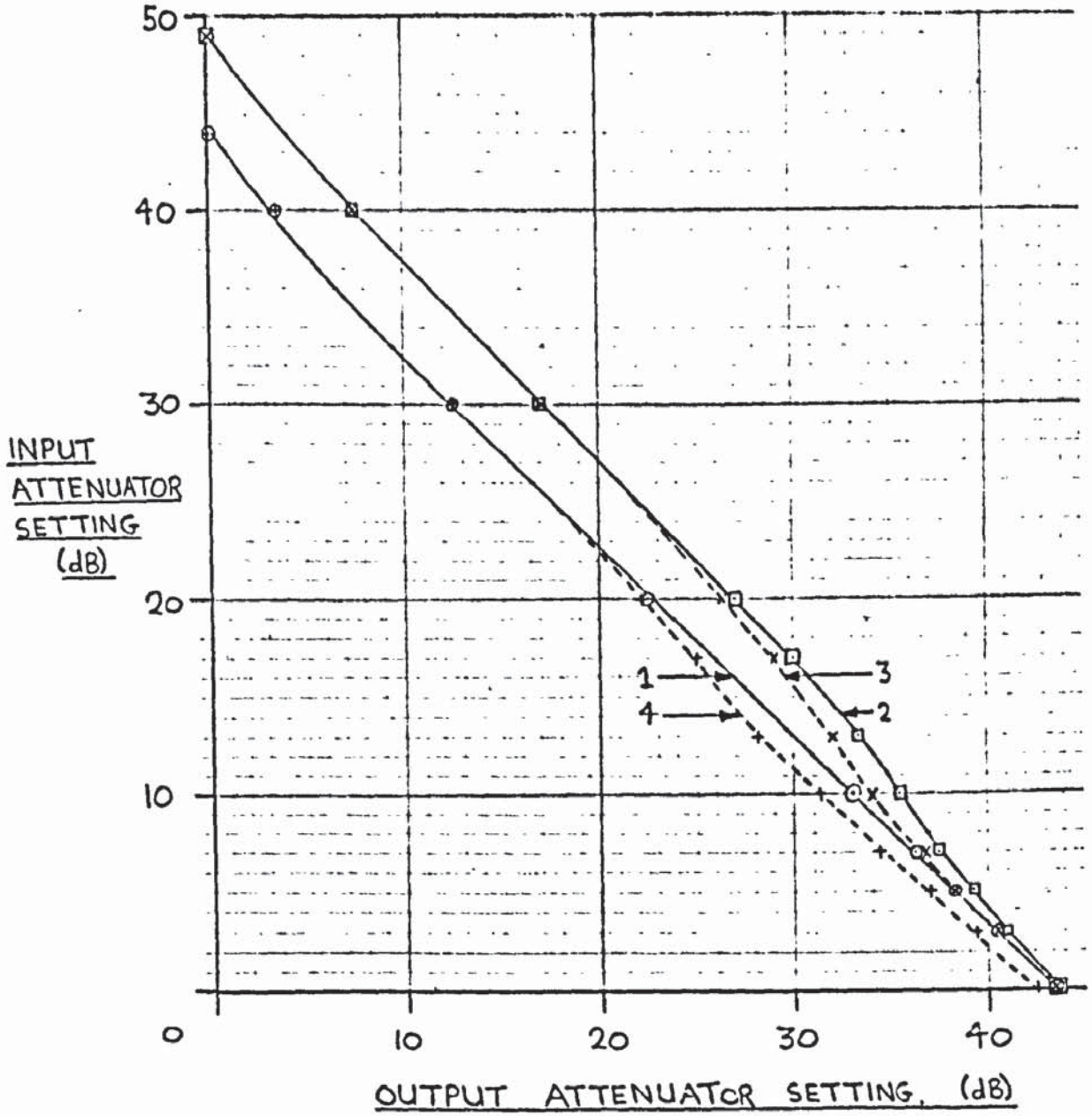

$\frac{\omega_c}{\omega} = \cdot 05$

CURVE 1 : DARK CONDITION CALIBRATION.

FIELD ($V\ CM.^{-1}$)

2 : 1600

3 : 1400

4 : SMALL SIGNAL CROSS-OVER FIELD

FIG. 92. INPUT-OUTPUT CHARACTERISTICS AT 45 MHz.

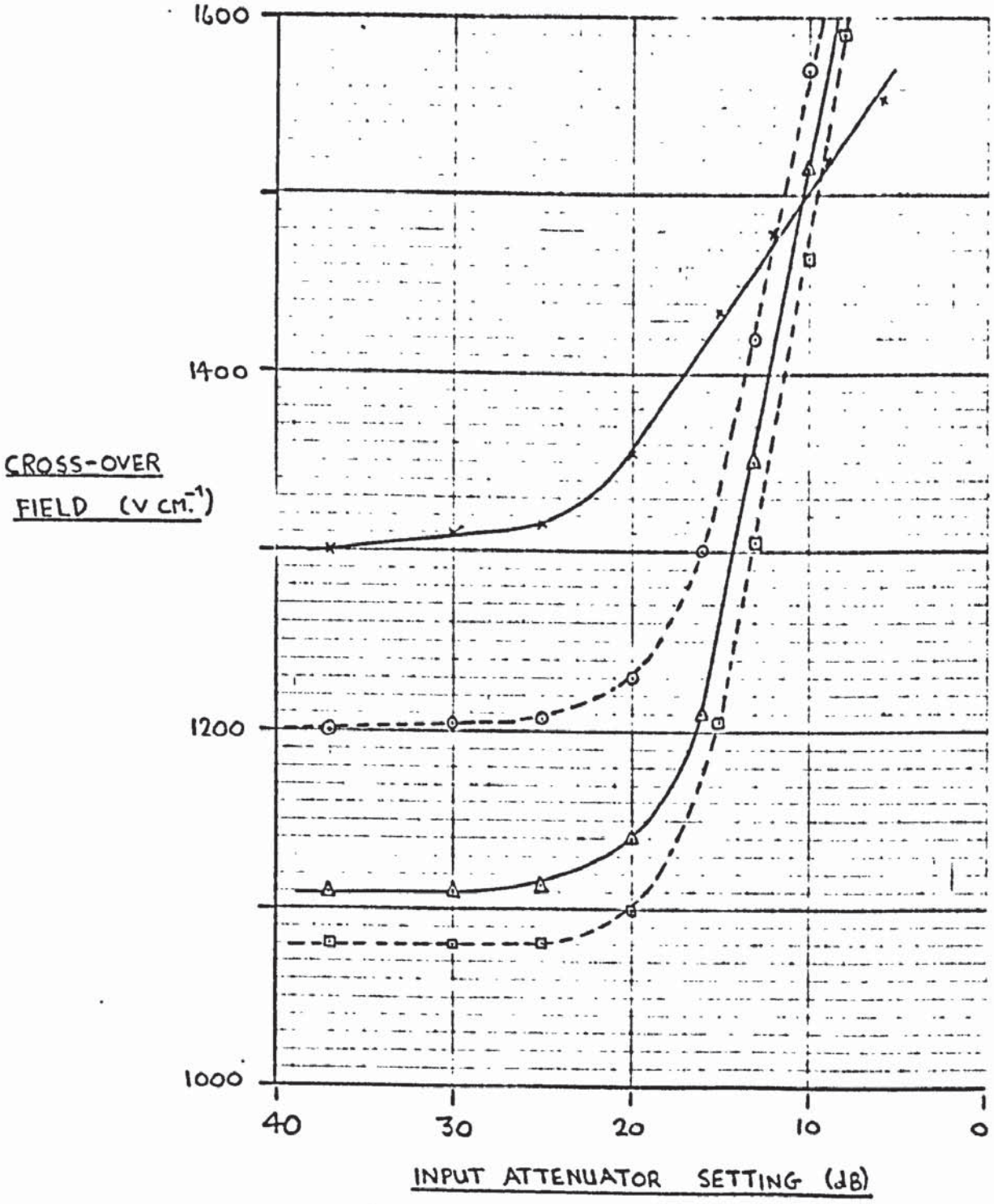

FIG. 93. VARIATION OF CROSS-OVER FIELD WITH INPUT ACOUSTIC INTENSITY AT 15 MHz.

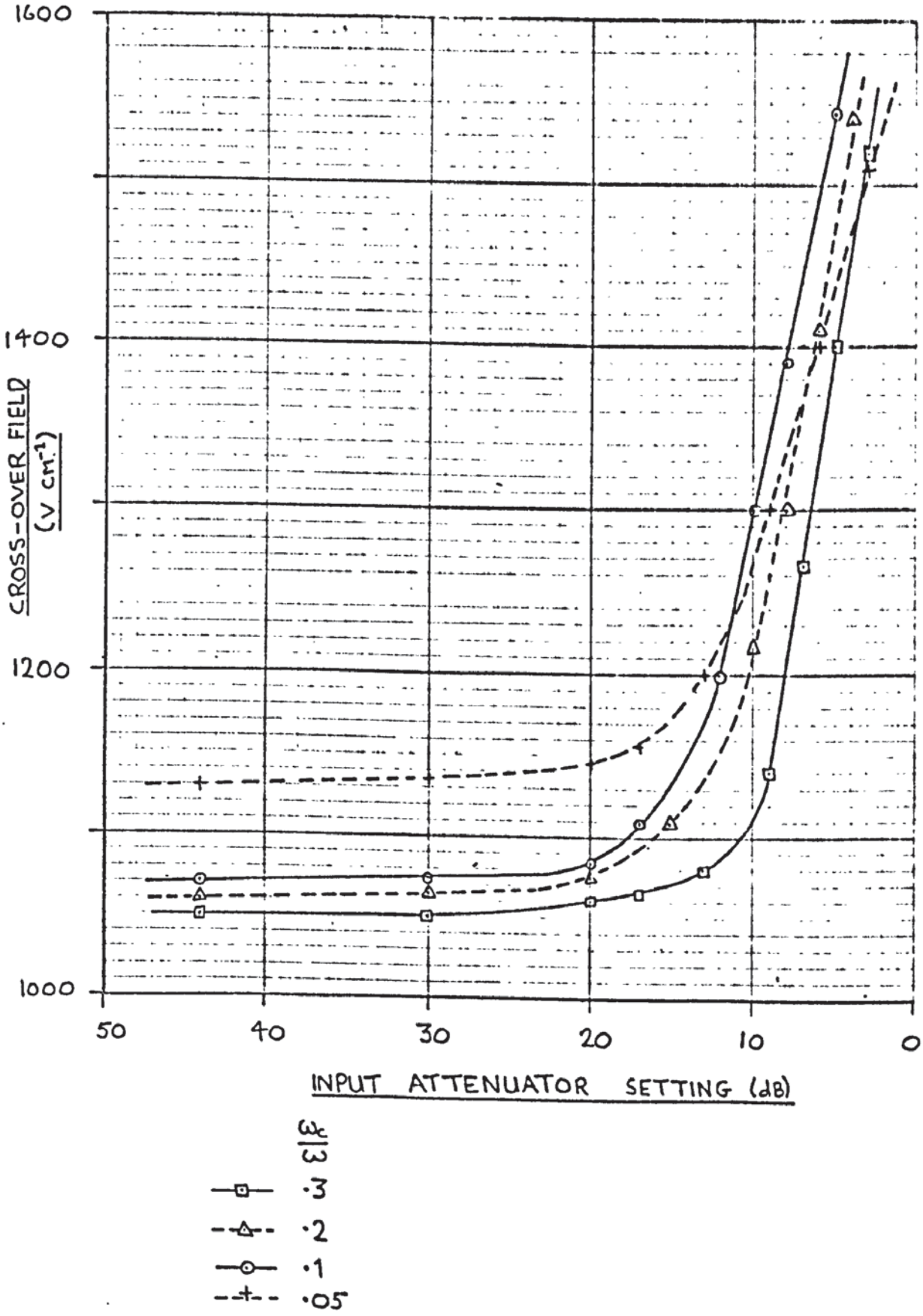

FIG. 94. VARIATION OF CROSS-OVER FIELD WITH INPUT ACOUSTIC INTENSITY AT 45 MHz.

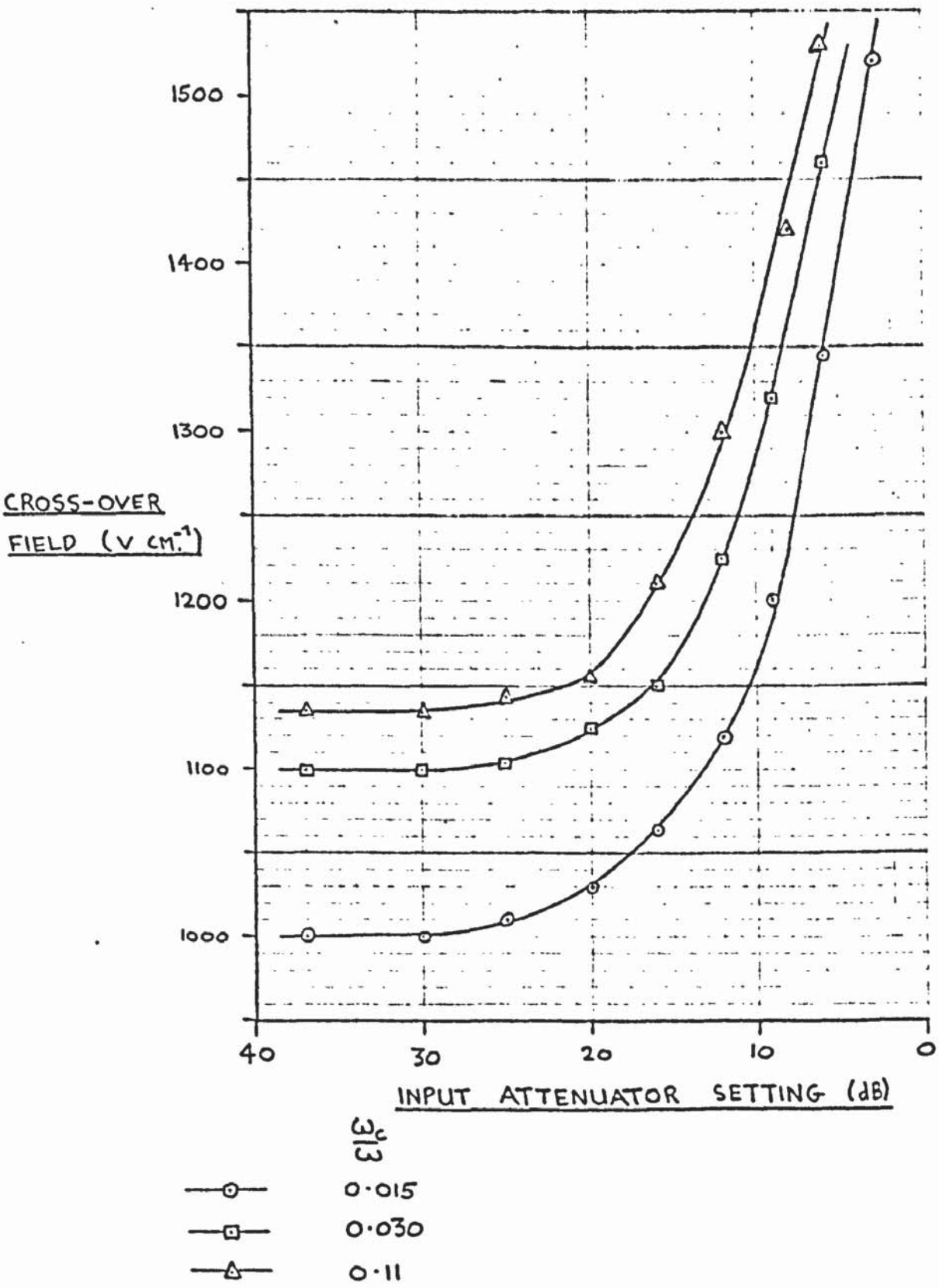

FIG. 95 VARIATION OF CROSS-OVER FIELD WITH INPUT ACOUSTIC INTENSITY AT 75 MHz.

The electro-acoustic non-linearity was small for the operating conditions pertaining to figs. 81 and 82. Fig. 83 shows the deviations from linearity, as obtained by two methods of measurement, for a given input attenuator setting. The results are consistent to about $\pm\frac{1}{2}$ db. Similarly fig. 86 shows a consistency of better than $\pm\frac{1}{2}$ db for the two methods. The non-linearity observed at 45 MHz was greater than that observed at 15 MHz for similar operating conditions.

5.6.2. Variation of cross-over field with acoustic power

The cross-over field is defined as that field for which the net electro-acoustic contribution to ultrasonic attenuation is zero. For the small signal case the cross-over field causes the electrons to travel at the velocity of the acoustic wave. In practice the cross-over field was determined by reference to the dark-condition ultrasonic signal level. With the CdS illuminated the applied voltage was increased until the signal from the receiver was the same as when the CdS was maintained in the dark. That the cross-over field varied with the input acoustic power is shown on fig.90 where if 30 db was in the input attenuator the amplification was about 14 db for curve 3 but with 4 db in the input attenuator the CdS attenuated 2 db.

Experiments were performed in which the cross-over voltage was determined for a range of settings on the input attenuator. Figs. 93 - 95 give the variation of the cross-over field with input acoustic power for 15, 45 and 75 MHz respectively.

5.6.3 Harmonic generation

As discussed in section 1.2.3 the electro-acoustic

interaction produces higher harmonics of the fundamental acoustic frequency. Also experiments were referred to in which the second harmonic was measured. The second harmonic is more intense than the third and higher harmonics. In experiments reported here the third and fifth harmonics of a 15 MHz input ultrasonic signal were measured. The third harmonic of a 45 MHz input ultrasonic signal was also measured.

The basic acoustic amplifier structure was used for harmonic generation experiments. The input acoustic frequency was set at either 15 or 45 MHz and the appropriate transformer was used to match the input attenuator to the transducer. The receiver was tuned to amplify the desired harmonic frequency, either 45, 75 or 135 MHz, and the appropriate transformer was used to match in the output transducer. An input-output acoustic characteristic was first taken with the CdS in a chosen operating condition and with generation and detection at the same frequency. With the CdS in the same operating condition an input-output curve was taken with generation at a given frequency and detection at a frequency three times higher. The procedure was repeated for the fifth harmonic in some cases. Figs. 96-99 give the observed characteristics for a range of operating conditions.

It was observed that for small acoustic inputs the slope of the third and fifth harmonic curves were 3.0 and 5.0 respectively. The ability of the tuned transformer to tune selectively only the desired harmonic frequency was confirmed by feeding its output straight into the oscilloscope and observing a sinusoidal

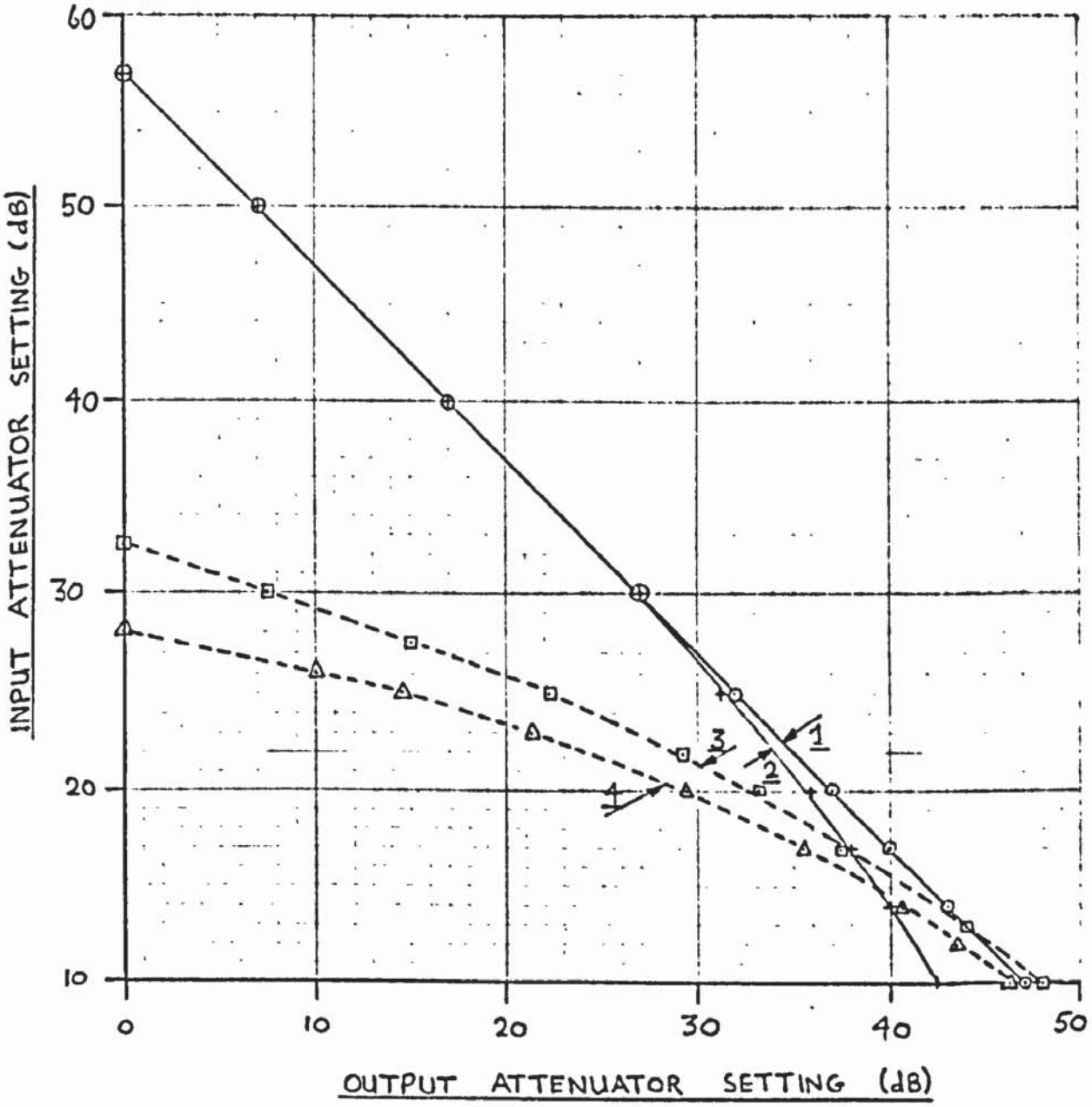

FIELD : 1450 V cm.$^{-1}$

ZERO FIELD ATTENUATION OF FUNDAMENTAL : 8·5 dB

CURVE 1 : DARK CONDITION CALIBRATION.

2 : FUNDAMENTAL SIGNAL, 15 MHz.

3 : 3RD HARMONIC, 45 MHz.

4 : 5TH HARMONIC, 75 MHz.

FIG. 96. HARMONIC GENERATION AT 15 MHz.
(FOR AMPLIFYING CONDITIONS)

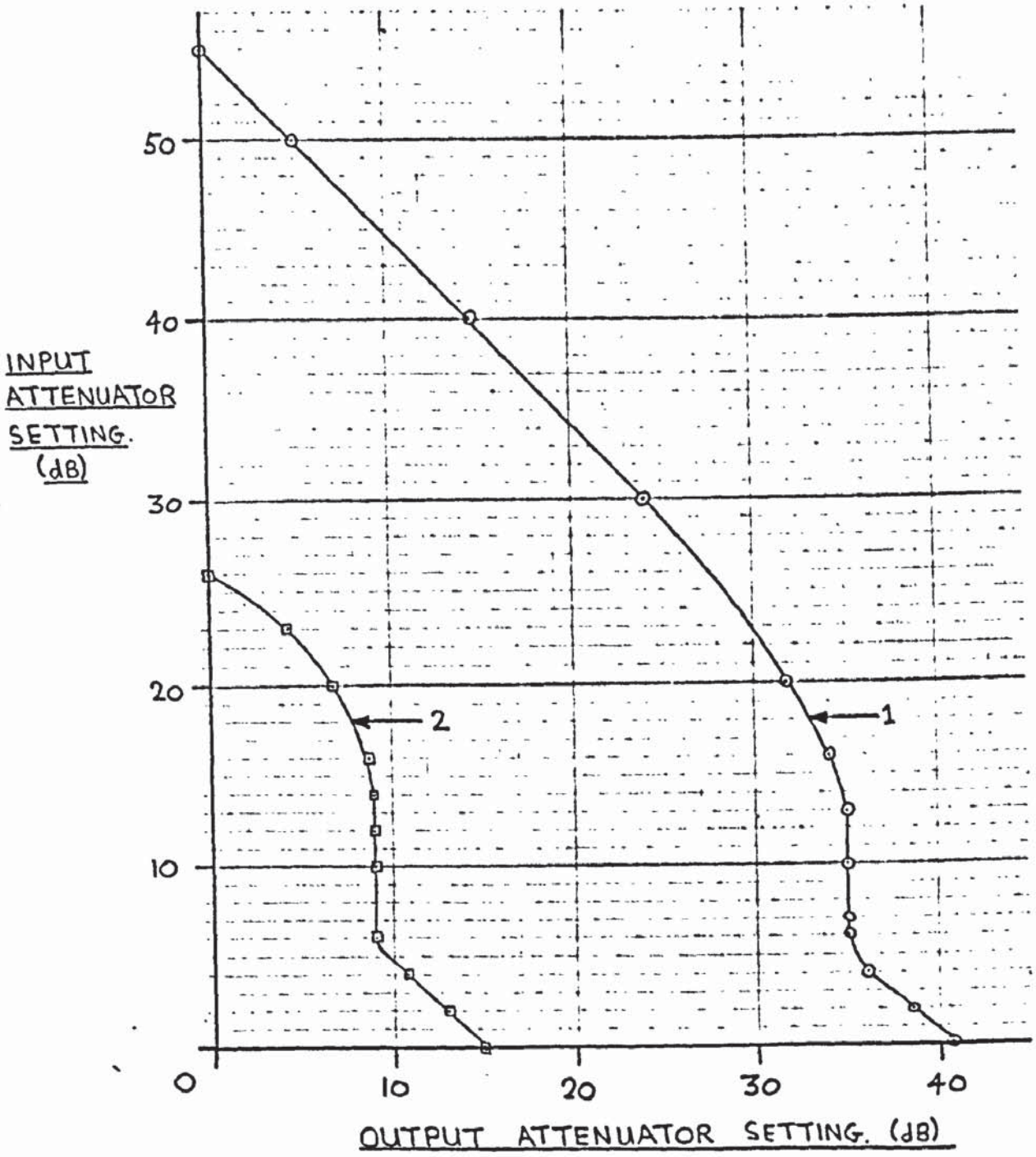

$\frac{\omega_c}{\omega} = 0.2$

FIELD : 1400 v cm.$^{-1}$

CURVE 1 : FUNDAMENTAL SIGNAL, 45 MHz.

2 : 3RD HARMONIC, 135 MHz.

FIG. 97. HARMONIC GENERATION AT 45 MHz.

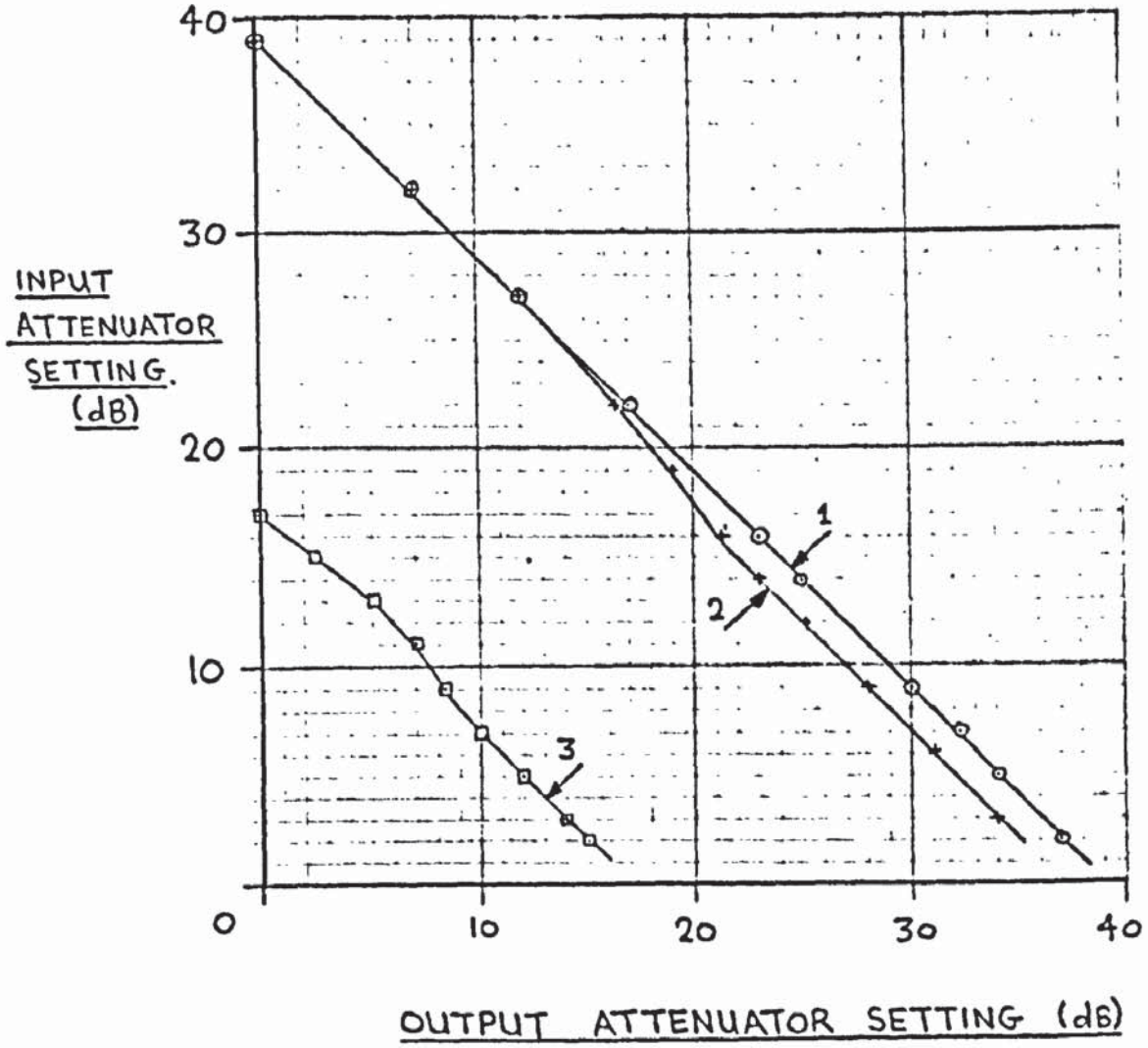

$\frac{3c}{13} = 0.05$

SMALL SIGNAL CROSS-OVER FIELD

CURVE 1 : DARK CONDITION CALIBRATION

2 : FUNDAMENTAL SIGNAL, 45 MH$_3$.

3 : 3RD HARMONIC, 135 MH$_3$.

FIG. 98. HARMONIC GENERATION AT 45 MH$_3$.

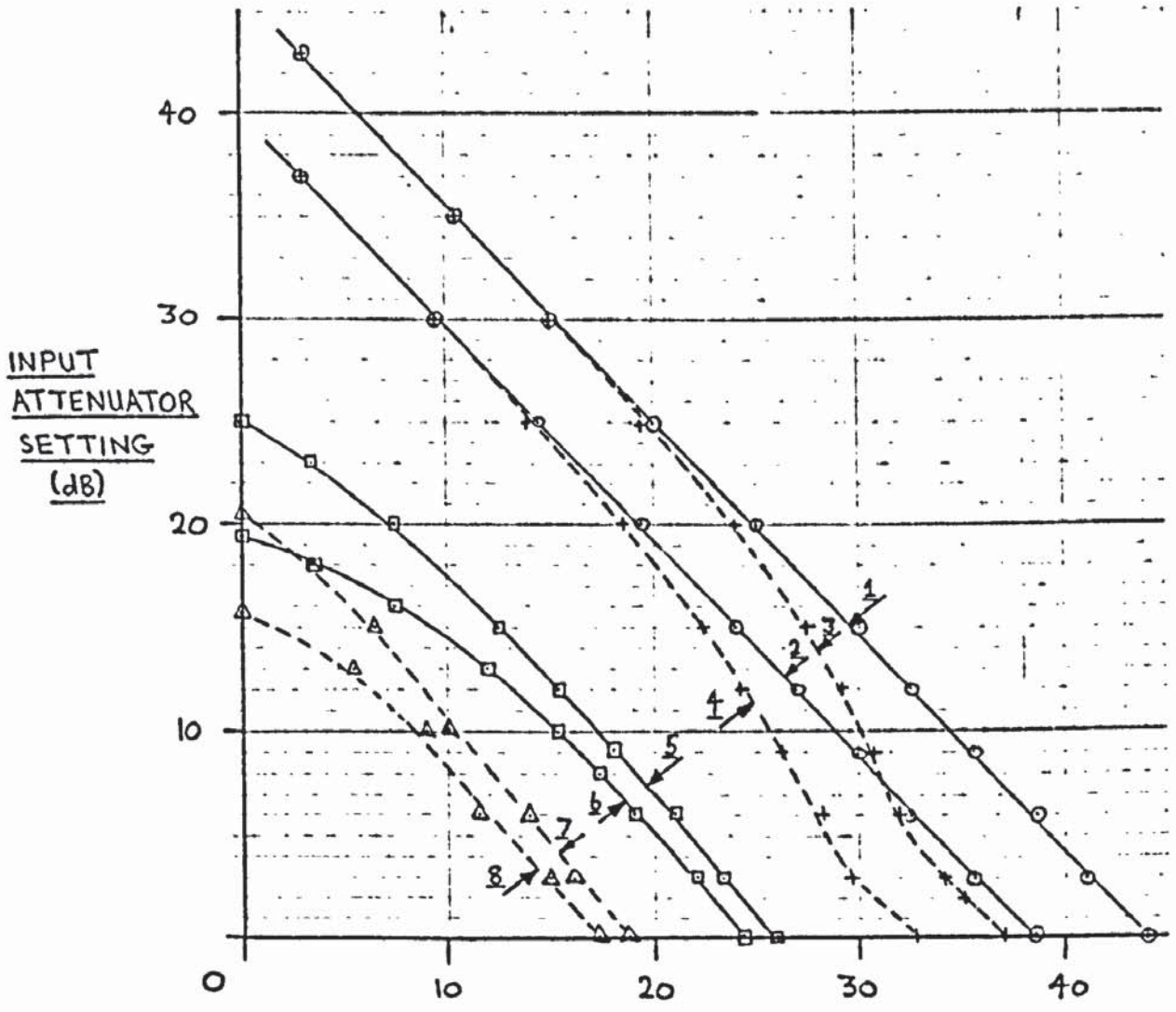

$\frac{3^{rd}}{1} = \cdot 60$

CURVES 1 & 2 : DARK CONDITION CALIBRATIONS.

3 : FUNDAMENTAL SIGNAL, 15 MH$_3$, 1600 V cm.$^{-1}$

4 : FUNDAMENTAL SIGNAL, 15 MH$_3$, CROSS-OVER FIELD.

5 : 3RD HARMONIC, 45 MH$_3$, 1600 V cm.$^{-1}$

6 : 3RD HARMONIC, 45 MH$_3$, CROSS-OVER FIELD.

7 : 5TH HARMONIC, 75 MH$_3$, 1600 V cm.$^{-1}$

8 : 5TH HARMONIC, 75 MH$_3$, CROSS-OVER FIELD.

FIG. 99 HARMONIC GENERATION AT 15 MH$_3$.

variation of the correct frequency.

The harmonics could not be detected at all when the CdS was maintained in the dark.

5.6.4. Measurement of acoustic power levels.

Using the insertion loss technique described in section 4.3.4 the peak ultrasonic power entering the CdS was measured for operation at 45 MHz. For this measurement the r.f. pulse generator was triggered at 50 p.p.s. and the half-height width of the r.f. pulse was adjusted to 1.4μS. The following average values were obtained:

	Experiment	Result
1.	Ouput from r.f. pulse generator: (Matec r.f. pulse unit, output on full.)	125 V_{pp} into 50 ohm
2.	Insertion loss through entire amplifier structure (CdS in dark)	53.7 db
3.	Amplifier asymmetry. Comparison of acousto-electric voltage for pulse propagation from end A and end B of amplifier	Acousto-electric signal 1.8 db larger for propagation of pulse from end B to end A than vice-versa.

Using the information above and the relevant diffraction loss information from table 4 the peak power entering the CdS was determined as:

Experiment	Result
Peak input acoustic power to CdS (from end B) at 45 MHz	1.15 W cm^{-2}

The acousto-electric comparison of powers presented in section 5.4. gave the acousto-electric voltages produced for operation at three frequencies. The attenuator settings, pulse width and resistivity of the CdS had been set to standard values in each case. The ratios of the acousto-electric voltages were directly proportional to the ratios of the input acoustic powers to the CdS for the three operating frequencies. The results of fig.72 are summarised in table 10.

Table 10 Acousto-electric comparison of powers

Frequency (MHz)	Acousto-electric voltage for 6 db attenuation	Power ratio (compared to 45 MHz)
45	.0058	1.0
75	.0108	1.86
15	.030	5.2

The acoustic powers entering the CdS for operation at 15 and 75 MHz were calculated to be:

operation at 15 MHz : peak acoustic power = 5.97 W c.m.$^{-2}$

operation at 75 MHz : peak acoustic power = 2.14 W c.m.$^{-2}$

The relationship between the input acoustic intensity

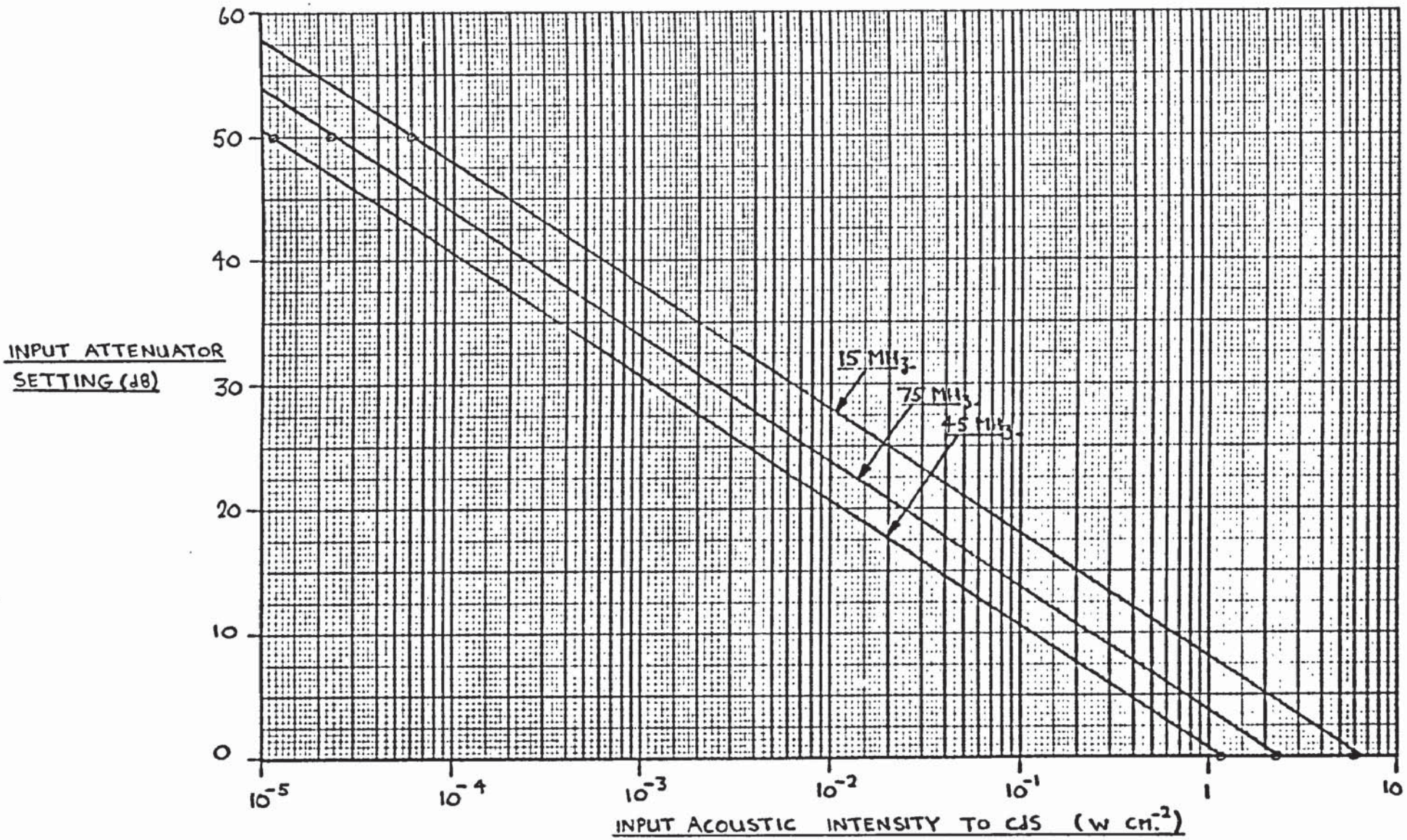

FIG. 100. INPUT ACOUSTIC INTENSITY AS A FUNCTION OF ATTENUATOR SETTING.

and the settings of the input attenuator is shown on fig.100.

SECTION 6

ANALYSIS OF RESULTS

6.1 Current-voltage characteristics

In the present research the investigation of the current-voltage characteristics of CdS crystals was carried out primarily to establish the suitability of particular CdS crystals for use in an amplifier structure. The following information can be obtained from a typical set of current-voltage characteristics such as fig. 47:

1) The range of crystal resistivities available by varying the illumination intensity.
2) The characteristics may be observed to be non-linear, which indicate that the acousto-electric effect is present.

The field at which the characteristics deviated from linearity in fig. 47 was about 1150 v $cm.^{-1}$ which implies an electron mobility of 152 $cm.^2$ $sec.^{-1}$ $volt^{-1}$ using a value of 1.75×10^5 cm. $sec.^{-1}$ for the shear wave velocity. Some crystals showed a marked change in the field necessary for the onset of non-linearity for different illumination levels, such that the critical field decreased for an increase in illumination level. This effect is due to the drift mobility of the electrons increasing when the electron density is made large compared to the trap density, Rose [107]. For the crystal used to obtain fig. 47 such trapping effects are not marked. The diffusion frequency ω_D is defined by the following equation,

Hutson and White [11]:

$$\omega_D = \left(\frac{q\beta}{f\mu}\right) v^2$$

q = electronic charge
f = trapping factor
β = $(kT)^{-1}$
μ = electron mobility
k = Boltzmann's constant
v = acoustic velocity
T = absolute temperature

Assuming $f = 1$, $T = 290^{\circ}K$, $v = 1.75 \times 10^5$ cm. sec.$^{-1}$ we obtain $\omega_D \simeq 8 \times 10^9$ sec.$^{-1}$. White[12] has shown that the angular frequency (ω) for maximum ultrasonic amplification is given by the equation:

$$\omega^2 = \omega_c \omega_D$$

ω_c = dielectric relaxation frequency.

Thus having determined ω_D for a particular crystal from the current-voltage characteristics the values of resistivity required to obtain large amplification coefficients over the frequency range of interest is calculated. The current-voltage characteristics indicate whether the crystal has a suitable resistivity range.

Figs. 45 and 46 show the current and voltage traces obtained by applying flat topped voltage pulses to a CdS crystal. The traces, which were obtained whilst illuminating the CdS uniformly, show a wide variation in the pattern of current decay for voltages greater than threshold. The current and voltage traces shown in fig. 51. were obtained for non-uniform illumination

and show that the pattern of current decay is sensitive to changes in the illumination conditions. The same CdS crystal was used for figs. 45, 46 and 51. These results suggest a useful preliminary test for the homogeneity of CdS crystals. If the oscillatory current decay for large applied voltage pulses and uniform illumination of a particular CdS crystal is altered by reversing the polarity of the voltage pulse then the crystal is asymmetrically inhomogeneous.

The current decay observed under high voltage conditions is due to the acousto-electric field produced by the acoustic flux built up by amplification of piezoelectric lattice waves, Hutson[35]. Fig. 49 shows the build up of the 45 MHz component of the wide-band acoustic flux and the corresponding current decay. The high correlation between the observed current decay and the production of an ultrasonic flux was demonstrated by fig. 50. In fig. 50a the current was decaying in an oscillatory manner whilst the acoustic flux was growing. In fig. 50b a large amplitude pulse of ultrasonics was injected into the CdS before the acoustic flux had reached large levels. The acousto-electric field of the injected pulse modified the initial current decay.

An investigation of the current-voltage characteristics of a particular CdS crystal, along the lines suggested in this section, was considered essential in view of the known wide variations in quality of commercially available CdS, before the crystal was used in the fabrication of an acoustic amplifier.

Suzuki's comment at the 1964 IEEE International Convention where he first presented the trapping theory summarised the state-

of-the-art at that date. One had to find a piece of "good natured CdS" in order to produce a successful amplifier and that kind of material was seldom found and then only by luck. During the present research an investigation of the current-voltage characteristics of several CdS crystals resulted in a successful choice of a crystal for fabrication into an amplifier structure.

6.2. Small signal attenuation and amplification

The general shape of the attenuation-field curves obtained for operation at 15, 45 and 75 MHz, figs. 52 - 54, was as expected from White's amplification theory. With the crystal in the dark no variation in the level of acoustic transmission was observed for applied voltages. With the crystal illuminated the attenuation initially increased to a maximum when the applied voltage was increased. For larger applied voltages the attenuation decreased until for a sufficiently large voltage the level of acoustic transmission was the same as that obtained with the CdS in the dark. This was the cross-over condition. For larger applied voltages the ultrasonics were amplified and generally there was a voltage corresponding to maximum amplification. For an increase in the applied voltage beyond this value the amplification was reduced and the curve asymptotically approached the dark condition propagation level. Figs. 55 - 57 show the asymptotic approach to the dark condition signal for negative voltages.

To characterise the extent of trapping effects on the attenuation-field curves the trapping parameter 'a' was evaluated by noting the ratio of maximum amplification (α' max) to maximum

attenuation (α'_{min}) and using the following equation (which was derived in section 2.3):

$$\left| \frac{\alpha'_{max}}{\alpha'_{min}} \right| = \frac{\sqrt{1 + a^2} - a}{\sqrt{1 + a^2} + a}$$

Table 11 gives the values of 'a' for operation at 15 and 45 MHz as derived from figs. 52 and 53.

Table 11

Frequency (MHz)	conductivity $ohms^{-1} cm.^{-1}$	$\left\|\frac{\alpha'_{max}}{\alpha'_{min}}\right\|$	'a'
45	5.9×10^{-6} (1)	1.0	0
45	1.2×10^{-5} (2)	.89	.06
45	2.4×10^{-5} (3)	.92	.045
45	4.7×10^{-5} (4)	.86	.075
45	7.1×10^{-5} (5)	.87	.070
45	9.5×10^{-5} (6)	.87	.070
15	as (1)	.79	.115
15	as (2)	.71	.17
15	as (3)	.76	.135
15	as (4)	.71 *	.17
15	as (5)	.69 *	.185
15	as (6)	.64 *	.225

* The experimental restriction of fields to 2000 v $cm.^{-1}$ to

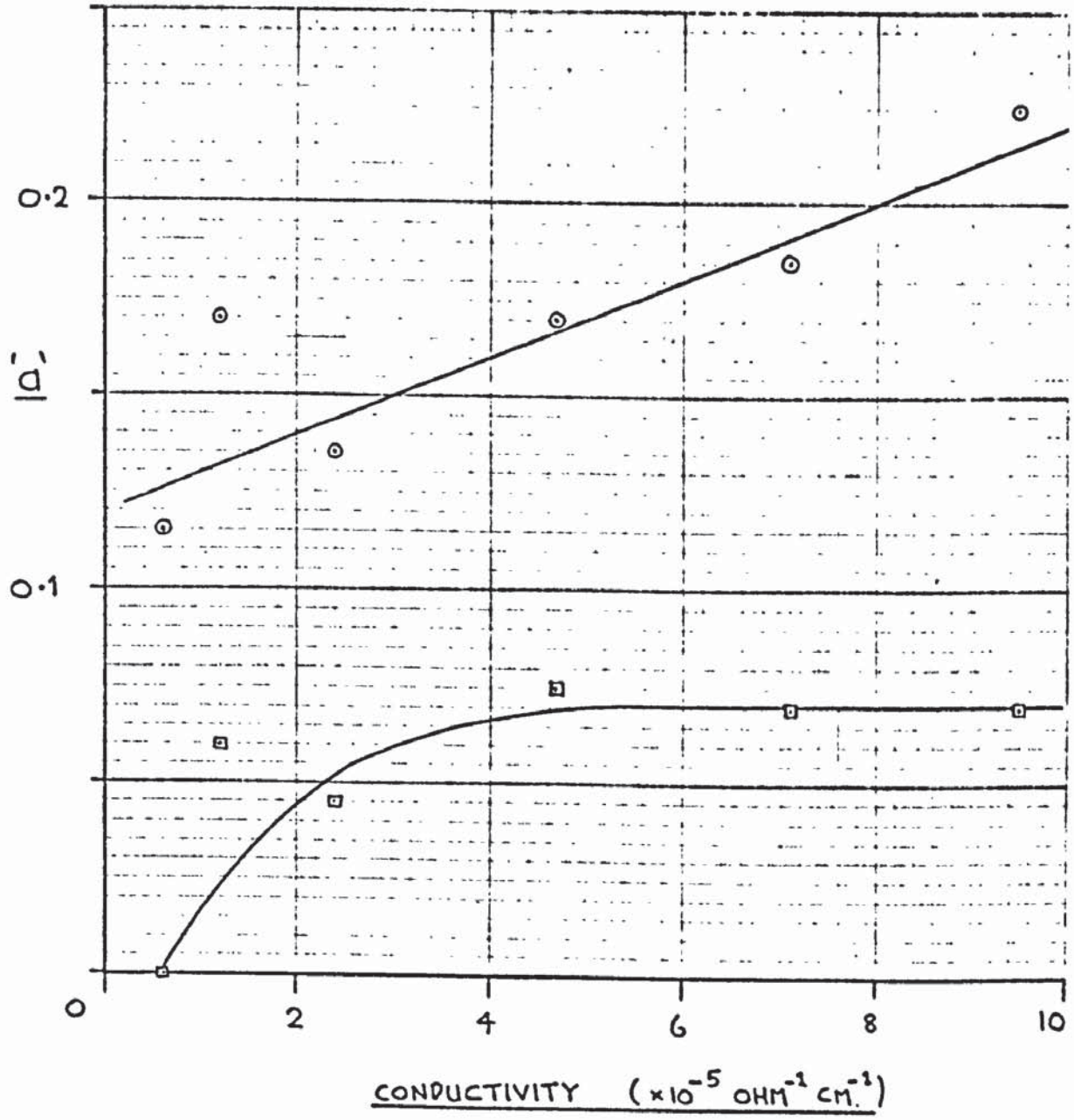

15 MHz.

45 MHz.

FIG. 101. TRAPPING PARAMETER 'a' VERSUS CRYSTAL CONDUCTIVITY.

prevent crystal breakdown is not sufficient to define (α'_{max}) accurately in these cases.

The values of 'a' are plotted against crystal conductivity in fig. 101 for operation at 15 and 45 MHz. The effects of trapping on the asymmetry of the attenuation-field curves was more marked at 15 MHz than 45 MHz. The trapping theory predicts that 'a' is nearly proportional to ω^{-1} (see section 2.3). This relationship was observed to be obeyed approximately in fig. 101.

The other trapping manifestation, change of cross-over field with conductivity, was also much more marked at 15 MHz. At 15 MHz the cross-over field varied from 1000 to 1300 v $cm.^{-1}$ (fig.52) whilst at 45 MHz the variation was from 1040 to 1150 v $cm.^{-1}$ (fig.53)

At frequencies from 105 to 345 MHz the change in cross-over field with conductivity was small. It should be noted however that the range of conductivities used was somewhat less than in the experiments at 15 to 75 MHz. At 75 MHz the asymmetries in the attenuation-voltage curves were not consistent. With $\frac{\omega_c}{\omega} = .06$ the value of the asymmetry ratio was 0.72 whilst at $\frac{\omega_c}{\omega} = .015$ it was 2.3 which meant that the maximum amplification was larger than the maximum attenuation. Similarly the variation in cross-over field was unusual in that cross-over was reached at 1000 v $cm.^{-1}$ for weak illumination and 1060 v $cm.^{-1}$ for strong illumination. It has not been possible to explain this pattern of behaviour.

The trapping effects observed with this crystal of CdS were small compared to those reported by Ishiguro et al [14].

The graphs of attenuation versus conductivity for no

applied voltages, figs. 63 and 64 were used to estimate the value of the electro-mechanical coupling coefficient of the CdS by using White's theory.

The equation derived by White for the amplification coefficient α is given below:

$$\alpha = \frac{K^2 \omega_c}{2V_s \gamma} \left[\frac{1}{1 + \frac{\omega_c^2}{\gamma^2 \omega^2} \left(1 + \frac{\omega^2}{\omega_c \omega_D} \right)^2} \right]$$

The meanings of the symbols are given in section 2.1.

For zero applied drift field $\gamma = 1$

For low light levels we have:

$$\frac{\omega_c^2}{\omega^2} \ll 1$$

and

$$\frac{\omega_c}{\omega} > \frac{\omega}{\omega_D} \quad \text{i.e.} \quad \frac{\omega^2}{\omega_c \omega_D} < 1$$

Under these conditions α is given by:

$$\alpha = \frac{K^2}{2} \frac{\omega_c}{V_s} \qquad \ldots\ldots\ldots\ldots .6.1$$

Thus, for low levels of illumination and no applied voltage, α is expected to be proportional to the crystal conductivity and independent of the ultrasonic frequency.

It was observed, figs. 63 and 64, that the attenuation was proportional to conductivity for small illumination levels. This condition was accurately obeyed for attenuation of up to about 6 db at 15 MHz, and 11 db at 45 and 75 MHz. Over these ranges the ratio of attenuation to conductivity was almost the same for each frequency of operation. Theoretical curves are plotted on figs. 63 and 64 in addition to the experimental curves. The theoretical curves were obtained using White's theory. Values of the square of the electromechanical coupling coefficient were chosen to obtain reasonable agreement with the slope of the experimental curves near the origin, for each operating frequency. The values of K^2 used to obtain a reasonable match were:

FREQUENCY (MHz)	K^2
15	.0112
45	.0107
75	.0097

An average value for K^2 was .0105. This values for K^2 is considerably below the figure of .0355 quoted by Jaffe et al[5]. Wilson [63] obtained an initial value of K^2 = .005 for a CdS crystal produced by Eagle Picher Co. He observed that the magnitude of the electro-mechanical coupling coefficient increased when the CdS was annealed and was able to correlate the increase in K with a reduction in the number of etch pits observed for a given area on the [0001] face. The etch pits were thought to indicate a localised reversal of the 'C' axis. Although a similar annealing procedure was not carried out on the CdS crystal used in the present research

it seems probable that it contained a similar number of the crystal defects observed by Wilson.

In section 2.3 the value of γ giving maximum attenuation and amplification was derived using the White theory. It was shown that:

$$\gamma = \pm \left(\frac{\omega_c}{\omega} + \frac{\omega}{\omega_D} \right)$$

For operation at 15 MHz we have the condition:

$$\frac{\omega_c}{\omega} >> \frac{\omega}{\omega_D}$$

so that

$$\gamma = \pm \frac{\omega_c}{\omega}$$

In fig.63 the experimental curve has reached a peak when $\frac{\omega_c}{\omega} \simeq 1.2$. For this curve $\gamma = 1$ (no applied voltage). There is reasonable agreement between experiment and White's theory for the variation of no-voltage attenuation with crystal conductivity.

Fig.102 shows the experimentally observed attenuation - field curve for operation at 45 MHz such that $\frac{\omega_c}{\omega} = .20$. The electron mobility was determined from the cross-over field and used to calculate ω_D by the formula given in section 6.1. Attenuation-field curves calculated for three values of $\frac{\omega_c}{\omega}$ for operation at 45 MHz using White's theory are shown on fig.102. A value of .0105 was used for K^2. The values of maximum attenuation and amplification predicted by White's theory were greater than experimentally observed. Also the fields required experimentally

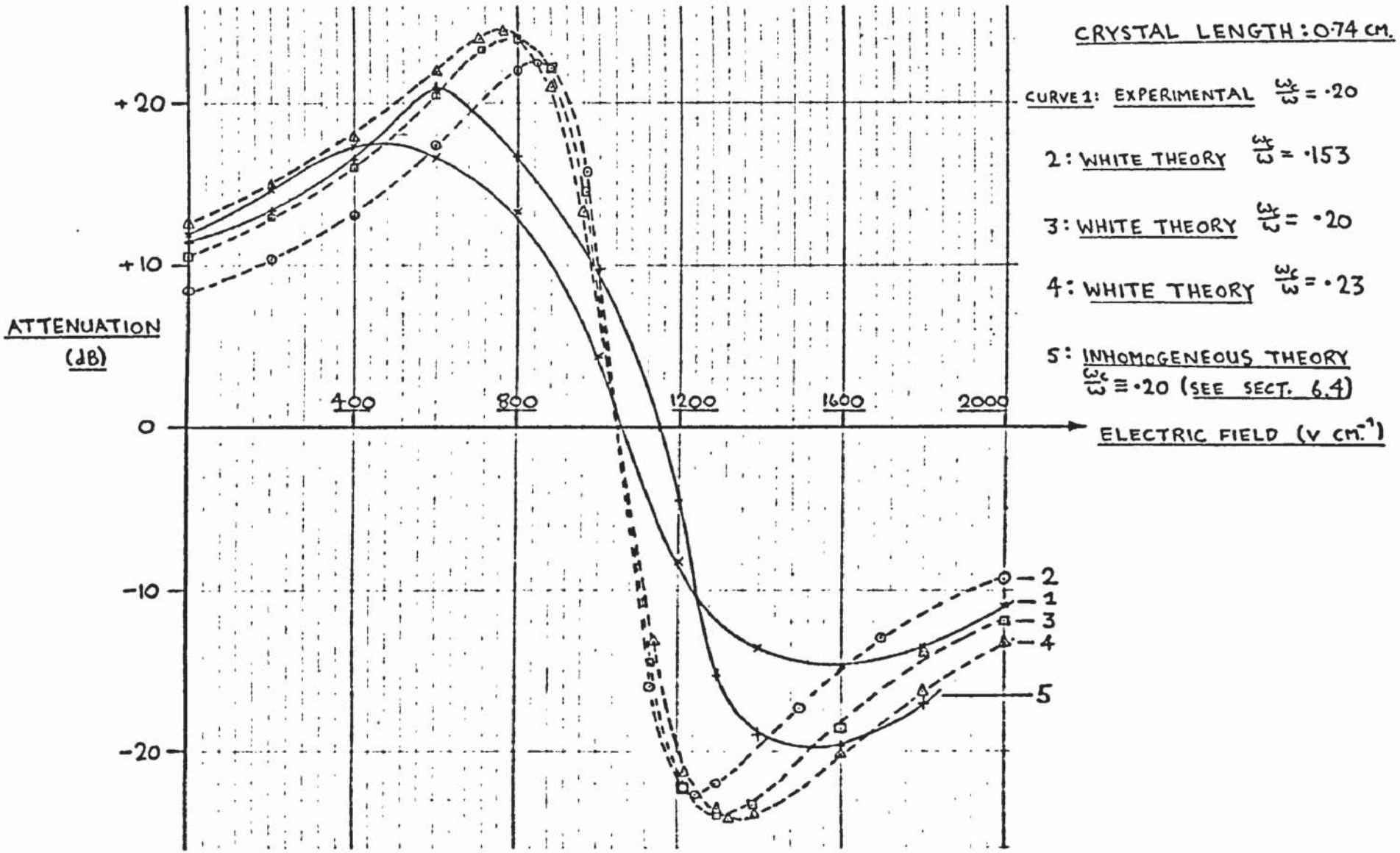

FIG. 102. ULTRASONIC ATTENUATION v. DRIFT FIELD AT 45 MHz.

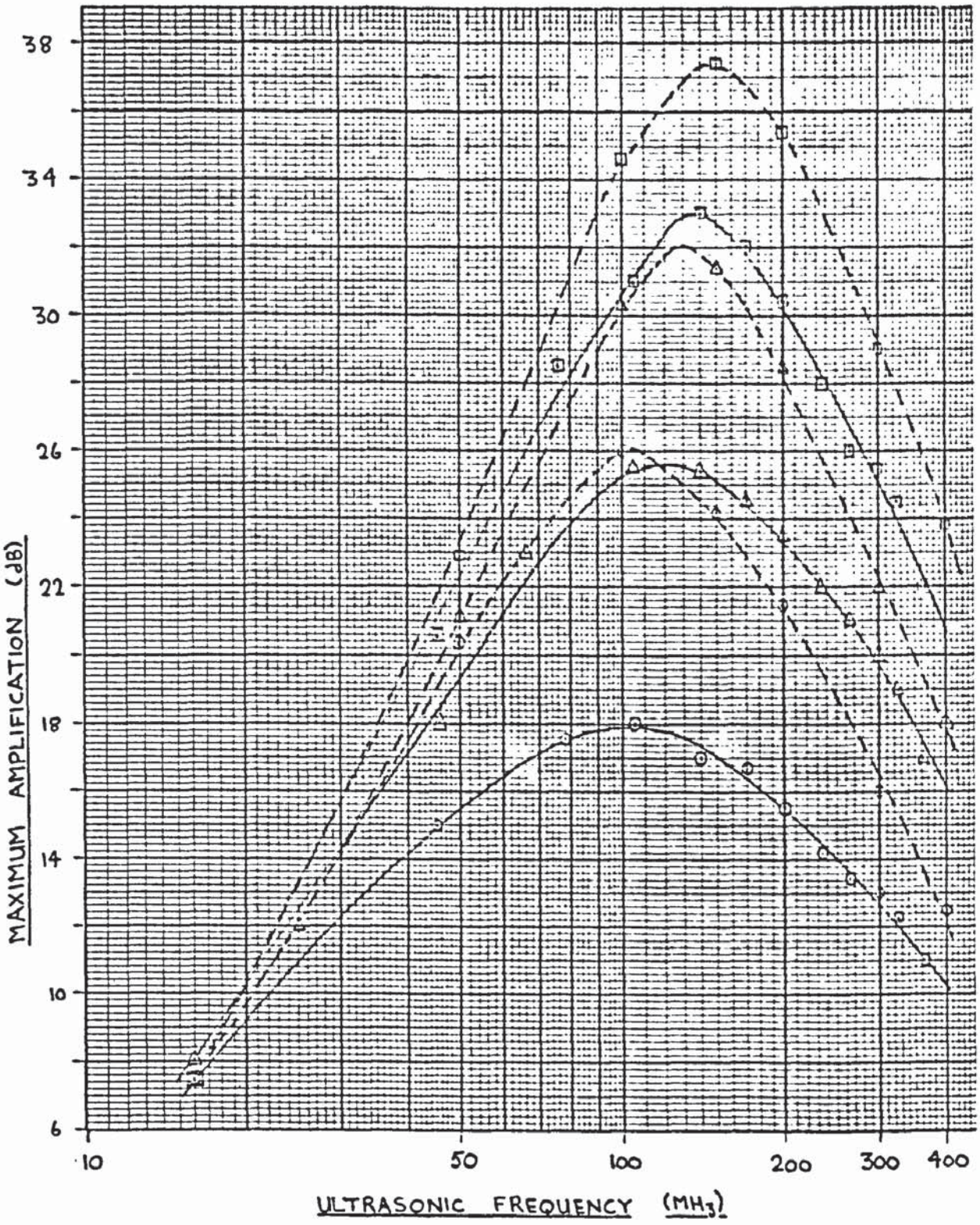

CRYSTAL LENGTH : 0·74 cm.

EXPERIMENTAL.	RESISTIVITY (Ω-cm).	THEORETICAL.
—□—	1.05×10^4	--□--
—△—	1.40×10^4	--△--
—○—	2.11×10^4	--○--

$K^2 = .009$

FIG. 103. MAXIMUM AMPLIFICATION v. ULTRASONIC FREQUENCY.

for maximum attenuation and amplification were smaller and larger respectively than predicted by Whites' theory. Earlier in this section it was shown that the trapping effects were small for operation at 45 MHz i.e. the effects of trapping produced only a small asymmetry in the attenuation-field curve. As shown in fig. 7 for the case of high conductivity the trapping effects cause only a very small change to the fields required for maximum attenuation and amplification even when the asymmetry is much larger than that of the experimental curve of fig. 102. It is believed that the deviation of the experimentally determined curve from that expected from theoretical considerations was at least partially due to the presence of regions of high resistivity in the CdS near the electrical contact areas. The experimental investigation of these regions is discussed in section 6.4. A theoretical curve is shown on fig. 102 in which the presence of the high resistivity regions has been allowed for. This curve is somewhat closer to the experimentally determined curve than the curves given by White's theory assuming a homogeneous crystal.

Figs. 52 - 54 and 58 - 62, which show the experimentally observed values of amplification achieved for ultrasonics having frequencies between 15 and 345 MHz, were used to produce fig. 103 in which the maximum amplification achieved at each frequency for a given crystal resistivity is plotted against frequency. The experimental curves had maximum values of amplification at the following frequencies:

Crystal Resistivity (ohm-cm)	Frequency for max. amplification (MHz)
1.05×10^4	103 ± 3
1.40×10^4	127 ± 5
2.11×10^4	140 ± 5

White's theory predicts that the value of the electron drift parameter γ needed for maximum amplification is given by the following equation:

$$-\gamma = \left(\frac{\omega_c}{\omega} + \frac{\omega}{\omega_D} \right) \quad \ldots\ldots\ldots\ldots\ldots 6.2$$

Substituting this value of γ into the White equation for the attenuation coefficient yields the following equation for the maximum amplification coefficient (α min):

$$\alpha_{min} = \frac{K^2}{4V_s} \left[\frac{\omega}{1 + \frac{\omega^2}{\omega_c \omega_D}} \right] \quad \ldots\ldots\ldots\ldots 6.3$$

This equation was used to calculate the three theoretical curves on fig.103. Values of .009 for K^2 and 7.1×10^9 sec.$^{-1}$ for ω_D were used in the calculations. The theoretical curves correspond to greater amplification than observed experimentally, but there was considerable agreement between theory and experiment in the values of frequency corresponding to maximum amplification. By differentiating equation 6.3 with respect to frequency and setting the resultant expression equal to zero the following equation giving the frequency

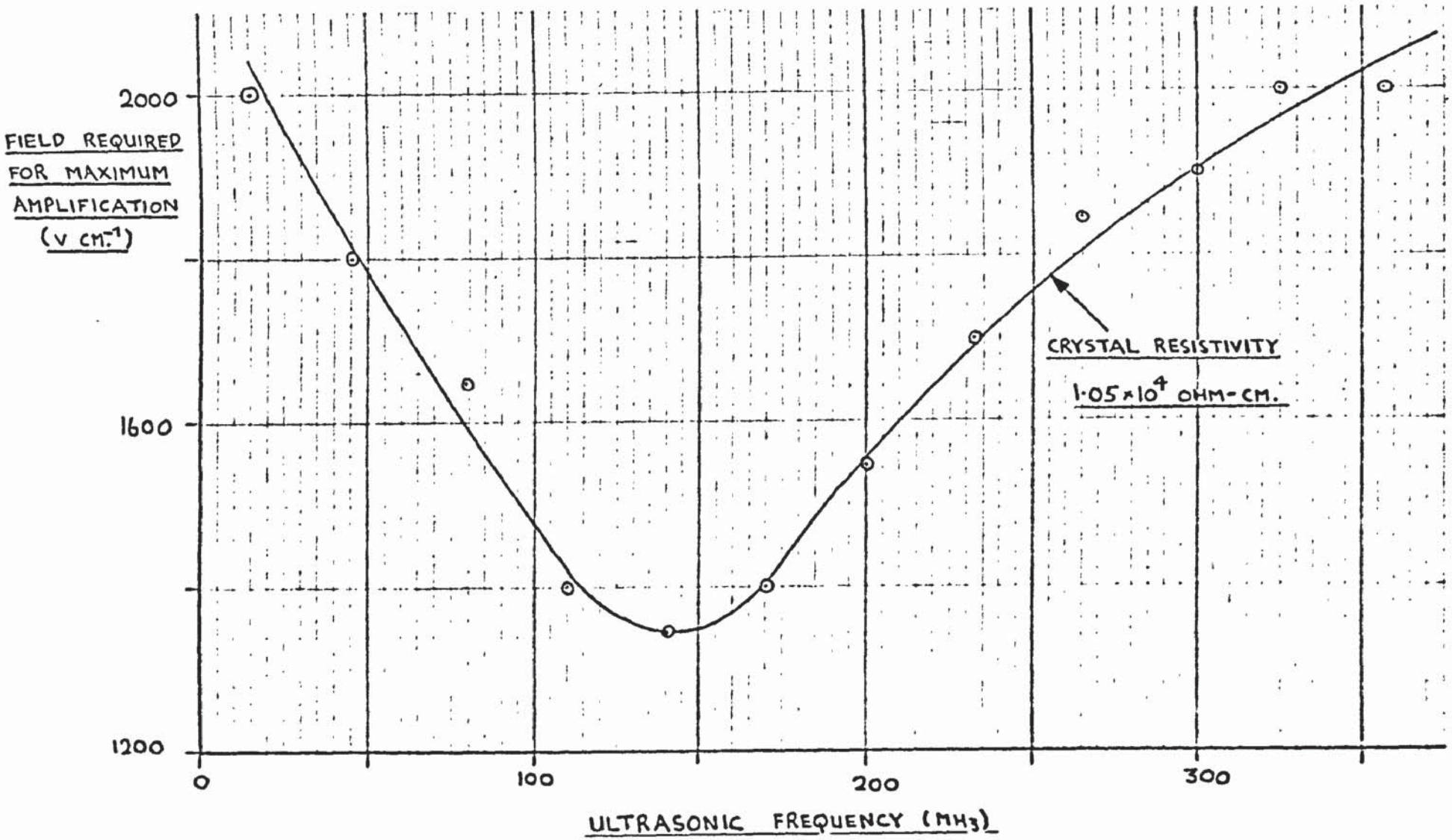

FIG. 104. ELECTRIC FIELD REQUIRED FOR MAXIMUM AMPLIFICATION. (EXPERIMENTAL)

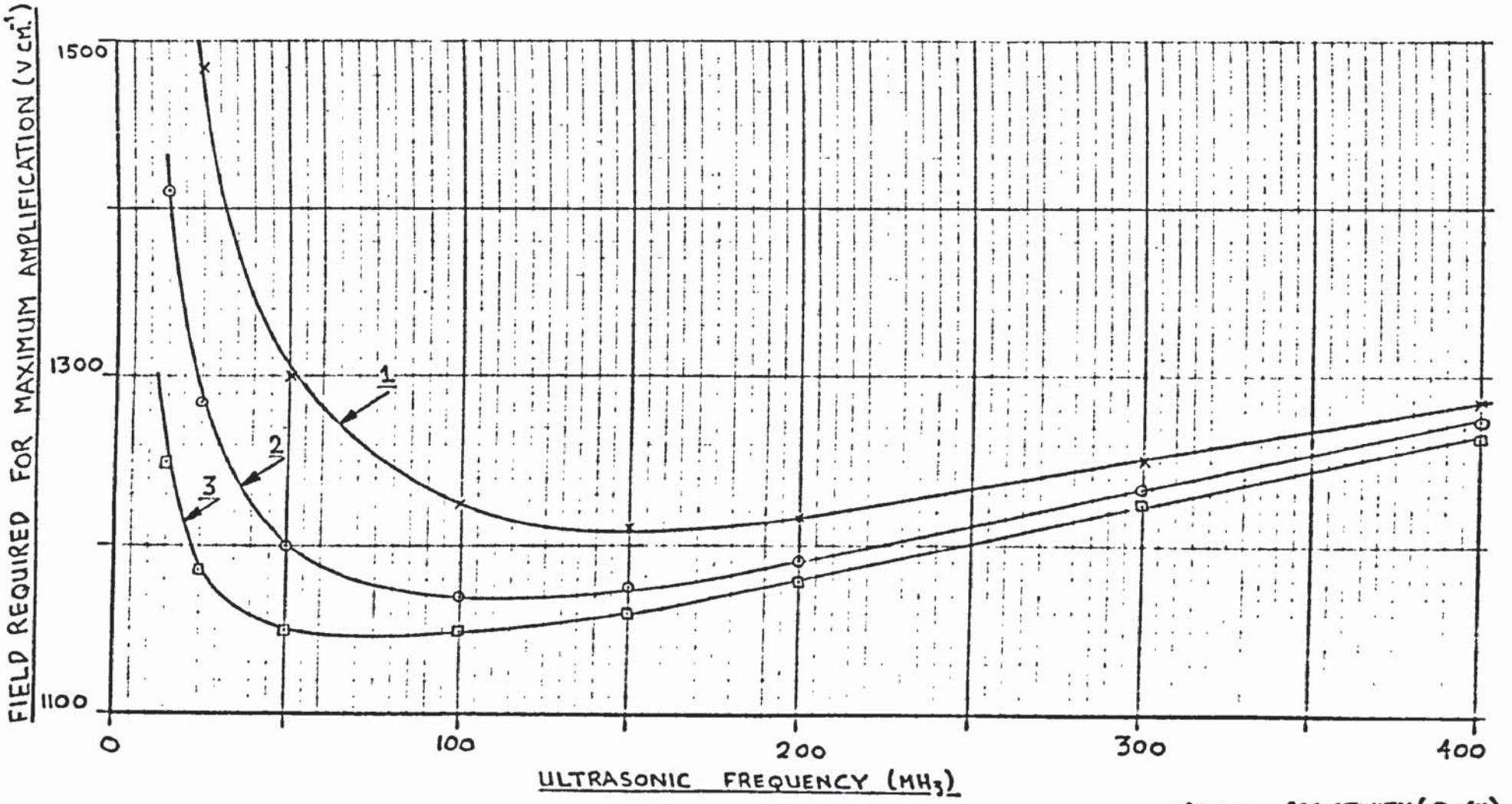

FIG. 105. ELECTRIC FIELD REQUIRED FOR MAXIMUM AMPLIFICATION (THEORETICAL)

for maximum amplification (ω_{max}) is obtained:

$$\omega^2_{max} = \omega_c \omega_D$$

Using the experimental values of ω_c and ω_D the following values of (ω_{max}) were obtained using the formula above:

Crystal resistivity (ohm-cm)	ω_{max} (MHz)
1.05×10^4	104
1.40×10^4	127
2.11×10^4	147

It can be seen that these values correspond well with those obtained experimentally, fig. 103. Fig. 104 shows the values of electric field that were needed to obtain maximum amplification at various frequencies. Fig. 105 shows theoretical curves, calculated using equation 6.2., of the field needed for maximum amplification. The experimental curve shows a minimum at the frequency corresponding to maximum amplification, as does the theoretical curves. The experimentally observed fields for (α_{min}) are larger than expected from White's theory and in particular the fields required for (α_{min}) for frequencies greater than (ω_{max}) are considerably in excess of theoretical predictions. The experimental curve plotted on fig. 104 corresponded to a crystal resistivity of 1.05×10^4 ohm-cm. Figs. 52 - 54 and 58 - 62 show that the curves of field necessary for maximum amplification versus frequency for resistivities of 1.40 and 2.11×10^4 ohm-cm. were almost identical to that obtained for a resistivity of 1.05×10^4 ohm-cm. Although it is considered that the presence of high resistivity regions at either end of the CdS caused the value of field required for (α_{min}) to be greater than expected from White's theory for a

uniform crystal it has not been possible to explain the variation of field for (α_{min}) with frequency.

To summarise the findings of this section it has been shown that the crystal used had an electro-mechanical coupling coefficient about 30% of that reported by Jaffe et al [5] but comparable to the pre-annealing result of Wilson [63]. The extent of trapping, as characterised by asymmetry in the attenuation-field curves, was not large even at the lowest frequency used. Whilst many features of the attenuation-field and no-voltage attenuation-conductivity curves were shown to be in agreement with White's theory there were several observations which could not be satisfactorily explained.

6.3. Acousto-electric voltages

Fig. 65 shows the measured acousto-electric voltage V_{ae} to be proportional to the input acoustic power for a given value of no-voltage attenuation. For convenience both V_{ae} and the input acoustic power are given in logarithmic form. The Weinreich relationship derived in section 2.2. is given below:

$$E_{ae} = \frac{2\alpha I}{n_{oq} v_s}$$

E_{ae} is the acousto-electric field produced across an element of the crystal having an acoustic attenuation coefficient α and an acoustic intensity I. E'_{ae} is the acousto-electric voltage produced across the whole crystal.

$$E_{ae} = k_1 \, E'_{ae}$$

k_1 is a constant which is determined by the time duration of the acoustic pulse.

$$E'_{ae} = k_2 V_{ae}$$

k_2 is a constant.

As shown on fig.66 E'_{ae} is the acousto-electric voltage developed across the crystal and V_{ae} is the value presented to the oscilloscope by the resistance network. For constant values of α and n_o we have

$$V_{ae} = k_3 I \qquad k_3 \text{ is a constant}$$

$$\log_{10} V_{ae} = \log_{10} k_3 + \log_{10} I$$

Hence the Weinreich equation, is consistent in form with the observed relationship between the input acoustic power and the measured acousto-electric voltage for a given no-voltage attenuation.

Fig.67 was obtained from fig. 65 by reading off values of V_{ae} for different values of no-voltage attenuation for given values of input acoustic power. The graph shows V_{ae} to be proportional to α for small values of α and gradually becoming less sensitive to changes in α. This behaviour can be explained by considering the equivalent circuit for the generation of acousto-electric voltages, given below:

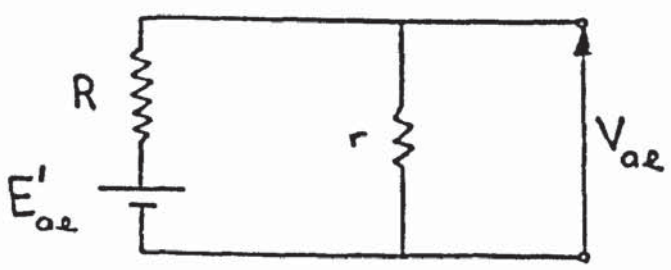

The CdS crystal in which the acousto-electric voltage was generated was represented by a battery of e.m.f. E'_{ae} and a series resistance R which was equal to the resistance of the CdS. The voltage V_{ae} was measured across a resistance r. We have the relationship

$$V_{ae} = \frac{r}{R+r} E'_{ae} \quad \ldots\ldots\ldots\ldots 6.5$$

The two cases of interest are $r << R$ and $r >> R$.

Case 1 $r << R$

we have $V_{ae} = \frac{r}{R} E'_{ae}$

$$= k_4 E'_{ae} \sigma \quad \ldots\ldots\ldots\ldots 6.6.$$

$\frac{1}{R}$ is proportion to σ

σ = crystal conductivity

k_4 is a constant

The Weinreich relationship is:

$$E_{ae} = \frac{2I\alpha}{n_{oq} v_s}$$

$$= k_1 E'_{ae}$$

$$\text{hence } \alpha I = \frac{k_1 E'_{ae} n_{oq} v_s}{2}$$

$$= k_5 E'_{ae} \sigma \qquad (\sigma = n_{oq} \mu)$$

k_5 is a constant

Using eqn. 6.6. we have:

$$\alpha I = k_6 V_{ae} \qquad k_6 \text{ is a constant}$$

Hence for constant power the measured acousto-electric voltage should be proportional to the attenuation, provided $r \ll R$.

Case 2. $r \gg R$

We have $V_{ae} = E'_{ae}$ using eqn. 6.5.

and $\alpha I = k_7 E'_{ae} \sigma$ k_7 is a constant

Equation 6.1.(section 6.2.) shows that White's theory predicts the no-voltage attenuation to be proportional to conductivity and fig.64 show this relationship to be valid experimentally for attenuations up to about 11 db at 45 MHz

Hence $I = k_8 V_{ae}$

k_8 is a constant

The measured acousto-electric voltage should be independent of the attenuation provided $r \gg R$.

The acousto-electric voltages shown on fig.67 were measured across about 100k Ω , fig.66. For $\alpha = 1.0$ the crystal resistance was 450 kΩ, whilst for $\alpha = 14$ the crystal resistance was 30 kΩ . Thus for $\alpha < 3$ db we have $r < R$ and V_{ae} is proportional to α . For $\alpha > 5$db $r > R$ and V_{ae} becomes decreasingly sensitive to changes in α . Thus the observed acousto-electric voltage behaves in the manner expected from theoretical considerations.

The variation of V_{ae} with α was further investigated in two sets of experiments in which the value of r was 1 M Ω and 4.3 kΩ . Fig.68 shows the variation of V_{ae} with input acoustic power in the two cases. Fig.69 shows the variation

of V_{ae} with α for a given input power. With r having a value of 4.3 k Ω, V_{ae} was proportional to α as expected. For α = 17.8db, R = 21 k Ω. With r having a value of 1 M Ω, V_{ac} was observed to be nearly independent of α . Thus the variation of V_{ac} with α for a given acoustic power depends on the value of the measuring resistor compared to the crystal resistance.

The development of the acousto-electric voltage in a CdS crystal shows directly the strong coupling between acoustic waves and electrons. The phenomena was utilised in the investigation of ultrasonic attenuation and amplification to compare the acoustic power entering the crystal for operation at different frequencies. It was also used in the insertion loss technique measurement of input power for determining the extent of asymmetry in the acoustic amplifier and transformers.

A measuring resistor of 4.3kΩ was used whilst V_{ae} was measured as a function of input acoustic power and attenuation for operation at 15, 45 and 75 MHz. The results, shown on figs. 70 and 71, have been used to prepare fig. 72 which shows V_{ae} against α for a given setting of the input attenuator. The values of α were chosen to be 8.5 db or less and for this condition the constant of proportionality between α and σ is sensibly constant for the three frequencies used. For a given value of α and σ the Weinreich equation reduces to:

$$V_{ae} = k_9 I \qquad k_9 \text{ is a constant.}$$

From fig. 72 the values of V_{ae} for α = 6db are:

FREQUENCY MHz	V_{ae}	Ratio of V_{ae} compared to 45 MHz case
15	.030	5.2
45	.0058	1.0
75	.0108	1.86

The Matec r.f. generator used in these experiments had separate oscillator coils for each of the three frequencies used above and it was not surprising that its output varied for each frequency used. The acousto-electric comparison of input power was used in conjunction with the insertion loss determination of input acoustic power at 45 MHz to estimate the input power level for operation at 15 and 75 MHz.

6.4. Voltage pulse phasing

As shown on fig. 74 the voltage pulse had a risetime of about 0.3μS and a fall time of about 5μS. When a voltage pulse having an 8.5μS flat top was applied to the CdS 22μS before the ultrasonic signal reached the output transducer then the voltage pulse had decayed from its peak value for over 5μS before the ultrasonics entered the CdS. The ultrasonic propagation time for one buffer and the CdS was 8.15μS. In fig. 77 the detected signal height for an 8.5μS voltage pulse applied 22 μ S before the ultrasonics were detected corresponded to ultrasonic propagation through the CdS with no-applied voltage. The same voltage pulse

applied 18 μ S before signal detection provided a field that averaged less than the pseudo cross-over field (see below) during the ultrasonic propagation through the CdS. Accordingly the detected signal was smaller than in the previous case. The pseudo cross-over field is defined in this work as that field on the attenuation-field curve which corresponds to an attenuation equal to that for no applied field. When the voltage pulse was applied 16.6 μS before signal detection the average field applied to the CdS during ultrasonic propagation through it corresponded to the pseudo cross-over field. In this case the level of ultrasonics transmitted through the CdS corresponded to the case of no applied voltage that was achieved by applying the voltage pulse 22μ S before signal reception. For smaller time intervals (T) between the application of the voltage pulse and the detection of an ultrasonic signal the average field during ultrasonic propagation exceeded the cross-over field.. When T was 12 μS the field was at its full value during the propagation of ultrasonics through the crystal. The difference between the signal heights corresponding to T = 22 and T = 12 μS was 16.5 db. For this experiment $\frac{\omega_c}{\omega} = .18$. Fig. 53 shows that the difference in attenuation for the $\frac{\omega_c}{\omega} = .20$ case for zero applied field and 1200V cm.$^{-1}$ was 19.5 db.

For voltage pulses that were of shorter duration than the time of acoustic propagation in the CdS the amplification obtained was not as large as in the previous case e.g. fig. 77.

If the CdS crystal was markedly inhomogeneous in its amplification properties and for example one half amplified more

strongly than the other half then the position of maximum amplification achieved with short voltage pulses would be different from that obtained if the crystal was homogeneous. Very short and well defined voltage pulses would have to be used if this method of assessing the degree of crystal inhomogeneity was to be sensitive to localised variation in amplification properties. Fig. 77 shows that the 2.0 μS voltage pulse had to be applied 7 μS before signal detection to achieve maximum amplification. Hence the voltage pulse was applied while the pulse of ultrasonics traversed the middle region of the CdS. For a uniform crystal the maximum amplification achieved by a short drift field pulse of a given length would be expected when the pulse was applied at this time. Thus the voltage phasing experiment, the results of which are shown in fig. 77, was not sensitive enough to provide information about the degree of crystal inhomogeneity.

As described in section 5.5.3 a variation of the above experiment was devised in order to establish the degree of homogeneity of the CdS crystal. By varying the time of application of an 8.0 μS voltage pulse with respect to the entry of the pulse of ultrasonics into the CdS an interesting series of curves were obtained, fig.78. The ultrasonic pulse length used was 0.5 μS. For a field of 400 V cm.$^{-1}$ the curve representing signal height versus time of pulse application rose in height from one level to another without any "overshoot". The curve for 600 v cm.$^{-1}$ initially dipped down before climbing to a higher level then falling back to a plateau. For fields near the pseudo cross-

over field the curves showed the largest "overshoot". For a field of 1400 v $cm.^{-1}$ the curve was rather like a mirror image of the 400 v $cm.^{-1}$ case. It was established experimentally that identical curves were obtained if the ultrasonics were propagated in the reverse direction and the polarity of the voltage pulse was reversed. Using negative voltages the curves obtained did not have any overshoot. The term negative voltages refers to voltages which cause the electrons to flow in the opposite direction from that of the acoustic wave. Such voltages produce attenuation-field curves of the type shown in figs. 55 - 57. The use of positive voltages produces electron drift in the direction of the acoustic wave and can lead to acoustic amplification, e.g. figs. 52-54. The attenuation produced by negative voltages asymptotically approaches the dark propagation level for large voltages, whereas for positive voltages the asymptotic approach to the dark level is preceded by regions of enhanced attenuation and amplification.

It was thought that crystal inhomogeneity was responsible for the observed effects. If large electric field variations were present in the CdS then for positive applied voltages the acoustic wave would be attenuated at markedly different rates in different regions. For negative applied voltages the variation in the attenuation of different regions would be less marked, for a given field variation, and no region could amplify the acoustic wave. To experimentally test the possibility that the observed effects, fig. 78, were caused by crystal inhomogeneity, neutral density filters, that transmitted 50% of incident light, were

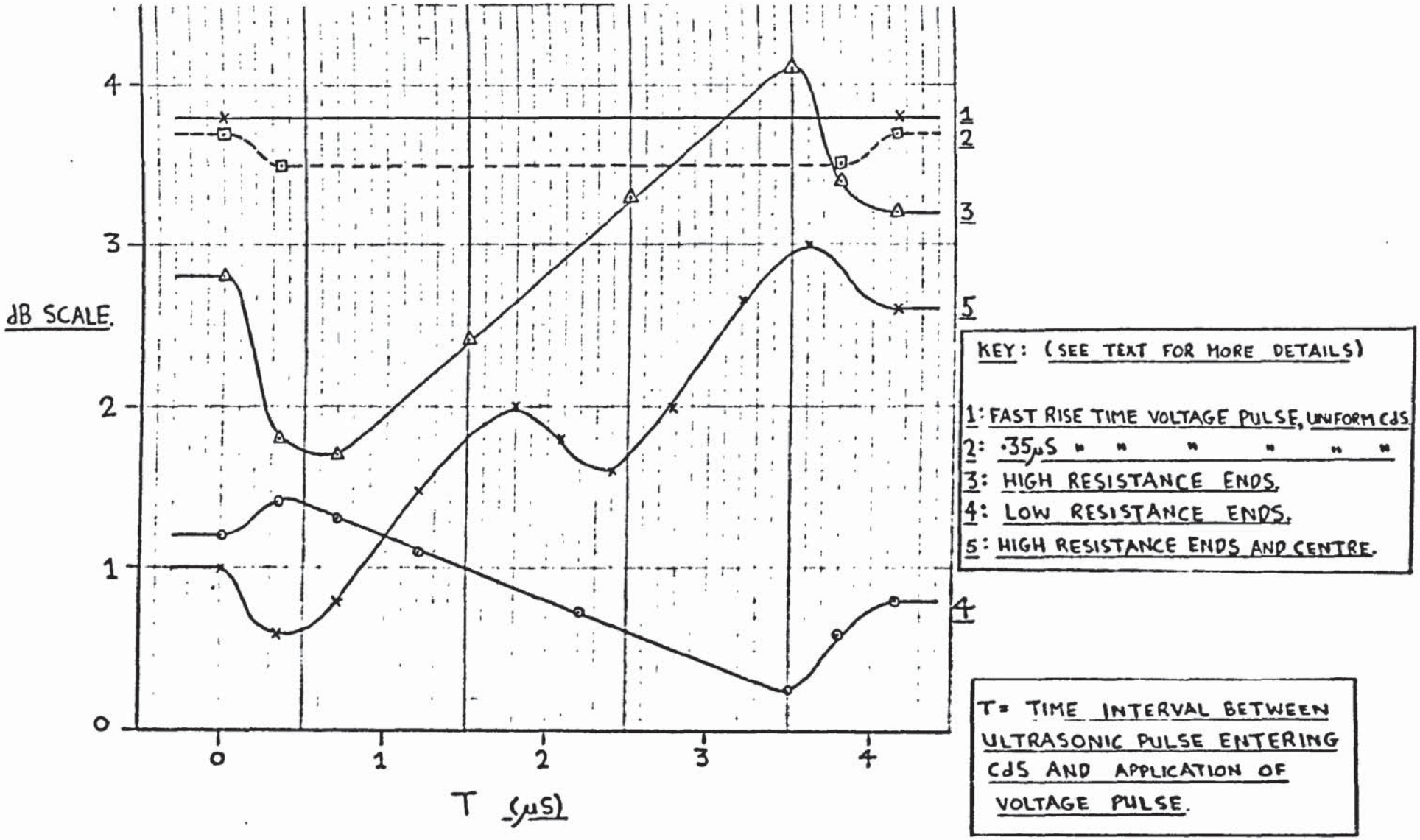

FIG. 106. THEORETICAL VOLTAGE PHASING EXPERIMENT AT 45MHz.

placed over a 1.5 m.m. distance at either end of the CdS and the crystal was illuminated as before. The curve obtained (curve 7 fig.78) showed a double overshoot at one end. This indicated that it was the end regions of the CdS that were largely responsible for the observed effects.

If a drift field equal to the pseudo cross-over field is applied to a homogeneous CdS crystal then the effect on ultrasonic propagation of phasing the voltage pulse with respect to the entry of the ultrasonics into the CdS is zero for a voltage pulse with extremely rapid rise and fall times, curve 1 fig. 106. Curve 2, fig. 106, shows that for a voltage pulse having a rise time of .35 μS the phasing produces a change of only 0.2 db, again for a homogeneous crystal. This figure was obtained by assuming a value of $\frac{\omega_c}{\omega} = .18$, for operation at 45 MHz, and using the experimentally determined curve of attenuation-field to find the average value of attenuation whilst the field was rising to the pseudo cross-over value. It was convenient for calculation purposes to assume that the acoustic pulse length was short compared to the rise time. Thus the ultrasonic pulse was in the CdS for 4.2 μS, as shown in curve 1. A longer ultrasonic pulse is partially in the CdS for a total time given by the transit time plus the pulse time duration. In this case the effects of voltage phasing are apparent for a period somewhat in excess of the transit time and the effect on the acoustic propagation of a localised region which is different from the bulk of the crystal is not quite as marked as for a very short pulse. The assumption of short acoustic pulses was not only

convenient for calculation purposes but showed the maximum effect that inhomogeneity could cause to acoustic propagation. For curve 3 it was assumed that at each end of the CdS there existed a region 0.06 cm. long having a resistivity twice that of the rest of the crystal (during the rise time period of 0.35μS the ultrasonics moved .060 cm). A voltage was assumed that would produce a field of 800 V cm.$^{-1}$ across a uniform crystal.

The steps necessary to obtain curve 3 are now briefly outlined.

A field of 800 V cm.$^{-1}$ would be produced by a voltage of 600 V applied to a uniform crystal of 0.74 cm. length. For the end regions, which have a resistivity twice that of the rest of the crystal, the application of this voltage produces a field of 1380 V cm.$^{-1}$ whilst for the rest of the crystal the field is 690 V cm.$^{-1}$ The bulk of the crystal is assumed to have $\frac{\omega_c}{\omega} = .18$. The field in the end regions was calculated at time intervals of .05μS and the appropriate attenuation was read from the experimental attenuation- field curve and averaged for the 0.35μS rise time period. This procedure was repeated for the middle region of the crystal. The attenuation produced in each region for the application of the full field and for no applied voltage was also taken from the experimental curves.

The experimentally determined curves of attenuation-field used to obtain data for the calculation of voltage phasing effects were themselves affected by the crystal non-uniformity. As referred to later in this section very similar results are

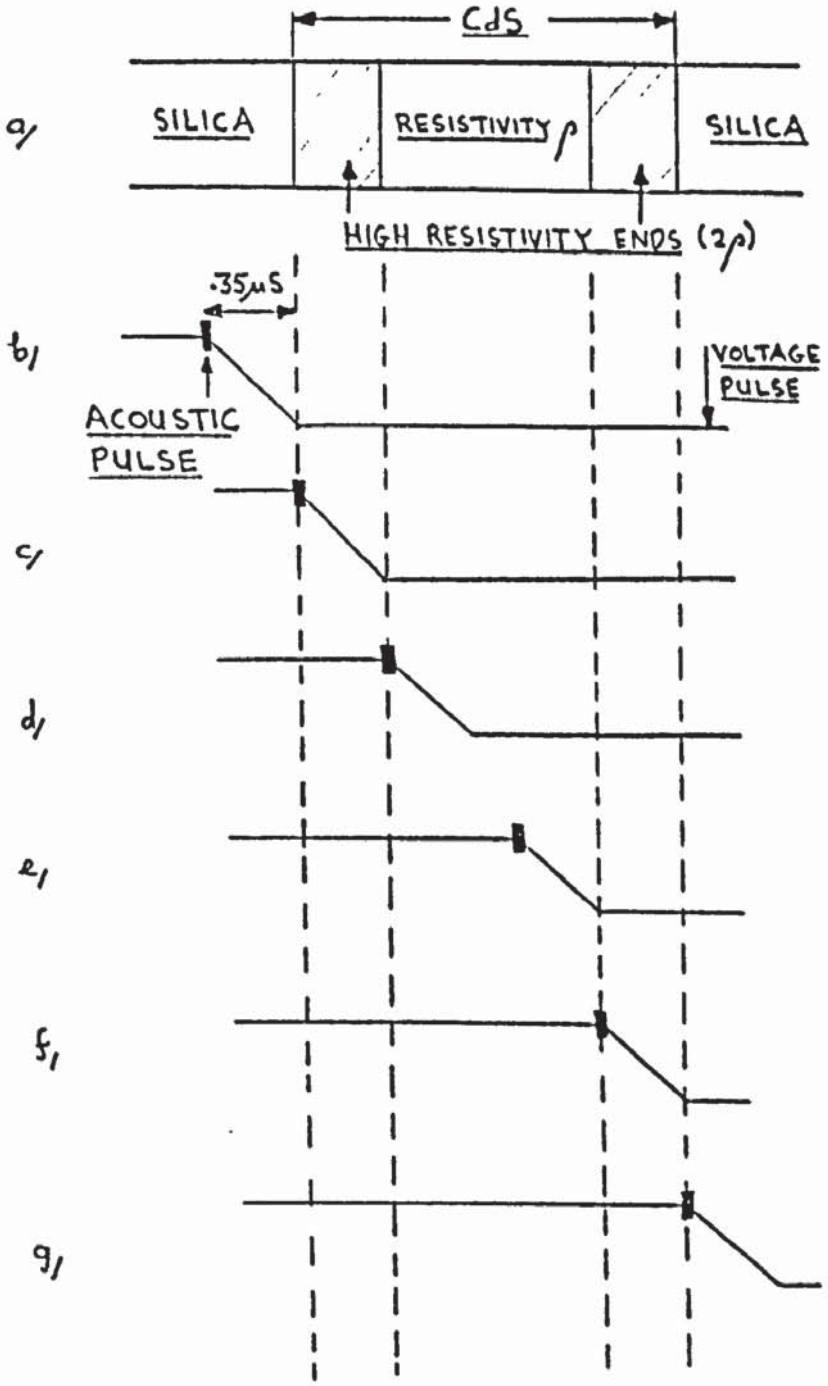

ATTENUATION FOR ACOUSTIC PROPAGATION THROUGH THE CdS. (db)
9·6
10·6
10·7
8·2
9·0
9·2

ULTRASONIC FREQUENCY : 45 MHz.

600 v APPLIED TO A CRYSTAL OF CdS 0·74 CM. LONG.

RISE TIME OF VOLTAGE PULSE : 0·35 μS.

RESISTIVITY ρ SUCH THAT $\frac{\omega\tau}{3/3} = 1.8$ FOR 45 MHz OPERATION

HIGH RESISTIVITY ENDS 0·060 CM. LONG.

FIG. 107. VOLTAGE PHASING EXPERIMENT.

obtained for the calculation of voltage phasing effects using White theory attenuation-field curves. Thus for convenience the experimentally determined curves have been used as a working basis.

Fig.107 shows the position of the acoustic pulse with respect to the time of application of the voltage pulse. In fig.107b for example the short acoustic pulse was in the silica when the voltage pulse was applied and it just reached the CdS-silica interface when the voltage pulse reached a maximum. The right hand column of figures shows the acoustic attenuation for each phasing condition, and they are plotted on fig. 106. For convenience in presenting several curves on fig.106 the attenuation scale has not been used to show the actual attenuation in each case but only the change from the starting condition. It is seen that curve 3 on fig. 106 is very similar to the experimentally observed curves. Curve 4, fig. 106, was obtained for a similar case to that of curve 3, namely 600 V applied and the middle region having $\frac{\omega_c}{\omega} = .18$, but <u>low</u> resistivity ends were used. The ends used were .06 cm. long with $\frac{\omega_c}{\omega} = .36$ i.e. half the resistivity of the middle region. For this case it can be seen that the "overshoots" are in the opposite direction from those experimentally observed and those obtained by calculation using high resistivity ends.

To obtain curve 5 the CdS resistivity pattern was as the diagram below :

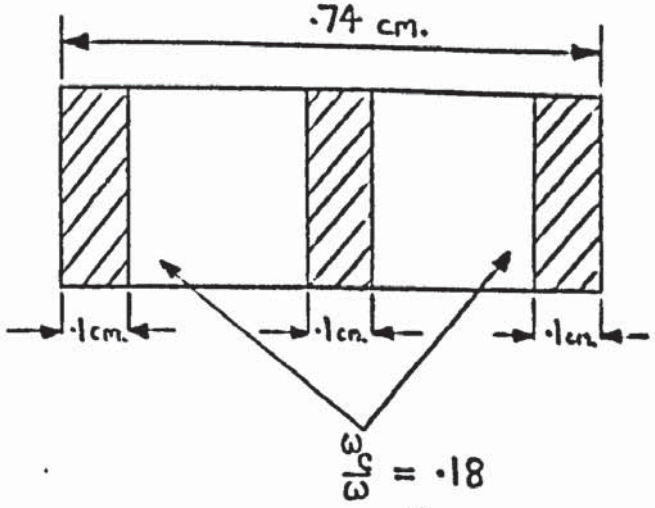

Shaded areas have $\frac{\omega_c}{\omega} = .09$

Besides the high resistivity ends a high resistivity region was inserted in the middle of the CdS. As shown on curve 5 the presence of the central high resistivity region causes a considerable dip in the theoretical curve. A voltage of 700 V was used to calculate curve 5.

Fig. 108 shows the theoretical curves for a given CdS resistivity configuration and a range of nominal applied fields. For example when a field of 400 v $cm.^{-1}$ is quoted it refers to the field that would be produced if the CdS were uniform. For fig.108 $\frac{\omega_c}{\omega}$=.18 in the middle region of the CdS and there are high resistance ends·.06 cm. long such that $\frac{\omega_c}{\omega}$ = .09. The theoretical curves exhibit the behaviour pattern observed experimentally, fig.78 . Curve 11, fig. 108, shows the result for a CdS crystal with resistivities as for the other curves on fig.108 but having high resistivity ends of .2 cm. length. This case was chosen to simulate the effect of placing filters at either end of the CdS, fig.78. The theoretical curve, like the experimental curve, showed a double overshoot at one end only.

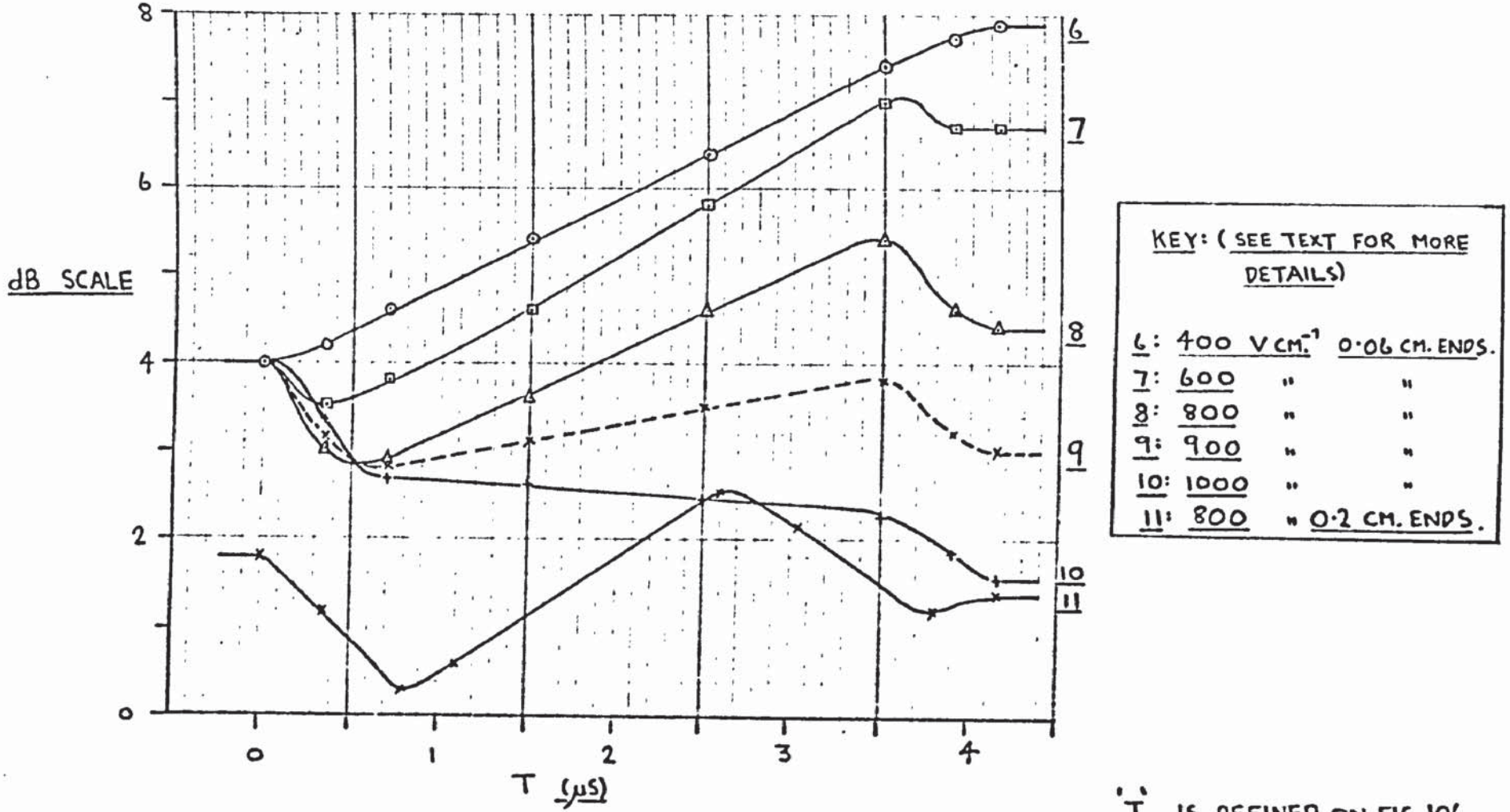

FIG. 108. THEORETICAL VOLTAGE PHASING EXPERIMENT AT 45 MH$_3$.

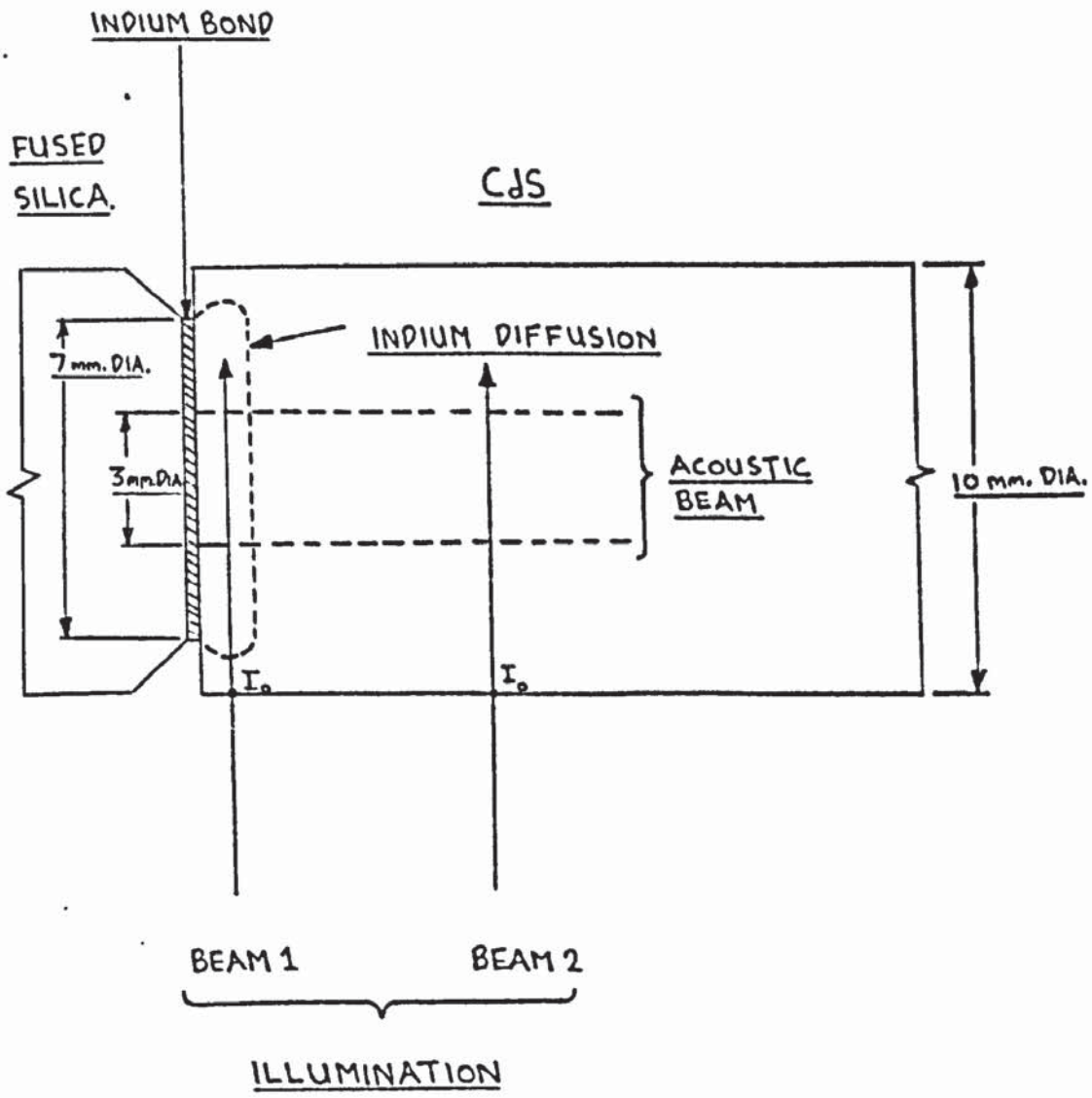

FIG. 109. LIGHT ABSORPTION IN ACOUSTIC AMPLIFIER.

The voltage phasing experiment thus yielded curves which were explained on the basis of a short length of high resistivity material in the acoustic path near the ends of the CdS. The high resistivity regions were believed to result from the effects on light absorption produced by diffusion of contact material into the bulk of the CdS. As shown in fig.26 light of wavelength 5800Å is more strongly absorbed in indium rich CdS. Fig. 26 was produced by obtaining first the absorption curve of a 0.11 cm. thick plate of high purity CdS. Indium was evaporated onto one side of the CdS and the crystal was maintained at 250°C for 1 hour in a nitrogen atmosphere whilst the indium diffused into the CdS. The excess indium was polished off the surface and the absorption curve retaken. The absorption coefficients for the untreated and treated CdS were 2.9 and 6.2 $cm.^{-1}$ respectively for a wavelength of 5800Å. Fig.28 shows the variation of illumination intensity inside the CdS for the two absorption coefficients. Fig.109 shows that beam 1 traverses .15 cm. of normal CdS followed by .2 cm. of indium doped CdS before traversing the acoustic beam region of .3 cm. of indium doped CdS. The average light intensity over the acoustic area is about 10% of that when the beam had just entered the CdS. For beam 2 the traverse to and across the acoustic beam region is entirely in normal CdS. The average light intensity over the acoustic area is about 26% of that when the beam just entered the CdS.

Szeto and Somorjai [108] have shown that the dominant mechanism by which light of wavelength longer than that corresponding

to the band gap of CdS is absorbed is the excitation of electrons from the valence band to traps, from which the electrons jump to the conduction band by thermal means.

For beam 1 the intensity falls from 19.5 to 3.0% of I_o during the traverse of the acoustic beam i.e. energy representing 16.5% of I_o was used for production of conduction electrons in this region. For beam 2 the beam intensity fell from 36% to 16% , a fall of 20%. Thus the local density of photo-electrons in the acoustic beam region is somewhat greater in the bulk of the CdS than in the region near the contacts. The CdS amplifier was maintained at 125°C for 24 hours during the indium bonding process. It is quite possible that the CdS specimen doped with indium for 1 hour at 250°C did not have such a high indium concentration as that in the end regions of the CdS amplifier. If this were so then the variation in density of photo-electrons in the two regions of the CdS amplifier would be larger.

The diffusion of indium into the end regions of the CdS amplifier would be expected to be approximately exponential. For convenience in calculating the theoretical curves it was considered that the regions were localised and sharply defined.

The reason why the voltage phasing experiment using a fast rise time pulse could easily detect a region of about ½ m.m. long having a resistivity twice that of the rest of the crystal can be seen by considering fig. 107. For the situation represented by fig.107b the end region had a field of 1380 V $cm.^{-1}$ applied and the acoustic pulse was amplified 0.8 db during its transit across

the region. For fig.107c the voltage pulse was rising to its maximum value as the short acoustic pulse propagated across the end region. The acoustic pulse was attenuated 0.2 db during this transit of the high resistivity region. For fig.107d the acoustic pulse propagated through the end region with no voltage applied and suffered an attenuation of 0.4 db. Thus by moving the voltage pulse by 0.7μS with respect to the acoustic pulse the propagation level through the CdS altered by about 1 db. The general agreement of theory with experiment supports the explanation given, that the observed effects were due to high resistivity ends that amplified when the voltage applied to the crystal did not cause amplification in the bulk of the crystal. The investigation of homogeneity of CdS crystal by Robertson and Ash [73] using an amplitude modulated light beam showed many crystals to have high resistivity end regions. However the electron mobility in these regions appeared to be almost a mirror image of the resistivity i.e. the resistivity increased as much as the mobility decreased. Under these conditions the end regions would be much less likely to produce that supersonic electron drift and consequently amplification which the present results strongly suggest. Comparison of the experimental variation of attenuation produced by voltage phasing with the magnitude expected from the resistivity profiles adopted in the theoretical model shows that at least the values of amplification calculated for the end regions are needed. The relative resistivities of end region to central region in the model were of the same order as those given by

Robertson and Ash. However if their apparent decrease in mobility were present this would very much diminish the chance of amplification in the end regions.

Robertson and Ash formulated their equations for resistivity variation under the assumption that there was no variation in current density in the plane normal to the direction of current flow. Fig. 28 shows that even with weakly absorbed light there is a considerable variation in the density of primary photo-electrons throughout the thickness of the crystal. Robertson and Ash used CdS crystals having electrical contact regions extending completely over the end faces of the crystal. The variation in current density in the plane normal to the direction of current flow must have been considerable under these conditions. They obtained the resistivity variation by measuring the a.c. component of current produced by the modulated light beam incident on various cross-sections of the CdS. It is considered that the geometry of the amplifier used (in particular the electrical contacts extending across the end faces) meant that the current modulation measured did not relate particularly to the region of the cross-section traversed by the acoustic beam but to the cross-section of the whole crystal. As such the resistivity variation obtained cannot be stated to be characteristic of the region of acoustic transmission. In contrast the voltage phasing experiment monitored the level of acoustic propagation produced by phasing the drift field voltage pulse and the variation of attenuation of different regions of the CdS was obtained for the acoustic beam region exclusively. Accordingly the

alternating optical probe measurement of resistivity would not be expected to record expressly the high resistivity regions of the acoustic beam produced by the effects on light absorption of indium diffusion. However the measured variation of the a.c. component of acoustic propagation would have been expected to reveal any such regions. The heat treatment given to the CdS in the present research was more prolonged than that used by Robertson and Ash and the extent of indium diffusion in their crystals would be expected to be smaller than that in the present research. D.J. Larner (private communication) has used an acousto-electric technique to confirm the existence of high resistance ends in a piece of CdS given a similar heat treatment to that used in the present research. The acousto-electric voltage produced by a pulse of ultrasonics of short duration compared to the acoustic transit time was observed to change sign when the field was increased so as to produce acoustic amplification instead of attenuation. For a field corresponding to the small signal cross-over case the acousto-electric voltage appeared as below.

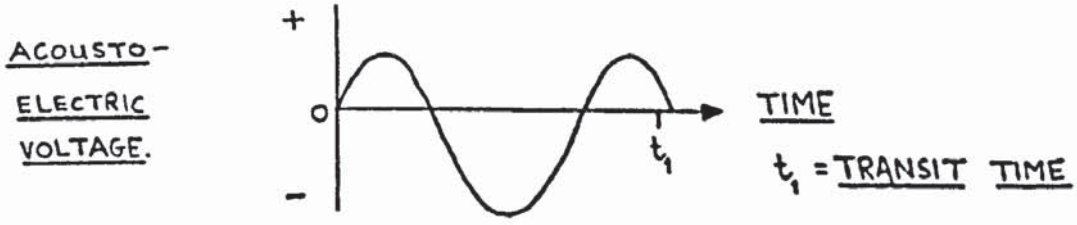

The pulse of ultrasonics was amplified whilst traversing the end regions of the crystal and attenuated during passage through the central portion of the CdS. This behaviour was as observed in the voltage phasing experiment.

The experimentally determined curves of attenuation-field were used in this section to calculate the expected results of voltage phasing experiments. The theoretical curves for voltage phasing showed the same pattern of behaviour as observed experimentally. Very similar results have been obtained when the White equation for the attenuation coefficient was used in conjunction with exponential variations of resistivity at each end of the crystal, Cotterhill [109].

The effect of high resistivity ends on the determination of the electro-mechanical coupling coefficient was investigated using the White equation for α and a resistivity profile as below:

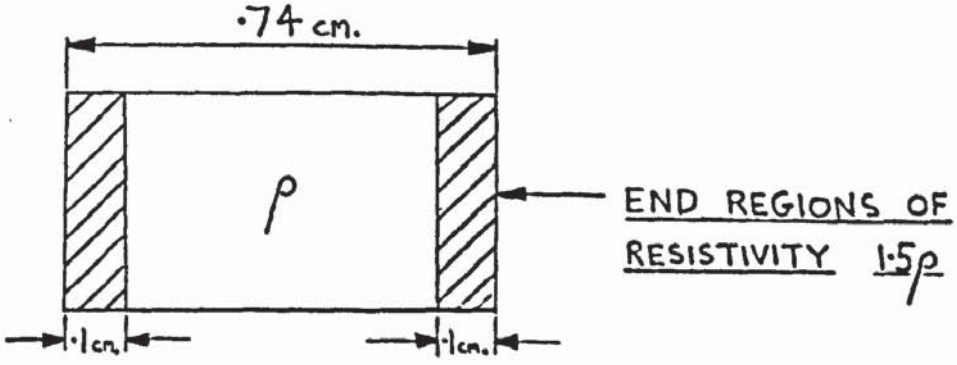

The variation of acoustic attenuation for no applied field with conductivity was calculated for a uniform CdS crystal having $K^2 = .0105$ for operation at 45 MHz. The results are plotted on fig.110. The attenuation for no applied voltage as a function of apparent resistivity was calculated using the resistivity profile above. If the measured resistance of the uniform crystal was such that $\frac{\omega_c}{\omega} = .2$ then when the non-uniform crystal had the same resistance the middle portion had $\frac{\omega_c}{\omega} = .229$ and the ends had $\frac{\omega_c}{\omega} = .153$. The results, shown on fig.110, indicate that if the electro-mechanical coupling coefficient was

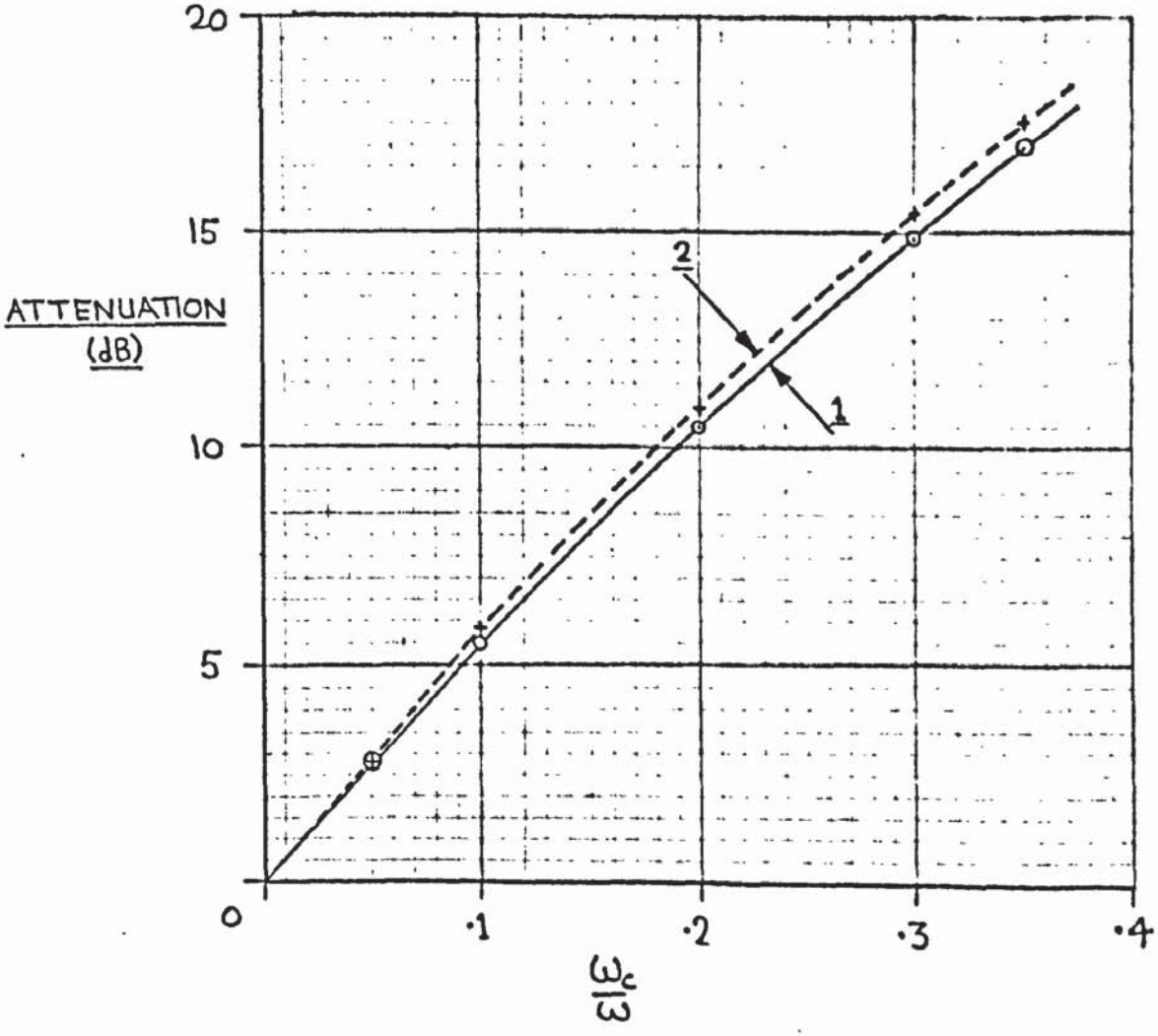

ULTRASONIC FREQUENCY : 45 MHz.

CRYSTAL LENGTH : 0·74 cm.

ZERO APPLIED FIELD.

1: UNIFORM CRYSTAL

2: CRYSTAL WITH HIGH RESISTANCE ENDS.

(SEE TEXT FOR DETAILS)

FIG. 110. THEORETICAL CURVES OF NO-VOLTAGE ATTENUATION VERSUS ω_c/ω AT 45 MHz.

determined by measuring the slope of the curves at the origin then the sandwich structure would yield a value for K^2 only some 3% different from the value for the uniform crystal.

Fig.102 shows the experimentally obtained curve of attenuation-field for $\frac{\omega_c}{\omega} = .2$ at 45 MHz. Also shown are three curves calculated using White's theory and assuming a uniform crystal. If a resistivity profile the same as the case above was assumed then the theoretical attenuation-field curve was considerably different from that for a uniform crystal. The positions of the maximum attenuation and amplification regions moved nearer to the experimentally obtained curve both in the magnitude of the attenuation and the field required. The situation would still be the same if a slightly lower value of cross-over field had been chosen for the White theory curves such that the attenuation-field curve for the sandwich structure had the same cross-over field as experimentally observed.

6.5. Large amplitude ultrasonics

Fig.80 shows that the propagation of ultrasonics in CdS maintained in the dark, was independent of the acoustic amplitude for the range of acoustic powers available from the Matec r.f. pulse generator at 45 MHz. The graph was obtained by direct measurement of the input and output voltages of the acoustic amplifier. The results have been expressed on a decibel scale. With the CdS in the dark the crystal resistivity was greater than 5×10^9 ohm-cm. Under this condition the propagation of ultrasonics was not observed to change at all for applied fields up to ± 2000 V cm.$^{-1}$

Thus with the crystal in the dark the electro-acoustic interaction was very small and the CdS behaved as a passive material. When the input attenuator was correctly matched to the input transducer the maximum acoustic intensity entering the CdS was 1.15 W cm.$^{-2}$ for operation at 45 MHz. The maximum strain produced was 3×10^{-5}. Thus the maximum strain was small enough to ensure that a linear relationship existed between applied stress and the resultant strain.

For the measurement of input-output characteristics shown on figs. 81 - 92 both attenuators were matched to their respective transducers. The input attenuator was used to regulate the input acoustic power level to the CdS and the output attenuator was adjusted so as to maintain a constant receiver output level.

One of the most remarkable features of the input-output characteristics was the saturation of gain that was observed for large acoustic inputs, fig.90. For the dark condition the attenuators were set at 43:0 db. For convenience the nomenclature used is to quote the setting of the input attenuator followed by the output attenuator setting, both figures being decibels. With $\frac{\omega_c}{\omega} = .2$ and a field of 1400 V cm.$^{-1}$ the attenuator settings were 57:0 for the standard receiver output i.e. an acoustic gain of 14 db. With 15 db in the input attenuator the output saturated. The attenuator settings at this point were 15:34.5. For the dark condition curve the appropriate settings were 15:26.5 i.e. the acoustic gain had fallen to 8 db. With the input attenuator set at 8 db the net effect on acoustic propagation in the CdS was neither amplification or attenuation compared to the dark level propagation.

For a smaller setting of the input attenuator the acoustic wave was attenuated during propagation in the CdS. For attenutor settings less than 4 db there was an increase in the level of acoustic output and the attenuation remained constant at 4 db. This break away from a saturated condition has not been reported in the literature. The saturation plateau has been reported by Ishiguro et al [14], Hanlon [110] and Hickernel et al [21]. It is generally accepted that the saturation occurs when the acoustic power level is such that the limit of concentration of bunched electrons is reached i.e. the electron density involved in bunching, n_{so}, is equal to the average electron density in the conduction band n_o.

For curve 3, fig.90 the saturation started when the attenuator settings were 15:34.5 and the acoustic gain was 8 db. Thus the acoustic intensity in the crystal just before the pulse left the CdS was 7 db down on the standard figure of 1.15 W cm^{-2}

The equation for n_{so} given by the White theory is given below:

$$n_{so}\, e^{(j\theta_5)} = \frac{\sigma\, e S_o}{q v_s \epsilon} \frac{\left[\gamma - j \left(\frac{\omega_c}{\omega} + \frac{\omega}{\omega_D} \right) \right]}{\left[\gamma^2 + \left(\frac{\omega_c}{\omega} + \frac{\omega}{\omega_D} \right)^2 \right]}$$

$$n_{so} = \frac{\sigma\, e\, S_o}{q v_s \epsilon} \left[\gamma^2 + \left(\frac{\omega_c}{\omega} + \frac{\omega}{\omega_D} \right)^2 \right]^{-\frac{1}{2}}$$

n_o was calculated from the conductivity equation:

$$\sigma = n_o q \mu$$

The following values were used to calculate n_{so} and n_o:

$s_o = 1.30 \times 10^{-5}$

$e = 0.22$ coulombs $M.^{-2}$

$q = 1.6 \times 10^{-19}$ coulombs

$v_s = 1.75 \times 10^{-3}$ M. sec^{-1}

$\epsilon = 9.0 \times 10^{-11}$ F. $M.^{-1}$

$\omega = 2.95 \times 10^{8}$ $sec.^{-1}$

$\omega_D = 7.1 \times 10^{9}$ $sec.^{-1}$

$\sigma = 4.75 \times 10^{-3}$ ohm^{-1} $M.^{-1}$

$\gamma = -0.33$

For this example $n_{so} = 1.82 \times 10^{12}$ $cm.^{-3}$ compared to $n_o = 1.7 \times 10^{12}$ $cm.^{-3}$ Table 12 gives the calculated values of n_{so} corresponding to the onset of gain saturation. The agreement between n_{so} and n_o is regarded as satisfactory considering the possible error in the acoustic power measurement, as described in section 4.3.4.

TABLE 12.

Input-output characteristics at 45 MHz

$\frac{\omega_c}{\omega}$	FIELD V cm.$^{-1}$	n_o ($\times 10^{12}$ cm.$^{-3}$)	n_∞ FOR ONSET OF SATURATION ($\times 10^{12}$ cm.$^{-3}$)
.2	1600	1.7	1.5
"	1400	"	1.82
"	1200	"	1.7
.3	1600	2.5	2.6
"	1400	"	2.3
"	1200	"	2.2

The case of $\frac{\omega_c}{\omega} = .2$ with a field of 1400 V cm.$^{-1}$, fig.90, is now considered in more detail and a possible explanation of the behaviour is put forward. With 15 db in the input attenuator the acoustic signal was amplified 8db during propagation through the CdS. The $n_{so} = n_o$ condition was achieved only at the output end of the CdS. The acoustic signal was amplified by the interaction with the drifting electrons whilst at the same time it lost energy due to the generation of harmonics, the net amplification being 8 db. With 4 db in the input attenuator the CdS was in an attenuating state such that the input acoustic intensity was 0.46 W cm.$^{-2}$ and the output acoustic intensity was 0.205 W cm.$^{-2}$

The output acoustic intensity corresponded to the $n_{so} = n_o$ condition whilst at the input end the electron density in the conduction band also limited the density of bunched electrons such that $n_{so} = n_o$. Under these conditions the drifting electrons were unable to amplify the acoustic wave. Losses incurred by the generation of harmonics produced an attenuation of 4 db. For larger acoustic inputs to the CdS the input-output characteristic became parallel to the dark condition curve. The attenuation resulting from the generation of harmonics remained constant at 4 db whilst the setting of the input attenuator was altered from 4 db to 0 db. This behaviour suggested that the amplitude of the harmonics generated increased proportionally to the amplitude of the input signal for input attenuator settings of less than 4 db. Later experiments, e.g. fig.97, confirmed this hypothesis and are discussed later.

The curve corresponding to the small signal cross-over

field, fig.90, did not exhibit gain saturation. For settings of the input attenuator between 43 and 20 db the input-output characteristic was within 1 db of that corresponding to the dark condition. Thus under this illumination condition and this range of input acoustic powers the applied field maintained the attenuation at the level characteristic of the dark level propagation. Smaller values of input attenuation produced an increase in the acoustic attenuation due to the generation of harmonics. Settings of the input attenuator below 5 db produced a constant acoustic attenuation of 8 db. When the characteristic became parallel to the dark condition curve the value of n_{so} was 1.8×10^{12} cm.$^{-3}$ at the output end of the CdS. Thus for the case of small signal cross-over field the input-output characteristic became parallel to the dark condition curve when the CdS was in an attenuating state and the bunching limitation was produced at the output end of the CdS. The break-away from gain saturation previously discussed occurred under similar conditions.

For operation at 45 MHz the input-output characteristics obtained for illumination conditions such that $\frac{\omega_c}{\omega} = 0.1$ and .05 did not show marked gain saturation mainly because the amplification available was small. In all cases the input-output characteristic became parallel to the dark curve when the condition $n_{so}=n_o$ was attained at the output end of the CdS. Table 13 gives the calculated values of n_{so} for the onset of this parallel condition.

TABLE 13

Input-output characteristics at 45 MHz

$\frac{\omega_c}{\omega}$	Field V cm.$^{-1}$	n_o x 10^{11} cm.$^{-3}$	n_{eo} for onset of parallel condition. x 10^{11} cm.$^{-3}$
.2	1050 C.O.	17	18
.1	1600	8.8	7.8
"	1400	"	9.1
"	1200	"	9.4
"	1070 C.O.	"	7.7
.05	1600	4.4	5.1
"	1400	"	4.3
"	1130 C.O.	"	5.8

It was observed that the extent of non-linearity in the input-output characteristics was less marked at 15 MHz than 45 MHz the probable explanation being that the acoustic amplification available at 15 MHz was less than at 45 MHz (see for example fig.88).

Fig.87 shows typical input-output characteristics obtained for operation at 15 MHz for cross-over and amplifying fields. For this case $n_o = 1.7 \times 10^{12} cm.^{-3}$. For curve 1 it was calculated that $n_{so} = 2.0 \times 10^{12} cm.^{-3}$ at the output end of the CdS when it became parallel to the dark curve. For curve 2 the corresponding figure was $1.8 \times 10^{12} cm.^{-3}$

The generation of the second harmonic of a fundamental acoustic wave propagating in CdS has been reported by several workers, as referred to in section 1.2.3. In these experiments the input transducer was operated at its fundamental frequency and the output transducer, which was chosen to have a fundamental frequency of twice that of the input transducer, detected the second harmonic which was produced by the non-linearity of the electro-acoustic interaction. In the present research both transducers had a fundamental frequency of 15 MHz and the third and fifth harmonics were monitored rather than the second. The advantage of this approach was that an experiment was carried out with generation and detection at a given frequency and then repeated under identical operating conditions but with one of the harmonics being monitored.

Fig. 96 shows the input-output characteristics for a 15 MHz fundamental and third and fifth harmonics. The slope of the fifth harmonic curve was 5.0 when the settings of the input

attenuator were 25 db or greater. The slope of the third harmonic curve was 3.0 for the same range of input attenuator settings. At a setting of 25 db in the input attenuator the fundamental signal was within 0.5 db of the dark condition curve. For less input attenuation the slope of the harmonics approached that of the dark-condition curve. The harmonics were small compared to the fundamental signal and the receiver gain was set at a higher level than was usual when generation and detection were at a given frequency. In the present research the shape of the harmonic input-output curves was studied and an absolute calibration of the harmonic intensities was not carried out. In the graphs presented of harmonic generation the settings of the output attenuator applicable to the harmonic curves corresponded to a higher receiver gain than used for the fundamental and in all cases the amplitude of the fundamental was larger than the amplitude of the third harmonic which in turn was of larger amplitude than the fifth harmonic.

Fig.97 shows the gain saturation of a 45 MHz signal and the behaviour of the third harmonic at 135 MHz. When the fundamental signal deviated from gain saturation the level of the third harmonic moved in sympathy. For sufficiently large input signals such that the electron bunching is limited by the equality $n_{so} = n_o$ throughout the CdS the gain mechanism provided by supersonic electron drift is ineffective and the fundamental signal is depleted during propagation along the CdS by harmonic processes. For larger acoustic inputs than required for break-away from

saturation the attenuation was constant and the behaviour of the third harmonic was such as to maintain the attenuation at a constant value.

Fig.98 shows the behaviour of the third harmonic for a quite different case, namely for small-signal cross-over field and weak illumination. Again, when the fundamental curve became parallel to the dark condition curve the third harmonic curve also had the same slope.

Fig.99 shows similar behaviour for the third and fifth harmonics of a 15 MHz input for both cross-over and amplifying conditions.

Thus the behaviour of the third and fifth harmonics was consistent with the observed input-output characteristics of the fundamental. No previous record either of the breakaway from saturation or the measurement of the third and fifth harmonics was known.

The non-linearity observed for attenuating field conditions was in general much smaller than observed for cross-over and amplifying fields. For example on fig.86 the deviation between the dark-condition curve and that obtained under operating conditions was less than 4 db. For convenience the appropriate value of no-voltage attenuation was quoted rather than $\frac{\omega_c}{\omega}$: fig.63 provides the relationship between them. The deviations from linearity observed for no applied field were even smaller, fig.83. For no applied field and an attenuating field results were obtained by the normalizing technique and by individual calibration, as described in section 5.6.1.

The results were consistent to $\pm$ 0.5 db. When the CdS was biased into an amplifying state the propagation of large signals not only reduced the efficiency of the amplification process but the amplification of the fundamental was further reduced by energy lost to harmonics. For attenuating conditions however the two effects work in opposite directions. For very large signals the limitations of electron bunching prevent the acoustic wave from being attenuated as severly as a small signal, thus the attenuation is reduced. On the other hand the loss mechanism provided by harmonic generation can increase the attenuation. The deviation shown in fig.86 is thought to result from the competition between the two mechanisms. It is considered that the quantitative analysis of such effects would require knowledge of the absolute intensities of the major harmonics i.e. the 2nd, 3rd, 4th etc. and such investigation was not carried out in the present research.

The curves on fig. 82 having α between 2.5 and 9.3 db have not achieved the parallel condition with their respective calibration curves. Table 14 gives the calculated values of n_{so} at the output end of the CdS, for 3 db input attenuator setting.

TABLE 14. Input-output characteristics at 15 MHz (For fig.82)

no. of curve	α db	n_o x 10^{11} cm.$^{-3}$	n_{so} x 10^{11} cm.$^{-3}$
4	2.5	3.4	3.15
3	4.5	6.8	5.4
2	7.0	12	7
1	9.3	18	7

Thus the deviations would be expected to increase for larger acoustic inputs, with the possible exception of curve 4. For the attenuating field case of fig.85 several of the curves have almost reached the parallel condition. Table 15 gives the calculated values of n_{so} at the output end of the CdS, for an input attenuator setting of 3 db.

TABLE 15

Input-output characteristics at 15 MHz

(For fig.85)

no. of curve	α db	n_o $\times 10^{11}$ cm.$^{-3}$	n_{so} $\times 10^{11}$cm.$^{-3}$
5	1.8	2.4	3.6
4	4.5	7.1	7.6
1	10.5	27	21

For this case curves 5 and 4 have almost reached the parallel condition but curve 1 would be expected to show a much larger deviation from linearity for larger acoustic inputs.

The input-output characteristics gave the minimum value of input attenuator settings such that the CdS behaved linearly, for the full range of operating conditions. This knowledge was essential if experiments such as attenuation-applied field were to be carried out under small signal conditions. Table 16 gives the minimum input attenuator settings for sensibly linear operation

under various conditions.

TABLE 16

Minimum attenuator settings for linearity

Frequency MHz	Operating conditions	Minimum input attenuator settings for linearity to $\pm\frac{1}{2}$ db db
15	no applied field	10
"	600 V $cm.^{-1}$	15
"	cross-over field	22
"	amplifying fields	25
45	no applied field	10
"	600 V $cm.^{-1}$	17
"	cross-over field	22
"	amplifying field	25

Thus for operation at 45 MHz where the attenuation caused by the applied field was up to 24 db the receiving equipment had to be sensitive enough to produce a suitably large signal for display on the oscilloscope whilst the input attenuator setting was in excess of 40 db and the CdS was maintained in the dark.

Figs. 93 - 95 are the result of an experiment in which the cross-over condition was achieved for a small acoustic input. For small signal conditions the variation of cross-over field with crystal conductivity is attributed to trapping effects, Ishiguro et al [14].

For an increase in acoustic input the loss to harmonics increased, as shown in fig.96, and the field applied to the CdS was increased in order to amplify the depleted fundamental signal up to the standard level. The cross-over field was seen to vary drastically for large acoustic inputs. The results confirmed the need for a stringent limitation on input acoustic power when carrying out attenuation-field experiments.

SECTION 7

Conclusions and suggestions for further work

7.1 Summary of the research and general conclusions

CdS was chosen as the most suitable material available for an investigation of the propagation of ultrasonics in piezoelectric semiconductors. The objects of the research were:-

(1) To investigate the attenuation of MHz ultrasonics in CdS as a function of ultrasonic frequency, crystal resistivity, applied field and input acoustic power level.

(2) To assess the extent of non-uniformity in the material used and its effect on the attenuation measurements.

Both objects were carried out as described in previous sections of this thesis.

Techniques were developed for the fabrication and operation of an acoustic amplifier structure. Considerable attention was paid to the accuracy of orientation and the mechanical tolerances of the amplifier components. The effect on ultrasonic propagation of illuminating the crystal with light of various wavelengths was investigated. The fabrication procedure was time consuming and only one acoustic amplifier was assembled, using a selected crystal. The wide scope of the measurements undertaken would not have been possible if each experiment was carried out for more than one crystal. The choice between crystals was made on the basis of their current-voltage characteristics. The

properties investigated were expected to be general features of the material although the magnitudes of the effects considered may vary from crystal to crystal. Thus the conclusions are of more general application than might otherwise be thought.

The investigation of the acousto-electric voltage produced in CdS by ultrasonic pulses showed in a direct manner the interaction of acoustic waves and electrons. The observed variations of acousto-electric voltage with acoustic power for a given crystal conductivity and with attenuation for a given acoustic power were explained using Weinreich's relationship. The measurement of acousto-electric voltage was used in the insertion loss determination of acoustic power to quantify the acoustic transmission asymmetry of the amplifier and it was also used to compare acoustic power for operation at several frequencies.

The attenuation-field characteristics taken under small signal conditions showed many features which were explained on the basis of White's amplification theory. These included the variation of amplification with frequency and the attenuation-conductivity curves for zero applied field. The field required for maximum amplification however did not vary with frequency in the manner of the theoretical curves derived from White's theory. The application of trapping theory to the attenuation-field characteristics observed at 15 and 45 MHz revealed a consistent pattern of behaviour. The asymmetries observed in the attenuation-field curves for 75 MHz were not as expected from trapping considerations.

Theoretical attenuation-field curves were derived by applying White's theory to a model of a CdS crystal containing a resistivity variation corresponding to that determined by a voltage phasing experiment at 45 MHz. The theoretical curves for such a model were closer to those experimentally observed than ones calculated under the assumption of crystal uniformity. The observed variation of the field required for maximum gain as a function of frequency and the asymmetry of the 75 MHz attenuation - field curves could not be accounted for by the experimentally determined crystal non-uniformity.

The methods developed to study the propagation of large amplitude ultrasonic signals were based on input-output characteristics. Analysis showed that many of the observed effects such as gain saturation and the development of the "parallel" condition were related to limitations of electron bunching. The third and fifth acoustic harmonics generated by the propagation of large amplitude signals were monitored and their behaviour was shown to be consistent with that expected from the input-output characteristics of the fundamental signal. The input-output characteristics established the upper limit for acoustic intensity in the CdS, under various operating conditions, such that linear behaviour was observed. This information was used to ensure that the attenuation-field curves were taken under small signal conditions.

An important feature of the research was the determination of the degree of crystal homogeneity by means of an experiment in which the time of application of the drift field pulse was varied

with respect to the entry of the ultrasonic pulse into the CdS. This method of investigating crystal inhomogeneity did so only over the cross-sectional area of the acoustic beam unlike optical methods which produce an average value for the whole crystal cross-section or methods involving surface probes which again do not relate directly to the region of acoustic propagation.

The investigation of the propagation of ultrasonics in CdS was comprehensive and many previously unreported findings were observed which are of importance in assessment of the possibilities of amplifiers using the electro-acoustic interaction.

7.2 Suggestions for future work

The measuring techniques used in the present research could be used, without modification, to study the electro-acoustic interaction in other piezo-electric semiconductors as these become available in single crystal form of convenient size and reasonable quality. Although the quality of individual CdS crystals and the variation in behaviour between different CdS crystals is not very satisfactory the quality of piezo-electric semi-conductors such as CdSe, CdTe and ZnO is generally regarded as considerably inferior to that of CdS at present.

It is considered that the type of amplifier structure incorporating buffers used in the present research is more suitable for a wide range of electro-acoustic experiments than the bufferless type amplifier favoured by many workers interested in device applications. The attenuation of shear waves in fused silica is not large at normal operating frequencies and does not contribute

much to the measured insertion loss of the amplifier. Fraser et al [111] have reported the attenuation of shear waves in fused silica at room temperature to be 3×10^{-2} db $cm.^{-1}$ at 45 MHz rising to 1.0 db $cm.^{-1}$ at 280 MHz and 4.1 db $cm.^{-1}$ at 500 MHz. If experiments were to be undertaken at frequencies in excess of 500 MHz the attenuation in the buffers could be reduced considerably by the use of such low loss materials as sapphire ($Al_2 O_3$), yttrium iron garnet, yttrium aluminium garnet (YAG), and rutile ($Ti O_2$). Olsen et al [112] have given attenuation data for these materials for frequencies up to 4 GHz. The attenuation of shear waves in YAG at room temperature was observed to be 0.16 db $cm.^{-1}$ at 500 MHz rising to 0.9 db $cm.^{-1}$ at 4 GHz.

One of the advantages of attaching transducers to buffers with an organic material such as "Salol" is that the transducers can be easily changed if they suffer breakdown or transducers of a different fundamental frequency are required. For a bufferless system where the transducers are usually bonded to the CdS by an indium bond the effort involved in changing a transducer may be equivalent to fabricating an amplifier. With a buffer-type amplifier a series of experiments could be performed with generation and detection at a given frequency then one transducer could be easily changed for one having a fundamental frequency twice that of the remaining transducer and the second harmonic efficiently detected. Spector and Southgate [50] believed that interaction of the piezoelectrically active shear wave with the shear wave polarised at 90° to it was responsible for an observed saturation of

attenuation in CdS. With a buffer type amplifier the receiving transducer could easily be rotated 90° to detect such a spurious mode. The salol bonding process has the advantage that extremely thin transducers, having a fundamental frequency of 150 MHz and more, can be attached to an amplifier in order to achieve higher efficiency transduction than obtained with high overtone operation. On the other hand considerable pressures have to be applied to the CdS and transducers during the indium bonding process and extremely thin transducers cannot be affixed without breakage.

In practice at high frequencies the acoustic bonds would be expected to cause considerably more attenuation than caused by propagation in buffers of low loss dielectric crystals. The optical contact bonding process, Smith [113], offers the possibility of reducing bond losses.

In the present research the limitation of electron bunching was not attained for certain operating conditions. The input acoustic power could be increased by an increase in the output of the r.f. pulse generator. An alternative approach would be to combine the best features of the buffer and the buffer-less amplifiers. An input transducer affixed directly to the CdS, as the buffer-less amplifier, would enable the ultrasonics to enter the CdS with the very minimum of attenuation. By attaching a buffer to the other end of the CdS and affixing a transducer with "Salol" one of the advantages of the buffer type amplifier would be available, namely the ability to change the receiving transducer easily for detection of harmonics or orthogonal shear

modes.

The work reported to date on harmonic generation in CdS has been restricted to the second harmonic only. As shown in the present work higher harmonics are detectable. It should be possible to measure in a quantitative way the intensity of the first six harmonics in order to estimate how much energy is being channeled into harmonic generation under various operating conditions. The experimental arrangement envisaged would be a large transmitting transducer with two much smaller transducers in the acoustic beam at the other end of the amplifier. One receiving transducer would be of the fundamental frequency and, as in the present research, detect the 3rd and 5th harmonics. The other transducer, of double the fundamental frequency of the transmitting transducer, would detect the 2nd, 4th and 6th harmonics. Such an arrangement would enable the intensity of the harmonics to be monitored whilst the CdS was in a given operating condition.

The high resistance ends observed with the present amplifier were believed to be caused by the increased adsorption of light in indium rich CdS near the contact areas. An interesting and useful line of research would be to investigate this phenomena in a quantitative and thorough way. A CdS crystal could have indium evaporated on one end face and then receive an identical heat treatment to the amplifier structure before being sectioned in order to monitor the extent of indium diffusion quantitatively using an electron-beam microprobe analyser. Thin CdS specimens could be prepared with measured average amounts of

indium diffused into them and their optical absorption curves measured. In this way a chart showing optical absorption of light of 5800Å wavelength against indium concentration could be prepared. From this chart the intensity of the light traversing different regions of the indium doping profile revealed by micro-probe analysis could be calculated. Hence the relative numbers of photo-electrons produced in different regions of the acoustic beam could be calculated.

The extent of indium diffusion into the CdS could be reduced by reducing the time allowed at elevated temperatures for bond formation. In the present research a pressure of 250 - 300 p.s.i. was applied to the amplifier whilst bond formation occurred. This pressure was held far below the figure of 1200 - 3500 p.s.i. quoted in the patent literature [94,95]. in order not to fracture the CdS which is more delicate than the delay line materials that were the subject of interest in the patents. It is possible that the CdS will withstand a much higher pressure and that by this means the time that the amplifier is maintained at elevated temperatures could be reduced possibly to a quarter of the 24 hours period used in the present research. It should be noted that the references given above suggest that temperatures below 95°C do not produce satisfactory bonds.

APPENDIX 1

Growth and heat treatment of single crystal CdS

The CdS crystals obtained for the present research were grown by vapour phase deposition. The procedure used for the growth and heat treatment of CdS crystals is outlined in this section.

The CdS powder is first sintered inside a clear fused silica tube at 800°C under vacuum for 1 hour, and then fired under argon at 1200°C for 1 hour. This densifies the powder and also removes the more volatile impurities.

The sintered CdS slug is removed from the quartz tube and then grown into a crystal by subliming the sintered slug and allowing it to deposit in a cooler section of the quartz growth tube. The actual sublimation of approximately 500 grams of sintered material requires about 4 days at 1300°C at a pressure of about 800 m.m. of Argon absolute. However the resulting crystal boules obtained in this manner are seldom, if ever, single. Instead a polycrystalline ingot forms, but due to grain boundary migration, one crystal may become larger at the expense of another which becomes smaller. Therefore the run is permitted to remain at growth temperature for 2 to 3 weeks so that the polycrystalline ingot will tend to become more nearly single. Unfortunately the run cannot be held indefinitely to obtain a completely single crystal because devitrification of the quartz is constantly

occurring. This could eventually become a source of silica contamination. At the end of approximately 19 days on the average the furnace is slow-cooled to room temperature over a 4 day period. This is done to minimise cracking and relieve strains that are encountered if the furnace power supply were abruptly turned off. These strains develop because CdS, being hexagonal, has different coefficients of expansion depending on the orientation, and since the ingot is still polycrystalline the interlocking crystals tend to set up strains. Hence these strains are minimised with a slow cool.

After removing the boule, single crystal sections are then sliced out. The CdS has typically a resistivity of 0.1 to 5 ohm-cm. To produce high resistivity and photoconducting crystals the CdS is sulphur compensated by further heat treatment. The crystal to be heat treated is sealed under vacuum into a quartz tube that contains enough sulphur to give a pressure of sulphur of about 0.2 of an atmosphere at 850°C. After about 24 hours in a furnace at this temperature the tube is withdrawn and quickly quenched in cold water. This entraps the sulphur and gives the crystal high resistivity and photo-conductivity. The quenching procedure is, of course, only done on single crystals that have been cut out from the polycrystalline boule.

The CdS crystal fabricated into an amplifier was Eagle-Picher Co., material designated "high purity CdS, Grade B". The grade refers to the range of resistivity available by varying the illumination intensity.

An analysis of a piece of CdS having the same classification was carried out using an A.E.I. m.s.7 spark source mass spectrometer. The sample was ground in an agate mortar and mixed with ultra-pure carbon powder and compressed to form conducting electrodes. The impurity concentration measured is given in table 17. The impurity contribution from the carbon is given in the second column of figures.

TABLE 17

m.s.7 Analysis of CdS sample

Element	Impurity concentration (p.p.m. atomic)	
	CdS	Carbon Blank
P_b	1.2	1.2
In	61	n.d.
Ag	4.0	1
Br	1.0	n.d.
Zn	4,700	n.d.
Cu	2.4	n.d.
Cr	21	n.d.
K	0.7	0.7
Cl	26	n.d.
Al	19.5	n.d.
F	0.6	n.d.

n.d. = not detected

APPENDIX 2

X-ray orientation

The CdS crystals and quartz transducers were orientated using X-rays as described in sections 3.2.1 and 3.2.3. In this appendix the relevant X-ray diffraction patterns are discussed.

The thickness of the CdS crystals used prohibited X-ray transmission, therefore the Laue back reflection technique was used for CdS orientation.

A back reflection photograph with the incident X-ray beam parallel to the CdS 'C' axis shows hexagonal symmetry, fig.11a. If the CdS is rotated about the 'C' axis so that the hexagon represented by the six inner images has two faces in the vertical plane then the crystal has a plane of the group $\{11\bar{2}0\}$ vertical and a plane of the group $\{\bar{1}100\}$ horizontal. For fabrication of a shear wave device the crystal would be cut to expose these faces. For the introduction of shear waves into CdS the faces $\{11\bar{2}0\}$ and $\{1\bar{1}00\}$ are equivalent as the appropriate piezoelectric constants (d_{15}, d_{24}) and elastic constants (S_{44}, S_{55}) are equal. When using the orientation-grinding device described in section 3.2.3 back reflection photographs were taken with the X-ray beam perpendicular to these faces, fig.11 b, c. The reflected diffraction patterns from these planes were symmetric.

The reflection diffraction patterns show in fig.11 were obtained using a nickel filter to suppress the K_β component of

the characteristic radiation. A relatively small number of additional images appeared if the filter was removed. Analysis, using the Ewald sphere construction, showed that the images were not due to the K_α and K_β components but to the 'white' radiation background. The oscillating-crystal method was used to obtain diffraction patterns where the images were due to the K_α component. Measurement of the layer line separation gave a value for the lattice constant C_o in agreement with the value quoted in the ASTM Index. The diffraction images observed with the oscillating-crystal method were indexed and the orientation of the surfaces established.

The transducers, of α-quartz, were thin enough to allow transmission diffraction patterns to be obtained, fig.21. Analysis showed that the majority of images were due to the 'white' radiation background. The oscillating-crystal method was used to obtain lattice constants and index images in order to confirm the crystal orientation.

REFERENCES

1)	A.R. Hutson	J. Phys. Chem.Solids 8, 467, 1959
2)	Debye model of lattice heat capacity discussed in C. Kittell:	Introduction to Solid State Physics. J. Wiley, N.Y., 1956 p.125
3)	A.R. Hutson	PRL 4,505, 1960.
4)	H.D. Nine	PRL 4,359, 1960.
5)	H. Jaffe, D. Berlincourt et al.	Proc. 14th Symp. Frequency Control. U.S. Army Res.Dev.Lab., Fort Monmouth, 1960. p.20.
6)	D. Berlincourt, H. Jaffe, L. Shiozawa.	PR 129, 1009, 1963
7)	H.D. Nine, R. Truell	PR 123, 799, 1961.
8)	J.H. McFee	Physical Acoustics - vol IV part A. Academic Press, London, 1966, Ed. W.P. Mason.
9)	G. Weinreich.	PR 104, 321, 1956.
10)	A.R. Hutson, J.H. McFee, D.L. White.	PRL 7, 237, 1961.
11)	A.R. Hutson, D.L. White	JAP 33, 40, 1962.
12)	D.L. White.	JAP 33, 2547, 1962.
13)	I. Uchida, T. Ishiguro et al.	JPS JAP. 19, 647, 1964.
14)	T. Ishiguro, I. Uchida, T. Suzuki.	IEEE Int.Conf.Record 12, 93, 1964.
15)	D.I. Bolef et al.	J. Phys. Chem. Solids. 17, 143, 1960.
16)	D.N. Astrov et al	Sov. P-SS 7, 524, 1965
17)	J.H. McFee	JAP 34, 1548, 1963.
18)	S. Wanuga.	Proc. IEEE 53, 555, 1965.
19)	W.C. Wang, J. Pua	Proc. IEEE 51, 1235, 1963.

20)	R.M. White.	IEEE Trans. on Sonics and Ultrasonics. SU-13, 69, 1966.
21)	F.S. Hickernell, N.G. Sakiotis.	Proc. IEEE. 52, 194, 1964.
22)	J.E. May.	Proc. IEEE. 53, 1465, 1965.
23)	J.T. Hanlon.	Proc. IEEE 56, 237, 1968.
24)	R.B. Hemphill et al.	Proc. IEEE 56, 218, 1968.
25)	D.L. White, W.C. Wang.	PR 149, 628, 1966.
26)	D.L. White, E.T. Handelman, J.T. Hanlon.	Proc. IEEE 53, 2157, 1965.
27)	J.T. Hanlon.	Proc. IEEE 55, 1128, 1967.
28)	K. Blotekjaer, C.F. Quate.	Proc. IEEE 52, 360, 1964.
29)	W.H. Haydl, C.F. Quate.	Ap. PL 7, 45, 1965.
30)	H.R. Carleton et al.	Proc. IEEE 53, 1452, 1965.
31)	H. Kroger et al.	PRL 11, 246, 1963.
32)	G.D. Mahon, J.J. Hopfield.	PRL 12, 241, 1964.
33)	J.D. Maines, E.G.S. Paige.	PL 7, 45, 1965.
34)	R.W. Smith.	PRL 9, 87, 1962.
35)	A.R. Hutson.	PRL 9, 296, 1962.
36)	C. Hamaguchi et al	J.P.S. Jap. 20, 1279, 1965.
37)	W.E. Spear, P.G. Le Comber.	PRL 13, 434, 1964.
38)	A.R. Moore.	PRL 12, 47, 1964.
39)	C. Hamaguchi et al.	Jap. JAP 3, 491, 1964.
40)	A.R. Moore, R.W. Smith.	PR 138, A1250, 1965.
41)	J. Okada, H. Machino.	Jap. JAP 2, 736, 1963
42)	R. Yamamoto	Jap. JAP 5, 351, 1966
43)	I. Yamashita et al.	Jap. JAP 4, 470, 1965
44)	W.C. Wang	Ap.PL. 6, 81, 1965

45) E.L. Adler, G.W. Farnel. Proc. IEEE 53, 483, 1965.

46) S.I. Kalshnikov. Sov. P.-SS 6, 252, 1965.

47) R.H. Parmenter. PR 89, 990, 1953.

48) G. Weinrech, H.G. White. PR 106, 1104, 1957.

49) W.C. Wang. PRL 9, 443, 1962.

50) P.D. Southgate, M.N. Spector. JAP, 36, 3728, 1965.

51) B. Tell. PR 136, A772, 1964.

52) H. Kroger. Ap. P.L. 4, 190, 1964.

53) C. Elbaum, R. Truell. Ap. P.L. 4, 212, 1964.

54) W.E. Newell. Trans. Metal. Soc. AIME. 230, 315, 1964.

55) T.A. Midford. JAP 35, 3423, 1964.

56) R.L. Gordon et al. Proc. IEEE 54, 2014, 1966.

57) T. Ishiguro. Jap. JAP 5, 335, 1966.

58) F.S. Hickernell. IEEE Trans. on Sonics. and Ultrasonics. SU-13, 73, 1966.

59) R.H. Fahrig. Electro-chem. Technol. 1, 362, 1963.

60) M. Rubenstein et al. p. 402 1967. Int. Conf. II-VI semiconducting compounds. W.A. Benjamin. N.Y. 1967.

61) L. Clark, J. Woods. B. JAP. 17, 319, 1966.

62) M.R. Lorenz. p. 215, 1967. Int. Conf. II-VI semiconducting compounds. W.A. Benjamin, N.Y. 1967.

63) R.B. Wilson. JAP 37, 1932, 1966.

64) R.W. Smith. R.C.A. Review 12, 350, 1951.

65) J.D. Maines, E.G.S. Paige. S.S. Commun. 4, 381, 1966

66) W.H. Haydl, C.F. Quate. PL 20, 463, 1966.

67) J.H. McFee, P.K. Tien. JAP 37, 2754, 1966.

68) A. Ishida et al. JPS Jap. 21, 186, 1966.

69) J.B. Gunn. 7th Int. Conf. on Physics of Semiconductors. Part 2 - Plasma effects in solids. Academic Press, N.Y., 1965. p.199

70) J.D. Maines. Ap. P.L. 8, 67, 1966.

71) M.K. Parsons, F.L. English. Ap. P.L. 11, 283, 1967.

72) E.G.S. Paige Phonons in perfect lattices and in lattices with point imperfections. Oliver and Boyd, London, 1966. p 255 Ed. R.W.H. Stevenson.

73) G.I. Robertson, E.A. Ash. S.S. Elect. 11, 603, 1968.

74) A.B. Pippard Phil. Mag. 8, 161, 1963.

75) J. Blitz Fundamentals of Ultrasonics, Butterworth, London. 1963.

76) J.J. Kyame JASA 26, 990, 1954.

77) CdS crystals from: Koch Light Ltd.
Eagle-Picher Co.
Semi-elements Inc.

78) G.W. Fynn, W.J.A. Powell Research and Dev. April/May 1965.

79) W.L. Bond J.Sci.I. 38, 63, 1961.

80) A.G. Ingalls Amateur Telescope Making, Scientific American Pub.Co., N.Y., 1935.

81) J. Strong Modern Physical Laboratory Practice, Blackie, London, 1939.

82) W.E. Spear, J. Mort. Proc. PS 81, 130, 1963.

83) W.M. Butler, W. Muscheid. Ann. der Physik 6, 82, 1954.

84) D.J. Page, A.A. Kayali, G.T. Wright. Proc. PS. 80, 1133, 1962.

85) R.W. Smith PR 97, 1525, 1955.

86) F.A. Kroger, G. Diemer, H.A. Klasens. PR 103, 1279, 1956.

87) W.G. Spitzer, C.A. Mead — JAP. 34, 3061, 1963.

88) A.M. Goodman — JAP. 35, 573, 1964.

89) K.W. Boer, R.B. Hall — JAP. 37, 4739, 1966.

90) L.E. Kinsler, A.R. Frey — Fundamentals of Acoustics, Wiley, N.Y., 1950.

91) L. Clark, J. Woods — J.Sci. I. 42, 51, 1965.

92) Quartz transducers from: — Gooch and Housego Ltd. (Also acoustic buffers) Valpey Corp.

93) W.P. Mason — Physical Acoustics and the Properties of Solids, D. Van Nostrand, N.Y., 1958 p.96.

94) D.L. Arenberg. — U.S. Patent 2754238.

95) R.D. Brew — U.S. Patent 2671746.

96) A.P. Kapustin — Zhur. Tekh. Fiz. 22, 765, 1952.

97) R. Truell, C. Elbaum, A. Granto — JAP. 35, 1483, 1965.

98) A.E. Lord, R. Truell. — JAP. 37, 6431, 1966.

99) E.A. Davis, R.E. Drews. — JAP. 38, 2663, 1967.

100) E. Harnik, T. Yasar. — JAP. 36, 2068, 1965.

101) J.H. McFee, T.B. Bateman — JAP. 39, 4471, 1968.

102) A.O. Williams — JASA. 23, 1, 1951.

103) H. Seki, A. Granto, R. Truell. — JASA 28, 230, 1956.

104) E.P. Papadakin — JASA 31, 150, 1959.

105) R. Bass — JASA 30, 602, 1958.

106) Handbook of Chemistry and Physics — Chemical Rubber Co. 48th Edition.

107) A. Rose — R.C.A. Review. 12, 362, 1951.

108) W. Szeto, G.A. Somorjai. — J. Chem. Phys. 44, 3490, 1966.

109)	R.W. Cotterhill	Private communication.
110)	J.T. Hanlon	Proc. IEEE 53, 738, 1965.
111)	D.B. Fraser, J.T. Krause, A.H. Meitzler	Ap. PL. 11, 308, 1967.
112)	F.A. Olson, J.R. Yaeger, R.A. Wilson.	Paper D67. 5th Int. Conf. Acoustics, Liege, 1965.
113)	H.I. Smith	JASA 37, 928, 1965.

ABBREVIATIONS USED:

Ap.PL	Applied Physics Letters
B.JAP	British J. Applied Physics
Jap. JAP	Japanese J. Applied Physics
JAP	J. Applied Physics
JPS Jap.	J. Physical Society of Japan
PL	Physics Letters
PR	Physical Review
PRL	Physical Review Letters
Proc. PS	Proc. Physical Society
Sov. P-SS	Soviet Physics - Solid State
S.S. commun.	Solid State Communication
S.S. Elect.	Solid State Electronics.

LIST OF SYMBOLS

These and minor symbols are also explained in the text.

T.T. = trapping theory.

a	Trapping parameter. T.T.
A	Optical absorbance
b	Trapping parameter. T.T.
c	Elastic constant
c'	Modified elastic constant
d	Piezoelectric constant
D_n	Electron diffusion coefficient
D	Electrical displacement (general)
e	Piezoelectric constant ($e = \frac{d}{s}$)
E	Electric field (general)
E_o	Applied d.c. electric field
E_{ae}	Acousto-electric field
f	Fraction of space charge not trapped
I	Acoustic intensity
j	$\sqrt{-1}$
J	Electric current density
k	Propagation constant
k'	Modified propagation constant
K	Electro- mechanical coupling coefficient
$\bar{\ell}$	Electron mean free path

n_o	Number density of electrons - without acoustic propagation.
n_s	Number density of electrons - producing space charge Q.
q	Electronic charge.
Q	Space charge.
s	Elastic constant. ($s = \frac{1}{c}$)
S	Strain.
t	Time.
T	Stress.
u	Physical displacement of medium.
v_o	Phase Velocity of acoustic wave (passive material).
v_s	Phase velocity of acoustic wave (active material).
v_d	Electron drift velocity.
v'_d	Electron drift velocity. T.T.
α	Attenuation coefficient.
α'	Amplification coefficient. T.T.
γ	Electron drift parameter.
γ'	Electron drift parameter. T.T.
ϵ	Electrical permittivity.
λ	Acoustic wavelength.
μ	Electron mobility.
ν	Cyclic frequency of acoustic wave.
ρ	Mass density.
σ	Electrical conductivity.
τ	Electron trapping relaxation time.
ω	Angular frequency of acoustic wave.
ω_c	Dielectric relaxation frequency

ω_D Diffusion frequency.

ω'_D Diffusion frequency. T.T.

ACKNOWLEDGEMENTS

The research was carried out at the University of Aston in Birmingham during the tenure of an S.R.C. Research Studentship. The author would like to thank the following persons.

Dr. R.W. Cotterhill for suggesting the field of research and able supervision.

Professor S.E. Hunt, Head of the Physics Department, for encouragement of the work.

Mr. D.J. Larner for helpful discussion of the work.

Thanks are due also to the Science Research Council for the provision of the Research Studentship.